A MEASUREMENT OF THE SEMILEPTONIC BRANCHING FRACTION $\mathcal{B}(\bar{B}^0 \to D^{*+}\ell^-\bar{\nu})$ AT CLEO

A Dissertation

Presented to the Faculty of the Graduate School

of Cornell University

in Partial Fulfillment of the Requirements for the Degree of

Doctor of Philosophy

by

Bruce Edmond Berger

January 2001

A MEASUREMENT OF THE SEMILEPTONIC BRANCHING FRACTION $\mathcal{B}(\bar{B}^0 \to D^{*+}\ell^-\bar{\nu})$ AT CLEO

Bruce Edmond Berger, Ph.D.

Cornell University 2001

I present a measurement of the branching fraction of the semileptonic B decay $\bar{B}^0 \to D^{*+}\ell^-\bar{\nu}$ with the CLEO II dataset of 3.14 million $B\bar{B}$ decays. I obtain the result $\mathcal{B}(\bar{B}^0 \to D^{*+}\ell^-\bar{\nu}) = (5.40 \pm 0.18 \pm 0.42) \times 10^{-2}$. I make this measurement via full reconstruction of the $\bar{B}^0$ meson decay products, which entails observing the lepton and all the decay products of the D^{*+}, but not the weakly interacting neutrino. I extract the branching fraction through a fit to the distribution of $\cos\theta_{BY}$, where θ_{BY} is the angle between the parent $\bar{B}^0$ meson and the system Y of its observed decay products in the laboratory frame of reference. This fit separates the signal $\bar{B}^0 \to D^{*+}\ell^-\bar{\nu}$ events from the poorly-understood $B \to D^{*+}X\ell^-\bar{\nu}$ background.

I begin with a overview of the theoretical background for this measurement. I discuss notable features of the CLEO II experiment. I detail the event selection criteria and candidate reconstruction methods, and I describe the methods I use to

model backgrounds. I present the branching fraction fit, and I quantify the various sources of measurement error. I present detailed studies of the reconstruction efficiency for slow charged pions, an important source of systematic uncertainty for this analysis. I conclude by discussing my result in the context of semileptonic B physics.

BIOGRAPHICAL SKETCH

Bruce Edmond Berger was born in 1969 in Berkeley, California. Soon after, he relocated with his parents, Susan and Edmond L. Berger, to Illinois, where Bruce's father works in theoretical particle physics at Argonne National Laboratory. Bruce grew up and attended public schools in Downers Grove, Illinois. The family also spent a total of three years near Geneva, Switzerland, where Bruce's father worked at CERN, and a year in Palo Alto, California, where his father worked at SLAC. Bruce has a younger sister, Catherine and a younger brother, Stephen.

Bruce was first introduced to particle physics by his father. His interest was reinforced by participation in the "Saturday Morning Physics" program at Fermilab during his senior year of high school, and by summer jobs at Argonne and Fermilab during high school and college. Unlike his father, Bruce chose to work in experimental particle physics, as he enjoys working on hardware.

Bruce did his undergraduate work at Princeton University. He earned his A. B. in Physics in 1992. Bruce chose Cornell University for his graduate studies largely because of the presence of the CLEO experiment on campus. Bruce was an active member of the CLEO collaboration, and worked on a number of projects in addition to his analysis of the $\bar{B}^0 \to D^{*+}\ell^-\bar{\nu}$ branching fraction. He was involved in the maintenance and calibration of DR2, the CLEO II drift chamber, and he participated in prototype development for DR3, the CLEO III drift chamber.

Bruce did a number of important studies of the CLEO II slow pion reconstruction efficiency. He was also involved in tuning the VD charge division residuals as part of the CLEO II recompress Monte Carlo project.

Bruce met Francesca Diane Pardo, his wife-to-be, soon after he began his graduate studies at Cornell. The two married in Boston in 1999.

Following his graduation from Cornell, Bruce will move back to California to work at Lawrence Berkeley National Laboratory. He will be involved with the KamLAND neutrino oscillation experiment, located in the Kamioka mine under Mt. Ikenoyama in Japan.

To Francesca

my beloved wife

ACKNOWLEDGEMENTS

I would first like to thank my wife, Francesca Pardo Berger, for her love and support as I worked to complete my graduate degree. I particularly appreciate her patience during this past year, while we have been married but living on opposite coasts.

I thank my father, Edmond L. Berger, for years of reliable advice, support, and encouragement.

I thank Ritchie Patterson, my advisor, for her guidance, feedback, and physics insights, and for a number of good suggestions. Ritchie has always been willing to discuss the analysis and to take the time to understand problems in detail. I would also like to thank Ritchie — and Lawrence — for giving me a place to stay as I worked to finally complete this dissertation.

I thank Persis Drell for getting me started on $D^{*}\ell^{-}\bar{\nu}$ and on the slow pion efficiency studies, and for her confidence in my abilities.

My measurement of the $\bar{B}^{0} \to D^{*+}\ell^{-}\bar{\nu}$ branching fraction was done with a large amount of assistance from others. The other members members of the $B \to D^{*}\ell^{-}\bar{\nu}$ group, namely Bonnie Valant-Spaight, Karl Ecklund, Ritchie Patterson, and Mark Dickson, have been great collaborators. They have provided regular feedback and were the source of many of the ideas incorporated in the analysis. I also thank the $B \to D^{*}\ell^{-}\bar{\nu}$ paper committee, David Cassel, Jon Thaler, Yuichi Kaboto, and

Mark Palmer, who took the time to understand the analysis, and who gave us many useful comments and suggestions.

The slow pion efficiency studies required custom jerry-rigged routines, solutions to the failure modes of using standard routines in unorthodox ways, and a great deal of archaeology in the CLEO code libraries. These studies could not have been done without help from other people at critical times, and I am grateful to them. Ken Bloom got me started with the embedding machinery. Mike Sivertz, Craig Prescott, and Roy Briere were all instrumental in solving or walking me through key problems. I particularly want to thank Lawrence Gibbons for the insight that finally let me get around the worst roadblock, a bug in rerunning `PASS2` on 4s2–3 `.fzx` data skims.

I thank my officemates, Karl Ecklund, Lauren Hsu, Ye Liu, Tom Meyer, Anto Romano, and Bonnie Valant-Spaight, for interesting conversations and commiseration, for helping to provide a comfortable, if occasionally noisy, working environment, and for tolerating my foibles. I also thank my former officemates, Ken Bloom and Dave Crowcroft, for the same reasons, and for sharing my love of baseball.

I gratefully acknowledge the effort of the CESR staff in providing CLEO with excellent luminosity and running conditions.

Finally, I would like to thank everyone else at CLEO who has contributed in some way to the work I did on my measurement of $\mathcal{B}(\bar{B}^0 \to D^{*+}\ell^-\bar{\nu})$ and related projects. These are: Rich Baker, Selden Ball, Alain Bellerive, Véronique Boisvert, Dan Bliss, Adrian Cho, Alexey Ershov, Vitaliy Fadeyev, Andy Foland, Brian Heltsley, J. Kandaswamy, Dave Kreinick, Scott Menary, Ken McLean, David Jaffe, Dan

Peterson, Scott Roberts Steve Richichi, Suzanne Richichi, Ed Thorndike, and Jon Urheim.

TABLE OF CONTENTS

LIST OF TABLES

LIST OF FIGURES

CHAPTER 1

THEORETICAL MOTIVATION

In this work, I describe a measurement of the semileptonic B-meson branching fraction $\mathcal{B}(\bar{B}^0 \to D^{*+}\ell^-\bar{\nu})$, where the charged lepton ℓ is either an electron or a muon. Together, the electron and muon modes account for roughly 10% of neutral B decays. A precise understanding of this decay mode therefore improves our overall knowledge of the B branching fractions. The $\bar{B}^0 \to D^{*+}\ell^-\bar{\nu}$ decay mode is also of particular physics interest, because study of its differential decay rate can be used to measure the CKM matrix element $|V_{cb}|$, one of the fundamental parameters of the standard model.

I present the Feynman diagram for $\bar{B}^0 \to D^{*+}\ell^-\bar{\nu}$ in Figure 1.1. In this decay, a b quark is converted to a c quark through the emission of a virtual W^- boson. The CKM matrix element $|V_{cb}|$ is associated with this vertex. The c quark recombines with the spectator $\bar{d}$ quark to form the D^* vector meson. The virtual W^- decays to a negatively-charged lepton plus an antineutrino. The label q refers to the four-momentum of the virtual W^-, or equivalently, the four-momentum of the lepton-neutrino system. The invariant mass of this system is q^2, the square of the four-momentum transfer.

Figure 1.1 is valid for all three lepton generations. However, I only study

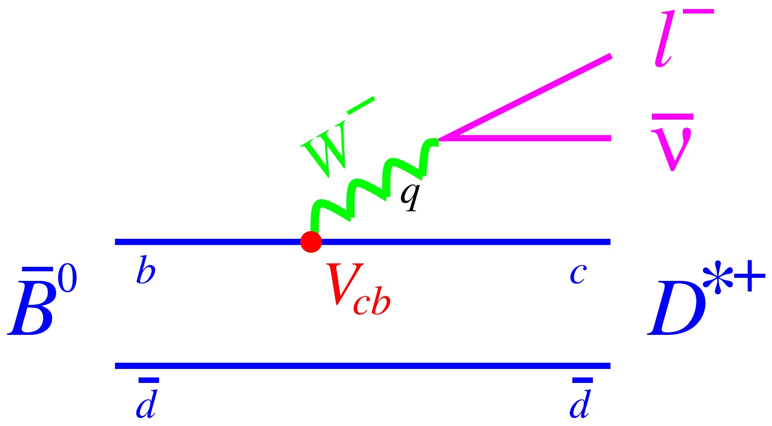

Figure 1.1: The Feynman diagram for $\bar{B}^0 \to D^{*+}\ell^-\bar{\nu}$. The CKM matrix element $|V_{cb}|$ is associated with the vertex of the virtual W and the b and c quarks. The four-momentum of the virtual W boson is labeled q.

those $\bar{B}^0 \to D^{*+}\ell^-\bar{\nu}$ decays in which the final-state charged lepton is either an electron (e) or a muon (μ). Either particle is light enough that I may neglect its mass, unlike the heavier tau (τ). Furthermore, we can observe electrons and muons directly with the CLEO II detector, whereas taus must be reconstructed from their decay products. All tau decays involve a tau neutrino (ν_τ), which we cannot observe. The missing energy of the ν_τ makes the analysis of $\bar{B}^0 \to D^{*+}\tau^-\bar{\nu}_\tau$ difficult. In this work, I use the symbol ℓ to refer to either an electron or muon.

I refer to the decay $\bar{B}^0 \to D^{*+}\ell^-\bar{\nu}$ as a shorthand for both this decay and its charge-conjugate mode $B^0 \to D^{*-}\ell^+\nu$. My analysis combines decays of both charge varieties. Throughout this work, all references to particular decay modes imply the charge conjugate modes as well.

In Section 1.1, I discuss the CKM matrix and the role of the matrix element $|V_{cb}|$ in the unitarity triangle. In Section 1.2, I give a qualitative description of "heavy-quark effective theory," the theoretical framework that describes heavy-meson decays such as $\bar{B}^0 \to D^{*+}\ell^-\bar{\nu}$, and I present several key results from this approach. In Section 1.3, I provide specific formulae for the differential cross section of $\bar{B}^0 \to D^{*+}\ell^-\bar{\nu}$, to which I refer in later chapters.

1.1 The CKM Matrix

Flavor-changing quark transitions in the standard model are described by the coupling of the charged weak current

$$\mathcal{J}^\mu = \bar{u}_i \gamma^\mu \frac{1}{2}(1-\gamma_5) V_{ij} d_j, \tag{1.1}$$

to the W boson via the interaction Lagrangian

$$\mathcal{L}_{int} = -\frac{g}{\sqrt{2}}(\mathcal{J}^\mu W_\mu^+ + \mathcal{J}^{\mu\dagger} W_\mu^-). \tag{1.2}$$

The indices i and j in Equation 1.1 refer to the three quark generations, so that $(u_1, u_2, u_3) \equiv (u, c, t)$, the annihilation operators for the three up-type quarks. Likewise, $(d_1, d_2, d_3) \equiv (d, s, b)$. The unitary matrix V_{ij} is the Cabibbo-Kobayashi-Maskawa (CKM) matrix [1]. This matrix is not diagonal for the familiar quark mass eigenstates. This feature gives rise to the generation-changing quark transitions in the standard model.

The CKM matrix can be thought of as a rotation between the down-type mass eigenstates d, s, and b to a set of weak interaction eigenstates which couple to the up-type quarks only within each quark generation. This rotation can be written:

$$\begin{pmatrix} d' \\ s' \\ b' \end{pmatrix} = \begin{pmatrix} V_{ud} & V_{us} & V_{ub} \\ V_{cd} & V_{cs} & V_{cb} \\ V_{td} & V_{ts} & V_{tb} \end{pmatrix} \begin{pmatrix} d \\ s \\ b \end{pmatrix}. \tag{1.3}$$

While a general unitary 3×3 matrix has 9 independent parameters, the phase invariance of the Lagrangian can be exploited to remove 5 relative phases between quark fields. These relative phases are not physically measurable quantities. A standard general parameterization [2] writes the CKM matrix in terms of three real angles θ_{12}, θ_{13}, and θ_{23}, and one phase δ_{13},

$$V = \begin{pmatrix} c_{12}c_{13} & s_{12}c_{13} & s_{13}e^{-i\delta_{13}} \\ -s_{12}c_{23} - c_{12}s_{23}s_{13}e^{i\delta_{13}} & c_{12}c_{23} - s_{12}s_{23}s_{13}e^{i\delta_{13}} & s_{23}c_{13} \\ s_{12}s_{23} - c_{12}c_{23}s_{13}e^{i\delta_{13}} & -c_{12}s_{23} - s_{12}c_{23}s_{13}e^{i\delta_{13}} & c_{23}c_{13} \end{pmatrix}. \tag{1.4}$$

Here $c_{ij} \equiv \cos\theta_{ij}$ and $s_{ij} \equiv \sin\theta_{ij}$. The presence of the complex phase δ_{13} allows the existence of CP violation in the standard model. As there is a complex phase in the CKM matrix, the rates of charge-conjugate processes need not be exactly the same.

The values of the CKM matrix elements have been measured in a variety of experiments. Assuming the matrix is unitary, the bounds on the CKM matrix elements at the 90% confidence level are [3]:

$$\begin{pmatrix} 0.9745 - 0.9760 & 0.217 - 0.224 & 0.0018 - 0.0045 \\ 0.217 - 0.224 & 0.9737 - 0.9753 & 0.036 - 0.042 \\ 0.004 - 0.013 & 0.035 - 0.042 & 0.9991 - 0.9994 \end{pmatrix}. \tag{1.5}$$

A hierarchy can be discerned in the values of the CKM matrix elements. The on-diagonal elements are close to unity, while the off-diagonal elements follow a pattern,

$$V_{ud}, V_{cs}, V_{tb} \gg V_{us}, V_{cd} \gg V_{cb}, V_{ts} \gg V_{ub}, V_{td}. \tag{1.6}$$

Each successive set of elements is reduced from the previous by a factor of roughly 0.2. This hierarchy is exploited by the Wolfenstein parameterization [4], in which one defines

$$\begin{aligned} s_{12} &\equiv \lambda, && (1.7) \\ s_{23} &\equiv A\lambda^2, && (1.8) \\ s_{13}e^{-\mathrm{i}\delta_{13}} &\equiv A\lambda^3(\rho - \mathrm{i}\eta). && (1.9) \end{aligned}$$

This parameterization has been chosen such that λ accounts for the scale of the matrix elements, while the parameters A, ρ, and η are of order unity. In this scheme, the CKM matrix is written

$$V = \begin{pmatrix} 1-\lambda^2/2 & \lambda & A\lambda^3(\rho - \mathrm{i}\eta) \\ -\lambda & 1-\lambda^2/2 & A\lambda^2 \\ A\lambda^3(1-\rho-\mathrm{i}\eta) & -A\lambda^2 & 1 \end{pmatrix} + \mathcal{O}(\lambda^4). \tag{1.10}$$

Unitary matrices have the property that each column is orthogonal to the complex conjugate of every other column; the same is true of the rows. That is, for $i \neq k$,

$$\begin{aligned} \sum_j V_{ij}V^*_{kj} &= 0, && (1.11) \\ \sum_j V_{ji}V^*_{jk} &= 0. && (1.12) \end{aligned}$$

As each term in the sum is a complex number, these identities can be viewed as triangles in the complex plane. In terms of the Wolfenstein parameterization, four of the six such triangles are near-degenerate, in the sense that one side is of higher order in λ than the other two. One of the remaining two triangles is commonly called the "unitarity triangle," defined by applying Equation 1.12 to the first and third columns of the CKM matrix:

$$V_{ud}V_{ub}^* + V_{cd}V_{cb}^* + V_{td}V_{tb}^* = 0 \tag{1.13}$$

The other non-degenerate triangle, the product of the first and third rows, is simply a mirror image of this one.

I illustrate the unitarity triangle in Figure 1.2. Figure 1.2a shows the graphical representation of Equation 1.13. I also show the angles α, β, and γ. In the Wolfenstein parameterization, to leading order in λ each side of this triangle is proportional to the product $A\lambda^3$. If I scale each side of the triangle down by this factor, I obtain a triangle with unit base length and an apex at the point (ρ, η). Experimental constraints on the unitarity triangle are commonly displayed in this representation, which I illustrate in Figure 1.2b.

The precise measurement of the unitarity triangle is one of the central goals of heavy-flavor physics. This program is not motivated solely by a desire to determine the standard model parameters as well as possible, but to test the standard model itself. If the standard model is not a complete description of the physical world — for example if there is a fourth generation of quarks — then the unitarity triangle may not be a triangle at all. Alternatively, if experiments that study CKM parameters are affected by new physics, the unitary triangle may appear not to close. Thus, the program of measurements of the unitarity triangle is also a

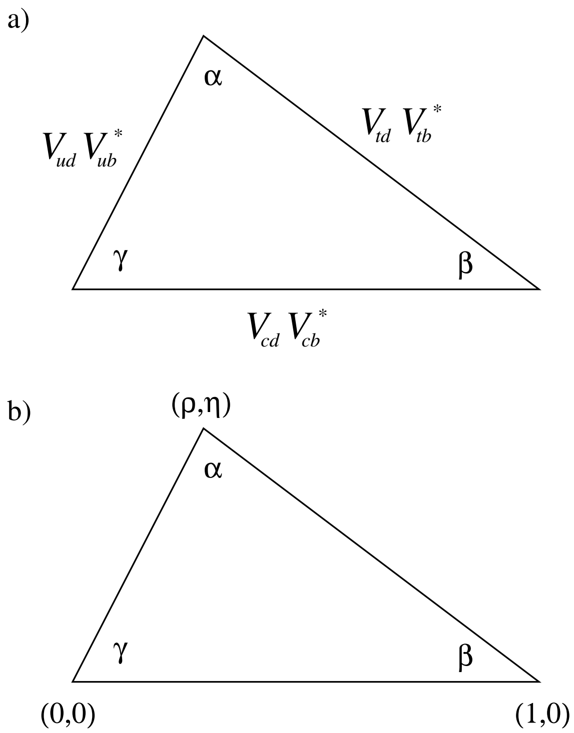

Figure 1.2: The Unitarity Triangle. Figure (a) is the representation of Equation 1.13 in the complex plane, with the lengths of the sides indicated in terms of the CKM matrix elements. Figure (b) show the scaled triangle with vertices $(0,0)$, $(1,0)$, and (ρ,η).

search for signs of physics beyond the standard model.

An examination of Figure 1.2 shows the importance of the matrix element $|V_{cb}|$ in the study of the unitarity triangle. In Figure 1.2a, $|V_{cb}|$ sets the size of the base of the triangle. In terms of the Wolfenstein parameters, $|V_{cb}| \simeq A\lambda^2$ defines the size of the parameter A, as the parameter λ is known to the 1% level based on measurements of kaon decay. Thus, measurement of $|V_{cb}|$ sets the scale of the unitarity triangle via the scaling of Figure 1.2b.

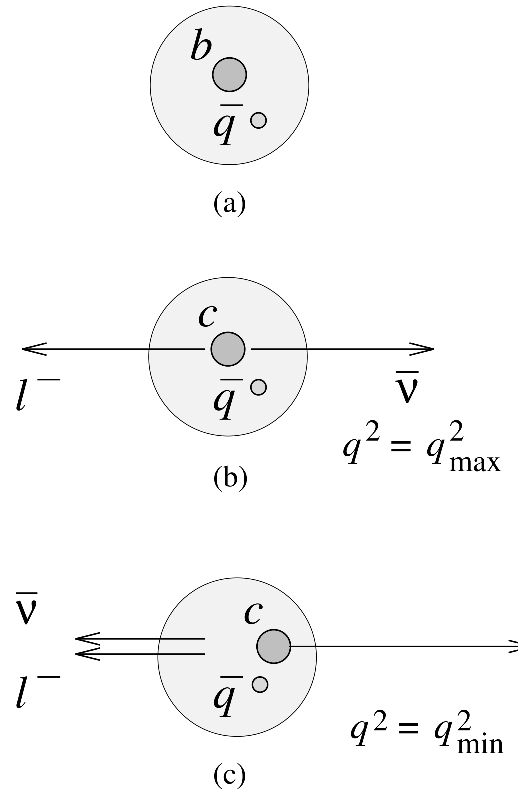

Figure 1.3: Kinematic configurations in semileptonic B decay: (a) the B meson before it decays; (b) the decay configuration $q^2 = q^2_{\rm max}$, or $w = 1$; (c) the decay configuration $q^2 = q^2_{\rm min}$. (Figure excerpted from Reference [5]).

1.2 Heavy-Quark Effective Theory

Heavy-quark effective theory, or HQET, is a theoretical approach used to describe meson systems that contain one heavy quark (b or c) and one light quark (u, d, or s). One can view such systems as analogues of the hydrogen atom. The hydrogen atom can be treated as an electron moving in the central electromagnetic field of the much heavier proton. Likewise, one can approach a heavy-light meson as a light quark moving in the central color field of the heavy quark. I illustrate this description for a B meson in Figure 1.3a. As for the electron in the hydrogen atom, the light quark wavefunctions in the heavy-light meson are then independent of the heavy quark mass and spin orientation, up to hyperfine corrections. Such corrections manifest themselves, for example, as the mass splittings between pseudoscalar and vector mesons, such as the D^*–D mass difference.

To the extent that the light-quark wavefunctions do not depend on the heavy-quark properties, they must be the same in systems with different heavy-quark masses. This property is known as heavy-quark symmetry. This symmetry is exact in the limit that the heavy-quark mass is infinite, in particular, when it is much larger than Λ_{QCD}, the characteristic energy scale of QCD quark binding. This energy scale is on the order of 100 MeV.

In the HQET context, it is possible to make several statements about the form factors of various decays. The form factor of a decay is simply a function that describes the probability of a particular final state configuration. In the decays of heavy-light mesons, the light quark starts in the central color field of the heavy meson. The heavy quark then decays, and in the process it generally acquires some motion relative to its initial state. Figure 1.3c illustrates an extreme case, in which the minimum possible q^2 has been transferred to the lepton-neutrino system in a semileptonic B decay. For a given q^2, the form factor tells us how likely it is that the light quark and the moving heavy quark will reassemble into a particular final state meson. The form factor is similar to an overlap integral between the wavefunction of the light quark in the initial, static color field and the wavefunction in the final, moving color field.

A key result of HQET is that, in the heavy-quark symmetry limit, all decays from one heavy-light meson state to another are described by a single, common form factor. As the initial and final-state light-quark wavefunctions do not depend on the heavy quark, the form factor cannot either. It can depend only on the motion of the final-state heavy quark relative to the heavy quark in the initial state.

The universal form factor is known as the Isgur-Wise function [6], and is written $\xi(w)$. The Isgur-Wise function is written in terms of the variable w, which is defined as

$$w \equiv v \cdot v' = \frac{m_B^2 + m_{D^*}^2 - q^2}{2 m_B m_{D^*}}. \tag{1.14}$$

In this equation, v and v' are the four-velocities of the initial and final mesons in units of the speed of light. In the heavy-quark symmetry limit, these meson four-velocities are identical to the heavy-quark four-velocities. HQET characteristically works in terms of the four-velocities of particles, rather than their four-momenta. The variable w explicitly refers to the relative motion of the initial and final heavy mesons, but it factors out the masses of these particles in such a way that w values across different decay modes can be related.

The shape of $\xi(w)$ is not predicted by HQET. However, its value at $w = 1$ is well-defined. This value corresponds to a special kinematic point in HQET, at which $v = v'$: the final-state meson is at rest relative to the initial meson. It also corresponds to the maximum possible value of q^2. I show this configuration in Figure 1.3b. In this configuration, the color field of the final-state heavy quark is stationary relative to the initial heavy quark. In the heavy-quark symmetry limit, in which the heavy-quark properties do not affect the light-quark wavefunction, the overlap between the initial and final wavefunctions is therefore perfect. The light quark is insensitive to the heavy-quark decay at $w = 1$. As a result, the Isgur-Wise function at $w = 1$ must be equal to unity, that is, $\xi(1) = 1$.

Under the assumption of heavy-quark symmetry, the differential decay rate for $\bar{B}^0 \to D^{*+}\ell^-\bar{\nu}$ can be written in terms of $\xi(w)$ as

$$\begin{aligned} \frac{\mathrm{d}\Gamma(\bar{B}^0 \to D^{*+}\ell^-\bar{\nu})}{\mathrm{d}w} &= \frac{G_F^2}{48\pi^3} m_{D^*}^3 (m_B - m_{D^*})^2 \sqrt{w^2-1}(w+1)^2 \\ &\times \left[1 + \frac{4w}{w+1}\frac{1-2wr+r^2}{(1-r)^2}\right] |V_{cb}|^2 [\xi(w)]^2, \end{aligned} \tag{1.15}$$

where $r = m_{D^*}/m_B$. Outside of the heavy-quark symmetry limit, this equation is no longer valid. The Isgur-Wise function $\xi(w)$ is replaced by a general function $\mathcal{F}(w)$, which takes into account the hyperfine corrections in powers of $\Lambda_{\mathrm{QCD}}/m_b$ and $\Lambda_{\mathrm{QCD}}/m_c$. Unlike $\xi(1)$, the value of $\mathcal{F}(1)$ is shifted away from unity by these corrections. However, an important advantage of the $\bar{B}^0 \to D^{*+}\ell^-\bar{\nu}$ decay mode is that the first-order corrections to $\mathcal{F}(1)$ vanish as a consequence of Luke's theorem [7]. The leading corrections are of order $(\Lambda_{\mathrm{QCD}}/m_b)^2$, $(\Lambda_{\mathrm{QCD}}/m_c)^2$. As a result, $\mathcal{F}(1)$ is known theoretically to about the 5% level [8]:

$$\mathcal{F}(1) = 0.913 \pm 0.042. \tag{1.16}$$

The basic approach used to determine $|V_{cb}|$ is to measure the differential cross section of $\bar{B}^0 \to D^{*+}\ell^-\bar{\nu}$, and then to fit the data with a simple functional form for $\mathcal{F}(w)$. The value of $\mathcal{F}(1)|V_{cb}|$ can then be inferred from the fit function at $w = 1$. This approach was used in a previous CLEO measurement [9]. In that

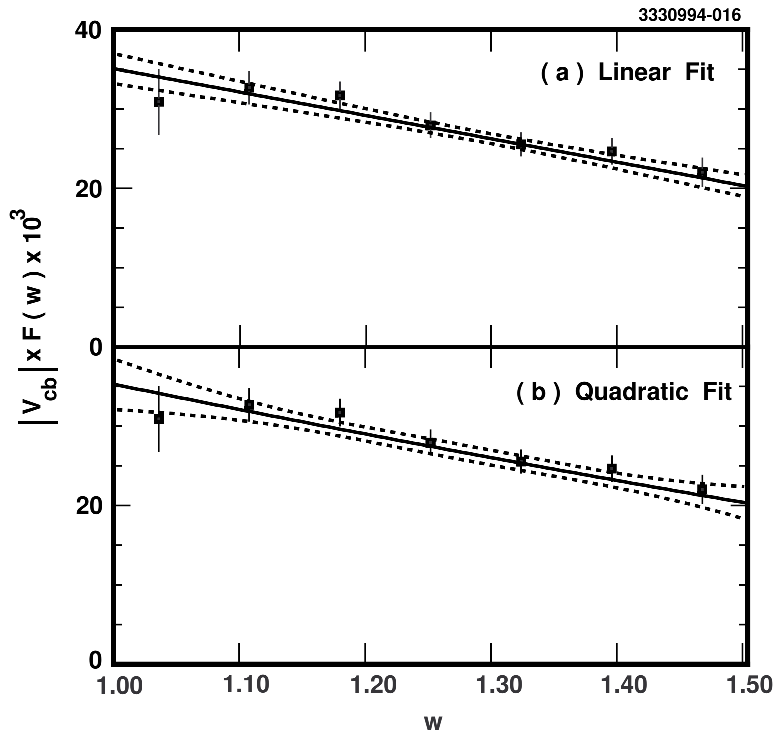

Figure 1.4: The measurement of $|V_{cb}|\mathcal{F}(w)$ in the 1995 CLEO $B \to D^* \ell^- \bar{\nu}$ analysis. The fit (a) assumes a linear form of $\mathcal{F}(w)$, while (b) assumes a quadratic form. The solid curves are the fits, the dotted represent variations in the fit parameters of one standard deviation. (Figure excerpted from Reference [9])

analysis, both $\bar{B}^0 \to D^{*+} \ell^- \bar{\nu}$ and $B^- \to D^{*0} \ell^- \bar{\nu}$ were reconstructed in bins of w. The data were then fit with both linear and quadratic forms of $\mathcal{F}(w)$. I show the results of the fit in Figure 1.4. In this figure, the data have been scaled to account for both the reconstruction efficiencies and the all factors in Equation 1.15 other than $\mathcal{F}(w)|V_{cb}|$. The result of this analysis, corrected to account for subsequent improvements in measurements of the $\bar{B}^0$ and B^+ lifetimes and the D^{*+} decay branching fractions, is

$$\mathcal{F}(1)|V_{cb}| = 0.0354 \pm 0.0019 \pm 0.0019 \pm 0.0003. \tag{1.17}$$

The three errors here are statistical, systematic, and that due to the lifetime measurement.

1.3 The $\bar{B}^0 \to D^{*+}\ell^-\bar{\nu}$ Decay Distribution

In this section, I provide formulae for the differential decay rate of $\bar{B}^0 \to D^{*+}\ell^-\bar{\nu}$ in terms of several form factors. This decay can be fully described by a set of three independent form factors, and there are a number of different ways to define such sets. I will mention a few of these sets and define the relationships between them. Finally, I will specify two HQET parameterizations in terms of these form factors. One is the "linear HQET" parameterization assumed in a previous CLEO analysis [10] of the $B \to D^*\ell^-\bar{\nu}$ form factors. The other is the theoretical result of Caprini, Lellouch, and Neubert [11], derived in the HQET framework through the application of dispersive bounds and unitarity constraints.

In general, I follow the notation of Richman and Burchat [5]. The exception is that I write formulae specific to $\bar{B}^0 \to D^{*+}\ell^-\bar{\nu}$ where they give more general expressions for semileptonic decays of pseudoscalar to vector mesons $P \to V\ell\nu$.

A $\bar{B}^0 \to D^{*+}\ell^-\bar{\nu}$ decay can be fully described by the four kinematic variables q^2, $\cos\theta_\ell$, $\cos\theta_{D^*}$, and χ. The first, q^2, is the invariant mass of the virtual W boson, or equivalently that of the lepton-neutrino system. The other three are decay angles illustrated in Figure 1.5. The angle θ_ℓ is that between the charged lepton

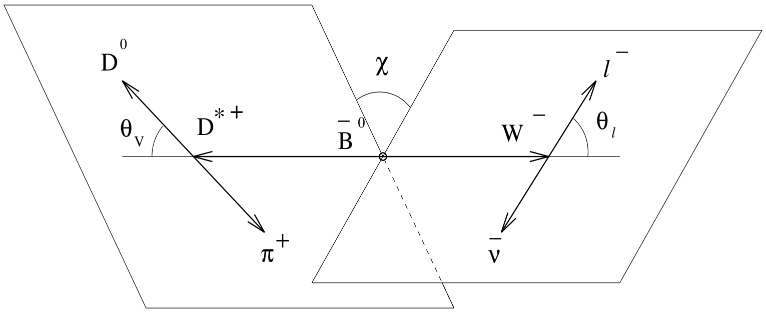

Figure 1.5: The definition of the angles θ_ℓ, $\theta_{D^*}(\equiv \theta_V)$, and χ. The D^* and W are drawn in the B rest frame, in which they are back-to-back. The lepton and neutrino are drawn back-to-back in the W rest fame. Likewise, the D and slow π are shown back-to-back in the D^* rest frame.

in the W rest frame and and the direction of motion of the W in the B rest frame. Similarly, θ_{D^*} is the angle between the D in the D^* rest frame and the direction of the D^* in the B rest frame. Finally, χ is the angle between the two decay planes; specifically, it is the angle in the B rest frame between the projections of the ℓ and the D onto the plane perpendicular to the D^*–W decay axis.

These definitions represent a particular choice between the two pseudoscalar daughters of the D^*. One can consistently replace the D in the definitions above with the slow π. In that case $\theta_{D^*} \to \pi - \theta_{D^*}$ and $\chi \to \pi - \chi$. All the formulae I give below are invariant under such transformations.

The differential decay rate for $\bar{B}^0 \to D^{*+}\ell^-\bar{\nu}$ can be written in terms of these four kinematic variables as:

$$\frac{\mathrm{d}\Gamma(\bar{B}^0 \to D^{*+}\ell^-\bar{\nu}, D^{*+} \to D^0\pi^+)}{\mathrm{d}q^2\,\mathrm{d}\cos\theta_\ell\,\mathrm{d}\cos\theta_{D^*}\,\mathrm{d}\chi} = \frac{3G_F^2|V_{cb}|^2 p_{D^*} q^2}{8(4\pi)^4 m_B^2}\mathcal{B}(D^{*+} \to D^0\pi^+)$$

$$\times \Big\{ \quad (1-\cos\theta_\ell)^2 \sin^2\theta_{D^*}[H_+(q^2)]^2$$

$$
\begin{aligned}
&+ \quad (1+\cos\theta_\ell)^2 \sin^2\theta_{D^*} [H_-(q^2)]^2 \\
&+ \quad 4\sin^2\theta_\ell \cos^2\theta_{D^*} [H_0(q^2)]^2 \\
&- \quad 4\sin\theta_\ell\,(1-\cos\theta_\ell)\sin\theta_{D^*}\cos\theta_{D^*}\cos\chi\, H_+(q^2)\, H_0(q^2) \\
&+ \quad 4\sin\theta_\ell\,(1+\cos\theta_\ell)\sin\theta_{D^*}\cos\theta_{D^*}\cos\chi\, H_-(q^2)\, H_0(q^2) \\
&- \quad 2\sin^2\theta_\ell \sin^2\theta_{D^*}\cos 2\chi\, H_+(q^2)\, H_-(q^2) \quad \Big\}. \qquad (1.18)
\end{aligned}
$$

This formula is fairly general. It assumes only the $(V-A)$ structure of the lepton current in the standard model and that the lepton mass may be neglected. As the B has spin zero, the W and D^* must have opposite helicity in the decay. The functions $H_\pm(q^2)$, $H_0(q^2)$ are simply the helicity amplitudes for the three possible helicity states of the virtual W. These helicity amplitudes, which are one complete set of $D^{*+}\ell^-\bar{\nu}$ form factors, must be specified by a particular theory or model.

In equation 1.18, the quantity p_{D^*} is the magnitude of the three-momentum of the D^* meson in the B rest frame. It is related to w by the equation:

$$p_{D^*} = m_{D^*}\sqrt{w^2-1}. \qquad (1.19)$$

As w depends solely on q^2 and the masses of the B and D^* mesons (Equation 1.14), p_{D^*} depends only on q^2, and not on any of the other kinematic variables.

As an example, in Figure 1.6 I plot the shape of the differential form factor expression of Equation 1.18 versus the four kinematic variables. Each plot is integrated over the other three variables. I obtained these shapes from the distribution of events in the signal Monte Carlo sample, which I describe in more detail in Section 3.3.1. I describe the form factors used to generate these events below.

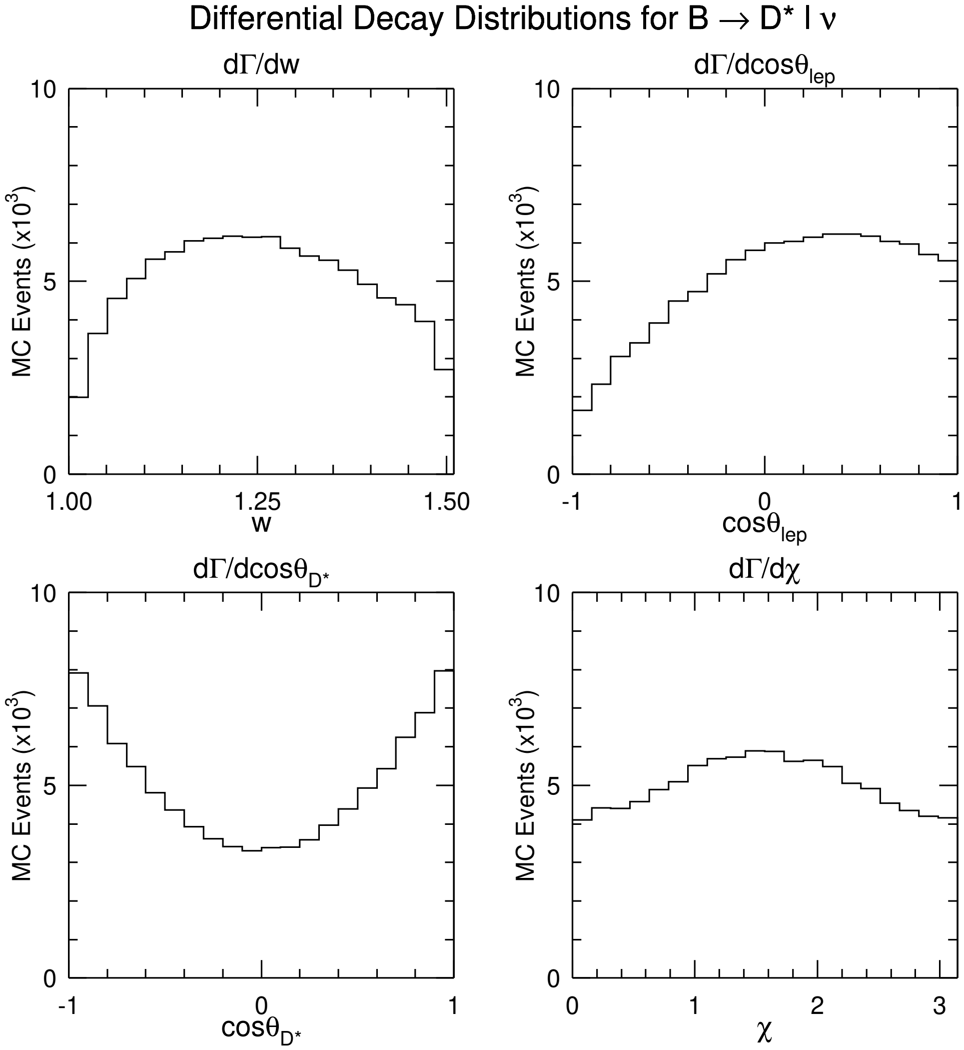

Figure 1.6: The differential decay rate distributions of $\bar{B}^0 \to D^{*+}\ell^-\bar{\nu}$ Monte Carlo events. I show the distribution of 100,000 signal Monte Carlo events at generator level versus the four kinematic variables w, $\cos\theta_\ell$ ($\equiv \cos\theta_{\rm lep}$), $\cos\theta_{D^*}$, and χ. These curves are equivalent to the shape of the differential distribution versus each variable with the other three integrated out. The events were generated with a linear HQET parameterization (Equation 1.36), with the parameters $\rho^2_{h_{A_1}} = 0.92$, $R_1 = 1.24$, and R_2=0.72.

Another common set of form factors is $A_1(q^2)$, $A_2(q^2)$, and $V(q^2)$. These functions are defined by writing the matrix element for the $\bar{B}^0 \to D^{*+}\ell^-\bar{\nu}$ decay in the form:

$$\begin{aligned}
\langle D^*(p_{D^*},\varepsilon)|(V^\mu - A^\mu)|B(p_B)\rangle &= \frac{2\mathrm{i}\epsilon^{\mu\nu\alpha\beta}}{m_B + m_{D^*}}\varepsilon^*_\nu(p_{D^*})_\alpha(p_B)_\beta V(q^2) \\
&- (m_B + m_{D^*})\varepsilon^{*\mu}A_1(q^2) \\
&+ \frac{\varepsilon^*\cdot q}{m_B + m_{D^*}}(p_B + p_{D^*})^\mu A_2(q^2). \quad (1.20)
\end{aligned}$$

Here ϵ is the polarization four-vector of the D^{*+}. This formula is again a general one that assumes only a $(V - A)$ current and that the lepton mass is negligible.

The helicity amplitudes $H_\pm(q^2)$, $H_0(q^2)$ are related to the form factors $A_1(q^2)$, $A_2(q^2)$, and $V(q^2)$ by the expressions:

$$H_0(q^2) = \frac{1}{2m_{D^*}\sqrt{q^2}}\left[(m_B^2 - m_{D^*}^2 - q^2)(m_B + m_{D^*})A_1(q^2) - \frac{4m_B^2 p_{D^*}^2}{m_B + m_{D^*}}A_2(q^2)\right], \quad (1.21)$$

$$H_\pm(q^2) = (m_B + m_{D^*})A_1(q^2) \mp \frac{2m_B p_{D^*}}{m_B + m_{D^*}}V(q^2). \quad (1.22)$$

I now turn to the framework of heavy-quark effective theory. HQET is written in terms of the four-velocities v_B and v_{D^*} instead of the four-momenta p_B and p_{D^*}. The $\bar{B}^0 \to D^{*+}\ell^-\bar{\nu}$ matrix element is

$$\begin{aligned}
\langle D^*(v_{D^*},\varepsilon)|(V^\mu - A^\mu)|B(v_B)\rangle &= \sqrt{m_B m_{D^*}}\,\big[\mathrm{i}h_V(w)\epsilon^{\mu\nu\alpha\beta}\varepsilon^*_\nu(v_{D^*})_\alpha(v_B)_\beta \\
&- h_{A_1}(w)\varepsilon^{*\mu}(w+1) + h_{A_2}(w)(v_B)^\mu\varepsilon^*\cdot v_B \\
&+ h_{A_3}(w)(v_{D^*})^\mu\varepsilon^*\cdot v_B\big]. \quad (1.23)
\end{aligned}$$

This equation contains four HQET form factors, $h_V(w)$, $h_{A_1}(w)$, $h_{A_2}(w)$ and $h_{A_3}(w)$. However, there are only three independent form factors, as $h_{A_2}(w)$ and

$h_{A_3}(w)$ alway occur in observables in the combination:

$$h_{A_3}(w) + r\, h_{A_2}(w), \tag{1.24}$$

where $r = m_{D^*}/m_B$ again. These HQET form factors are related to $V(q^2)$, $A_1(q^2)$, and $A_2(q^2)$ by:

$$\begin{aligned} \frac{2\sqrt{m_B m_{D^*}}}{m_B + m_{D^*}} V(q^2) &= h_V(w) \\ \frac{m_B + m_{D^*}}{2\sqrt{m_B m_{D^*}}} A_1(q^2) &= \frac{w+1}{2} h_{A_1}(w) \\ \frac{2\sqrt{m_B m_{D^*}}}{m_B + m_{D^*}} A_2(q^2) &= h_{A_3}(w) + r\, h_{A_2}(w). \end{aligned} \tag{1.25}$$

Following Neubert [12], I write two ratios of form factors:

$$\begin{aligned} R_1(w) &\equiv \frac{h_V(w)}{h_{A_1}(w)} = \left[1 - \frac{q^2}{(m_B + m_{D^*})^2}\right] \frac{V(q^2)}{A_1(q^2)}, \\ R_2(w) &\equiv \frac{h_{A_3}(w) + r\, h_{A_2}(w)}{h_{A_1}(w)} = \left[1 - \frac{q^2}{(m_B + m_{D^*})^2}\right] \frac{A_2(q^2)}{A_1(q^2)}. \end{aligned} \tag{1.26}$$

These ratios are motivated by heavy-quark symmetry considerations. In the heavy-quark symmetry limit, the HQET form factors have the relations:

$$h_V(w) = h_{A_1}(w) = h_{A_3}(w) = \xi(w), \tag{1.27}$$

$$h_{A_2}(w) = 0, \tag{1.28}$$

where $\xi(w)$ is the Isgur-Wise function. In this limit, the form factor ratios are simply unity for all w. Outside the heavy-quark symmetry limit, $R_1(1)$ and $R_2(1)$ are corrected to values away from unity, just as $\mathcal{F}(1)$ differs from unity. However, the expected w dependence of $R_1(w)$ and $R_2(w)$ is very weak.

The helicity amplitudes $H_0(w)$, $H_\pm(w)$ can be expressed in terms of $h_{A_1}(w)$, $R_1(w)$, and $R_2(w)$. These relations are

$$H_0(w) = (m_B - m_{D^*})\sqrt{\frac{m_B m_{D^*}}{q^2(w)}}(w+1)h_{A_1}(w)\left[1 + \left(\frac{w-1}{1-r}\right)(1 - R_2(w))\right], \quad (1.29)$$

and

$$\begin{aligned} H_\pm(w) = (m_B - m_{D^*})\sqrt{\frac{m_B m_{D^*}}{q^2(w)}}(w+1)h_{A_1}(w) \\ \times \frac{\sqrt{1 - 2wr + r^2}}{1-r}\left[1 \mp \sqrt{\frac{w-1}{w+1}}R_1(w)\right]. \end{aligned} \quad (1.30)$$

Equation 1.18 for the full differential cross section can be integrated over $\cos\theta_\ell$, $\cos\theta_{D^*}$ and χ to give the differential cross section versus w. This result is generally written in a form parallel to Equation 1.15,

$$\begin{aligned} \frac{d\Gamma(\bar{B}^0 \to D^{*+}\ell^-\bar{\nu})}{dw} &= \frac{G_F^2}{48\pi^3} m_{D^*}^3 (m_B - m_{D^*})^2 \sqrt{w^2-1}(w+1)^2 \\ &\times \left[1 + \frac{4w}{w+1}\frac{1 - 2wr + r^2}{(1-r)^2}\right] |V_{cb}|^2 [\mathcal{F}(w)]^2. \end{aligned} \quad (1.31)$$

In this equation, $\mathcal{F}(w)$ is a function of form factors given by:

$$\mathcal{F}(w) = h_{A_1}(w)\left[1 + 4\frac{w}{w+1}\frac{1 - 2wr + r^2}{(1-r)^2}\right]^{-\frac{1}{2}} \sqrt{[\tilde{H}_0(w)]^2 + [\tilde{H}_+(w)]^2 + [\tilde{H}_-(w)]^2}, \quad (1.32)$$

where $\tilde{H}_0(w)$, $\tilde{H}_\pm(w)$ are related to the form factor ratios $R_1(w)$ and $R_2(w)$ by:

$$\tilde{H}_0(w) = 1 + \left(\frac{w-1}{1-r}\right)(1 - R_2(w)), \quad (1.33)$$

and

$$\tilde{H}_\pm(w) = \frac{\sqrt{1 - 2wr + r^2}}{1-r}\left[1 \mp \sqrt{\frac{w-1}{w+1}}R_1(w)\right]. \quad (1.34)$$

Comparison of Equations 1.29 and 1.30 with Equations 1.33 and 1.34 gives the relations between the $H_{0,\pm}(w)$'s and the $\tilde{H}_{0,\pm}(w)$'s:

$$H_{0,\pm}(w) = (m_B - m_{D^*})\sqrt{\frac{m_B m_{D^*}}{q^2(w)}}(w+1)h_{A_1}(w)\tilde{H}_{0,\pm}(w). \tag{1.35}$$

Within the framework of HQET, one can define a particular parameterization for $\bar{B}^0 \to D^{*+}\ell^-\bar{\nu}$ by simply writing down the forms of $h_{A_1}(w)/h_{A_1}(1)$, $R_1(w)$, and $R_2(w)$ with some number of free parameters. A simple, "linear HQET" parameterization is:

$$\begin{aligned} h_{A_1}(w)/h_{A_1}(1) &= 1 - \rho^2_{h_{A_1}}(w-1), \\ R_1(w) &= R_1(1), \\ R_2(w) &= R_2(1). \end{aligned} \tag{1.36}$$

This description has three free parameters: $\rho^2_{h_{A_1}}$, $R_1(1)$, and $R_2(1)$. It assumes that $h_{A_1}(w)$ is linear in w, and that the form factor ratios $R_1(w)$ and $R_2(w)$ are constant. This parameterization was assumed in the CLEO measurement [10] of the $\bar{B}^0 \to D^{*+}\ell^-\bar{\nu}$ form factor. That analysis fit the full differential decay distribution of the form 1.18 to the distribution of the data in the four kinematic variables with an unbinned maximum likelihood technique. It measured $R_1 = 1.18 \pm 0.30 \pm 0.12$, $R_2 = 0.71 \pm 0.22 \pm 0.07$, and $\rho^2_{h_{A_1}} = 0.91 \pm 0.15 \pm 0.06$, where the first errors are statistical and the second systematic. The correlation coefficients of these measurements were $C(\rho^2_{h_{A_1}}, R_1) = 0.60$, $C(\rho^2_{h_{A_1}}, R_2) = -0.80$, and $C(R_1, R_2) = -0.82$.

Caprini, Lellouch, and Neubert [11] provide a more theoretically driven parameterization based on techniques involving unitarity constraints and dispersive bounds. They obtain the forms:

$$\begin{aligned} h_{A_1}(w)/h_{A_1}(1) &= 1 - 8\rho^2_{h_{A_1}} z + (53\rho^2_{h_{A_1}} - 15)z^2 - (231\rho^2_{h_{A_1}} - 91)z^3, \\ R_1(w) &= 1.27 - 0.12(w-1) + 0.05(w-1)^2, \\ R_2(w) &= 0.80 + 0.11(w-1) - 0.06(w-1)^2. \end{aligned} \tag{1.37}$$

In this parameterization, the form factor $h_{A_1}(w)$ is written in terms of the variable z, which is related to w by

$$z = \frac{\sqrt{w+1} - \sqrt{2}}{\sqrt{w+1} + \sqrt{2}}. \tag{1.38}$$

The slope $\rho^2_{h_{A_1}}$ in the expression for $h_{A_1}(w)$ has the same meaning in both HQET parameterizations. It is the slope of the function $h_{A_1}(w)/h_{A_1}(1)$ versus w, evaluated at the point $w = 1$. (Note that Caprini *et al.* use a somewhat different notation than I do. Their $A_1(w)$ is equivalent to my $h_{A_1}(w)$, and their $\rho^2_{A_1}$ is equivalent to my $\rho^2_{h_{A_1}}$.)

The linear HQET parameterization is less sophisticated than that of Caprini *et al.*, but it does contain the right basic structure. In Figure 1.7, I show the w dependence of $R_1(w)$ and $R_2(w)$ in Equation 1.37. The dependence is clearly very weak. For comparison, I also show the results of the CLEO form-factor analysis, which assumed constant values for R_1 and R_2. The theoretical uncertainties [12] in the predictions for $R_1(1)$ and $R_2(1)$ are about 0.1 and 0.2 respectively, so theory and experiment are in excellent agreement. In addition, as the scale of the w dependence is substantially smaller than the experimental uncertainty, the assumption of constant R_1 and R_2 is clearly a small error.

The greater difference between the parameterizations is in the shape of $h_{A_1}(w)$.

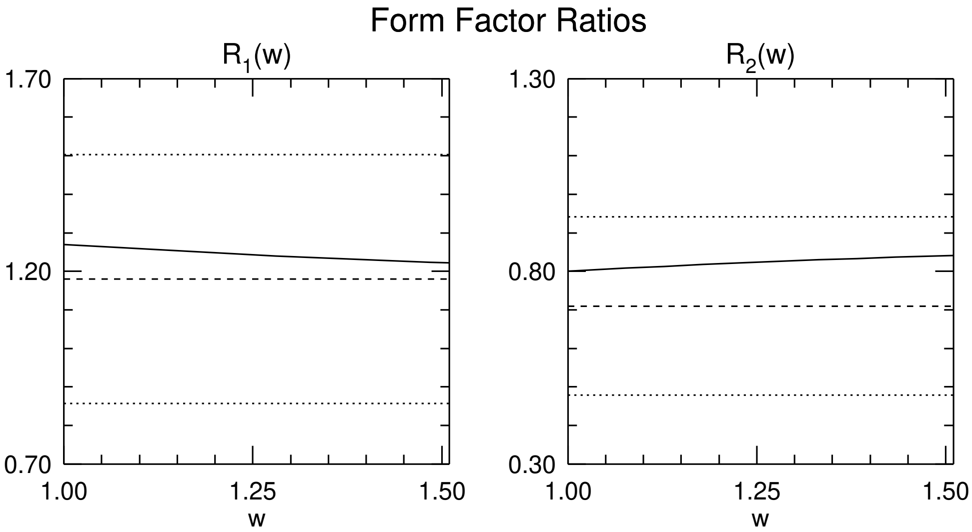

Figure 1.7: The form factor ratios $R_1(w)$ and $R_2(w)$. The solid curves show the w dependence of these functions as predicted by Caprini *et al.* (Equation 1.37). The dashed constant lines give the values measured in the CLEO form-factor analysis, which assumed R_1 and R_2 to be constant. The dotted lines are the errors on the CLEO determinations.

Figure 1.8 compares the shape of $\mathcal{F}(w)$ between the parameterization of Equation 1.37 and a linear form similar to that used in the 1995 CLEO $|V_{cb}|$ analysis [9]. The two forms have similar values over most of the w region, and differ only near the ends of the distributions. Due to the limited phase space available, few events populate these high and low w regions, as can be seen in Figure 1.6. Thus, for simply describing the bulk of the events, the difference between the two parameterizations is small. However, in order to reliably extract $|V_{cb}|$, it is critical that the extrapolation in the low-w region be as correct as possible, and the linear shape appears to underestimate the true value of $|V_{cb}|$. The fits of Caprini *et al.* suggest that the linear fits systematically underestimate $|V_{cb}|$ by roughly 6%. Fu-

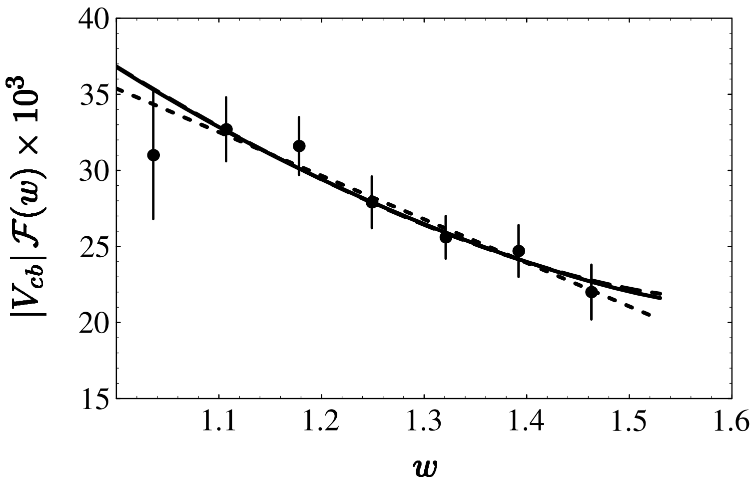

Figure 1.8: A comparison of a linear form of $\mathcal{F}(w)$ to one consistent with the parameterization of Caprini *et al.* (Equation 1.37). The solid curve is the Caprini *et al.* shape, while the (barely visible) curve in long dashes is a second parameterization by the same authors. The dashed line is a straight-line fit. All three curves are ad-hoc fits to the points, which derive from the 1995 CLEO $B \to D^*\ell^-\bar{\nu}$ analysis [9]. (Figure excerpted from Reference [11]).

ture $|V_{cb}|$ analyses should take advantage of the additional knowledge of the form factors contained in the parameterization of Equation 1.37.

Both shapes in Figure 1.8 are *ad hoc* fits directly to the points, which represent the same data shown in Figure 1.4. This approach is, of course, not how such fits are done in practice. Operationally, one first convolves a form factor parameterization with a smearing matrix. The smearing matrix includes both the reconstruction efficiency as a function of w and the probabilities that events will be reconstructed in different w bins. Such a matrix is calculated with signal Monte Carlo events. The convolved shape is compared directly to the event yields from the data as a function of w, and the parameterization adjusted to obtain the best fit.

1.4 Summary

In this chapter, I have outlined both why the CKM matrix element $|V_{cb}|$ is of interest, and how it can be measured through an analysis of the differential decay rate of $\bar{B}^0 \to D^{*+}\ell^-\bar{\nu}$.

To make such a measurement, one must be able to determine accurately the number of $\bar{B}^0 \to D^{*+}\ell^-\bar{\nu}$ events observed as a function of w, accounting correctly for multiple sources of background. One then fits HQET parameterizations to these data, accounting for the w dependence of the parameterization, the efficiency of the reconstruction algorithm, and the smearing between true and reconstructed w. The first step in this process is to learn to measure the overall number of $\bar{B}^0 \to D^{*+}\ell^-\bar{\nu}$ events, and thus the branching ratio for this process. My analysis, which I detail in the following chapters, is devoted to this first step.

CHAPTER 2

THE CLEO II EXPERIMENT

I make my measurement of $\mathcal{B}(\bar{B}^0 \to D^{*+}\ell^-\bar{\nu})$ with data taken by the CLEO II experiment. This experiment collected data from electron-positron collisions at the $\Upsilon(4S)$ resonance produced in the Cornell Electron Storage Ring (CESR). In this chapter, I first outline how B mesons are produced in CESR. I then describe the various components of the CLEO detector used to detect the products of B decay. Finally, I mention some of the tools that I use in my analysis, in particular Monte Carlo simulation of the CLEO data.

2.1 The Cornell Electron Storage Ring (CESR)

The Cornell Electron Storage Ring, or CESR, is a symmetric electron-positron collider located on the campus of Cornell University in Ithaca, New York. This machine collides beams of electrons and positrons in the center of the CLEO detector. The two beams counterrotate within the same accelerator, and both positrons and electrons are accelerated in the same radiofrequency cavities. The two beams share the same orbits within the machine, up to small "pretzel-orbit" perturbations that prevent parasitic beam crossings outside the CLEO interaction point. As a

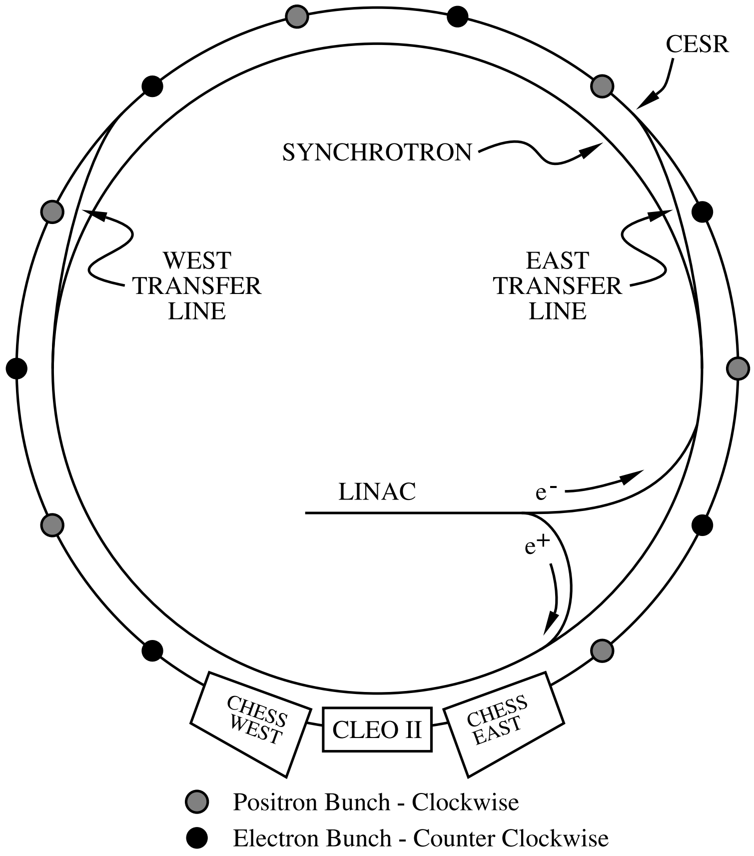

Figure 2.1: A schematic drawing of the accelerators in the Wilson Synchrotron Laboratory. The accelerators and particle bunches are not drawn to scale.

result, the electron and positron beams have the same energy, typically 5.29 GeV.

I show a schematic of the accelerators at the Wilson Synchrotron Laboratory in Figure 2.1. Electrons are first accelerated to energies of approximately 200 MeV in a linear accelerator, or LINAC. These electrons are then directed into the synchrotron, a circular accelerator 768 meters in circumference. The electrons are accelerated to an energy of 5 GeV after about 4000 turns through this machine.

During this process, the strength of both the radiofrequency (RF) accelerating fields and the magnetic fields that bend the beams into circular orbits are increased in synchrony with the increasing energy of the particle beam; hence the term "synchrotron."

After acceleration in the synchrotron, the electron beam is moved into CESR, the storage ring. CESR "stores" the beam of electrons, keeping it rotating counterclockwise at a constant energy. The storage ring resides in the same underground tunnel as the synchrotron. The entire process of acceleration is repeated multiple times to build up a large current of electrons in CESR.

Wilson Laboratory produces positrons by colliding electrons accelerated in the LINAC with a tungsten target. These collisions generate positrons in sprays of many types of particles. The electron beam induces the production of electron-positron pairs when it passes through the strong electric field of the high-Z tungsten nuclei. Some of the positrons thus produced are collected via magnetic collimation of the spray of particles. These positrons are injected into the synchrotron, accelerated to 5 GeV, then transferred to CESR. As with the electron beam, the stored positron beam current is built up through repetition of the process above.

Both the electron and positron beams are held in circular orbits by a series of 86 dipole magnets. The dipole magnets accelerate the electrons and positrons towards the center of the CESR ring to hold them in circular orbits. The charged particles in the beam therefore radiate photons, as does every charged particle that undergoes acceleration. This radiation emerges parallel to the beam. It is characteristic of synchrotron operation, and is known as synchrotron radiation. At

CESR, the beam particles typically radiate 1.2 MeV of energy per turn as X-ray photons. To keep the beams at constant energy, they are accelerated slightly at every turn by a series of RF cavities. At Wilson Lab, some of the synchrotron X-rays are used for various studies of material properties at the Cornell High-Energy Synchrotron Source, or CHESS.

The CESR beams are discrete rather than rather than continuous, each consisting of a number of separate bunches. The number of stored bunches has changed through the history of CESR. The storage ring was originally run with one bunch each of electrons and positrons. In 1982, CESR switched to three-bunch operation (three bunches of each species), and in 1987 to seven bunches. In 1994, the storage ring began circulating nine “trains” of closely spaced bunches. At that point, each train contained two “cars” spaced 42 nanoseconds apart. As of this writing, each train contains five cars, the maximum number, with a 14 ns spacing.

The CESR bunch structure is constrained by the requirement that electron and positron bunches collide at only one point, the center of the CLEO detector. If the beams were guided only with magnetic fields, both beams would follow exactly the same orbit, in opposite directions. CESR uses a scheme of “pretzel orbits” to allow a single interaction point, an approach first developed at Wilson Laboratory. Horizontal and vertical separators — essentially large capacitors — deflect the electron and positron beams in opposite directions. These deflections cause the beam to oscillate around a central orbit. The combination of horizontal and vertical deflections makes the two beams spiral around each other — hence the term “pretzel orbits.” Even with the pretzel scheme, the electron and positron orbits still intersect at multiple locations around the ring. This situation poses no problems so long as these orbit intersections do not correspond to parasitic crossing points — the points at which electron and positron bunches would otherwise collide. However, the parasitic crossing points must be well-separated from the orbit intersections; this requirement sets a maximum on the number of bunches possible in a symmetric single-ring collider.

The CESR beams are focused by 106 quadrupole magnets spaced around the ring. They are further focused down to small size by additional quadrupole magnets near the interaction point to maximize probability of interactions. At the interaction point, each bunch is about 2 cm long, 0.3 mm wide, and 8 μm high.

CESR's performance is measured by its integrated luminosity. The rate of a particular physics process is given by the product of the cross section for that process with the luminosity, so higher luminosities mean more physics data. The CESR luminosity is given by

$$\mathcal{L} = fn\frac{N_{e^+}N_{e^-}}{A}, \tag{2.1}$$

where f is the frequency of revolution, 396 kHz, n is the number of bunches, N_{e^+} and N_{e^-} are the numbers of particles in each bunch, on the order of 1.5×10^{11} per bunch, and A is the cross-sectional area of the beams at the interaction point. Luminosity is measured in units of $\mathrm{cm}^{-2}\mathrm{s}^{-1}$. Integrated luminosities are typically given in inverse picobarns (pb^{-1}) or inverse femtobarns (fb^{-1}). A barn is unit of cross-sectional area; $1\,\mathrm{fb}^{-1} = 10^{39}\,\mathrm{cm}^{-32}$.

I illustrate the performance of CESR in Figure 2.2. This figure gives the

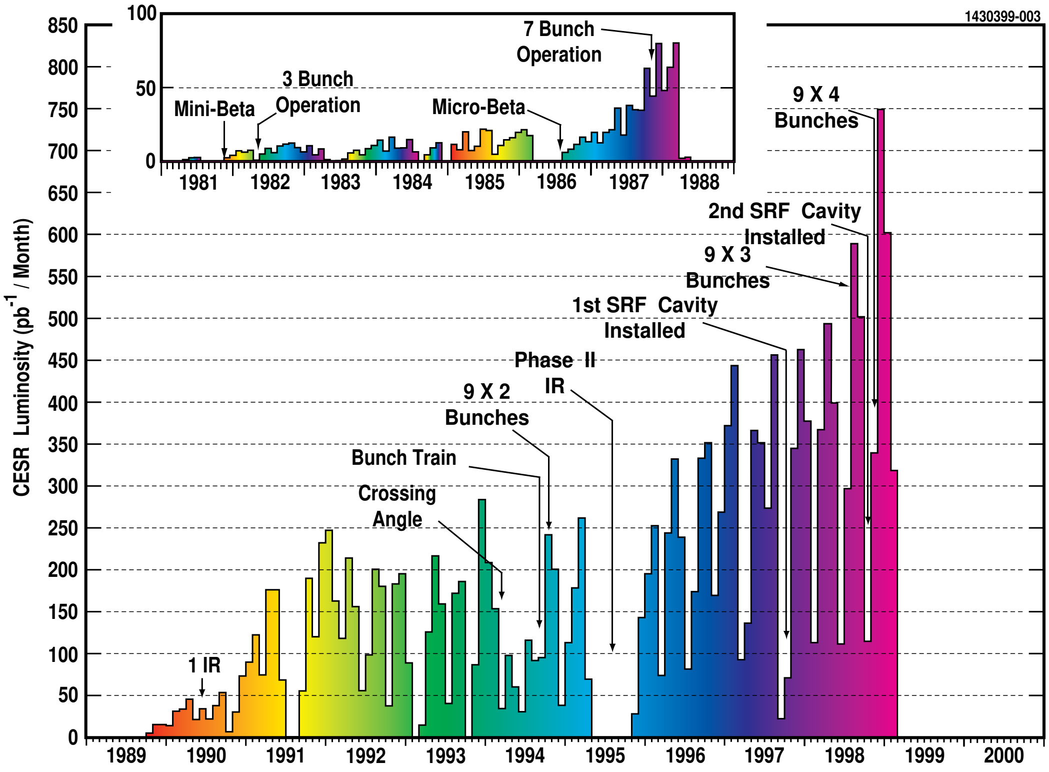

Figure 2.2: The CESR monthly integrated luminosity history. Notable machine upgrades are indicated on the figure.

monthly integrated luminosity during the history of the CLEO, CLEO II, and CLEO II.V detectors. The steady improvement in CESR performance over two decades is a testament to the work of many accelerator physicists at Wilson Laboratory. The original CLEO detector collected data during the decade of the 1980's; CESR luminosities during that era are shown in the inset. My analysis is based on data taken during CLEO II operation between 1989 and 1995. Both the CESR and the CLEO II detector were upgraded during a shutdown in 1995. The CLEO II.V detector then collected data through early 1999. Figure 2.2 also indicates when various storage ring upgraded were performed. CESR's peak luminosity record, set at the end of CLEO II.V running, is $8 \times 10^{32}\,\mathrm{cm}^{-2}\mathrm{s}^{-1}$. The daily and monthly luminosity records are $40\,\mathrm{pb}^{-1}$ and $750\,\mathrm{pb}^{-1}$, respectively. The CLEO collaboration collected a total of $4.7\,\mathrm{fb}^{-1}$ of data during CLEO II operation.

2.2 The $\Upsilon(4S)$ Resonance

We produce B mesons at Wilson lab by colliding the electron and positron beams in CESR at a center-of-mass energy of approximately 10.58 GeV. This energy falls at the peak of the $\Upsilon(4S)$ resonance. The $\Upsilon(4S)$ is a bound state of a b and a $\bar{b}$ quark. The "$4S$" indicates that the $\Upsilon(4S)$ is an S-wave state and that is the fourth such state in the $b\bar{b}$ energy spectrum. The $\Upsilon(4S)$ decays essentially all of the time to pairs of B mesons.

I show the hadronic cross section near the first four Υ states in Figure 2.3. (These data were taken with the CUSB experiment [13], which ran at Wilson Laboratory in parallel with the original CLEO experiment.) The data show the production rates of hadronic final states as a function of e^+e^- center-of-mass energy. This figure illustrates two important features of the Υ resonances. First, the $\Upsilon(4S)$ is wider than the lower three resonances. This difference occurs because the first three resonances do not have sufficient mass to decay to pairs of B mesons. They can decay by reannihilation of the b and $\bar{b}$ quarks. The $\Upsilon(2S)$ and $\Upsilon(3S)$ can also decay to lower Υ resonances plus pairs of pions or photons, or they can decay radiatively to the P-wave χ_b $b\bar{b}$ states. The $\Upsilon(4S)$, on the other hand, has

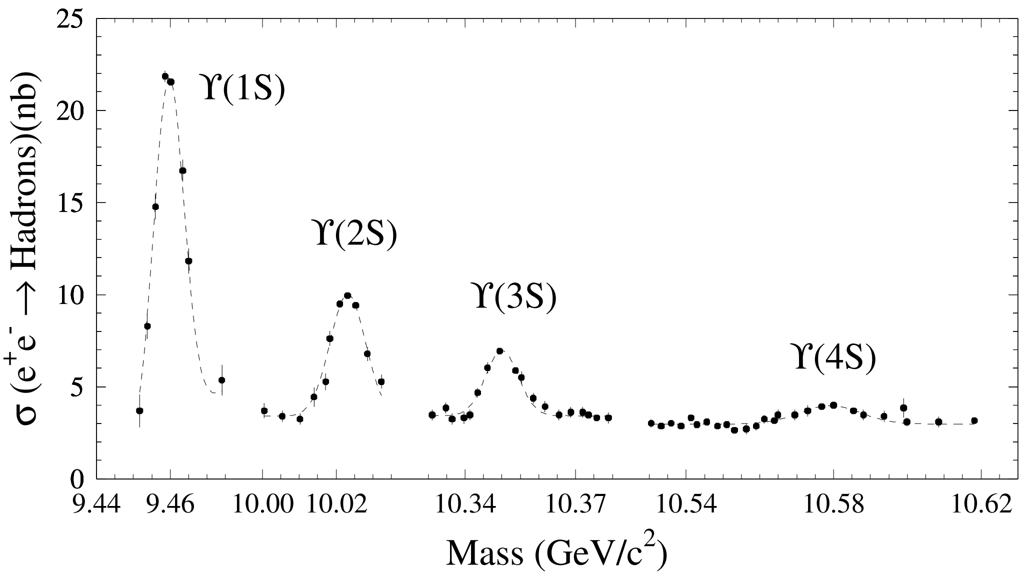

Figure 2.3: The first four S-wave Υ resonances. The figure shows the hadronic cross section versus energy near each Υ mass. Note the difference in resonance amplitude and width between the $\Upsilon(4S)$ and the lower resonances and the significant continuum background.

sufficient energy to dissociate into a pair of B mesons. The rate for this disassociation process is much higher than that of the annihilation or radiation processes, so the $\Upsilon(4S)$ is a shorter-lived state and thus a wider resonance than the lower Υ states. The intrinsic widths of the first three Υ resonances are on the order of 50 keV or less; their observed widths in Figure 2.3 are due to the energy resolution of the CESR beam, which is about 5 MeV. The $\Upsilon(4S)$, on the other hand, has an intrinsic width 10 MeV, large enough to be wider than the lower resonances in the figure.

Figure 2.3 also indicates that the maximum production cross sections are smaller for the higher Υ states than for the lower. This effect has a simple quantum-mechanical explanation. The e^+e^- production cross section for each resonance is related to the rate of $\Upsilon \to e^+e^-$ decay, which is simply the production process in reverse. This decay rate depends on the wavefunction of the Υ state in terms of the typical separation of b and $\bar{b}$ quarks; specifically, the square of the wavefunction at zero separation. This quantity is smaller for the higher Υ states than for the lower, as the typical b–$\bar{b}$ separation is greater.

Another important feature in Figure 2.3 is the large "continuum" background. The cross section for $\Upsilon(4S)$ production at the peak of the resonance is 1.1 nb. However, there are several other physics processes in e^+e^- collisions at this energy that also give rise to hadronic final states. These processes, collectively referred to as the continuum background as they take place both above and below the $\Upsilon(4S)$ resonance, have a total hadronic cross section three times as large as the $\Upsilon(4S)$. The continuum cross section has been measured at CLEO to be 3.35 ± 0.04 nb [15]. Continuum events provide a background to a number of CLEO B-physics analyses. To measure these backgrounds, we take roughly one-third of our data below the $\Upsilon(4S)$ resonance, at a center-of-mass energy of 5.26 GeV.

The continuum consists primarily of $e^+e^- \to q\bar{q}$ events, where q is any quark lighter than a b. Continuum events are a copious source of charm mesons and baryons, and the properties of these states are also studied at CLEO. Some of the hadronic cross section is also due to tau-pair production, $e^+e^- \to \tau^+\tau^-$, where one or both taus decay to hadronic final states. CLEO has a large sample of such tau-pair events, and members of the collaboration conduct active research in tau physics. Finally, various two-photon processes can also produce hadronic states. In such events, both the electron and the positron radiate photons, and the two radiated photons interact to produce hadrons. The decay therefore proceeds as $e^+e^- \to e^+e^-\gamma\gamma \to e^+e^-X$. In such events the final-state electron and positron generally travel down the beampipe and are not observed, so the total visible energy in the event is much less than the center-of-mass energy. In addition to B physics, charm physics, and tau physics, some research on two-photon physics is also carried out at CLEO.

Non-hadronic e^+e^- processes also take place at the $\Upsilon(4S)$ energy, in particular $e^+e^- \to e^+e^-$, Bhabha scattering, and $e^+e^- \to \mu^+\mu^-$, muon-pair production. We also observe radiative versions of these types of events, that is, $e^+e^- \to e^+e^-\gamma$ and $e^+e^- \to \mu^+\mu^-\gamma$. The physics of these processes is well understood, and CLEO collects samples of such events for calibration purposes.

2.3 The CLEO II Detector

I perform my analysis on data collected by the CLEO II detector. I show a cross-sectional view of the entire detector in Figure 2.4. Figure 2.5 is a blowup of one quadrant of the detector. As the CLEO detector is described in detail in a paper published in *Nuclear Instruments and Methods* [14], in this section I only outline the functions of the various elements of the CLEO II detector.

The CLEO II detector has a cylindrical geometry, with its axis along the CESR beampipe. The inner three detector components are charged particle tracking

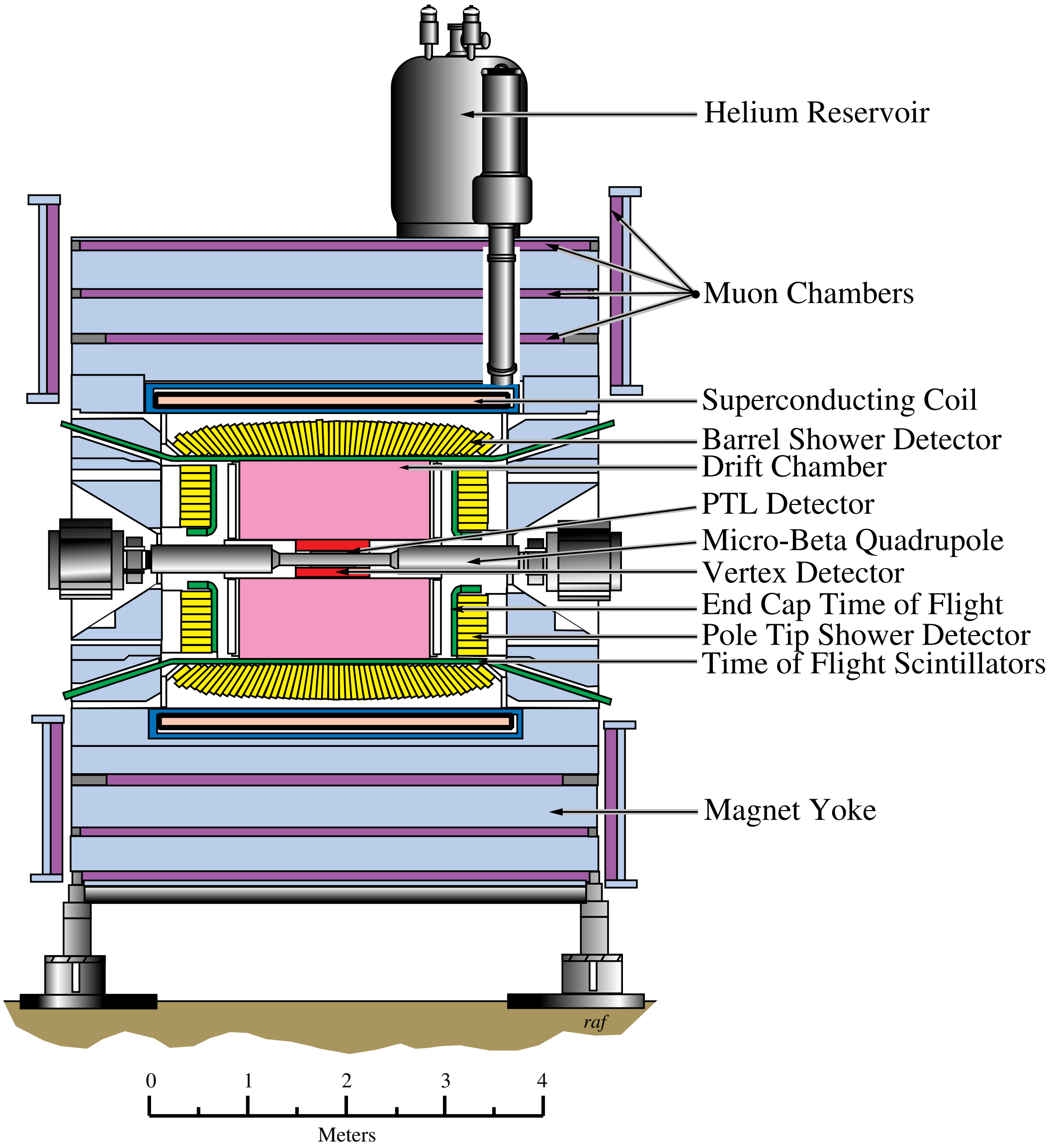

Figure 2.4: A cross-sectional view of the CLEO II detector.

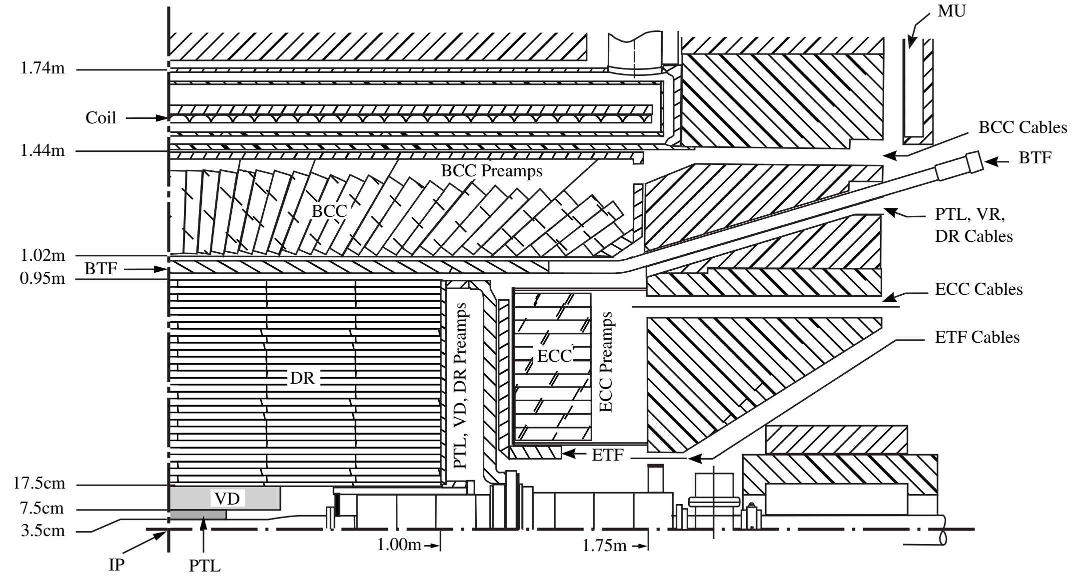

Figure 2.5: A blowup of one quadrant of the CLEO II detector.

devices. Closest to the interaction point are the "Precision Tracking Layers," generally abbreviated PTL or PT. Next out is the "Vertex Detector," or VD. Outside of the VD is the main drift chamber, or DR. My analysis is based primarily on tracking information.

A time-of-flight system (TF) encloses the three tracking chambers. The TF system includes both barrel (BTF in Figure 2.5) and endcap elements (ETF). Beyond the time-of-flight is the cesium-iodide crystal calorimeter (CC), which likewise consists of both barrel (BCC) and endcap (ECC) components. I use calorimeter information only to identify electrons in my analysis.

A superconducting coil magnet sits outside the calorimeter. This magnet provides a 1.5 Tesla field in the tracking chambers, which allows us to measure track momenta. The coil is primarily composed of niobium wire; it runs at liquid helium temperatures. The liquid helium reservoir and refrigeration systems sit atop the CLEO II detector.

Most of the remaining volume of the CLEO II detector is the iron magnet return yoke. The iron in the endcap region can be removed to provide access to the interior components of the detector. The barrel of the return yoke is actually octagonal is cross section rather than circular. The barrel iron is instrumented with streamer counters that serve as a muon detection system (MU). I use this system to identify muons in my analysis.

CLEO uses a standard coordinate system to specify positions within the detector volume. The origin is set at the interaction point, which is the center of the detector. The longitudinal coordinate z runs along the axis of the detector. This axis runs approximately east-west; the positive-z direction is west. The positron beam travels from east to west through the beampipe, the electron beam from west to east. The polar angle θ is measured relative to the positive-z axis. The coordinate r is used at CLEO to mean the radial distance from the axis of the detector; that is, the radius in cylindrical coordinates. Finally, the azimuthal angle ϕ is the angular position in cylindrical coordinates. This angle is measured relative to the horizontal plane at CLEO, with $\phi = 0$ being south.

2.3.1 Tracking Detectors

The three tracking chambers in CLEO II — the PT, VD, and DR — are collectively referred to as the CD, which stands for Central Detector. These chambers all operate on the same basic principles. The active element in each detector is a volume of a gas mixture such as argon-ethane. When charged particles pass through the gas, they ionize gas molecules. Electric fields within the chamber attract the ionized electrons towards sense wires held at high positive voltages, typically 2000 V. The ionized electrons drift towards the sense wires with a velocity characteristic of the gas mixture. As they near a sense wire, the electrons accelerate and begin to induce secondary ionization. For each electron initially ionized by the charged particle, an avalanche of electrons finally reaches the sense wire. This avalanche produces a current on the high-voltage sense wire, and that current is detected and amplified by the detector electronics. The size of the avalanche depends on both the specific gas mixture and the voltage of the sense wire. The increase in the signal from a small number of ionization electrons to a detectable pulse on the sense wire is called the gas gain.

The main information we obtain from a "hit" on a tracking chamber sense wire is the time at which the signal occurred. This time is related to the distance of closest approach of the charged particle to the sense wire. The closer the particle came to the wire, the lower the total drift time, and the earlier the tracking chamber hit. In order to extract these distances of closest approach, we perform careful calibrations of the time-to-distance relationships in our tracking chambers. Our position resolutions are on the order of 150 μm.

Each tracking chamber contains a large array of sense wires strung axially and arranged in multiple concentric layers. As a charged particle traverses the chambers, each layer provides a measurement of its position. From this information

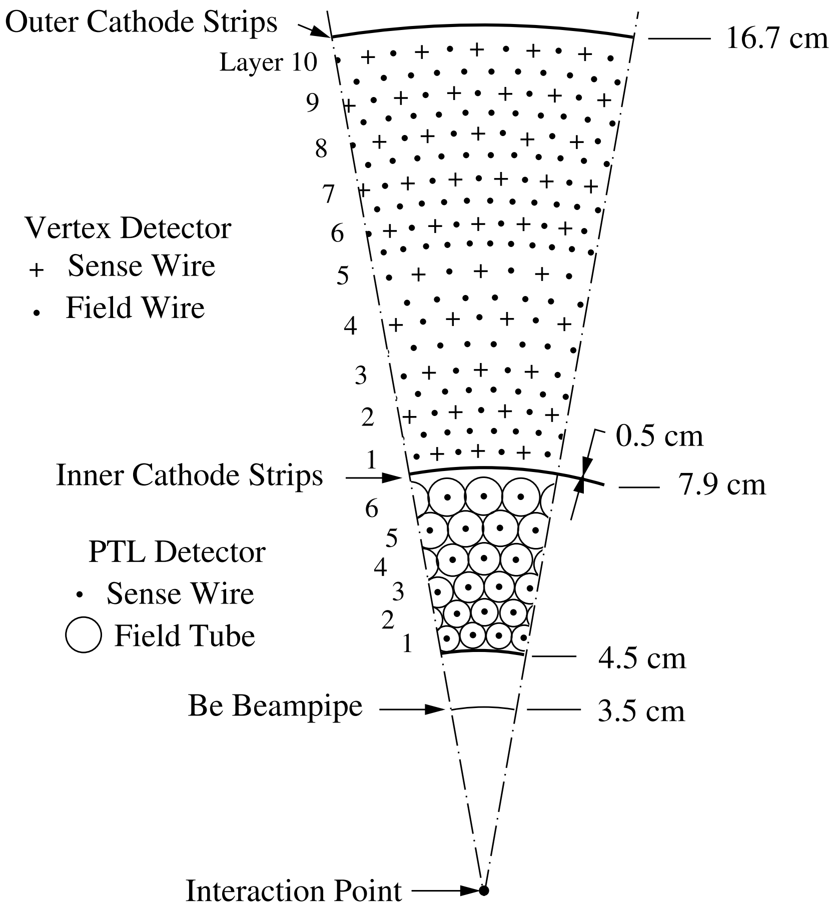

Figure 2.6: A radial cross section of the PT and VD detectors.

we reconstruct the path, or "track," the charged particle took through our detector. The curvature of the track in the 1.5 T magnetic field tells us the momentum of the charged particle. We also extrapolate the track back to the interaction point to learn the initial direction of the charged particle.

The Precision Tracker (PT)

The PT is the innermost component of the CLEO II detector, occupying the region between 4.5 and 7.5 centimeters in radius. I show a radial cross section of this detector in Figure 2.6. The active region of the PT is 50 cm long, 25 on each side of the interaction point. The PT consists of 6 layers of straw tube detectors of increasing size. Each layer contains 64 Mylar tubes, so the PT has a total of 384 active channels. The inner surfaces of the tubes are coated with aluminum and act as a cathode. The anode sense wires, which run down the middle of the straw tubes, are held at high voltage, while the cathodes are held at ground. This configuration provides a radial electric field relative to the center of each tube. The tubes are glued together, and the anode wires are held at either end by an endplate of G10 plastic. The PT was first run with a 50-50 argon-ethane gas mixture. In 1994, the gas was changed to dimethyl ether (DME), which has a lower drift velocity and allows better position resolution.

The Vertex Detector (VD)

The VD sits outside the PT in CLEO II, between 8.1 and 16.4 centimeters. It is also illustrated in Figure 2.6. The active length of the VD is 70 cm, 35 to each side of the interaction point. The VD is a ten-layer wire chamber containing a total of 800 sense wires. Unlike the PT, the entire VD is one continuous gas volume. The electric field "cells" for each high-voltage sense wire are set up by hexagonal arrangements of field wires, held at ground. The endplates are again made of G10. The VD uses at 50-50 mix of argon-ethane gas.

The inner and outer surfaces of the VD act as cathodes for the field cells of the first and last layers of sense wires. The cathode surfaces are segmented finely in z and instrumented. This configuration allows us to detect the image charge of avalanches on wires in the first and last VD layers. We can thus reconstruct the longitudinal position of the tracks as they pass through the first and last VD layers. This measurement is a very important one. Our tracking chambers determine the r–ϕ positions of tracks very well, but as the wires are strung axially, they give little information about the z-positions of tracks. The cathodes provide z-position measurements with a resolution of 1.8 mm.

The VD sense wires are instrumented at both ends of the chamber, whereas PT and DR sense wires are only instrumented at one end. The VD wires are resistive, so the relative amount of charge detected at the two ends of each wire is related to the longitudinal position of the avalanche. This "charge-division" measurement of z position has low resolution, on the order of 2.5 cm, but it is a critical tool in the reconstruction of low-momentum tracks.

The Main Drift Chamber (DR)

The main drift chamber lies between 17.5 and 95 centimeters from the detector axis. It is a total of 192.4 cm long, half to either side of the interaction point. I show the DR cell structure in Figure 2.7. The DR contains a total of 12,240 sense wires arranged in 51 layers. The DR, like the VD, is one continuous gas volume. The field cells are square in shape, formed by 36,270 field wires. As in the VD, the inner and outer DR surfaces act as cathodes for the first and last layers of

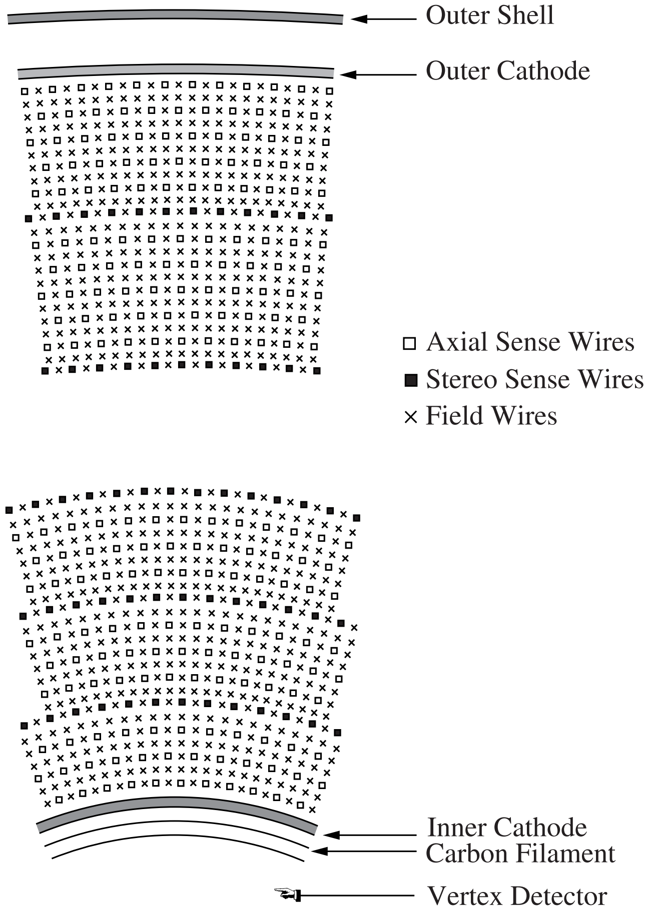

Figure 2.7: A cross-sectional view of the DR cell structure. DR layers 29–39 are omitted from the figure.

sense wires, and these cathodes are segmented and instrumented to measure the z positions of charged tracks. The DR endplates are made of aluminum. The DR uses the same 50-50 argon-ethane gas mixture as the VD.

Most of the DR sense wires are strung axially. However, eleven layers are strung at a small "stereo" angle relative to the axial direction. This arrangement allows us to deduce some z information about charged tracks.

In the DR, we also measure the size of the electronic signal collected on each sense wire. This signal size is proportional to the amount of ionization the charged track induced in that cell. At a given momentum, different species of particle produce different levels of ionization. The amount of ionization can therefore be used to help determine what type of charged particle passed through the detector.

2.3.2 Time-of-Flight System (TF)

The CLEO II time-of-flight system measures the time at which charged particles pass through the device. This information is useful for several reasons. First, the system has very good timing resolution, about 150 picoseconds. CESR timing information allows us to know when each possible bunch collision takes place. We can therefore calculate how long it took a particle to travel from the interaction point to the TF system — hence the term "time of flight." As different particle species have different masses, the relationship between momentum and velocity depends on the type of particle. We can therefore use the time-of-flight system to distinguish different types of particles, in particular, electrons from heavier particles below 800 MeV.

When CESR is run with charged particles in multiple cars per bunch train, there is a discrete ambiguity in the CESR timing information. A signal from CESR informs CLEO that two trains have crossed, but not which two cars collided. The 150 ps resolution of the TF system allows us to resolve this ambiguity between bunch crossings spaced 42 ns apart. The time-of-flight information is used in a "bunchfinder" that decides exactly when the collision takes place.

Finally, the time-of-flight system has a very fast response time. We use signals from the TF in the "trigger," the process that decides when a physics event may have occurred in the detector and the detector data should be "read out" and stored for later analysis.

The time-of-flight system is built of plastic scintillator bars and phototubes. When charged particles pass through the scintillator, they cause the emission of optical wavelength scintillation photons. These photons are detected and amplified by photomultiplier tubes. The barrel time-of-flight system covers the region in polar angle θ between 35° and 90°, measured relative to the detector axis. It is a cylinder of 64 scintillator bars, each 5 cm thick, 10 cm wide, and 279.4 cm long. Each bar is optically connected at each end to a lucite light-guide that conveys the scintillation photons to a phototube outside the CLEO magnetic field. The bars are wrapped in aluminum foil and black tape to prevent the photons from escaping the device. The endcap TF covers the region 18–37°. It is made of wedges of scintillator optically connected directly to phototubes inside the 1.5 T field. We use special high-magnetic-field phototubes for this application, as conventional phototubes will not function in such a high-field environment.

2.3.3 Cesium-Iodide Crystal Calorimeter (CC)

A calorimeter is a device that measures amounts of energy. The CLEO II calorimeter measures the energy of the particles we produce in e^+e^- collisions. Unlike the tracking and time-of-flight systems, which record the passage of particles, the calorimeter operates by stopping the particles it detects. While the total amount of material in front of the calorimeter in the center of the barrel region is only 2.5% of a radiation length, the calorimeter is 16 radiation lengths thick.

The CLEO II calorimeter is made of 7800 crystals of cesium iodide (CsI) doped with thallium. A typical crystal is 5 cm square by 30 cm long. The 6,144 barrel crystals fill the region between 1.02 and 1.44 meters from the detector axis. Each barrel crystal is angled to face towards the interaction point. This alignment is deliberately imperfect, however, to avoid particles slipping between adjacent crystals. The endcap crystals, 828 per end, simply face parallel to the detector axis. The z position of the front faces of the endcap crystals is 1.25 m from the interaction point.

The cesium iodide crystals scintillate when they absorb energy from incident particles. These crystals produce a large amount of light per unit energy, which makes them ideal for use in a calorimeter. Furthermore, the number of photons produced is very nearly a linear function of the amount of energy deposited. This property allows us to measure accurately the energy deposited in the calorimeter. We detect the scintillation light with four photodiodes attached to the back of each CsI crystal.

Both charged and neutral particles deposit energy in the calorimeter. As the other CLEO detector components do not detect neutral species, we reconstruct particles such as photons (γ's) and neutral pions (π^0's) with calorimeter information only. Photons produce electromagnetic showers in the crystals. The incident photon deposits energy, some of which creates electron-positron pairs, which in turn radiate more photons, and so on. The shower typically spreads over multiple crystals, but it is well-localized. A measure of this localization is that the amount of energy deposited in a central 3×3 core of nine crystals (E_9) is close to the total amount of energy deposited in a larger 5×5 block of 25 crystals (E_{25}); that is, $E_9/E_{25} \simeq 1$. We reconstruct the photon energy by summing the energy deposited in a cluster of crystals. We also measure the shower centroid position. If we assume that the photon originated at the interaction point, the fine segmentation of the CC allows us to determine the initial photon direction precisely. In the barrel calorimeter, the photon energy resolution is 1.5% at 5 GeV and 3.8% at 100 MeV, while the angular resolution is 3 mrad at 5 GeV and 11 mrad at 100 MeV. In the endcap, the resolutions are 2.6% and 9 mrad at 5 GeV, and 5.0% and 19 mrad at 100 MeV. We measure neutral pions in the calorimeter by reconstructing the decay $\pi^0 \to \gamma\gamma$ with two photon showers found in the calorimeter. We reconstruct π^0's with a typical mass resolution of 6.5 MeV.

Charged particles also deposit energy in the calorimeter. We project charged tracks from the drift chamber into the calorimeter to match them with reconstructed tracks. In fact, one criterion in photon reconstruction is that a CC shower not be matched to a charged track. Different types of charged particles leave very different shower shapes in the calorimeter. Electrons produce electromagnetic showers like those of photons, with $E_9/E_{25} \simeq 1$. They also deposit all of their energy in the calorimeter, so the ratio of an electron's shower energy E to its track momentum p will be close to unity, $E/p \simeq 1$. Muons, on the other hand, interact minimally in the calorimeter, and are therefore termed "minimum-ionizing particles," or MIP's. They have E/p much less than unity. Charged hadrons, such as pions ($\pi^{\pm}$'s) and kaons ($K^{\pm}$'s) are also MIP's. Unlike the charged leptons, these particles also have strong interactions with with CsI nuclei. Such interactions often produce secondary hadrons which travel to nearby crystals in the calorimeter. Compared to electromagnetic showers, these hadronic showers spread more broadly and extend more deeply into the crystals. They are less well localized, and therefore have E_9/E_{25} values significantly less than unity. I use these differences between the calorimeter signals left by electrons and other charged particles to identify electrons in my analysis.

2.3.4 Muon Detectors (MU)

Muons are far less interactive than the other species of charged particles we produce at CLEO. They are able to penetrate many interaction lengths of the iron magnetic field return yoke. The CLEO II muon system takes advantage of this property to distinguish muons from other charged particles. We instrument the return yoke with streamer counters at depths of 36, 72, and 108 centimeters of iron, as can be seen in Figure 2.4. Additional endcap counters are located at the two ends of the detector. The system detects charged particles that penetrate through the yoke iron to reach the layers of streamer counters. Muons can be expected to penetrate the iron and leave signals in multiple streamer tube layers; other charged particles will not. I use this property to identify muons in my analysis. The muon system covers the angular region in $|\theta|$ from 30° to 90°.

The streamer tubes operate on similar principles to the tracking chambers. I show a cross-sectional view of a portion of the muon system in Figure 2.8. Each

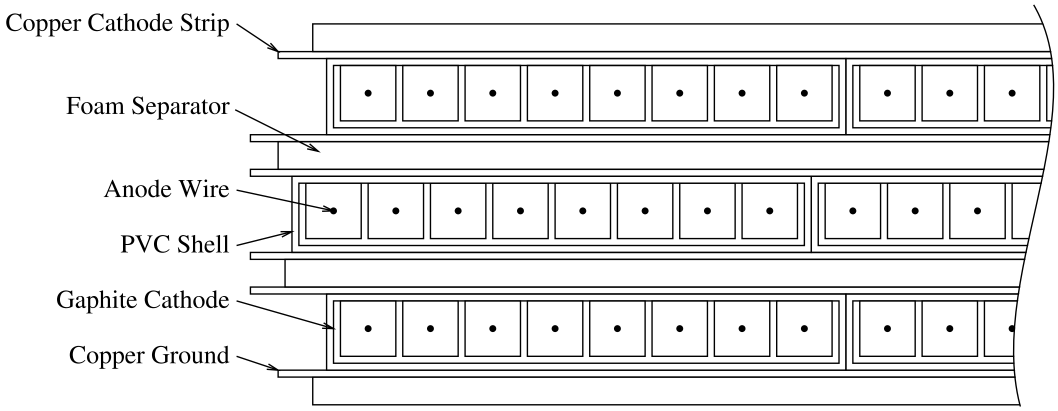

Figure 2.8: A cross-sectional view of a muon superlayer. (Figure excerpted from Reference [30].)

tube has a rectangular profile, 9 mm by 10 mm, and is 5 m long. An anode wire runs down the center of the tube. Three sides of the tube, made of plastic coated with graphite, act as the cathode. The tubes are filled with the same 50-50 argon-ethane gas mixture as the VD and DR. Unlike the tracking chambers, the proportional tubes are only expected to tell us whether a charged particle passed through or not. Multiple anode wires are ganged together, and we determine the position of the track in the direction parallel to the tubes via charge division with a resolution of 2.5 cm. We also measure the position perpendicular to the wires with external copper readout strips that detect the image charge collected on the wires. Charge-division measurements with the copper strips allow position measurement with a resolution of 5.3 cm. The streamer tubes are arranged in three-layer superlayers at each of the three depths, for a total of nine layers of streamer tubes. Like the magnet return yoke, the muon system is octagonal in cross section.

2.3.5 Trigger and Data Acquisition Systems

The subsystems of the CLEO detector transform the effects of various particles — the pulses on sense wires and flashes of light — into electronic signals. The potential amount of information involved is enormous. There are over 20,000 electronics channels in the CLEO II detector, and the CESR bunch train crossings occur at a rate of 3.6 MHz. Furthermore, the process of reading information out of the detector introduces "dead time," periods during which the detector cannot record physics data. We must be judicious in selecting when to save detector information for later analysis.

The trigger is the process through which we select which events to commit to permanent storage. This process is broken up into several stages, or "levels." Each level of the trigger must accept a smaller event rate, but can take more time and can use more detector information. Blocks of the detector are typically grouped together in trigger decisions. The trigger therefore looks at the detector with much lower resolution than a physics analysis job. This approach allows the trigger processes to work more rapidly.

The first, "Level 0," trigger decision is made in 20 ns. It uses information from the VD, TF, and CC systems. The Level 0 trigger reduces the 3.6 MHz bunch train crossing rate to the order of tens of kilohertz. The "Level 1" trigger adds information from the DR to select events that contain charged tracks. It takes 1 μs of processing time and reduces the trigger rate to around 25 Hz. The "Level 2" trigger uses more sophisticated tracking information; it uses roughly 30 μs per event and reduces the trigger rate to a few Hertz.

The Level 2 trigger begins the process of classifying events according to different physics categories. Physics events of interest at CLEO contain at least three charged tracks. However, we also use samples of Bhabha and muon-pair events for calibration, and such events contain only two charged tracks. The Level 2 trigger prescales the number of two-track events; that is, it accepts only a fraction of the two-track events sufficient for detector calibration. For events with three or more charged tracks, the trigger efficiency is effectively 100%.

The Level 2 trigger signals the data-acquisition system (DAQ) to read event information out from the detector. The analog signals in each detector component are first digitized. The digitization occurs in parallel across all detector channels. Next the data are sparsified: the digital pulseheights are compared to preset threshold levels. Only channels above threshold are read out. This sparsification greatly reduces the amount of information stored for each event. In the calorimeter, the clustering of groups of crystals into showers occurs during sparsification. The sparsified data are read out of the detector and saved in `ZEBRA` format, a Fortran data-storage format developed at CERN. `ZEBRA` format data files at CLEO carry the filename extension "`.fzx`," so they are often referred to as `.fzx` files.

There is one more stage in the data-acquisition process, namely "Level 3" event selection. This stage is performed by a program appropriately named `LEVEL3` [16]. `LEVEL3` rejects events in which a beam particle has interacted with either the CLEO beampipe wall or residual gas in the evacuated beampipe. These events are termed beam-wall or beam-gas events. `LEVEL3` rejects about 45% of Level 2 triggers. We store the events that pass Level 3 cuts for later analysis.

2.4 Analysis Tools

In this section I describe several of the key CLEO analysis tools I use in my measurement of $\mathcal{B}(\bar{B}^0 \to D^{*+}\ell^-\bar{\nu})$.

2.4.1 The `PASS2` Reconstruction Program

Certain event reconstruction processes are common to all CLEO physics analyses. These procedures include the reconstruction of charged tracks in the CD, the reconstruction of showers in the calorimeter, matching tracks to showers, and the identification of charged leptons. These precision calculations all require careful calibration of the detector. These calibrations tell us how to convert the raw detector information into physically meaningful parameters such as energies, times, and distances. They involve a detailed understanding of the physics of particle detection, and include a variety of corrections that depend on such variables as position within a detector element, particle momentum, and entrance angle. We do these calibrations offline with large samples of data. The standard event reconstruction processes are therefore done in a second pass through the data some time after it has been taken.

The program that performs these event-reconstruction tasks is called `PASS2`. The `PASS2` job runs on data stored in the `.fzx` format. The program produces output in either the `ZEBRA .fzx` format or a CLEO-specific form called `ROAR` format. The quantities calculated by `PASS2`, such as track momenta and shower energies, can be stored in either format. Specific physics analysis jobs at CLEO are generally written in the framework of a program called `DRIVER`; `DRIVER` jobs run on `ROAR` files. Files in `ROAR` format carry the extension "`.rp`."

The process of running `PASS2` on `.fzx` files to produce `ROAR` files is sometimes called compressing the data. In principle, it reduces the large amount of raw detector information, such as times and pulseheights, to a smaller set of useful physics information, such as track momenta and shower energies. In practice, `PASS2` has evolved to compute a large variety of reconstructed quantities, and the raw hit information is often propagated to the `ROAR` output. As a result, "compressed" events often take more storage space than the raw event data.

Both the detector calibration and the event reconstruction algorithms improved during the history of CLEO II. As a result, much of the CLEO II data were processed multiple times by different versions of `PASS2`. The CLEO II data are broken up into datasets defined by changes in operation and running conditions; the $\Upsilon(4S)$ datasets are numbered 4s1–4s9, and then 4sA–4sG. The 4s2 dataset was reprocessed by `PASS2` a total of six times; the 4s4 dataset seven times. The final pass through the data, called the "recompress," was done in 1996–7, after the end of CLEO II data collection. The recompress applied the same event reconstruction algorithms to all CLEO II data. Previously, the `PASS2` jobs run on later datasets were more sophisticated than those run on earlier datasets — for example, they used better pattern recognition algorithms to find charged tracks. Furthermore, the recompress greatly improved track fitting, as I describe in the next section. My analysis is done with the CLEO II data processed by the recompress `PASS2`.

2.4.2 Track Reconstruction

Several steps are involved in reconstructing the properties of charged particles from the hits they leave in the CLEO II tracking chambers. The first step is pattern recognition, logically assembling a series of CD hits into a track. The next step is track fitting, deducing the direction and momentum of the charged particle from the drift distances and wire positions. Finally, we need tools to assess the quality of reconstructed tracks, to be sure that they accurately represent physical particles. In this section, I describe how each of these issues is addressed in CLEO track reconstruction.

The first level of pattern recognition is the `TRIO` processor [17], which runs as part of the `PASS2` program. `TRIO` searches for three-layer track segments in r–ϕ in which adjacent sense wires are hit in successive layers. The processor only considers axial wire hits in this stage. It next takes track segments at different radii and tries to join them with intermediate track segments. After `TRIO` has finished linking track segments together, it next tries to add single hits that were not assigned to segments. The processor fits tracks to circles in r–ϕ. The last step in `TRIO` is adding stereo-layer z hits by intersecting stereo wires with the fitted circle. The `TRIO` processor does not use cathode information.

The `TRIO` tracks are fed as seeds into `DUET`, a second `PASS2` job processor. `TRIO` tends to miss certain classes of tracks. One is low momentum tracks, which curve strongly in the CLEO magnetic field, and often do not have adjacent hits on subsequent layers. `TRIO` also misses many tracks with small polar angles, as they do not pass through enough stereo layers to allow `TRIO` to establish the z position of the track. The TRIO seeds are supplemented by the SF pattern recognition algorithm within DUET, which specifically addresses these issues.

DUET uses only the parameters of seed tracks — it ignores the list of hits TRIO used to generate the track seed. DUET links together "roads" of hits around the seed track. DUET works in all three dimensions, not only in the r–ϕ directions, and includes the stereo and cathode hits. The processor then fits these chains of hits to helical tracks. DUET attempts to assign every hit to one and only one track. As a final step, it tries to string together any leftover hits into useful track seeds, and then passes these seeds back into the main processor. Such seed tracks are called "dredge" seeds.

While the SF algorithm makes it possible for DUET to find low-momentum tracks, it does not handle these tracks especially well. Tracks below 200 MeV typically "curl" in the drift chamber, turning over and heading back towards the interaction point. DUET only allows one hit per layer, thus throwing away otherwise useful hits in the turnover region. In addition, DUET implicitly assumes that all tracks proceed from the interaction point outwards. It therefore frequently fits the "back half" of a curler, the part of the track heading back towards the interaction point, with a separate track, of the opposite, charge heading outwards. Due to energy loss, the back half of a curlers generally does not pass through the interaction point. The DUET processor does attempt to distinguish the back halves of curlers. Regrettably, it does a poor job — it frequently fails to associate the front and back halves of curlers, it spuriously rejects perfectly good tracks, and it passes tracks that are actually the back halves of curlers.

DUET generates a simple track-quality variable, kincd. Tracks with kincd $= 0$ are those DUET considers good. (Tracks with kincd $= 2$ are initially assigned kincd $= 0$ by DUET; their kincd values are later increased if they are assigned to secondary vertices by other processors.) DUET assigns kincd $= -1$ to tracks with no z information, kincd $= -2$ to tracks it claims to be the back halves of curlers, and kincd $= -3$ those that fall in both categories.

Before the recompress of CLEO II data, the DUET track helices were used directly in CLEO analyses. This procedure introduced two problems. First, charged particles gradually deposit energy in the detector material — it is this very property that allows us to detect them. As a result, they do not travel along truly helical paths, but rather spirals of decreasing radii. Before the recompress, reconstructed track parameters had to be corrected to account for these effects [18]. Second, DUET track fit error matrices were not reliable.

The recompress PASS2 added a Kalman fitter [19] to correct these problems. This track fitter refits the DUET tracks in a more sophisticated way. It starts from the outer end of the track with an estimate of the track parameters and their errors. It then works inward along the track, adding hits. As each hit is added, the track parameters are updated to account for both the information from the new hit and the amount of material traversed by the track. The Kalman fitter implicitly takes account of the energy lost by particles traveling through material. As this loss depends on the particle species, we perform separate Kalman fits for different particle hypotheses. The Kalman fit furthermore returns reliable error matrices, allowing us to vertex multiple tracks to deduce the properties of parent particles. Both improvements are of great benefit to the analysis of $\bar{B}^0 \to D^{*+}\ell^-\bar{\nu}$, as I discuss in Chapter 3.

Even with the benefit of the Kalman fitter, we still must deal with questions of track quality. Even Kalman-fit tracks are only as good as the hits used to form them. Fortunately, CLEO has a number of tools that can be used to assess the quality of tracks.

For many physics analyses, we can reject several classes of tracks based solely on their origins. Tracks which lack z information ($\texttt{kincd} = -1$ or -3) are obviously not likely to be good representations of real charged particles. Dredge seed tracks are likewise not good representations of physical particles. Another class of poorly-reconstructed tracks is z escapes. These tracks have small polar angles and exit the endplate of the DR. If `DUET` lacks sufficient z information to fit the track in the conventional way, it uses the inferred exit point as an additional z constraint. Tracks fit in this manner have been found not to represent real particles well.

To better control some of the pathologies of track reconstruction, we use a sophisticated track-quality package known as Trackman [20]. This package is run in `PASS2` by the `TMNG` processor. Trackman uses a variety of tests to associate the front and back halves of curlers, and to pick out the front halves with greater reliability than `DUET`. After joining two soft tracks into a curler, Trackman will often prefer a track with $\texttt{kincd} = -2$ to a partner with $\texttt{kincd} = 0$. For this reason, it is recommended that CLEO data analyses accept all tracks with $\texttt{kincd} = -2$ by default, and use Trackman to reject the back halves of curlers.

Trackman also discards spurious tracks of a number of types, most notably "ghost pairs." This term refers to pairs of tracks fit to the hits left in the tracking system by one charged particle. They often have very similar track parameters. Ghost pairs can arise when poor seed tracks are fed to `DUET`, such that only some of the tracking hits fall within the `DUET` hit-collection road. The remaining hits can then be collected into a second track. Trackman does a fine job of selecting the track which best represents the original charged particle.

Finally, we can make track-quality cuts based on how close the fitted track comes to the interaction point. The variable `z0cd` is the z coordinate of the point of closest approach to the detector origin. CLEO analyses typically require the magnitude of this variable to be less than five centimeters or so. The variable `dbcd` measures the distance of closest approach of the track to the (x, y) position of the beam, which CLEO measures on a run-by-run basis. The magnitude of `dbcd` is typically required to be less than five millimeters. The difference in the magnitude of these cuts reflects both CLEO's better tracking resolution in the r–ϕ directions than the z direction and the larger extent of the interaction region in the longitudinal direction. Both cuts are very loose - each accepts over 99% of tracks in candidate $\bar{B}^0 \to D^{*+}\ell^-\bar{\nu}$ events in my analysis.

2.4.3 Monte Carlo (MC)

In the context of the analysis of particle physics data, "Monte Carlo" refers to the generation of simulated physics events. These Monte Carlo-simulated events are frequently referred to simply as "Monte Carlo events," or just "MC events." These simulated events are an an essential tool in nearly all such analyses. We use Monte

Carlo simulation for three main purposes. We use large samples of Monte Carlo events to test and develop physics analysis procedures. We also model certain physics backgrounds with simulated events. Finally, we measure the efficiency of our event reconstruction procedure on Monte Carlo events. Because we use Monte Carlo simulation for this purpose, it is critical that the simulated events resemble real events in CLEO data as closely as possible, as any differences between the two may introduce systematic errors to our physics measurements.

We generate Monte Carlo events at CLEO with a two-stage process. In the first stage, we simulate the basic physics of e^+e^- collisions with a program called `QQ`. The `QQ` program is based on an extensive table of decay branching fractions stored in the file `decay.dec`. `QQ` creates sample physics events using random number generation. The program starts with a particular initial state, for example an $\Upsilon(4S)$ resonance at rest. It then uses random numbers to select a particular decay mode from the table in `decay.dec`. `QQ` iterates this process until is it left with only relatively stable particles, such as pions, kaons, electrons, muons, protons, and neutrinos. `QQ` attempts to simulate the correct kinematic distributions for each decay mode. A sub-program, `EvtGen`, simulates several of the more complicated decay modes, including the decay of $\bar{B}^0 \to D^{*+}\ell^-\bar{\nu}$ according to the linear HQET form-factor parameterization I discuss in Chapter 1. The properties of the particles generated by `QQ` are often referred to as "generator-level" information.

CLEO analyses typically use two distinct varieties of Monte Carlo event samples: "generic" Monte Carlo and "signal" Monte Carlo. Generic Monte Carlo refers to the full simulation of $\Upsilon(4S)$ decay. In this mode, we use our full knowledge of all

B decay modes and the decay modes of all possible daughter particles. Of course, not all decay modes have been measured, so the generic Monte Carlo simulation relies on some theoretical input and educated guesses. We have attempted to tune various decay parameters so that important inclusive decay distributions in generic Monte Carlo event samples are similar to those we observe in the data. These distributions include the lepton momentum spectrum, the number of charged tracks observed, and the shower energy spectrum. The parameters of our generic Monte Carlo model are the branching fractions stored in `decay.dec`.

Signal Monte Carlo refers to the simulation of only one specific physics process, or a small set of physics processes. We typically generate signal Monte Carlo events to obtain large statistical samples of particular decay modes, sometimes modes not present in `decay.dec`. Most signal Monte Carlo events are actually a hybrid of signal and generic Monte Carlo — one B in the event decays to the signal mode, while the other decays generically. CLEO uses two methods to generate signal Monte Carlo events. This first approach is to use a custom `decay.dec` file, one which allows only the signal decay mode. This approach has the disadvantage that it frequently affects the decays of both B mesons in an event. It often cannot be used to generate events with one signal and one generic B decay. The second approach involves a user-defined `ISELECT` function. With this method, `QQ` generates generic B decays, and the `ISELECT` function determines whether or not they contain a signal decay. Only events that contain signal decays are kept. For rare B-decay modes, this approach consumes large amounts of CPU time.

Once we have generated the underlying physics of an event with `QQ`, the second stage of Monte Carlo generation is the simulation of the CLEO II detector. We use the program `CLEOG` to simulate the interaction of various particles in the detector. This program is based on the `GEANT` package [21] developed at CERN. The simulation is based on a detailed description of the structure of the CLEO II detector, including both the amount and types of different materials and their exact physical locations. The `GEANT` section of the simulation propagates particles through the detector material, accounting carefully for the amount of energy different species lose in transit. This part of the program also models the decays of particles induced by the detector material.

The `CLEOG` software then translates these interactions into the same types of physical signals produced by the detector — pulseheights and times — in the `.fzx` format. This translation is based on careful tuning of a set of Monte Carlo simulation constants. The CLEO II recompress project included a painstaking re-tuning of these Monte Carlo constants [22]. This dataset-by-dataset re-tuning took place between 1997–1999. After we tuned each dataset, we generated generic $B\bar{B}$ Monte Carlo samples containing five times the number of $B\bar{B}$ events as the data.

We analyze Monte Carlo `.fzx` files exactly as we do those of data. We run `PASS2` to produce Monte Carlo `ROAR` files, and we analyze these `ROAR` files with `DRIVER` jobs. We have an additional handle on Monte Carlo events that we do not have when we analyze events in the CLEO II data — we know which underlying physics processes produced each event. Furthermore, in Monte Carlo events we can determine exactly how the raw hits and reconstructed tracks and showers were produced. In addition to the data-style detector information, such as the times and pulseheights in the tracking chambers, the Monte Carlo `.fzx` files store Monte Carlo hits. In the tracking chambers, this information includes which charged particle went through each cell, where it went through, and how much energy it deposited in that cell.

We use this information to "tag" Monte Carlo tracks. We start with the list of wire hits used to form a track, or crystals used to form a shower. We then look up which Monte Carlo particle produced those hits in the detector. We thus associate reconstructed tracks and showers with the generator-level particles. This process is performed during `PASS2` by the `TAGR` processor. `TAGR` sometimes finds that multiple particles contributed hits to a particular track or shower; in these cases it lists multiple matches according to how much of the track or shower information was due to each generated particle. Tagging is an very useful tool for disentangling various event misreconstructions — in particular, combinatoric background events, in which random track combinations mimic physics processes of interest.

2.4.4 Electron Identification

Many CLEO physics analyses involve decays that include light charged leptons, namely electrons and muons. To reconstruct such decay modes, we need to be able to identify these particle with high efficiency. We also want our lepton identification algorithms to have low fake rates — that is, they should rarely mistake other particle species for leptons. In this section I describe how CLEO identifies electrons; in the next I describe how we identify muons. Both types of lepton identification are essential to my measurement of $\mathcal{B}(\bar{B}^0 \to D^{*+}\ell^-\bar{\nu})$.

Electron identification involves information from multiple detector components. Our algorithms use the reconstructed charged tracks, energy loss in the DR, shower information in the CC, and, in certain momentum regions, timing information from the TF system. CLEO has developed two different electron identification packages: the Cornell Electron Identification package `CEID` [23], and the Rochester Electron Identification package `REID` [24]. Each algorithm was developed by a group at the respective university. Both are run during `PASS2`. I use the `CEID` package in my analysis, so I will focus here on the operation of that package.

`CEID` examines seven different quantities to determine if a track is an electron. Each quantity has some ability to distinguish electrons from other charged particles. The first is the amount of ionization the track produces in the main drift chamber, as measured by the size of the pulses on the anode sense wires. The rate of ionization depends on the amount of energy a charged particle loses per unit distance, written $\mathrm{d}E/\mathrm{d}x$. The energy loss by a charged particle traveling through a medium is described by the Bethe-Bloch equation [3],

$$\frac{\mathrm{d}E}{\mathrm{d}x} = -Kz^2\frac{Z}{A}\frac{1}{\beta^2}\left[\frac{1}{2}\ln\frac{2m_e\beta^2\gamma^2T_{\mathrm{max}}}{I^2} - \beta^2 - \frac{\delta}{2}\right]. \tag{2.2}$$

Here $K = 4\pi N_A r_e^2 m_e$, where N_A is Avagadro's number, r_e is the classical electron radius, and m_e is the mass of the electron. The quantity z is the charge of the particle losing energy, while β is the particle's velocity in units of the speed of light, c; $\gamma^2 = 1/(1-\beta^2)$ as usual. The maximum kinetic energy that can be imparted to a free electron in a single collision is T_{max}, which can be approximated

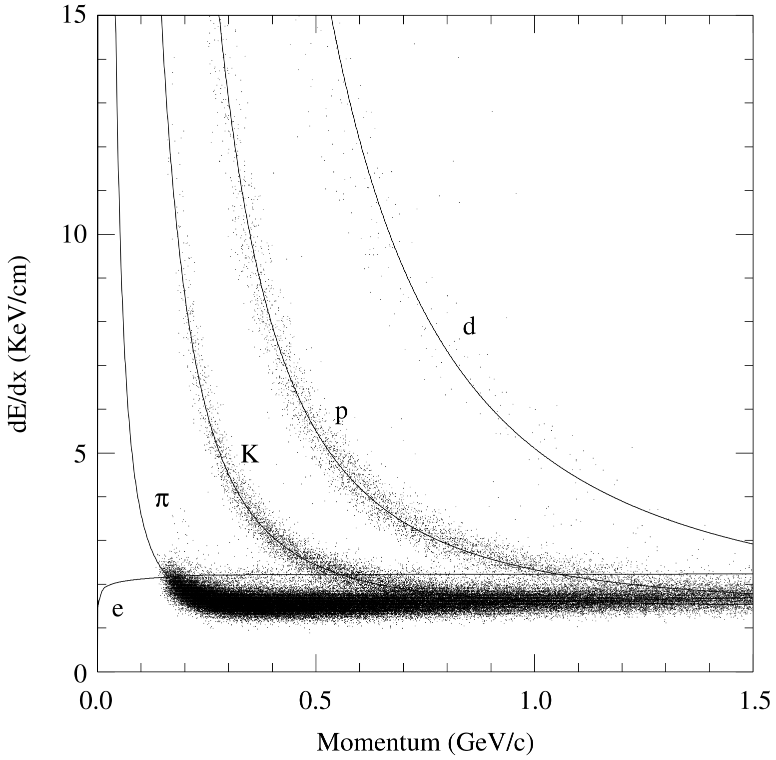

Figure 2.9: A scatter plot of particle energy losses versus momentum in the CLEO II main drift chamber. The solid curves show the central values expected from Equation 2.2 for the particle types indicated.

by $T_{\max} \simeq 2m_e\beta^2\gamma^2$. The medium the particle travels through is described by its atomic number, Z, and its mass, A, measured in grams per mole. The quantity I is a material-dependent mean excitation energy, it scales approximately with Z. Finally, δ is a small correction term that depends on the charged particle momentum.

I show a scatter plot of measured $\mathrm{d}E/\mathrm{d}x$ values in Figure 2.9. One can clearly distinguish the bands corresponding to different charged particle types. The visible scatter is due primarily to the intrinsic statistical variation in the number of ionization electrons. At 1.5 GeV the hadronic particles are minimum-ionizing and cannot be distinguished from each other. The $\mathrm{d}E/\mathrm{d}x$ values for electrons are somewhat separated from the hadronic species over a broad momentum range.

CLEO software takes the difference between the measured $\mathrm{d}E/\mathrm{d}x$ value and the expected value for various particle species and divides it by the experimental resolution for that species. This calculation gives the number of standard deviations the $\mathrm{d}E/\mathrm{d}x$ measurement is away from the expected value. For electrons, the result is saved as the quantity `sgeldi`. This quantity is the $\mathrm{d}E/\mathrm{d}x$ measurement used in electron identification by `CEID`. The corresponding variables for other particle types have analogous names: `sgpidi` for pions, `sgkadi` for kaons, etc. If no good $\mathrm{d}E/\mathrm{d}x$ information is available, the variable `iqaldi` is set to a value less than zero.

The $\mathrm{d}E/\mathrm{d}x$ information used in electron identification comes from the DR, part of the same tracking system that we use to find charged tracks in the first place. The next five electron identification variables depend on information from the calorimeter. The `CDCC` processor [25], run during `PASS2`, matches tracks to CC showers. It extrapolates tracks outwards from the CD to the calorimeter, and then finds showers located near the projected track location. Two `CEID` variables combine CD and CC information; they are the ratio of the shower energy to the track momentum, E/p, and the distance from the projected track position to the shower centroid. Three more `CEID` variables depend only on the shower; these variables are the ratio E_9/E_{25}, which I discuss above in Section 2.3.3, the total width of the shower, and the ratio of the shower width in the θ direction to that in the ϕ direction.

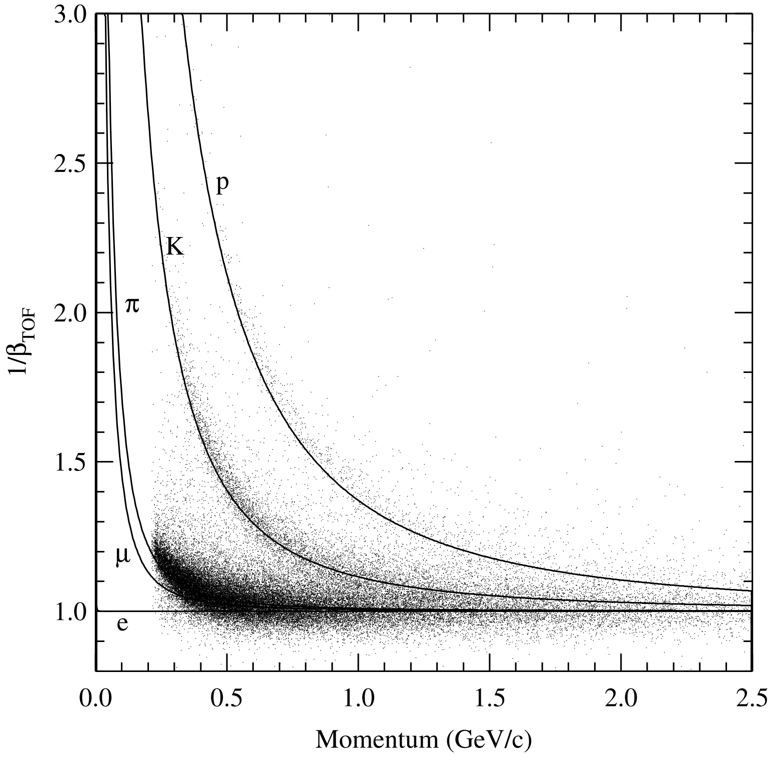

Figure 2.10: A scatter plot of particle times of fight versus momentum in the CLEO II TF system. The solid curves show the central values expected from Equation 2.3 for the particle types indicated.

The final `CEID` variable is based on information from the time-of-flight system. We project tracks into the TF system in much the same manner as is done by `CDCC` in the calorimeter. We then calculate the inverse particle velocity $1/\beta$ from the recorded time of flight and the track path length. $1/\beta$ is related to the particle momentum p and mass m by,

$$\frac{1}{\beta} = \frac{\sqrt{1 + (p/m)^2}}{p/m}. \tag{2.3}$$

I show a scatter plot of measured $1/\beta$ values in Figure 2.10. As with the $\mathrm{d}E/\mathrm{d}x$

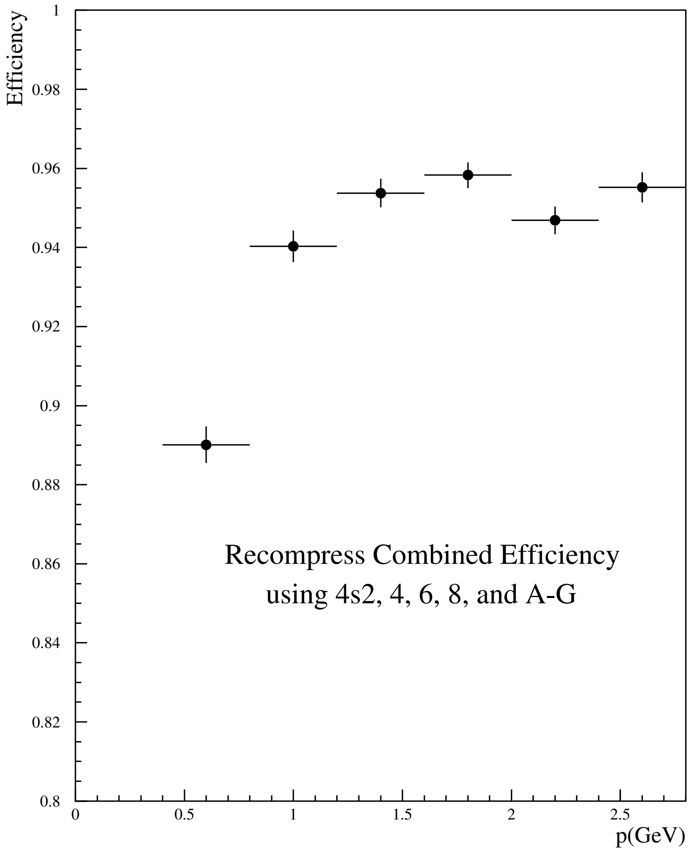

Figure 2.11: The electron identification efficiency as a function of momentum for the cut `r2elec` > 3. (Figure courtesy of Mark Palmer.)

plot of Figure 2.9, the bands corresponding to different charged particle types are clearly visible. However, the time of flight cannot distinguish electrons from the dominant background of pions except at low momentum. For this reason, the `CEID` package does not use time-of-flight information to identify electrons above 800 MeV. The time-of-flight variables are analogous to those used for $\mathrm{d}E/\mathrm{d}x$; for example, consistency with the electron hypothesis is recorded in `sgeltf`.

The output of the `CEID` package is the “log-likelihood” `r2elec`, calculated as follows for each candidate electron. The `CEID` algorithm considers in turn each of the variables used to distinguish electrons from other particles. Given the value of a variable, `CEID` computes the probability P_e that a electron would produce that measured value, and the probability $P_{\not e}$ that a particle other than an electron would do so. `CEID` uses probabilities P_e measured in bins of momentum and track angle θ with electrons from radiative Bhabha events embedded into hadronic events, and probabilities $P_{\not e}$ measured with tracks from hadronic $\Upsilon(1S)$ decays. The value of `r2elec` is a logarithmic sum of the ratio of these probabilities,

$$\texttt{r2elec} = \sum_{\text{variables}} \ln \left(\frac{P_e}{P_{\not e}} \right). \tag{2.4}$$

If the information for any variable is not available, in particular $\mathrm{d}E/\mathrm{d}x$ information, that variable is simply omitted from the sum. A typical electron identification cut is `r2elec` > 3. I show the efficiency versus momentum for this cut in Figure 2.11. The identification efficiency for electrons above 1 GeV is around 95%. The fake rate for this cut value is well under 1% [26, 27].

The `CEID` package does not use the algorithm I describe above to calculate `r2elec` for Monte Carlo tracks. That approach would require that all the variables used by `CEID` be well-simulated by our Monte Carlo, a questionable assumption. Instead, we take advantage of the Monte Carlo track-tagging algorithm I describe in Section 2.4.3. Tracks tagged as electrons are randomly assigned a value of `r2elec` according to the measured distribution of this variable for the radiative Bhabha tracks embedded in hadronic events. Similarly, non-electron tracks are randomly assigned `r2elec` values according to the measured distribution in `CEID`'s hadronic track sample. This approach forces the electron identification efficiency in Monte Carlo to be exactly what is measured in data. The level of agreement between Monte Carlo and the CLEO II data is therefore just the uncertainty in the electron identification efficiency. The current estimate for this uncertainty is 2.4% [28].

2.4.5 Muon Identification

Like electron identification, muon identification with the CLEO II detector requires information from more than one detector subsystem. However, the muon identification process is much simpler than that for electrons. The key muon identification variable is simply how deeply a track penetrates into the iron of the magnet return yoke.

We project tracks from the CD into the muon system and match hits from the muon chambers onto the tracks. We expect good muon candidates to leave hits in at least two of the three muon layers in each superlayer. If a candidate fails this requirement at one depth but appears to leave hits at a greater depth, we set the variable `muqual` to a nonzero value. We store the number of interaction lengths of iron penetrated by the track in the variable `dpthmu`. Muons are identified in physics analyses with the requirements that `muqual` $= 0$ and that `dpthmu` be greater than a particular value, typically 3, 5, or 7.

As the CLEO II muon system is coarsely segmented, with counters at only three depths of iron, the muon reconstruction efficiency depends strongly on both track direction and momentum. The efficiency for a given cut is greatest at $\cos\theta = 0$, and

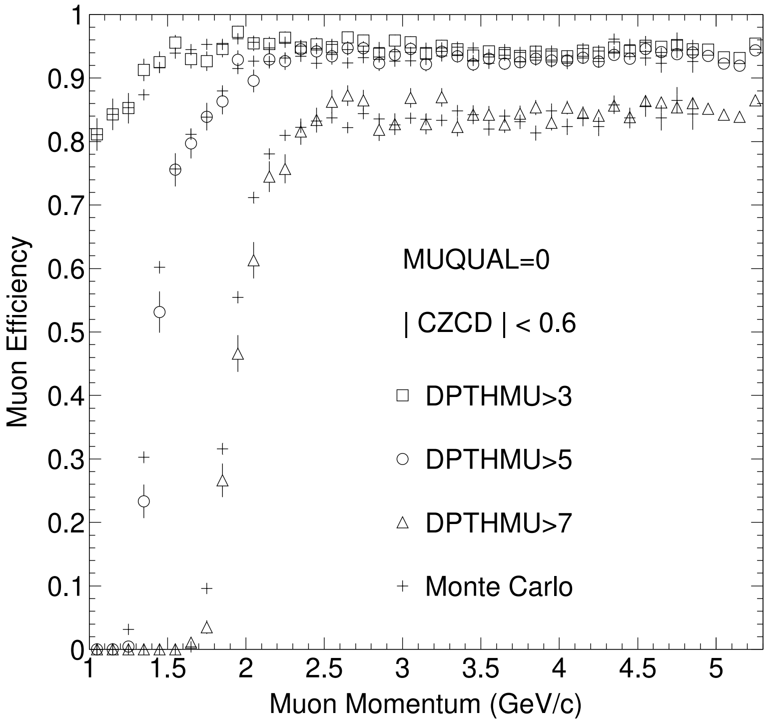

Figure 2.12: Muon identification efficiency as a function of momentum for different values of `dpthmu`. The open shapes show the efficiencies measured in data for different cut values, while the crosses give the corresponding efficiencies in Monte Carlo. These efficiencies were calculated with the requirement `muqual` $= 0$; the variable `czcd` is equivalent to the track angle $\cos\theta$. (Figure excerpted from Reference [29].)

falls off for larger values of $|\cos\theta|$. This falloff is a consequence of the granularity of the system. The same number of muon counter layers must be reached to pass a given cut, but the amount of material in front of those counters increases. The `dpthmu` cuts impose a momentum threshold on the muon identification algorithm, as muons below a given momentum cannot penetrate sufficient iron to pass these cuts. This threshold effect is illustrated in Figure 2.12.

I use the cuts `dpthmu` > 5 and $|\cos\theta| < 0.7071$ in my analysis. For these cuts, the muon efficiency is over 95% [29] for muons with momenta greater than 1.4 GeV, and the fake rate is on the order of 1% [26, 27]. We reconstruct muons in Monte Carlo events in the same manner as in the data. The Monte Carlo simulation was tuned before the recompress such that the MC muon efficiencies agree with the data to the 1% level [30]. Recent work suggests a 1.6% agreement in the recompress [31].

2.4.6 CLEO Event Displays

In studies of both physics processes and the properties of the CLEO detector, it is extremely important to be able to visualize the pattern of detector hits in sample events. CLEO has developed several event display programs for this purpose. In particular, the CleoXD program displays events stored in `.fzx` format, while the RoarXD program displays those stored in `ROAR` format.

In Figure 2.13, I show a sample event from the CLEO II data as represented by CleoXD. I show several events in this format in later chapters, so I will describe the important features of the event display here. The viewpoint is generally at the west end of the detector. The $\phi = 0$ direction is to the right. This display shows information from nearly all the detector subsystems. CleoXD allows the display of various parts of the detector to be toggled and allows the user to "zoom in," to focus on particular features of an event.

The inner section of the event display shows the hits in the three tracking chambers, the PT, VD, and DR. These detectors are shown in an r–ϕ cross-sectional view. Concentric circles show the inner and outer radii of these chambers. Dots

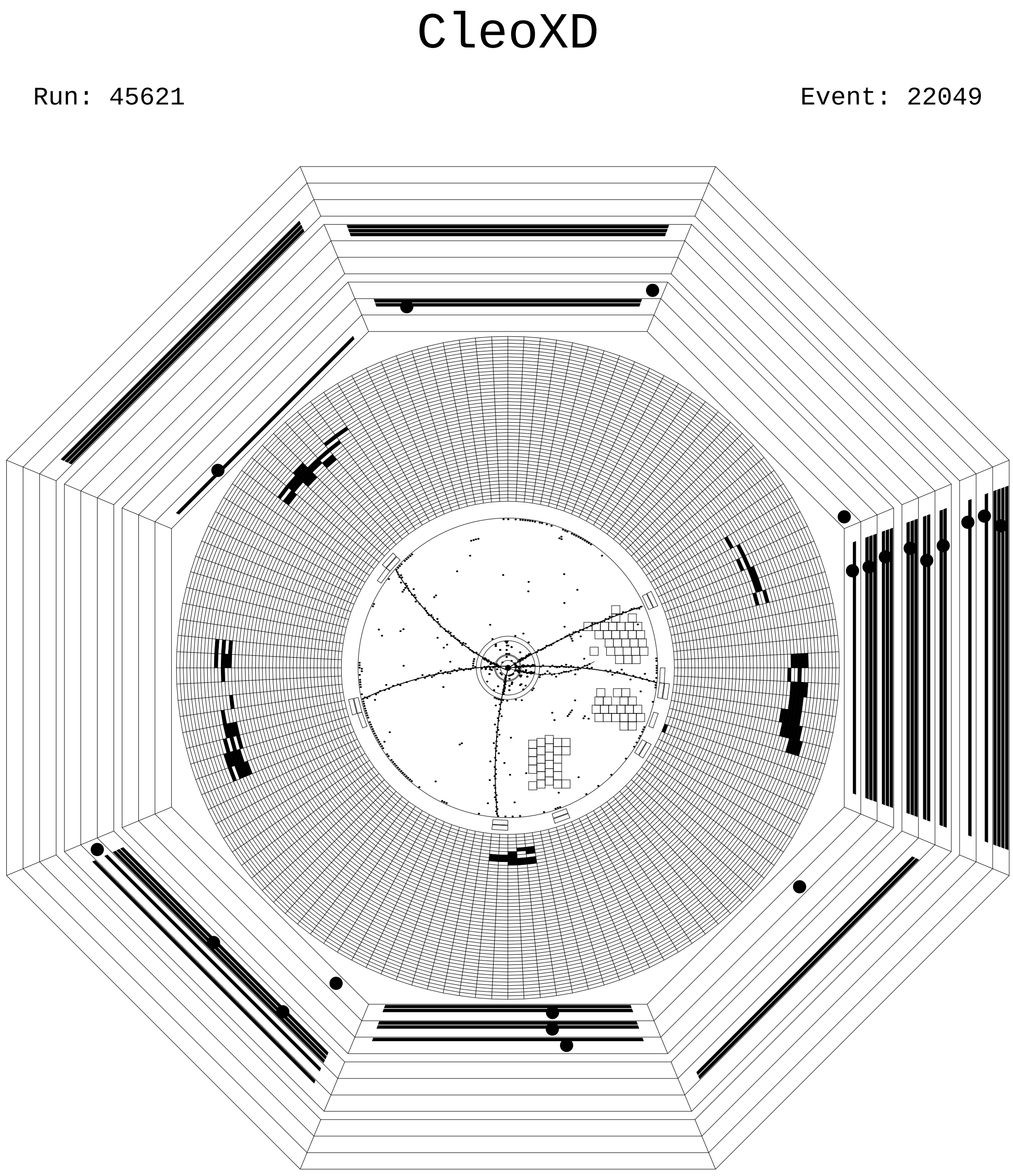

Figure 2.13: A CleoXD display of a sample event from the CLEO II data. The features of the event display are described in the text.

show sense wires which have recorded hits; sense wires without hits are not shown. The solid curves through strings of points represent the paths of reconstructed tracks. Negatively charged particles produce tracks that curve to the right as they travel outwards in this view; positively charged tracks curve to the left. In addition to the tracks, noise hits are visible in the tracking chambers, particularly in the last layer of the DR. The event display also shows several blocks of four adjacent wires in the same layer; these channels in the DR are always read out for calibration purposes. (The groups of open squares within the radial region of the DR represent endcap calorimeter hits.)

CleoXD shows hits in the barrel time-of-flight system as rectangles just past the outer DR radius. Hits in the TF phototubes at the west end of the detector are shown at smaller radius than those at the east end. This particular event display does not show any endcap time-of-flight hits; these hits are represented as wedge shapes overlaid on the inner part of the detector.

Proceeding radially outward in the figure, we come to the calorimeter hits. In the tracking chambers, the radial position of a hit wire in the display corresponds to the position of the wire in the detector. CleoXD presents the calorimeter information in a different manner. Each of the 6,144 barrel crystals is represented by a small rectangle. The radial position of each rectangle shows the z position of the crystal. The display is much like looking down the inside of a barrel, where the rectangles are the inner faces of the calorimeter crystals. The view is from the west end of the detector, so the inner crystals in the CleoXD display are at the east end of the detector. The radial space accorded the CC in the event display is much larger than the proportional physical extent of the device.

The filled-in rectangles correspond to calorimeter crystals with hits. Five showers in the barrel calorimeter can be seen in the display. The display also shows three showers in the endcap calorimeter. The endcap crystals with hits are shown as open squares at their actual r–ϕ positions; endcap crystals without hits are not shown.

Finally, the muon system is shown outside the calorimeter. As with the CC, the event display does not show the radial position of muon chambers accurately. The nine layers of the muon system are shown as trapezoids; the gaps between superlayers correspond to the 36 cm of magnet-return iron. Solid circles show the ϕ positions of muon chamber hits. The solid bars drawn along the length of the trapezoids illustrate the z positions of hits: the radial placement of a bar within a trapezoid is related to the position of the hit. The octant at the right of the event display shows clear evidence for the passage of a muon. The hits in the bottom octant are most likely due to a minimum-ionizing particle other than a muon, as the particle penetrates only the first 36 cm of iron.

CHAPTER 3

METHOD

In my analysis of CLEO II data, I measure the branching fraction $\mathcal{B}(\bar{B}^0 \to D^{*+}\ell^-\bar{\nu})$ via full reconstruction of the B meson decay products. This reconstruction entails observing the lepton and all the decay products of the D^{*+}, but not the weakly interacting neutrino. I give the criteria I use to select candidate $D^{*+}\ell^-\bar{\nu}$ events and go through the mechanics of event reconstruction in Section 3.1. Though my selection criteria are designed to minimize the number of background events, a variety of other processes also contribute to my sample. I describe these backgrounds and the methods I use to estimate them in Section 3.2. As explained below, I extract the $\bar{B}^0 \to D^{*+}\ell^-\bar{\nu}$ branching fraction through a fit of the reconstructed event distribution in the variable $\cos\theta_{BY}$. In Section 3.3, I describe a test of this approach on Monte Carlo, and I present the results I obtain from the data.

3.1 Reconstruction of $\bar{B}^0 \to D^{*+}\ell^-\bar{\nu}$

In this section I describe how I reconstruct candidate $D^{*+}\ell^-\bar{\nu}$ events. I use exactly the same reconstruction techniques on both data and Monte Carlo events. I explain global event selection criteria, the reconstruction of D^{*+} mesons and charged leptons, and the calculation of the variable $\cos\theta_{BY}$ in $D^{*+}\ell^-\bar{\nu}$ candidate events, where θ_{BY} is the opening angle between the D^{*+} and the lepton.

3.1.1 Selection of $B\bar{B}$ Events

The first step in event reconstruction is to select a set of events to analyze. I do my analysis on the CLEO II data in the 4s2–G datasets. These datasets total $3.14\,\mathrm{fb}^{-1}$ of data collected on the $\Upsilon(4S)$ resonance and contain 3.32 million $B\bar{B}$ events. I also use $1.61\,\mathrm{fb}^{-1}$ of data collected off-resonance to understand the continuum background. I run my analysis code on the recompress hadron skims stored on disk in `ROAR` format. These files include 18.79 million on-resonance and 7.91 million off-resonance events. I also analyzed the 16.71 million events of recompress $B\bar{B}$ Monte Carlo.

I apply several cuts at the event level. The following two cuts suppress backgrounds from non-$B\bar{B}$ events:

- `klasgl` ≥ 10
- $R_2 \leq 0.4$

The variable `klasgl` is calculated by the `EVCLAS` package [32]. This algorithm distinguishes hadronic events from other types of physics events that can be produced in e^+e^- collisions, such as Bhabha and μ-pair events. It also classifies other event sources, such as beam-gas interactions and cosmic rays. `EVCLAS` uses several cuts to distinguish hadronic events, including the requirements that such events contain at least three charged tracks and that the visible tracks and showers account for at least 20% of the center-of-mass energy. `EVCLAS` assigns each hadronic event a `klasgl` value of 10 or 11. The hadron skims on disk contain the data events so classified.

The quantity $R_2 = H_2/H_0$ is a ratio of Fox-Wolfram moments [33]. These moments H_i are defined by

$$H_i = \sum_{a \neq b} \frac{p_a p_b}{E_{CM}^2} P_i(\cos\phi_{ab}). \tag{3.1}$$

Here P_i are the Legendre polynomials. The sum is over all pairs of observed particles a and b in the event, where by an observed particle I mean here either a track or a shower. The quantity p_a is the momentum of particle a, while ϕ_{ab} is the angle between the directions of particles a and b in the laboratory frame. Finally, E_{CM} is the center-of-mass energy of the events, which I take to be twice the recorded beam energy E_{beam}. In my calculation of R_2, I only use tracks approved by Trackman [20], and showers not matched to tracks as listed by the `MOTRSH` utility [34].

The R_2 variable contains information about the shape of an event. Its values range from zero to one. Events with small R_2 values tend to be isotropic, or "spherical," with particles carrying energy in all directions. $\Upsilon(4S) \to B\bar{B}$ events tend to be of this type. The $\Upsilon(4S)$ is produced and decays at rest. Each daughter B meson is produced nearly at rest, with an average momentum of just over 300 MeV. Each pseudoscalar B decays isotropically in its rest frame. B mesons tend to decay into many-body final states: the charged-track multiplicity of $B\bar{B}$ events

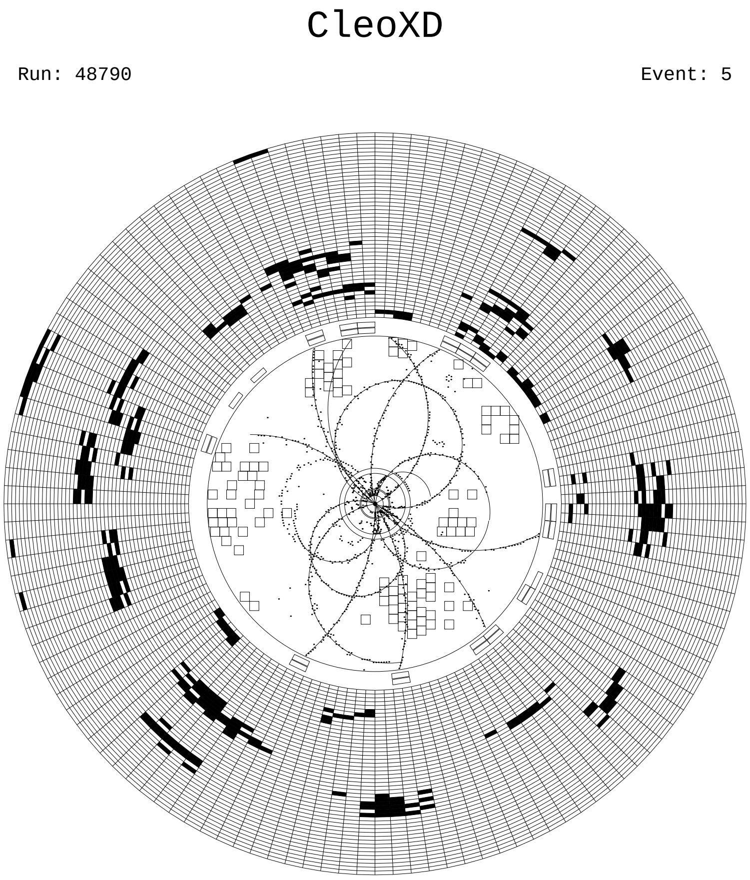

Figure 3.1: A CleoXD view of a spherical $B\bar{B}$ Monte Carlo event with a low value of R_2. The display of the muon system has been toggled off to highlight the track and shower distributions.

has been measured at CLEO to be around 10.7 [35], which means a typical B decay produces more than five charged tracks. I show a typical $B\bar{B}$ event with a low R_2 value in Figure 3.1.

Continuum events tend to be "jetty," with high values of R_2. In these events, the electron and positron annihilate to form a pair of light quarks $q\bar{q}$. The two quarks fly in opposite directions with high kinetic energy. Each quark then

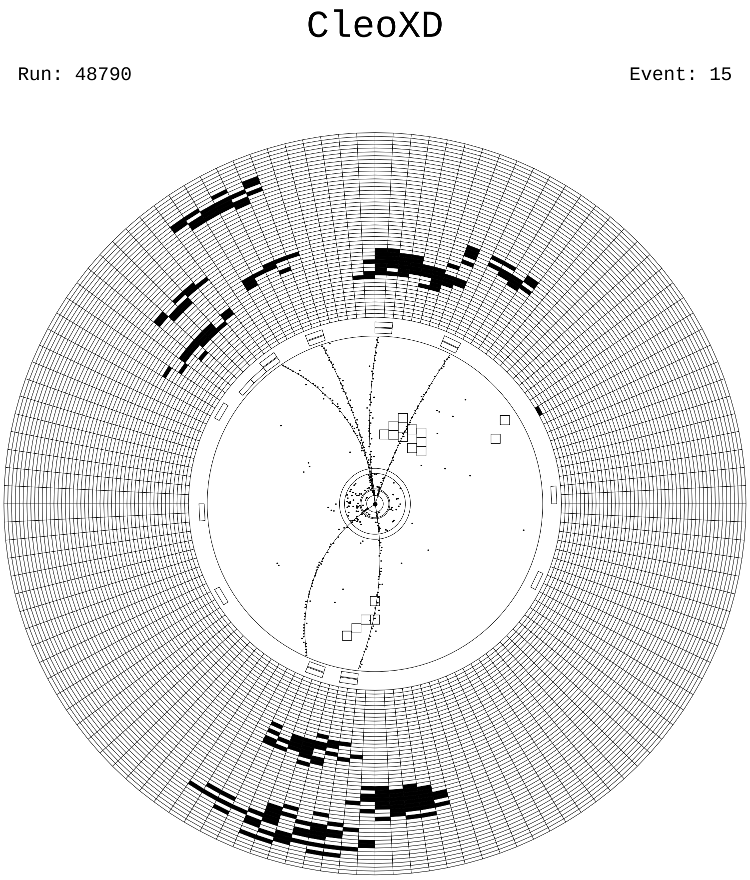

Figure 3.2: A CleoXD view of a jetty continuum Monte Carlo event with a high value of R_2. The display of the muon system has been toggled off to highlight the track and shower distributions.

hadronizes, producing a jet of particles. Continuum events tend to have a clear jet axis, with particles clustering along the original quark directions. I show a typical $q\bar{q}$ event with a high R_2 value in Figure 3.2.

I show the R_2 distributions for $B\bar{B}$ and continuum data events in Figure 3.3. The discrimination between the two types of events is clear. My R_2 cut at 0.4 is about 98% efficient for $B\bar{B}$ events, while suppressing roughly a third of the

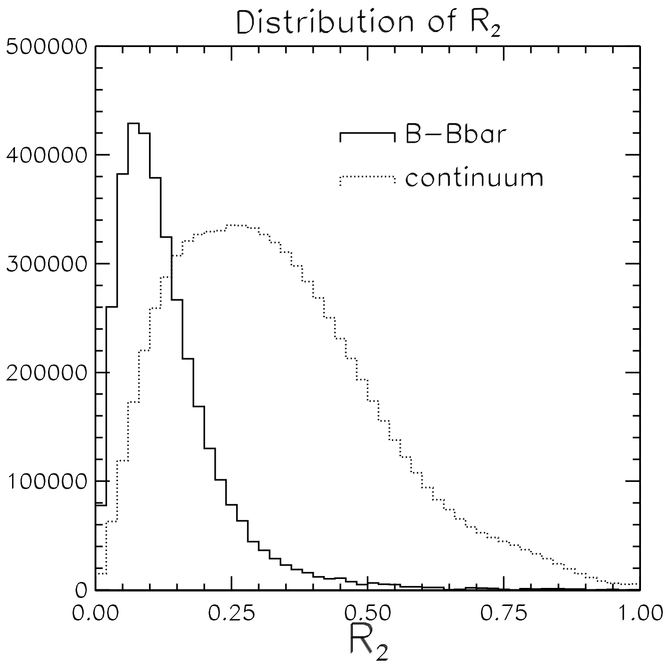

Figure 3.3: The R_2 distributions of $B\bar{B}$ and continuum events in data. The solid histogram shows the continuum-subtracted distribution from all on-resonance CLEO II data. The dashed histogram includes all off-resonance hadron skim data.

continuum background.

I also apply some event cuts based on the nominal beam energy $E_{\rm beam}$. This parameter is supplied by CESR on a run-by-run basis. For on-resonance data I require the beam energy to fall in the range $5.285 \leq E_{\rm beam} \leq 5.295\,{\rm GeV}$. This cut eliminates data taken away from the center of the $\Upsilon(4S)$ resonance. The $B\bar{B}$ production cross-section $\sigma(e^+e^- \to \Upsilon(4S) \to B\bar{B})$ decreases away from the center of the resonance. The uncertainty in the CESR beam energy is about $2\,{\rm MeV}$, and in regions away from the peak of the resonance this beam-energy uncertainty leads to a significant uncertainty in the number of $B\bar{B}$ events produced. I apply this same cut to Monte Carlo events for consistency. For off-resonance data I require $E_{\text{beam}} \leq 5.275\,\text{GeV}$.

3.1.2 D^{*+} Candidate Reconstruction

Once I have selected a set of events to analyze, I proceed to reconstruct $D^{*+}\ell^-\bar{\nu}$ candidates in these events. My first step is to reconstruct D^{*+} candidates, which I do in the decay mode $D^{*+} \to D^0\pi^+$, $D^0 \to K^-\pi^+$. I first form a D^0 candidate from two different tracks of opposite charges, each passing the following track cuts:

- not a z-escape track
- not a dredge-seed track
- `kincd` $\neq -1, -3$
- `tng` ≥ 0
- $|$`z0cd`$| < 0.005\,\text{m}$
- $|$`dbcd`$| < 0.05\,\text{m}$
- $|\cos\theta| \leq 0.9$

The first six cuts reject tracks that fail various track-quality standards. I describe these cuts in my discussion of track reconstruction in Section 2.4.2. The longitudinal momentum of z-escape tracks is inferred with the assumption that the track exited the DR endplate at the radius of the last hit. Dredge seed tracks are those by `DUET` with the hits left over after all other tracks have been reconstructed. Tracks in both classes rarely measure the properties of physical particles well. Tracks with `kincd` values of -1 or -3 lack longitudinal momentum measurements. The variable "`tng`" is the output of the Trackman algorithm; `tng` values less than zero imply that Trackman has rejected the track for one of several reasons. The `dbcd` and `z0cd` cuts require the reconstructed track to pass close to the interaction point.

The cut on $\cos\theta$ is not a track-quality cut *per se*. Tracks with $|\cos\theta| > 0.9$ pass through the endplate of the VD; above 0.96 they pass through the PT endplate. The detector electronics and associated cables lie beyond these endplates. We do not believe this material is modeled well in the Monte Carlo; it is therefore likewise not handled correctly by the Kalman fitter. I veto tracks in this angular region to avoid systematic errors associated with the reconstruction of these tracks.

I do not use any $\mathrm{d}E/\mathrm{d}x$ particle identification information in the reconstruction of either D^0 or D^{*+} candidates. In principle, I could require that the pion and kaon I use to form each D^0 candidate have `sgxxdi` values consistent with the assumed species. In fact, in a preliminary version of this analysis I did just that. Such cuts would reduce the combinatoric background of fake D^{*+} candidates formed from random combinations of tracks. The efficiencies of these $\mathrm{d}E/\mathrm{d}x$ cuts are consistent between data and Monte Carlo at the level of 1% per track. As a result, my use of these $\mathrm{d}E/\mathrm{d}x$ cuts introduced a 2% systematic uncertainty to my branching fraction measurement. I found that removing these cuts only added an 0.6% statistical uncertainty to my measurement, hence I no longer use this $\mathrm{d}E/\mathrm{d}x$ information in my analysis.

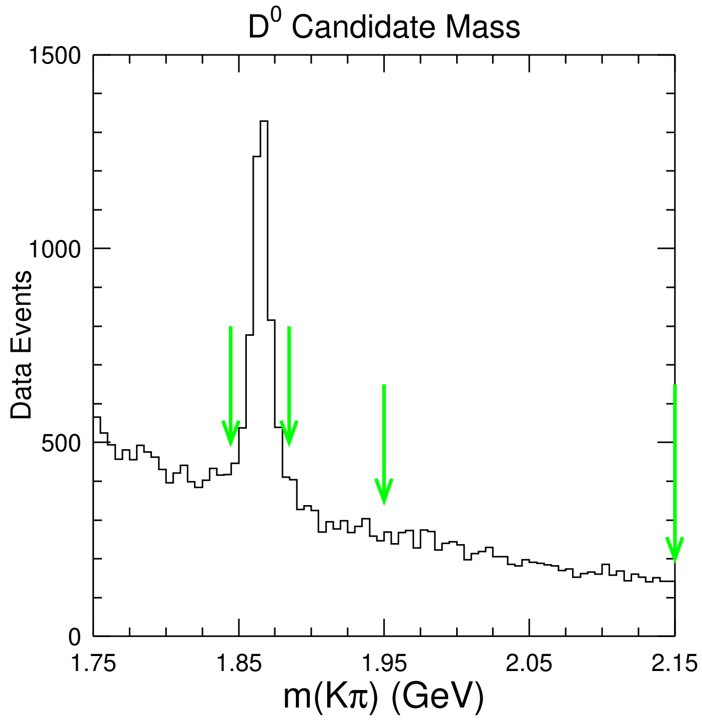

Figure 3.4: The reconstructed $m(K\pi)$ distribution. This plot shows the mass of all D^0 candidates which have been combined with slow pions and leptons to form $D^{*+}\ell^-\bar{\nu}$ candidates in on-resonance data, with a cut $\Delta m \leq 170\,\mathrm{MeV}$. The arrows indicate the signal and sideband regions I discuss in the text; the upper edge of the sideband region falls at the plot boundary.

I do a vertex-constrained fit of the kaon and pion tracks to form a D^0 meson candidate. I use the `VCFIT` package [36] to perform the fit. The track error matrices must be correct in order to do vertex-constrained fit, so I require both the kaon and pion to have good Kalman fits. I use the Kalman-fit track parameters corresponding to the particle hypothesis — e.g., the kaon Kalman fit if I am assuming the track is a kaon. I discard the candidate if the Kalman fit fails for any reason. While the tracks are constrained to a common vertex, this vertex is not otherwise constrained (to the beamspot, for example), and I do not impose a mass constraint. I use the parent pseudo-track returned by the fit as my D^0 candidate. I label the mass of the reconstructed D^0 candidate $m(K\pi)$. This quantity peaks at the known D^0 mass of 1.8646 GeV, as I show in Figure 3.4. My signal events fall in the region

$$1.8446 \leq m(K\pi) \leq 1.8846\,\text{GeV}. \tag{3.2}$$

This window extends 20 MeV to either side of the measured value of m_{D^0}, which is roughly three times the standard deviation of the observed peak in the distribution. I also retain events in the sideband region

$$1.95 \leq m(K\pi) \leq 2.15\,\text{GeV}. \tag{3.3}$$

These events are used in modeling the combinatoric background, as described in Section 3.2.2.

I form D^{*+} candidates by adding soft pion tracks to the candidate D^0 pseudo-tracks. The mass difference between the D^{*+} and D^0 mesons is very small, only 145.44 MeV. As a result, the pions produced in the decay $D^{*+} \to D^0\pi^+$ have low momenta. I will label these "slow" or "soft" pions π_s to distinguish them from the more energetic pions produced in the D^0 decay. For logical consistency, I require that the π_s be a different track from either the K or π used to reconstruct the D^0. I also require that the π_s charge be consistent with the flavor of the reconstructed D^0; that is, I combine only π_s^+ tracks with D^0 candidates, and π_s^- tracks with candidate $\bar{D}^0$ mesons. This requirement is equivalent to the condition that the π_s have the same sign as the π used to form the D^0, the sign opposite to that of the

K. I make the following track-quality cuts on the slow pion:

- not a z-escape track
- not a dredge-seed track
- `kincd` $\neq -1, -3$
- $|\cos\theta_{\pi_s}| \leq 0.9$
- $|\cos\theta_{\pi_s}| \leq 0.7071$ **if** charge division used

The first four cuts are a subset of those I make on the K and π tracks I use to form D^0 candidates. I do not make a Trackman cut on the slow pion, for reasons I discuss below. I do not accept slow pion tracks that are fit with charge-division information outside the "good barrel" angular region, as the charge-division constants used to convert raw detector information to a z position are only valid inside this angular range. This cut is only relevant for slow pions, as charge-division information is never used to fit hard tracks.

I do a second vertex-constrained fit to form a D^{*+} pseudo-track from the π_s track and the D^0 pseudo-track. I again do not impose a mass constraint, but in this fit I do constrain the vertex to the measured beamspot. I require a good Kalman fit for the slow pion track, and I discard the candidate if the vertex-constrained fit fails. I label the mass of the D^* candidate $m(K\pi\pi_s)$, and I define

$$\Delta m = m(K\pi\pi_s) - m(K\pi). \tag{3.4}$$

I calculate Δm for each candidate based on the D^{*+} and D^0 pseudo-tracks. (While the D^{*+} vertex-constrained fit returns new values for the four-momentum of the

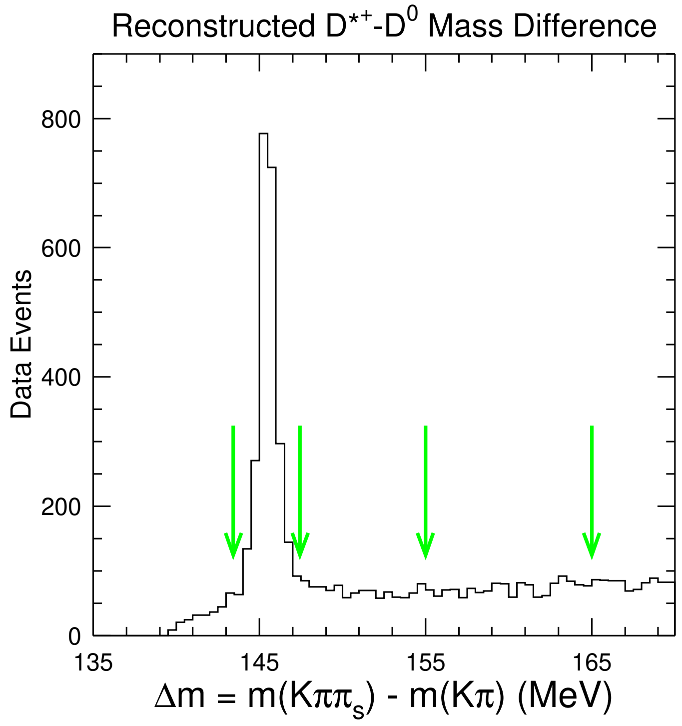

Figure 3.5: The reconstructed Δm distribution in the $m(K\pi)$ signal region ($1.8446 \leq m(K\pi) \leq 1.8846\,\mathrm{GeV}$). The entries are from D^{*+} candidates used to form $D^{*+}\ell^-\bar{\nu}$ candidates in on-resonance data.

D^0 pseudo-track, the D^0 pseudo-track mass is preserved by the fit.) The Δm distribution of D^{*+} candidates peaks strongly at the expected value of 145.44 MeV, as I show in Figure 3.5. My candidate signal events fall in the region

$$143.44 \leq \Delta m \leq 147.44\,\mathrm{MeV}. \tag{3.5}$$

This window extends 2 MeV to either side of the measured value of the D^{*+}–D^0 mass difference, which, again, is roughly three times the standard deviation of the observed peak. In addition, I retain events in the sideband region

$$155 \leq \Delta m \leq 165\,\mathrm{MeV}, \tag{3.6}$$

which I use to model the combinatoric background, as described in Section 3.2.2.

I place one additional consistency cut on the D^* candidates:

$$p_{D^*} \leq \frac{1}{2}\sqrt{E_B^2 - m_{D^*}^2} \tag{3.7}$$

Here E_B is the B meson energy in the event, which I set equal to the beam energy E_{beam} in this cut. The quantity m_{D^*} is the known D^{*+} mass, 2.010 GeV. This cut simply ensures that a D^{*+} candidate not carry more than half the available energy in the B meson decay.

The existence of curlers makes it possible for a single D^{*+} meson to be correctly reconstructed more than once from different sets of tracks. This duplication can occur when a spiraling slow pion creates two or more `DUET` tracks of the same sign. Such tracks often have similar three-momenta, and as a result, each can be reconstructed, in conjunction with a common D^0 candidate, as a distinct D^{*+} candidate. The D^{*+} candidates associated with the later passes of the curling π_s are not wrong so much as poorly measured, for all are produced by the same track. I find an average of 1.13 slow pions per D^0 candidate with $\Delta m < 170$ MeV.

The multiplicity of reconstructed D^{*+}'s associated with a single true D^{*+} raises the issue of double-counting. If a single D^{*+} contributes two entries in the signal region, it will inflate the signal yield. Worse, the multiplicity problem can induce a subtraction of events. If a single true D^{*+} provides candidates in both Δm signal and sideband regions, the combinatoric background subtraction (described in Section 3.2.2) will cause the event to over-subtract itself, and actually take away about three events from the signal region.

The Trackman algorithm attempts to weed out curlers and to select the parent track, but it does not always succeed. In particular, if the track completes several revolutions, `DUET` often does not reconstruct a track for every single curler pass. In such situations, Trackman will not group all the passes of the curler together but will instead make two or more curler groups. Trackman is therefore insufficient to eliminate the double-counting problem. Furthermore, the algorithm occasionally misidentifies the back half of a curler for the front. For these reasons I do not apply Trackman cuts to the slow pions in my analysis.

To avoid the double-counting problem, I allow only one D^{*+} candidate to be formed from each D^0 candidate. I form all the D^{*+} candidates for each D^0, but I then select only one to use in the analysis. I choose the D^{*+} candidate for which the slow pion contribution to the χ^2 of the D^{*+} vertex-constrained fit is least.

3.1.3 Lepton Reconstruction

I use two species of charged leptons in this analysis, electrons and muons. I apply the same track-quality requirements to lepton tracks as I do to the K and π tracks used to form D^0 candidates. These cuts are listed at the beginning of Section 3.1.2. While species-dependent Kalman fits can be done for electrons and muons, these fits were not done in either the recompress `PASS2` of the data or in the `PASS2` stage of recompress Monte Carlo generation. These fits do not give significantly different results from the pion-hypothesis track fit, so they were omitted to save processing time and storage space. I therefore use the parameters from the pion-hypothesis fit for my lepton candidates.

I use the Cornell Electron Identification package `CEID` to identify electrons. I describe this package in detail in Section 2.4.4. In data, this package combines E/p, the ratio of energy deposited in the calorimeter to the track momentum, information about the location and shape of the calorimeter shower, and $\mathrm{d}E/\mathrm{d}x$ information to compute the likelihood that a track and associated shower were produced by an electron. For Monte Carlo events, `CEID` uses tagging information to determine whether a particle is an electron or not, and then throws random numbers at measured electron efficiencies or fake rates. I make the following cuts on electron candidates:

- `r2elec` ≥ 3.0
- $0.8 \leq p_e \leq 2.4$
- $|\cos\theta_e| \leq 0.7071$

The quantity `r2elec` is the `CEID` electron-quality parameter. The variables p_e and θ_e are the momentum and polar angle of the electron track, respectively. I only use electrons in the "good barrel" region of the detector, defined by my cut on electron direction, as the electron efficiencies and fake rates are best understood there. In Monte Carlo, I use tagging information to require that candidate electrons tracks actually be produced by generator-level electrons.

Muons are identified based on their penetration into the muon system. This technique is only effective for higher energy muons. As a result, my muon yield is only around 40% of that for electrons. My muon cuts are:

- `muqual` $= 0$
- `dpthmu` ≥ 5.0
- $1.4 \leq p_\mu \leq 2.4$
- $|\cos\theta_\mu| \leq 0.7071$

The `muqual` cut indicates that the hits in the muon chambers are of good quality, with no suspicious gaps. The `dpthmu` cut requires that muon candidates penetrate at least five interaction lengths of iron. As with electrons, I require Monte Carlo muon candidates to be tagged as real muons.

I form each $D^{*+}\ell^-\bar{\nu}$ candidate by combining a D^{*+} and a lepton candidate in an event. For consistency, I require that the lepton not be the same track as any of the three tracks used to form the D^{*+} candidate, and that the lepton have the opposite sign to the D^{*+}. I do not make any attempt to vertex the lepton with the D^{*+} pseudo-track.

I place one additional cut on $D^{*+}\ell^-\bar{\nu}$ candidates. This cut is on the cosine of the angle between the D^{*+} and the lepton in the laboratory frame, $\cos\theta_{D^*\ell}$. In $D^{*+}\ell^-\bar{\nu}$ signal events, the D^{*+} and lepton tend to be emitted in opposite directions. Accordingly, signal events peak near $\cos\theta_{D^*\ell} = -1$. An important class of background is the uncorrelated-lepton background, the background due to D^{*+}'s and leptons that are produced in the decays of different B mesons in the same event. This background is symmetric about $\cos\theta_{D^*\ell} = 0$, the point at which I place my

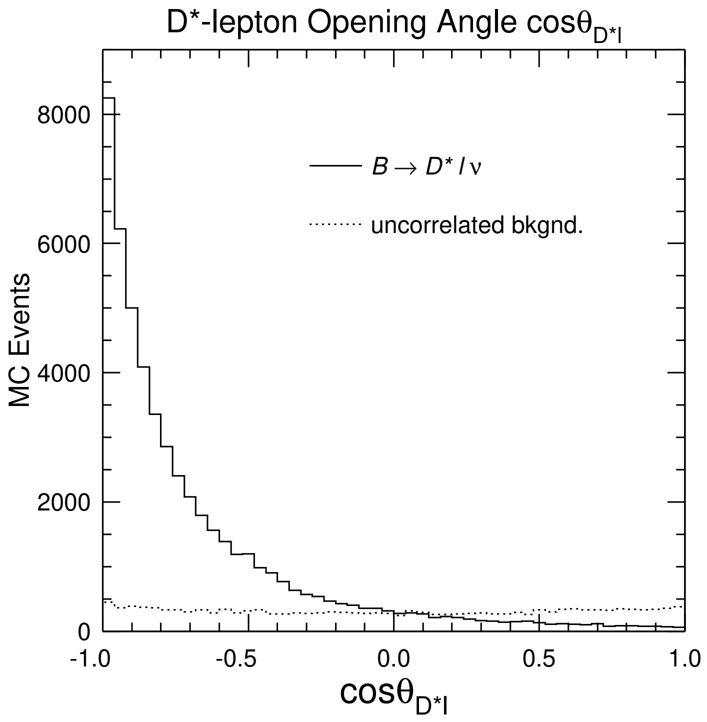

Figure 3.6: The distribution of $\cos\theta_{D^*\ell}$ in $\bar{B}^0 \to D^{*+}\ell^-\bar{\nu}$ events and in uncorrelated background events. The distributions are from from generator-level D^{*+}'s and leptons in Monte Carlo events, and reflect the lepton momentum cuts described in the text. I have also applied the cuts $|\cos\theta_{D^*}| \leq 0.8$ and $|\cos\theta_\ell| \leq 0.7071$ to mimic the acceptance of my analysis.

cut. This cut is about 90% efficient when applied after the lepton momentum cuts, and it eliminates half the uncorrelated-lepton background. I illustrate the $\cos\theta_{D^*\ell}$ distributions for signal and uncorrelated background events in Figure 3.6.

3.1.4 Calculation of $\cos\theta_{BY}$

The method I describe in the preceding sections reconstructs $\bar{B}^0 \to D^{*+}\ell^-\bar{\nu}$ events with an efficiency of about 16%. Several classes of background mimic the signal

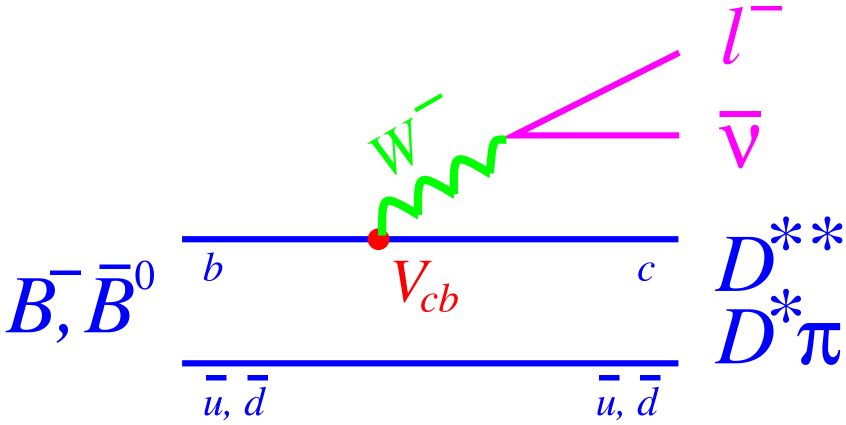

Figure 3.7: The Feynman diagram for $B \to D^{*+}X\ell^-\bar{\nu}$. The final state includes either a D^{**} meson or a non-resonant combination of a D^* and some other particle. Compare with the Feynman diagram for $\bar{B}^0 \to D^{*+}\ell^-\bar{\nu}$ in Figure 1.1.

events. The sources of most of these backgrounds are well-understood, and there are reliable ways to simulate their distributions. I list these background event classes and describe how I model them in Section 3.2.

The exception is the background from $B \to D^{*+}X\ell^-\bar{\nu}$ processes, in which I reconstruct the D^* and lepton as a $D^{*+}\ell^-\bar{\nu}$ candidate but do not observe a final-state particle X. In this work, I use "$D^{*+}X\ell^-\bar{\nu}$" to refer only to processes in which the charged lepton is produced in the initial B decay. I refer to background processes in which the lepton is the daughter of a particle in the B decay, such as a τ or a second charm meson, as the correlated-lepton background. The $D^{*+}X\ell^-\bar{\nu}$ background includes both non-resonant decays, such as $B \to D^{*+}\pi\ell^-\bar{\nu}$, and resonant $B \to D^{**}\ell^-\bar{\nu}$ decays, in which some higher excited D resonance D^{**} decays to a D^{*+} plus another particle. I show the Feynman diagram for these decays in

Figure 3.7. Both B^0 and $B^\pm$ mesons can contribute to this background, depending on the charge of the particle X.

Many of the modes that may contribute to the $D^{*+}X\ell^-\bar{\nu}$ background have not been measured. The exception is the decay $B \to D_1\ell^-\bar{\nu}$, which has been measured by the CLEO [37] and ALEPH [38] collaborations. These analyses also set upper limits on the $B \to D_2^*\ell^-\bar{\nu}$ branching fraction. (The ALEPH analysis also measures the total inclusive branching fraction $B \to D^{(*)}X\ell^-\bar{\nu}$, which includes non-resonant $DX\ell^-\bar{\nu}$ in addition to non-resonant $D^*X\ell^-\bar{\nu}$ and resonant $D^{**}\ell^-\bar{\nu}$ final states.) Furthermore, our knowledge of the form factors that govern these decays is minimal. To handle this background, I use a technique developed in Ye Liu's analysis of $B \to D\ell^-\bar{\nu}$ [39]. This technique makes use of a variable, $\cos\theta_{BY}$, that distinguishes signal $\bar{B}^0 \to D^{*+}\ell^-\bar{\nu}$ events from the $D^{*+}X\ell^-\bar{\nu}$ background. The level of $D^{*+}X\ell^-\bar{\nu}$ background is allowed to float in the fit, which allows the extraction of the $D^*\ell^-\bar{\nu}$ yield without knowledge of the various $D^{*+}X\ell^-\bar{\nu}$ branching fractions. Furthermore, this fit is relatively insensitive to the exact distribution of the $D^{*+}X\ell^-\bar{\nu}$ events, which allows me to make my branching fraction measurement without a detailed knowledge of either the $D^{*+}X\ell^-\bar{\nu}$ form factors or the relative contributions of different modes.

The variable $\cos\theta_{BY}$ is the cosine of the opening angle between the parent $\bar{B}^0$ meson and the system Y of the D^{*+} and the lepton. This angle is measured in the laboratory frame of reference. I derive a simple expression for the cosine of this angle for $\bar{B}^0 \to D^{*+}\ell^-\bar{\nu}$ decays as follows. By four-momentum conservation, the neutrino four-momentum p_ν is related to those of the B meson and the Y system by:

$$p_\nu = p_B - p_Y. \tag{3.8}$$

I square this equation and expand the right side to get:

$$p_\nu^2 = (E_B - E_Y)^2 - (\mathbf{p}_B - \mathbf{p}_Y)^2, \tag{3.9}$$

$$= (E_B - E_Y)^2 - p_B^2 - p_Y^2 + 2p_B p_Y \cos\theta_{BY}. \tag{3.10}$$

Here E_B and E_Y are the energies of the B and the D^*–ℓ system, $\mathbf{p}_B$ and $\mathbf{p}_Y$ are their three-momenta, and p_B and p_Y are the magnitudes of the three-momenta. The square of the neutrino four-momentum is simply its mass, which is zero for my purposes. I solve for $\cos\theta_{BY}$ to get:

$$\cos\theta_{BY} = -\frac{(E_B - E_Y)^2 - p_B^2 - p_Y^2}{2p_B p_Y}. \tag{3.11}$$

With this equation I can calculate $\cos\theta_{BY}$ for every $D^{*+}\ell^-\bar{\nu}$ candidate. As I have reconstructed the D^{*+} and the lepton, I have measured both E_Y and p_Y directly. The values of E_B and p_B in data are well-understood from other CLEO measurements; in Monte Carlo they are essentially input values. I explain where I get the values I use in my calculation of $\cos\theta_{BY}$ in the following section.

As θ_{BY} is a physical angle, its cosine must lie between -1 and 1. In only a small fraction of $\bar{B}^0 \to D^{*+}\ell^-\bar{\nu}$ events does the reconstructed value of $\cos\theta_{BY}$ fall outside this physical region. The situation is different for $B \to D^{*+}X\ell^-\bar{\nu}$ events. In these events, my calculation of $\cos\theta_{BY}$ neglects the particle X. To correct this omission, I must replace the neutrino in Equation 3.8 with the combination of the

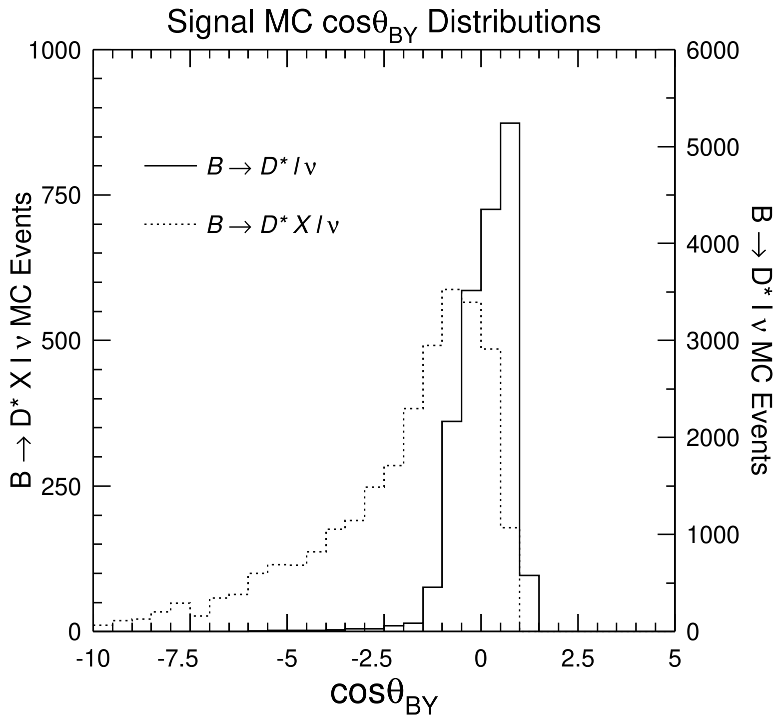

Figure 3.8: The $\cos\theta_{BY}$ distributions of reconstructed $\bar{B}^0 \to D^{*+}\ell^-\bar{\nu}$ and $B \to D^{*+}X\ell^-\bar{\nu}$ events. The solid histogram shows the reconstructed $\cos\theta_{BY}$ distribution from 100,000 $\bar{B}^0 \to D^{*+}\ell^-\bar{\nu}$ signal Monte Carlo events; the dotted from 40,000 $B \to D^{*+}X\ell^-\bar{\nu}$ events. In each case I have tagged the relevant decay mode to eliminate the small backgrounds present in these Monte Carlo samples. I show the two distributions on different vertical scales to emphasize the difference between their shapes.

particle X and the neutrino. Carrying this change through, I obtain:

$$\cos\theta_{BY} = -\frac{(E_B - E_Y)^2 - p_B^2 - p_Y^2 - m_{X\nu}^2}{2p_B p_Y}. \tag{3.12}$$

Here $m_{X\nu}$ is the invariant mass of the X–ν system, a quantity that is always positive. If I neglect this term when I calculate $\cos\theta_{BY}$ for a $D^{*+}X\ell^-\bar{\nu}$ event, my result will be less than the true value, and it can fall below the physical region. In Figure 3.8, I present the reconstructed $\cos\theta_{BY}$ distributions for both $\bar{B}^0 \to D^{*+}\ell^-\bar{\nu}$

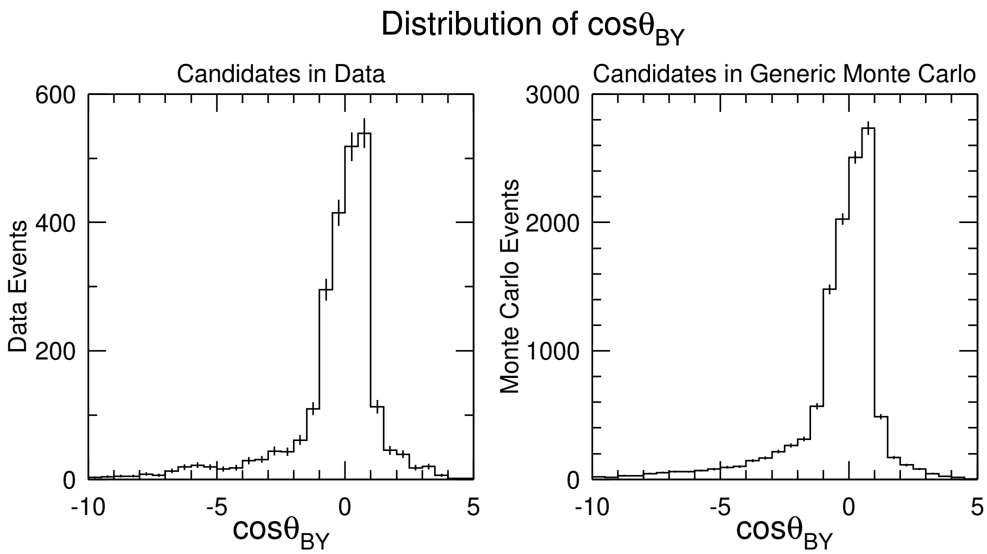

Figure 3.9: The total $\cos\theta_{BY}$ distribution in the signal region for data (left) and Monte Carlo (right). The data distribution is from all on-resonance data in the 4s2–G datasets. The Monte Carlo sample corresponds to 16.71 million generic Monte Carlo events.

signal and $B \to D^{*+}X\ell^-\bar{\nu}$ background events. The signal events lie primarily in the physical region from -1 to 1, while many of the background events fall in a long tail below $\cos\theta_{BY} = -1$.

In Figure 3.9, I show the reconstructed $\cos\theta_{BY}$ distributions for all $D^{*+}\ell^-\bar{\nu}$ candidates in the on-resonance data and in the generic Monte Carlo. Each shows the same general features. The peak of $\bar{B}^0 \to D^{*+}\ell^-\bar{\nu}$ events in the physical region is clear. There is an extended tail to negative values of $\cos\theta_{BY}$; this tail is partly due to the $D^{*+}X\ell^-\bar{\nu}$ background, and partly to the other background sources. There is also a shoulder of events with $\cos\theta_{BY} > 1$. No $D^{*+}X\ell^-\bar{\nu}$ events fall in this region, but events of several other background classes do.

In Section 3.2, I discuss the various sources of background, and detail how I calculate their $\cos\theta_{BY}$ distributions. Finally, in Section 3.3, I present my extraction of $\mathcal{B}(\bar{B}^0 \to D^{*+}\ell^-\bar{\nu})$ from fits to the distributions of Figure 3.9.

3.1.5 B momentum and mass values

My reconstruction of $\cos\theta_{BY}$ with Equation 3.11 requires independent knowledge of both the average B momentum in CLEO II events, p_B, and the B mass, m_B. In this section I explain the origin of the values I use for these B parameters.

I base my input B-momentum values on a careful study of B momentum in each dataset performed by Vitaliy Fadeyev [40]. This analysis fully reconstructs B-meson decays to a variety of two-body hadronic final states. The average B momentum varies from dataset to dataset, as CESR does not always run at exactly the same beam energy. As the B^0 and B^+ mesons need not have the same mass, Fadeyev presents separate results for the average neutral and charged B-meson momenta, $\langle p_{B^0}\rangle$ and $\langle p_{B^+}\rangle$. He also gives the results of running his study on the generic Monte Carlo.

Ritchie Patterson uses the results of Fadeyev's study to compute corrected average p_{B^0} and p_{B^+} values for each dataset [41]. The average B momenta in generic Monte Carlo can be extracted directly from generator-level information. Patterson therefore calculates and corrects for a small methodological bias in Fadeyev's study. She also constrains the difference in average B momentum, $\langle p_{B^+}\rangle - \langle p_{B^0}\rangle$,

Table 3.1: The average B^0 momenta for each CLEO II dataset. The average momenta used in reconstruction of data, generic Monte Carlo, and signal Monte Carlo events are listed.

Dataset	$\langle p_{B^0} \rangle$ (MeV)		
	data	generic MC	signal MC
4s2	292.0	298.50	296.86
4s3	326.5	332.62	333.81
4s4	331.4	337.15	336.98
4s5	298.6	302.73	305.92
4s6	326.5	329.81	329.46
4s7	313.1	319.93	319.10
4s8	300.1	310.92	313.03
4s9	303.6	313.10	311.87
4sA	296.0	287.98	284.63
4sB	345.7	342.47	343.15
4sC	288.0	295.15	294.13
4sD	277.1	291.05	290.56
4sE	294.4	296.05	300.44
4sF	290.2	297.82	296.17
4sG	284.5	291.27	291.10

to a constant value across all datasets. She obtains

$$\langle p_{B^+} \rangle - \langle p_{B^0} \rangle = 8.3 \pm 2.2 \pm 0.6 \pm 0.6\,\mathrm{MeV}, \tag{3.13}$$

where the three errors are associated with the fit for average B momentum across all datasets and the separate systematic biases of the $\langle p_{B^0} \rangle$ and $\langle p_{B^+} \rangle$ studies. I use the resulting corrected average $\langle p_{B^0} \rangle$ values in my computation of $\cos\theta_{BY}$ in data. I give these values in the first column of Table 3.1.

The B-meson masses were recently measured very precisely in a CLEO analysis by Alexey Ershov [42]. I take this measurement as the basis for the B^0 mass in my calculation of $\cos\theta_{BY}$. I again apply a small correction computed by Ritchie Patterson. She notes that the difference in average B momenta in Equation 3.13 corresponds to a mass difference

$$\Delta m_B = m_{B^+} - m_{B^0} = 0.47 \pm 0.14\,\mathrm{MeV}, \tag{3.14}$$

and corrects Ershov's B-mass values to incorporate this difference. Patterson obtains

$$m_{B^0} = 5279.4 \pm 0.76 \pm 0.1\,\mathrm{MeV}, \tag{3.15}$$

with errors due to Ershov's mass measurement and the mass difference calculation. I use this mass value and the average value of p_B to compute E_B for each dataset:

$$E_{B^0} = \sqrt{\langle p_{B^0}\rangle^2 + m_{B^0}^2} \tag{3.16}$$

It is this value of E_B that I use to compute $\cos\theta_{BY}$ in data.

In Monte Carlo things are slightly simpler. I look up the actual B momentum in every Monte Carlo event at generator level, and average across each dataset. My average B momenta in Monte Carlo are therefore exact, and introduce no systematic error to the branching fraction measurement. In contrast, as the measurement of average B momentum in data has an error, I must vary these averages to establish a systematic uncertainty. Dataset-by-dataset, the average B momenta are not the same in the recompress generic Monte Carlo and in my signal Monte Carlo, so I use different average momenta when reconstructing Monte Carlo events from these two sources. I present these averages in the second and third columns of Table 3.1. All the Monte Carlo that I use was generated with the B masses $m_{B^0} = m_{B^+} \equiv 5.2800\,\mathrm{GeV}$, so I use this value when calculating $\cos\theta_{BY}$ in Monte Carlo.

I do not use the CESR beam energy E_{beam} in any way in my calculation of $\cos\theta_{BY}$. In principle, using E_{beam} allows run-to-run corrections to the B momenta, and by not using these corrections I introduce some smearing to my $\cos\theta_{BY}$ distributions. However, the uncertainties in the calculation of E_{beam} would introduce larger systematic uncertainties to my measurement of the $\bar{B}^0 \to D^{*+}\ell^-\bar{\nu}$ branching fraction than the method I outline above. In fact, the calibration of E_{beam} is based on average B-momentum measurements similar to those I use directly.

3.2 Backgrounds

There are a number of backgrounds to $\bar{B}^0 \to D^{*+}\ell^-\bar{\nu}$ reconstruction, some larger than others, and some better understood that others. These reconstruction fall into six categories, namely continuum, combinatoric, fake-lepton, uncorrelated-lepton, correlated-lepton, and $D^{*+}X\ell^-\bar{\nu}$ background. In this section, I define these backgrounds and describe the methods I use to model them. I estimate several from the CLEO data, namely the continuum, combinatoric, and fake-lepton backgrounds. I model both the uncorrelated and correlated backgrounds with sums of Monte Carlo distributions. These two backgrounds are strongly constrained by a variety of measurements and introduce little error to my analysis. Least well understood is the $B \to D^{*+} X \ell^- \bar{\nu}$ background. The overall level of this background is allowed to float in a fit to the $\cos\theta_{BY}$ distribution, and I vary its shape to establish a systematic error.

3.2.1 Continuum Background

The $\Upsilon(4S)$ resonance sits atop a background of $e^+e^- \to q\bar{q}$ events. These events contribute a significant background to many CLEO analyses. In order to understand these backgrounds, CLEO collects roughly a third of its data below the $\Upsilon(4S)$ resonance. I run exactly the same reconstruction code on both on and off-resonance data. With the appropriate scaling to account for the different luminosities, and a small correction for the difference in $q\bar{q}$ cross section with energy, the continuum background can be estimated very well.

There is a logical conundrum in the calculation of $\cos\theta_{BY}$ for off-resonance events. This calculation requires a value of the B momentum, a physically meaningless quantity for off-resonance data. Since I analyze the off-resonance data only to estimate the continuum background in on-resonance data, I proceed exactly as with on-resonance data for the purposes of calculating $\cos\theta_{BY}$. When I reconstruct this variable in off-resonance events in each dataset, I use the average on-resonance B momentum $\langle p_{B^0} \rangle$ for that dataset.

I use the CLEO II 4s2–G datasets in my analysis. These datasets comprise $3137.0\,\mathrm{pb}^{-1}$ of on-resonance luminosity, and $1608.2\,\mathrm{pb}^{-1}$ off-resonance. The ratio of these integrated luminosities, 1.9506, is the on/off resonance scale factor. The average off-resonance beam energy is $5.261\,\mathrm{GeV}$. Since the continuum cross section

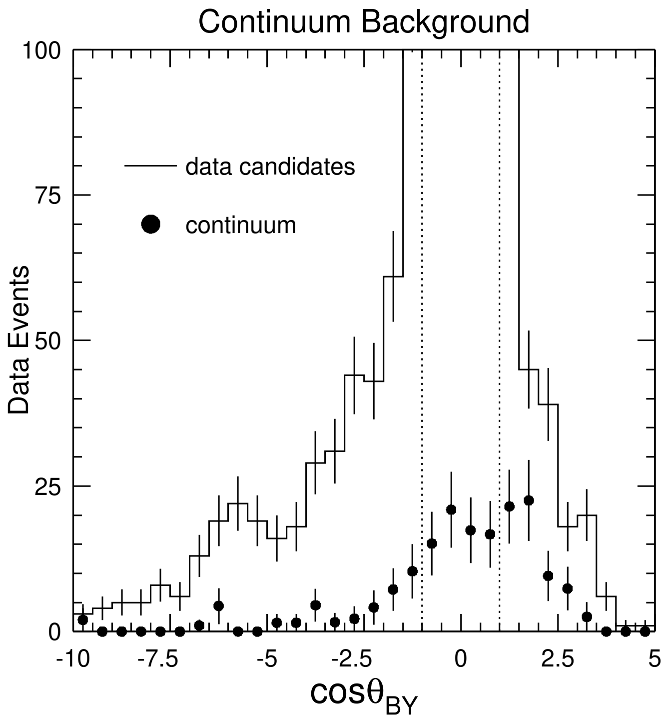

Figure 3.10: The $\cos\theta_{BY}$ distribution of the estimated continuum background. The solid histogram is a blowup of the $\cos\theta_{BY}$ distribution of all $\bar{B}^0 \rightarrow D^{*+}\ell^-\bar{\nu}$ candidates in data. The points give my estimate of the continuum background. The dotted lines mark the physical region $-1 < \cos\theta_{BY} < 1$. I derive this estimate from off-resonance data.

falls as the inverse square of the center-of-mass energy, the energy dependence implies a small correction of 0.9893 to the on/off scale factor.

I form my continuum background estimate by taking the distribution of off-resonance events in the $D^{*+}\ell^-\bar{\nu}$ signal region and scaling them up by the on/off resonance scale factor. In practice, I scale the off-resonance events to the on-resonance luminosity on a dataset-by-dataset level, as the on/off ratio varies considerably between datasets. I apply the cross-section correction uniformly across all datasets.

I plot the $\cos\theta_{BY}$ distribution of the estimated continuum background in the signal region in Figure 3.10. This background extends above the physical region of $\cos\theta_{BY}$, and tails off rapidly below it. The momentum spectra of continuum D^{*+}'s and leptons distributions are harder than those in $\Upsilon(4S)$ decays, and these harder tracks tend to populate the higher $\cos\theta_{BY}$ region.

There is, of course, no continuum background in the generic $B\bar{B}$ Monte Carlo.

3.2.2 Combinatoric Background

The combinatoric background is composed of events in which the three tracks used to form a D^{*+} candidate — the K, π, and π_s — did not actually originate from a $D^{*+} \to D^0\pi_s^+, D^0 \to K^-\pi^+$ decay. There are a number of ways in which such combinations can occur. Correctly reconstructed D^0's can be combined with random slow pions to produce a D^{*+} background that peaks in $m(K\pi)$ but not in Δm. A misreconstructed D^0 from a D^{*+} decay can be combined with the correct π_s, resulting in background that peaks in Δm, but not in $m(K\pi)$. In events containing a $D^{*+} \to D^0\pi_s^+$ decay, the D^0 can decay in a mode I do not reconstruct but be misreconstructed as $D^0 \to K^-\pi^+$. Finally, completely unrelated tracks can be combined, falling by chance into the signal region.

Two important tools help to significantly reduce these combinatoric backgrounds. The first is the Kalman fitter. CLEO measures slow pion tracks much more accurately with the Kalman fitter than without. Furthermore, the accurate error matrices allow the π_s to be vertexed, and the vertex constraint greatly improves the measurement of otherwise poorly-reconstructed slow pions. Vertexing thus increases the D^{*+} yield in the Δm signal region by almost a factor of two. The tracking improvements also decrease the width of the Δm peak. The Kalman fitter alone narrows the width of this peak by about a factor of two. With the Kalman, vertexing further narrows the peak by 20%. As a result of these improvements, my Δm signal region is half the size of the one used in the previous CLEO $\bar{B}^0 \to D^{*+}\ell^-\bar{\nu}$ analysis [9]. This improvement alone reduces the combinatoric background substantially.

The other tool is the correlation of the slow pion charge with the D^0 flavor. This correlation eliminates a type of background, termed "K–π swapping," which is an issue for $D^{*0} \to D^0\pi^0$ reconstruction in the CLEO $B^- \to D^{*0}\ell^-\bar{\nu}$ analysis [43]. In that analysis, the D^0 can be reconstructed with the kaon and pion swapped and still combined with the same π^0. In this analysis, the charge of the slow pion prevents such misreconstruction.

Figure 3.11 is a scatter plot of the variables $m(K\pi)$ versus Δm for candidate signal events. This plot has several notable features. Correctly reconstructed D^0 mesons appear as the horizontal band at the known D^0 mass, 1.8646 GeV. Correctly reconstructed D^{*+} mesons peak in both the $m(K\pi)$ and Δm signal windows, indicated as region "A" on the figure. Real D^0's paired with random slow pions fill the band to the right of region A. There is also vertical band, visible above and below the signal region, that fades rapidly away from the peak. This band is due to real D^{*+}'s in which the D^0 is poorly reconstructed. I choose my high $m(K\pi)$ sideband region well away from this tail of events.

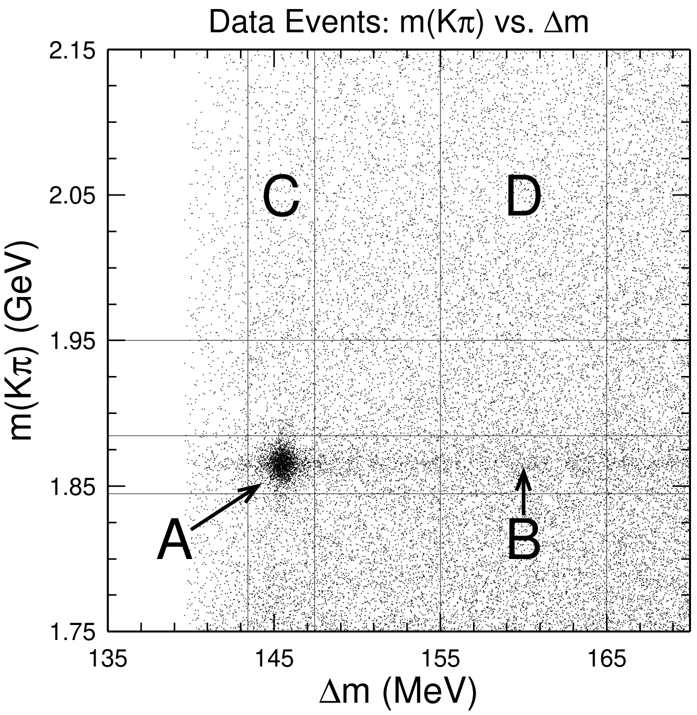

Figure 3.11: A scatter plot of reconstructed $m(K\pi)$ versus Δm for candidate $\bar{B}^0 \to D^{*+}\ell^-\bar{\nu}$ events in the on-resonance data. The vertical lines mark the Δm signal $(143.44 < \Delta m < 145.44\,\mathrm{MeV})$ and sideband $(155.0 < \Delta m < 165.0\,\mathrm{MeV})$ regions, while the horizontal lines indicate the $m(K\pi)$ signal $(1.8446 < m(K\pi) < 1.8846\,\mathrm{GeV})$ and sideband $(1.95 < m(K\pi) < 2.15\,\mathrm{GeV})$ regions. The labels A, B, C, and D indicate regions discussed in the text.

I model the $\cos\theta_{BY}$ distribution of the combinatoric background with events in the region labeled "B" in Figure 3.11. These events fall in the $m(K\pi)$ signal region, but are in the Δm sideband. I normalize the $\cos\theta_{BY}$ distribution of these events with a combinatoric scale factor. This factor should be the ratio between the number of combinatoric background events in the signal region A and the total number of events in the Δm sideband region B. I estimate the combinatoric scale

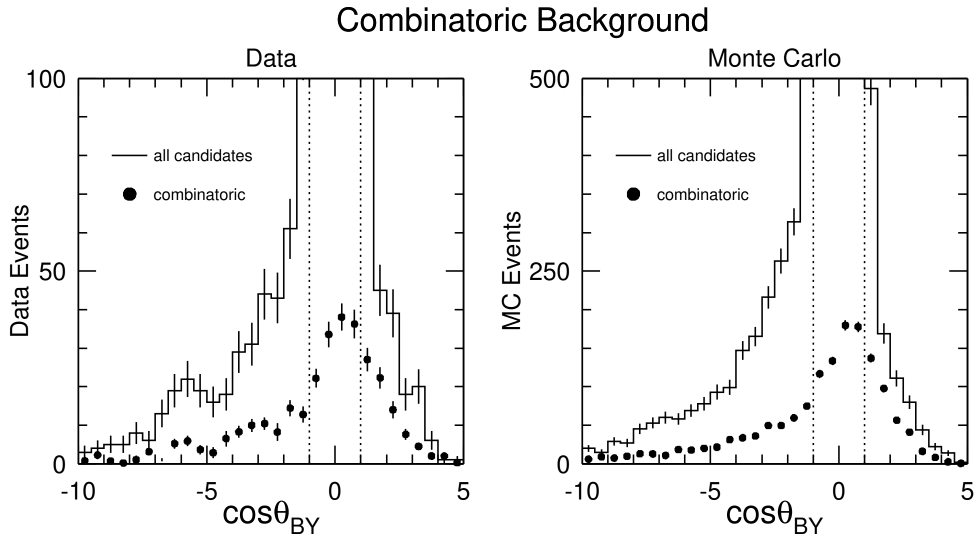

Figure 3.12: The $\cos\theta_{BY}$ distribution of the estimated combinatoric background. The left histogram shows data, the right generic Monte Carlo. Each solid histogram is a blowup of the $\cos\theta_{BY}$ distribution of all candidates. The points are the estimates of the combinatoric background distributions. The pairs of dotted lines mark the physical region $-1 < \cos\theta_{BY} < 1$.

factor with events in the high $m(K\pi)$ sideband region, $1.95 \le m(K\pi) \le 2.15\,\mathrm{GeV}$. To first order, it is the ratio of the number of events in the $m(K\pi)$ sideband, Δm signal region "C" to the number in the $m(K\pi)$ sideband, Δm sideband region "D."

In data, I measure the combinatoric scale factor following a continuum subtraction to the Δm distribution in all four signal and sideband regions. I obtain the value of 0.250 ± 0.015. This value includes a correction of -9.9% from Monte Carlo. The correction accounts for $D^0 \to \pi^+\pi^-$ events which populate the high $m(K\pi)$ sideband region and peak in Δm. I show my estimate of the combinatoric background in data in Figure 3.12. In generic Monte Carlo I remove the $D^0 \to \pi^+\pi^-$

events from the $m(K\pi)$ sideband regions using tagging information before I calculate the combinatoric scale factor. I obtain the value 0.206 ± 0.005. I also display my estimate of the combinatoric background in Monte Carlo in Figure 3.12. I defer the comparison of the estimated background to the tagged background in Monte Carlo to my systematic error discussion in Section 4.2.

The $\cos\theta_{BY}$ distributions of combinatoric background can be seen in Figure 3.12 to extend both above and below the physical region. As this background is due to misreconstructed D^{*+}'s, there is no particular constraint on $\cos\theta_{BY}$. However, some fraction of the combinatoric background is actually due to $B^- \to D^0\ell^-\bar{\nu}$ events in which a random slow pion track has been combined with the D^0 to form a fake D^{*+}. Since additional mass has been added to such $D^0\ell^-\bar{\nu}$ events, they populate the $\cos\theta_{BY}$ within and above the physical region, just as $B \to D^{*+}X\ell^-\bar{\nu}$ events fall within and below this region.

3.2.3 Fake-Lepton Background

Fake leptons are hadronic tracks that nonetheless pass the lepton identification cuts. The fake rate for both electrons and muons is quite low, so this background is small despite the the large numbers of hadronic tracks that could potentially fake leptons.

As mentioned in Section 2.4.4, the Monte Carlo electron identification package `CEID` uses tagging information to establish the particle species of a given track, and it then compares a random number to a table of fake rates. This arrangement makes a fake-lepton subtraction in Monte Carlo pointless. All one could hope

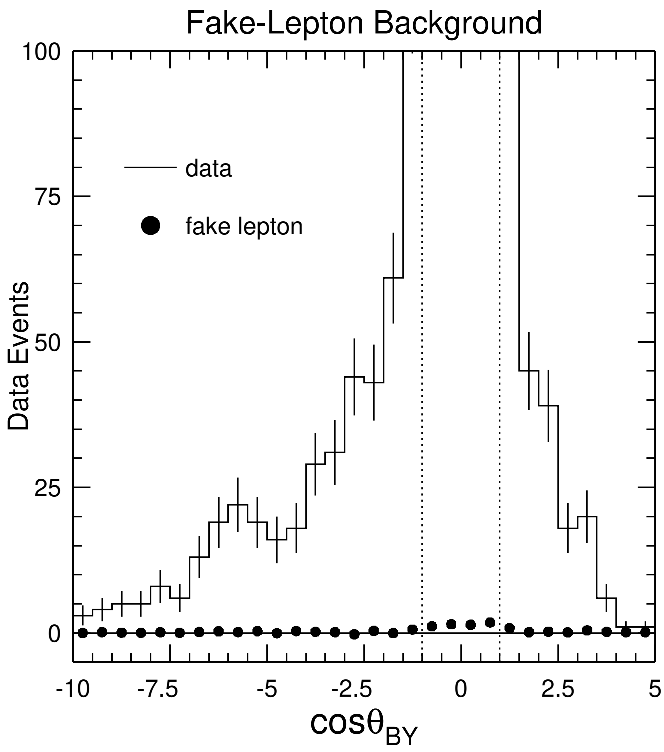

Figure 3.13: The $\cos\theta_{BY}$ distribution of the estimated fake-lepton background. The solid histogram is a blowup of the $\cos\theta_{BY}$ distribution of all $\bar{B}^0 \to D^{*+}\ell^-\bar{\nu}$ candidates in data. The points give my estimate of the fake-lepton background. The dotted lines mark the physical region $-1 < \cos\theta_{BY} < 1$. I derive this estimate from data as described in the text.

to learn is whether the Monte Carlo is correctly implementing the fake rates, something that has otherwise been tested. Therefore, in Monte Carlo I simply use tagging information to eliminate fake leptons.

In data, I take advantage of the abundance of hadronic tracks to model the fake-lepton background. In addition to lepton tracks that pass the cuts described in Section 3.1.3, I also count a fraction of those hadronic tracks that fail the lepton

Table 3.2: Lepton fake rates. The measured rates for hadronic tracks to pass the lepton-identification cuts in the given momentum regions.

	Electrons	Muons
$0.8 \leq E_\ell < 1.4\,\mathrm{GeV}$	$(0.07 \pm 0.05)\%$	—
$1.4 \leq E_\ell \leq 2.4\,\mathrm{GeV}$	$(0.15 \pm 0.10)\%$	$(0.5 \pm 0.5)\%$

identification cuts, but pass the lepton track-quality, momentum, and angular cuts. I record 10% of such tracks to model fake leptons. These tracks are combined with D^{*+} candidates in exactly the same manner as the real lepton candidates. I calculate the continuum and combinatoric backgrounds as for the real $D^{*+}\ell^-\bar{\nu}$ candidate events and subtract these backgrounds. Finally, I scale up the resulting fake-lepton distribution by the prescale factor of 10, and then down by the expected lepton fake rates.

I use the lepton fake rates given in Table 3.2. The electron values were compiled by Ye Liu for her $B \to D\ell^-\bar{\nu}$ analysis [39] based on the work of the Lepton Systematics Advisory Committee [26]. The muon value is based on an integration of muon fake rates measured in recompress data over the fake-muon momentum spectrum [44]. I show the $\cos\theta_{BY}$ distribution of the estimated fake-lepton background in Figure 3.13.

3.2.4 Uncorrelated-Lepton Background

The uncorrelated-lepton background consists of leptons and D^{*+}'s which are produced in the decays of different B mesons. As each each pseudoscalar B decays nearly at rest, the decays are close to isotropic. The D^{*+} and lepton directions are therefore not significantly correlated, hence the name of this background. To contribute a background to my analysis, the charged D^* and lepton must have opposite charges. However, in most $\Upsilon(4S)$ events in which one B decays to a charged D^* and the other to a lepton, the D^* and lepton have the same sign. $\bar{B}^0$'s and B^+'s tend to decay to D^{*+}'s and negative leptons, while B^0's and B^-'s preferentially decay to D^{*-}'s and positive leptons. As the $\Upsilon(4S)$ usually decays to a $B\bar{B}$ pair, D^*-lepton combinations from different B decays tend to have the wrong sign correlation to contribute background events to $\bar{B}^0 \to D^{*+}\ell^-\bar{\nu}$. However, if one B decay produces a "wrong-sign" D^* or lepton, the event can be counted as uncorrelated-lepton background. Uncorrelated-lepton background events can also result from B^0–$\bar{B}^0$ mixing. If both neutral B's decay in the same state, either both as B^0's or both as $\bar{B}^0$'s, any uncorrelated D^*-lepton pair they produce will likely have the right sign combination to contribute to this background.

I estimate the uncorrelated-lepton background, or uncorrelated background for short, with Monte Carlo events. I break down the different sources of uncorrelated background sketched above, and constrain each with several measurements of D^{*+} and lepton production. The exact procedure is intimately tied to the systematic error analysis for this background, so I defer a full discussion to Section 4.4.

I give the distribution of the estimated uncorrelated background in data in Figure 3.14. As the uncorrelated lepton background combines unrelated D^{*+}'s and leptons, there is no particular constraint on the $\cos\theta_{BY}$ distribution of this background. I also show the distribution of this background in Monte Carlo in Figure 3.14. In Monte Carlo, the background is simply tagged from the full set

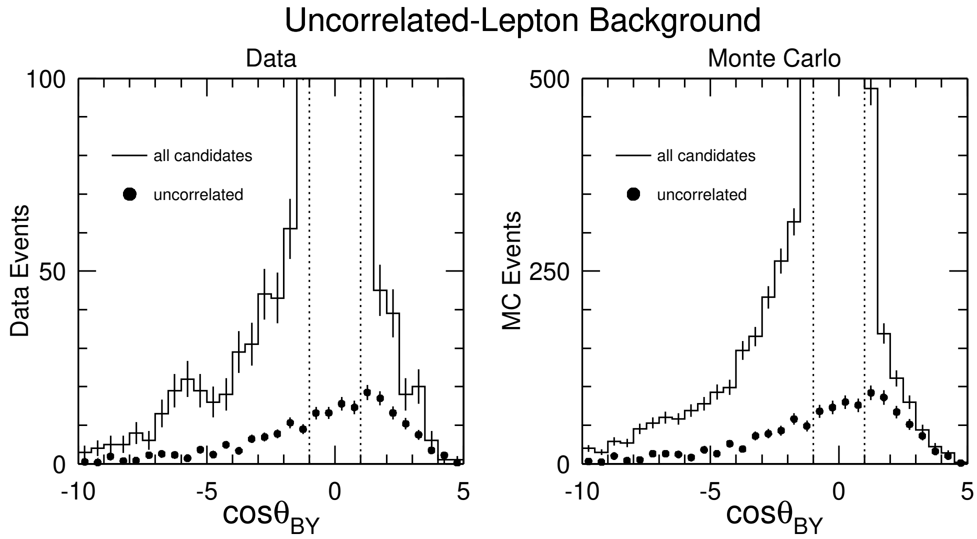

Figure 3.14: The $\cos\theta_{BY}$ distribution of the estimated uncorrelated-lepton background. The left histogram shows data, the right generic Monte Carlo. Each solid histogram is a blowup of the $\cos\theta_{BY}$ distribution of all candidates. The points are the estimates of the uncorrelated background distributions. The pairs of dotted lines mark the physical region $-1 < \cos\theta_{BY} < 1$.

of $\bar{B}^0 \to D^{*+}\ell^-\bar{\nu}$ candidates. As I use the Monte Carlo uncorrelated background events to construct the distribution of this background in data, and the Monte Carlo models inclusive D^{*+} and lepton production moderately well, the two distributions are perforce extremely similar.

3.2.5 Correlated-Lepton Background

The correlated-lepton background, or simply correlated background, is a subclass of backgrounds in which the D^{*+} and the lepton are produced in the same B decay. I classify any such background event in which the lepton is not a primary daughter of the B as correlated background. This definition is complementary to that of

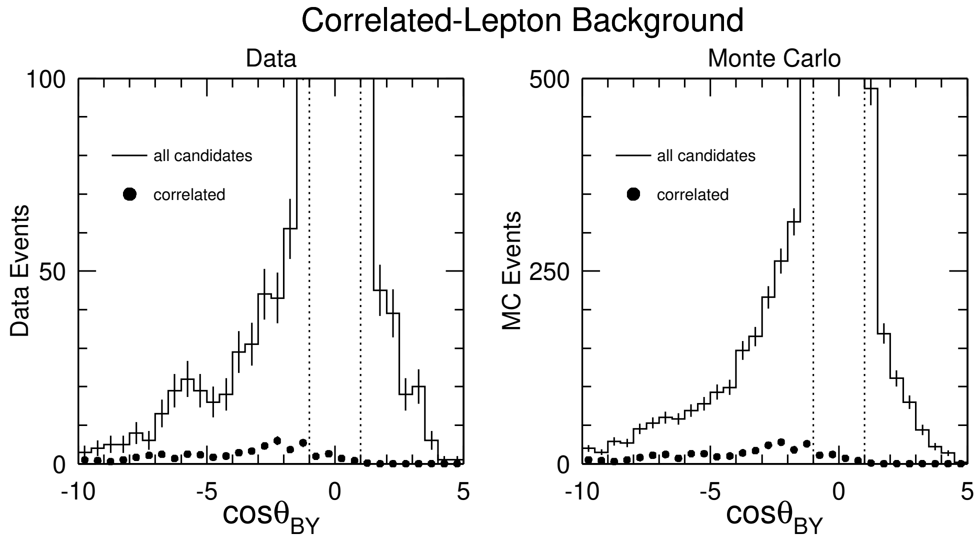

Figure 3.15: The $\cos\theta_{BY}$ distribution of the estimated correlated-lepton background. The left histogram shows data, the right generic Monte Carlo. Each solid histogram is a blowup of the $\cos\theta_{BY}$ distribution of all candidates. The points are the estimates of the correlated background distributions. The pairs of dotted lines mark the physical region $-1 < \cos\theta_{BY} < 1$.

the $D^{*+}X\ell^-\bar{\nu}$ background. All $\bar{B}^0 \to D^{*+}\ell^-\bar{\nu}$ backgrounds from single B decays fall into one of these two categories. I estimate the correlated background with the CLEO II recompress generic Monte Carlo.

I tabulate of all the decay modes that comprise this background in Section 4.5. Roughly 65% of correlated background events are due to B meson decays to pairs of charmed mesons. These decays occasionally include a third particle. In such events, one of the pair is the reconstructed D^{*+} meson, while the other produces a lepton in its decay chain. Another 25% of the correlated background is due to $B \to D^{*+}(X)\tau^-\bar{\nu}_\tau$ decays in which the τ decays leptonically. This background is both small and well-understood. The remaining 10% of the uncorrelated background is due to the decay of a B to a D^{*+} plus a lighter particle or several particles. Such events contribute correlated backgrounds through either photon conversions ($\gamma \to e^+e^-$) or Dalitz decays of π^0 or η mesons ($\pi^0 \to \gamma e^+e^-, \eta \to \gamma e^+e^-$).

While not all of these decay modes are well-understood, their total background contribution is small. I plot the $\cos\theta_{BY}$ distribution of the total correlated background in Figure 3.15. As was the case with the uncorrelated background, the data distribution is constructed with the events that comprise the Monte Carlo distribution, so the two background distributions are very similar. Since they arise from single B-meson decays, correlated background events must fall either within or below the physical region of $\cos\theta_{BY}$ by the same arguments that apply to $B \to D^{*+}X\ell^-\bar{\nu}$ events.

3.2.6 $B \to D^{*+}X\ell^-\bar{\nu}$ Background

The $B \to D^{*+}X\ell^-\bar{\nu}$ background is the least well-understood of my list of backgrounds. I use a sample of 40,000 $D^{*+}X\ell^-\bar{\nu}$ Monte Carlo events to model the shape of this distribution. In this sample, six different B-decay modes contribute to the $D^{*+}X\ell^-\bar{\nu}$ background. I list these modes in Table 3.3. The table also gives the `decay.dec` branching fractions used in Monte Carlo event generation and the model used to simulate each mode. The non-resonant $B \to D^{*+}\pi\ell^-\bar{\nu}$ decays are generated according to the model of Goity and Roberts (GR) [45], while the resonant $B \to D^{**}\ell^-\bar{\nu}$ decays are generated according to the ISGW2 model [46]. Table 3.3 also gives the decay chains by which the $D^{**}\ell^-\bar{\nu}$ modes contribute to the $D^{*+}X\ell^-\bar{\nu}$ background, and their `decay.dec` branching fractions. Finally, Ta-

Table 3.3: The $B \to D^{*+}X\ell^-\bar{\nu}$ modes included in the CLEO Monte Carlo. I give the branching fraction and model used in the simulation of each background mode. For the $D^{**}\ell^-\bar{\nu}$ modes I give the relevant decay chain.

B Decay Mode	$\mathcal{B}$ ($\times 10^{-2}$)	Model	(D^{**} Decay Mode)	$\mathcal{B}$	Net $\mathcal{B}$ ($\times 10^{-4}$)
$\bar{B}^0 \to D^{*+}\pi^0\ell^-\bar{\nu}$	0.23	GR	—	—	23.00
$\bar{B}^0 \to D_1^+\ell^-\bar{\nu}$	0.66	ISGW2	$D_1^+ \to D^{*+}\pi^0$	0.33	21.78
$\bar{B}^0 \to D_1^{*+}\ell^-\bar{\nu}$	0.11	ISGW2	$D_1^{*+} \to D^{*+}\pi^0$	0.33	3.63
$\bar{B}^0 \to D_2^{*+}\ell^-\bar{\nu}$	0.33	ISGW2	$D_2^{*+} \to D^{*+}\pi^0$	0.104	3.43
$\bar{B}^0 \to D'^+\ell^-\bar{\nu}$	0.02	ISGW2	$D'^+ \to D^{*+}\pi^0$	0.669*	1.34
$\bar{B}^0 \to D^{*\prime+}\ell^-\bar{\nu}$	0.22	ISGW2	$D^{*\prime+} \to D^{*+}\pi^0$	0.125	2.75
			$D^{*\prime+} \to D^{*+}\gamma$	0.001	0.02
			$D^{*\prime+} \to D_1^{*0}\pi^+$,	0.003*	
			$D_1^{*0} \to D^{*+}\pi^-$	0.67	0.04
			$D^{*\prime+} \to D_1^{*+}\pi^0$,	0.007*	
			$D_1^{*+} \to D^{*+}\pi^0$	0.33	0.05
$\bar{B}^0 \to D^{*+}X\ell^-\bar{\nu}$ sum					56.05
$B^- \to D^{*-}\pi^+\ell^-\bar{\nu}$	0.47	GR	—	—	47.00
$B^- \to D_1^0\ell^-\bar{\nu}$	0.66	ISGW2	$D_1^0 \to D^{*+}\pi^-$	0.67	44.22
$B^- \to D_1^{*0}\ell^-\bar{\nu}$	0.11	ISGW2	$D_1^{*0} \to D^{*+}\pi^-$	0.67	7.37
$B^- \to D_2^{*0}\ell^-\bar{\nu}$	0.33	ISGW2	$D_2^{*0} \to D^{*+}\pi^-$	0.208	6.86
$B^- \to D'^0\ell^-\bar{\nu}$	0.02	ISGW2	$D'^0 \to D^{*+}\pi^-$	0.659	1.32
$B^- \to D^{*\prime 0}\ell^-\bar{\nu}$	0.22	ISGW2	$D^{*\prime 0} \to D^{*+}\pi^-$	0.243	5.35
			$D^{*\prime 0} \to D_1^{*+}\pi^-$,	0.006	
			$D_1^{*+} \to D^{*+}\pi^0$	0.33	0.04
			$D^{*\prime 0} \to D_1^{*0}\pi^0$,	0.003	
			$D_1^{*0} \to D^{*+}\pi^-$	0.67	0.04
$B^- \to D^{*+}X\ell^-\bar{\nu}$ sum					112.21
$B \to D^{*+}X\ell^-\bar{\nu}$ average					84.13

ble 3.3 sums the total $D^{*+}X\ell^-\bar{\nu}$ branching fractions for $\bar{B}^0$ and B^- decay. The total $D^{*+}X\ell^-\bar{\nu}$ branching fraction is twice as high for B^- as for $\bar{B}^0$ decays. I average these two to obtain the overall $B \to D^{*+}X\ell^-\bar{\nu}$ branching fraction.

The CLEO Monte Carlo includes six D^{**} states. Four are orbitally-excited states, with orbital angular momentum $L = 1$. The D_1 is the singlet ${}^1P_1$ state, while the D_0^*, D_1^*, and D_2^* are the three triplet ${}^3P_0$, ${}^3P_1$, and ${}^3P_2$ states. In HQET, the properties of these states should be dominated by the light-quark degrees of freedom, with small corrections from the coupling to the heavy-quark spin. The orbitally-excited D^{**} states can be organized into two doublets characterized the quantum number j, the sum of the orbital angular momentum L with the light-quark spin s. The D_1 and D_2^* form a $j = 3/2$ doublet, while the D_0^* and D_1^* fall into a $j = 1/2$ doublet. The two $j = 3/2$ states can only undergo D-wave decays, and are therefore fairly narrow. Both states have been observed with the expected quantum numbers [3]. As predicted by HQET, the mass difference is small, about 35 MeV, and the states are fairly narrow, with widths on the order of 20–30 MeV. In contrast, the $j = 1/2$ doublet states can decay via S-wave, and are therefore expected to be very broad, with widths on the order of hundreds of MeV. The $j = 1/2$ states are therefore very hard to reconstruct. The only experimental evidence for these states is a preliminary CLEO observation of the D_1^{*0} [47].

The final two D^{**} states in the Monte Carlo are the two radially-excited $2S$ states. These are a ${}^1S_1$ state, the D', and a ${}^3S_1$ state, the $D^{*\prime}$. These states are analogous to the D and the D^*. The DELPHI collaboration has reported evidence for a state they tentatively identify with the $D^{*\prime}$, although the quantum numbers of the observed state have not been confirmed. The DELPHI state is narrow, in accordance with some theoretical calculations [48]. The CLEO Monte Carlo assumes that the D' and $D^{*\prime}$ are very wide, a more common theoretical expectation.

The branching fractions in Table 3.3 are for the most part educated guesses. Little information exists about the total $B \to D^{(*)}X\ell^-\bar{\nu}$ branching fraction and the relative contributions of different modes. The total $B- > D^{(*)}X\ell^-\bar{\nu}$ branching fraction in the Monte Carlo is 2.65×10^{-2}. (Here $D^{(*)}X$ includes DX and D^*X non-resonant states as well as D^{**} resonances.) This is somewhat higher than an ALEPH measurement of $(2.26 \pm 0.29 \pm 0.33) \times 10^{-2}$, where the errors are statistical and systematic. The Monte Carlo $B \to D_1\ell^-\bar{\nu}$ branching fractions are likewise above a CLEO measurement [37], $\mathcal{B}(B^- \to D_1^0\ell^-\bar{\nu}) = (5.6 \pm 1.3 \pm 0.9) \times 10^{-3}$, but below an ALEPH result [38], $\mathcal{B}(B \to D_1\ell^-\bar{\nu}(X)) = (7.4 \pm 1.6) \times 10^{-3}$. (In the ALEPH measurement the final state may include additional particles which are not observed.)

There is little experimental evidence on the P-wave D^{**} branching fractions, but these decay rates are on solid theoretical footing. The dominant decay mode for these states is pion emission to a $D^{(*)}\pi$ final state. By angular momentum conservation, the D-wave D_1 decay and the S-wave D_1^* decay must be to $D^*\pi$, and cannot be to $D\pi$. Conversely, the S-wave D_0^* decay can only be to $D\pi$, not to $D^*\pi$. $B \to D_0^*\ell^-\bar{\nu}$ decays are therefore not a background to $\bar{B}^0 \to D^{*+}\ell^-\bar{\nu}$. Both D-wave $D_2^* \to D\pi$ and $D_2^* \to D^*\pi$ transitions are allowed by angular momentum conservation, and both have been observed. The branching ratio of these two processes in the Monte Carlo is based on a CLEO measurement [49]. Otherwise, the

P-wave D^{**} branching fractions in `decay.dec` are based on isospin considerations. One expects, for example,

$$\frac{\mathcal{B}(D^{**+} \to D^{*+}\pi^0)}{\mathcal{B}(D^{**+} \to D^{*0}\pi^+)} = \frac{1}{2}. \tag{3.17}$$

These isospin considerations are the reason the $D^{*+}\pi^-\ell^-\bar{\nu}$ states typical of the $D^{*+}X\ell^-\bar{\nu}$ background from B^- decay occur twice as often as the $D^{*+}\pi^0\ell^-\bar{\nu}$ states from $\bar{B}^0$ decay.

The radially-excited D' and $D^{*\prime}$ decays are handled in a similar manner. Due to parity and angular momentum conservation, the D' decays via P-wave to to $D^*\pi$, while the $D^{*\prime}$ decays via P-wave to either $D\pi$ or $D^*\pi$. The CLEO Monte Carlo also includes $D\gamma$, $D^*\gamma$, and $D_1^*\pi$ final states at rates under 1%. Several clear errors in `decay.dec` are flagged by asterisks in Table 3.3. The isospin ratio similar to Equation 3.17 is reversed in the branching fractions of these decay modes.

I analyze the $D^{*+}X\ell^-\bar{\nu}$ Monte Carlo events in the same manner as data and generic Monte Carlo, though with the signal Monte Carlo $\langle p_{B^0}\rangle$ values in Table 3.1. I do a sideband subtraction using the scale factor from either data or generic Monte Carlo, depending on which I am trying to fit. There is very little combinatoric background in the $D^{*+}X\ell^-\bar{\nu}$ Monte Carlo, so this subtraction is done primarily to be sure that the tails of the Δm peak that leak into the Δm sideband region are handled consistently. I use tagging information to subtract the small levels of uncorrelated and correlated backgrounds, as well as the $D^{*+}\ell^-\bar{\nu}$ events that are present in the $D^{*+}X\ell^-\bar{\nu}$ Monte Carlo. The $\cos\theta_{BY}$ distribution of the $\bar{B}^0 \to D^{*+}X\ell^-\bar{\nu}$ background can be seen in Figure 3.8. (In this figure, I have actually removed the combinatoric background from both distributions by tagging, but this difference in the handling of the combinatoric background would not be visible in the plot.)

I allow the overall normalization of the $D^{*+}X\ell^-\bar{\nu}$ background to float in a fit to the $\cos\theta_{BY}$ distribution, so I do not need to know *a priori* the overall $D^{*+}X\ell^-\bar{\nu}$ normalization. The shape of the distribution is also uncertain, due to lack of information about both the relative contributions of the different modes and the form factors for each mode. I discuss the systematic error associated with this uncertainty in the event distribution in Section 4.6.

3.3 Fits to the $\cos\theta_{BY}$ Distribution

In this section I present the fit to the $\cos\theta_{BY}$ distribution that I use to extract the $\bar{B}^0 \to D^{*+}\ell^-\bar{\nu}$ branching fraction. I first describe the Monte Carlo sample I use to model the distribution of signal $D^{*+}\ell^-\bar{\nu}$ events. I next present a fit to the reconstructed $\cos\theta_{BY}$ distribution in generic Monte Carlo events as a test of the method. I then present the fit this distribution in the CLEO II data. I conclude with several cross-checks of the fit.

3.3.1 Monte Carlo $\bar{B}^0 \to D^{*+}\ell^-\bar{\nu}$ Signal Distribution

With the backgrounds assembled in Section 3.2, I need only one more ingredient to fit the reconstructed $\cos\theta_{BY}$ distribution of candidate events, namely the distribution of the signal $D^{*+}\ell^-\bar{\nu}$ events. I use a sample of 100,000 $\bar{B}^0 \to D^{*+}\ell^-\bar{\nu}$ Monte

Carlo events to obtain this distribution. These events are generated by `EvtGen` according to the linear HQET form-factor parameterization of Equation 1.36. The Monte Carlo uses a CLEO measurement of the form-factor parameters [50]:

$$\begin{aligned} R_1 &= 1.24 \pm 0.26 \pm 0.12, \\ R_2 &= 0.72 \pm 0.18 \pm 0.07, \\ \rho^2 &= 0.92 \pm 0.12 \pm 0.06. \end{aligned} \tag{3.18}$$

I analyze this signal Monte Carlo in the same manner as for other event samples, using the signal Monte Carlo $\langle p_{B^0} \rangle$ values given in Table 3.1. The reconstructed $\cos\theta_{BY}$ distribution of these events, with all background removed by tagging, is shown in Figure 3.8. To create the distribution used in the fit, I do a combinatoric background subtraction on the event sample in the same manner as is done for the $D^{*+}X\ell^-\bar{\nu}$ Monte Carlo, and I subtract out the tagged uncorrelated, correlated, and D^{**} backgrounds.

3.3.2 Generic Monte Carlo $\cos\theta_{BY}$ Fit

I first fit the generic Monte Carlo as a test of the $\cos\theta_{BY}$ fit method. I perform a χ^2 fit over the region $-6 < \cos\theta_{BY} < 1.5$. I hold the combinatoric, uncorrelated, and correlated background distributions fixed and allow the $B \to D^{*+}X\ell^-\bar{\nu}$ distribution to float in the fit. (The continuum and fake-lepton backgrounds are not present in the reconstructed generic Monte Carlo sample.) The statistical uncertainties in the background components are included in the fit. I display the fit results in Figure 3.16. The fit χ^2 is 12.0 for 13 degrees of freedom.

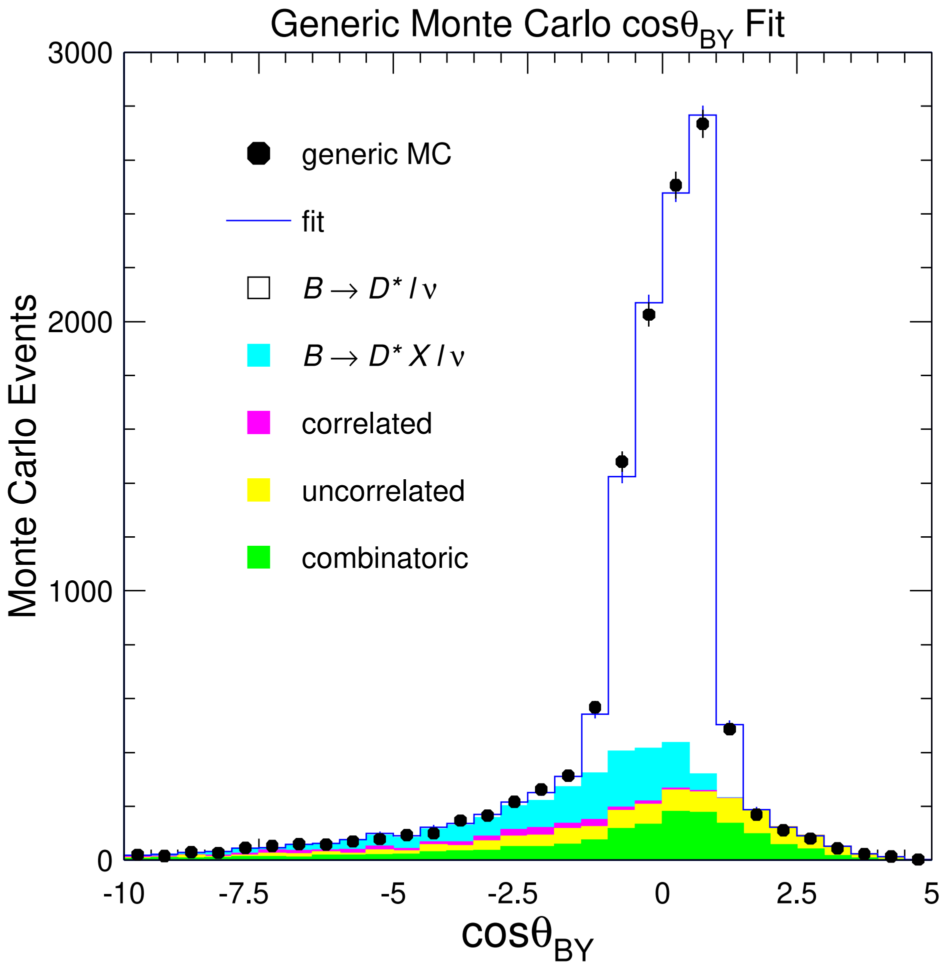

Figure 3.16: Fit to the reconstructed $\cos\theta_{BY}$ distribution in the generic Monte Carlo. The five fitting histograms are: 1) $\bar{B}^0 \to D^{*+}\ell^-\bar{\nu}$ signal distribution, 2) $B \to D^{*+}X\ell^-\bar{\nu}$ background distribution, 3) correlated-lepton background, 4) uncorrelated-lepton background, and 5) combinatoric background. The fit is performed over the region $-6 < \cos\theta_{BY} < 1.5$.

Extraction of the $D^{*+}\ell^-\bar{\nu}$ branching fraction from the fit requires several component branching fractions. I reconstruct D^{*+}'s via the decay chain $D^{*+} \to D^0\pi^+$, $D^0 \to K^-\pi^+$. The recompress Monte Carlo is generated with the branching fractions $\mathcal{B}(D^{*+} \to D^0\pi^+) = 67.59 \times 10^{-2}$ and $\mathcal{B}(D^0 \to K^-\pi^+) = 3.82 \times 10^{-2}$. Half of all Monte Carlo $\Upsilon(4S)$ decays are to $B^0\bar{B}^0$. Based on these values, the fit returns the branching fraction $\mathcal{B}(\bar{B}^0 \to D^{*+}\ell^-\bar{\nu}) = (5.45 \pm 0.09) \times 10^{-2}$, fully in accord with the Monte Carlo input branching fraction of 5.40×10^{-2}. Furthermore, the level of $D^{*+}X\ell^-\bar{\nu}$ background returned by the fit corresponds to the branching fraction $\mathcal{B}(B \to D^{*+}X\ell^-\bar{\nu}) = (8.15 \pm 0.57) \times 10^{-3}$, in agreement with the input level of 8.41×10^{-3} presented in Table 3.3. The fit to the $\cos\theta_{BY}$ distribution therefore works correctly in this test on generic Monte Carlo.

3.3.3 The $\cos\theta_{BY}$ Fit to CLEO II Data

To extract $\mathcal{B}(\bar{B}^0 \to D^{*+}\ell^-\bar{\nu})$ from data, I use the following measurements of the component branching fractions:

$$\mathcal{B}(D^{*+} \to D^0\pi^+) = (67.59 \pm 0.70) \times 10^{-2} \tag{3.19}$$

$$\mathcal{B}(D^0 \to K^-\pi^+) = (3.85 \pm 0.09) \times 10^{-2}. \tag{3.20}$$

These values are respectively a recent CLEO II result [51] and the Particle Data Group's fit result from multiple $\mathcal{B}(D^0 \to K^-\pi^+)$ measurements, presented in the 1998 *Review of Particle Properties* [3].

The measurement of $\mathcal{B}(\bar{B}^0 \to D^{*+}\ell^-\bar{\nu})$ also depends on the fraction of $\Upsilon(4S)$ decays to $B^0\bar{B}^0$, $f_{00} \equiv \mathcal{B}(\Upsilon(4S) \to B^0\bar{B}^0)$. The fraction of $\Upsilon(4S)$ decays to B^+B^-

is written $f_{+-} \equiv \mathcal{B}(\Upsilon(4S) \to B^+B^-)$. CLEO has recently measured [52] the ratio

$$\frac{f_{+-}}{f_{00}} = 1.04 \pm 0.07 \pm 0.04. \tag{3.21}$$

Here the first error is statistical, the second systematic. With the assumption $f_{00} + f_{+-} = 1$, that all $\Upsilon(4S)$ decays are to pairs of B mesons, I obtain

$$f_{00} = 0.49 \pm 0.02. \tag{3.22}$$

I use this value in my measurement.

I fit the data in the same manner as Monte Carlo. The continuum, combinatoric, fake-lepton, uncorrelated, and correlated background distributions are fixed, while the $B \to D^{*+}X\ell^-\bar{\nu}$ background is allowed to float. I plot the results of this fit in Figure 3.17. The χ^2 value of the fit is 6.6 for 13 degrees of freedom. The fit returns the branching fraction

$$\mathcal{B}(\bar{B}^0 \to D^{*+}\ell^-\bar{\nu}) = (5.40 \pm 0.19) \times 10^{-2}. \tag{3.23}$$

I discuss this result relative to other measurements of this branching fraction in Chapter 5.

Table 3.4 indicates the relative size of the $D^{*+}\ell^-\bar{\nu}$ signal and the various backgrounds in the $\cos\theta_{BY}$ branching-fraction fit. For each background category, I give the total number of events in both the fit region, $-6.0 < \cos\theta_{BY} < 1.5$, and the physical region, $-1 < \cos\theta_{BY} < 1$. I also list the total number of reconstructed candidates in the CLEO II data and the yield of $D^{*+}\ell^-\bar{\nu}$ events returned by the fit. The errors listed for the combinatoric, continuum, fake-lepton, uncorrelated,

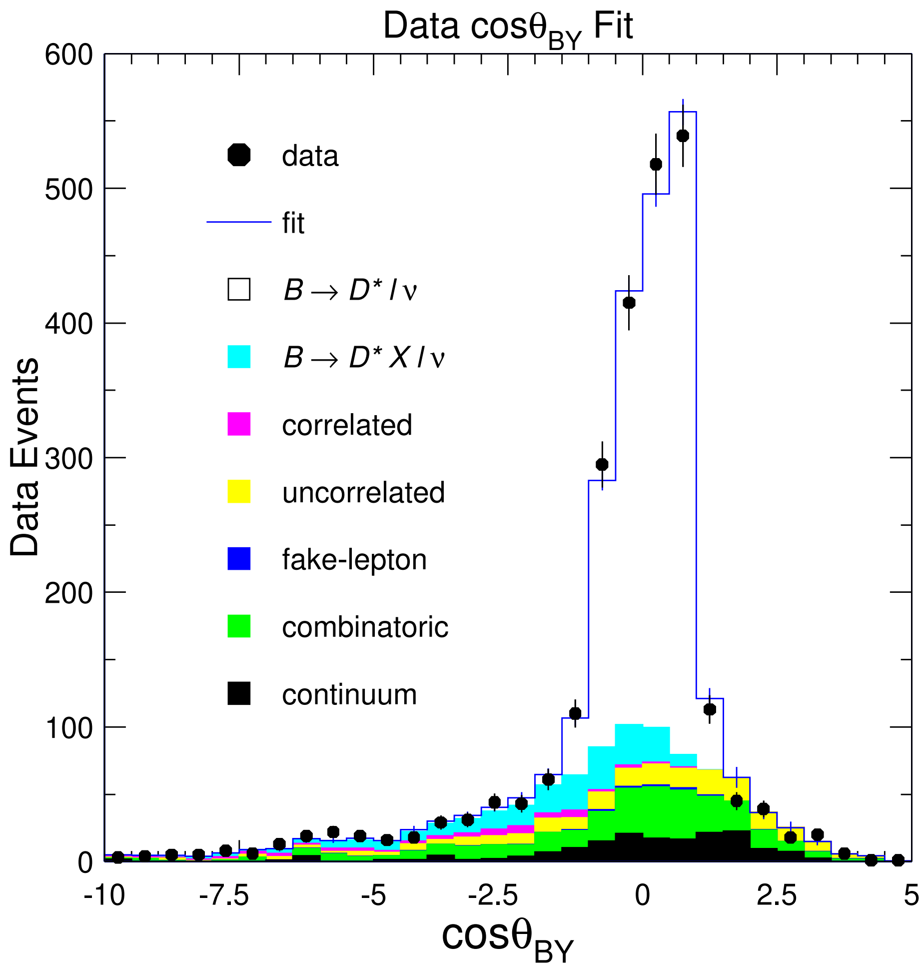

Figure 3.17: Fit to the $\cos\theta_{BY}$ distribution in data. The seven fitting histograms are: 1) $\bar{B}^0 \rightarrow D^{*+}\ell^-\bar{\nu}$ signal distribution, 2) $B \rightarrow D^{*+}X\ell^-\bar{\nu}$ background distribution, 3) correlated-lepton background, 4) uncorrelated-lepton background, 5) fake-lepton background, 6) combinatoric background, and 7) continuum background. The data are fit over the region $-6 < \cos\theta_{BY} < 1.5$.

Table 3.4: The signal and background contributions in the fit of the $\cos\theta_{BY}$ distribution in CLEO II data. The signal yield and number of background events are given in both the fit region ($-6.0 < \cos\theta_{BY} < 1.5$) and in the physical region ($-1 < \cos\theta_{BY} < 1$).

Event Category	Number of Events	
	$-6.0 < \cos\theta_{BY} < 1.5$	$-1 < \cos\theta_{BY} < 1$
All Data Candidates	2273	1767
Continuum Background	124.7 ± 15.5	70.1 ± 11.7
Combinatoric Background	240.1 ± 9.1	130.1 ± 6.5
Fake-Lepton Background	8.3 ± 1.1	5.8 ± 0.8
Uncorrelated Background	131.4 ± 5.1	56.5 ± 3.3
Correlated Background	41.0 ± 2.9	6.7 ± 1.2
$B \to D^{*+}X\ell^-\bar{\nu}$ Background	217.4 ± 41.0	97.1 ± 18.4
$\bar{B}^0 \to D^{*+}\ell^-\bar{\nu}$ Signal	1513.3 ± 54.8	1393.2 ± 50.6

and correlated backgrounds reflect only the statistical uncertainties in the estimation of these backgrounds from data or Monte Carlo event distributions. They do not include systematic uncertainties due to the methods I use to model these backgrounds. The errors given for the number of $B \to D^{*+}X\ell^-\bar{\nu}$ background and $\bar{B}^0 \to D^{*+}\ell^-\bar{\nu}$ signal events are primarily due to the uncertainty in the normalizations of these distributions returned by the fit. These errors also include Monte Carlo statistical uncertainties.

The statistical errors in Table 3.4 are incorporated in my fit to the $\cos\theta_{BY}$ distribution of the data. They are therefore reflected in the 3.54% statistical uncertainty in the branching fraction returned by the fit. My measurement of $\mathcal{B}(\bar{B}^0 \to D^{*+}\ell^-\bar{\nu})$ is also subject to a number of sources of systematic error. These sources include uncertainties in the normalization and distribution of the backgrounds, uncertainties about the level to which the Monte Carlo signal events correctly model both the underlying physics and the detector response, and uncertainties in the normalization of the final result. I discuss and quantify the various sources of systematic error in detail in the next chapter.

The $D^{*+}X\ell^-\bar{\nu}$ yield from the fit to the data corresponds to the branching fraction

$$\mathcal{B}(B \to D^{*+}X\ell^-\bar{\nu}) = (6.2 \pm 1.2) \times 10^{-3}. \tag{3.24}$$

This value is lower than the one assumed in the CLEO Monte Carlo. This difference is not of great significance, as the Monte Carlo input branching fractions are, at best, guesses. As mentioned in Section 3.2.6, they also exceed some other existing measurements. Furthermore, the $D^{*+}X\ell^-\bar{\nu}$ yield is subject to a number of sources of systematic error, and may not be a reliable measure of the physical branching fraction. As the $D^{*+}X\ell^-\bar{\nu}$ distribution is $\cos\theta_{BY}$ resembles that of other backgrounds to $\bar{B}^0 \to D^{*+}\ell^-\bar{\nu}$, in particular the correlated background, errors in the estimation of those backgrounds may be compensated by the normalization of the $D^{*+}X\ell^-\bar{\nu}$ distribution in the fit. The distribution of $D^{*+}X\ell^-\bar{\nu}$ events in $\cos\theta_{BY}$ is also influenced by both the relative branching fractions of the different $D^{*+}X\ell^-\bar{\nu}$ modes and the form factors used to model these modes, both of which have large uncertainties.

3.3.4 Cross-Checks

In this section I present several cross-checks of the $\bar{B}^0 \to D^{*+}\ell^-\bar{\nu}$ branching ratio fit to the CLEO II data. My fit is based only on the distribution of events in $\cos\theta_{BY}$. If the fit works well, the reconstructed distributions of other variables should agree with the sum of the signal and background components in those variables. I plot four such variables in Figures 3.18–3.20. These are the electron momentum for candidate events containing electrons, the muon momentum for candidate events containing muons, the D^{*+} momentum spectrum, and the variable $\cos\theta_{D^*\ell}$, the cosine of the opening angle between the D^{*+} and the lepton. The agreement is reasonable in each plot.

I also test the analysis by breaking the data into subsets, fitting each subset to extract a branching fraction, and comparing the results. I first split the data by lepton species. I separately fit candidate events which contain electrons and those which contain muons. I similarly divide the event sample I use to model backgrounds. In the electron sample, the fit returns a branching fraction of $(5.09 \pm 0.24) \times 10^{-2}$, while the fitted branching fraction from the muon sample is $(5.77 \pm 0.34) \times 10^{-2}$. The $\cos\theta_{BY}$ distribution in the muon sample has only a small tail to negative values as a consequence of 1.4 GeV muon momentum cut. I therefore only fit the muon sample over the region $-2 < \cos\theta_{BY} < 1.5$. The larger muon result is consistent with the distributions in Figures 3.18, in which the the number of reconstructed electrons candidates is less than the fit, while the number of muon candidates exceeds the fit. The branching fraction fits return only statistical uncertainties. Most of the systematic uncertainties in these two

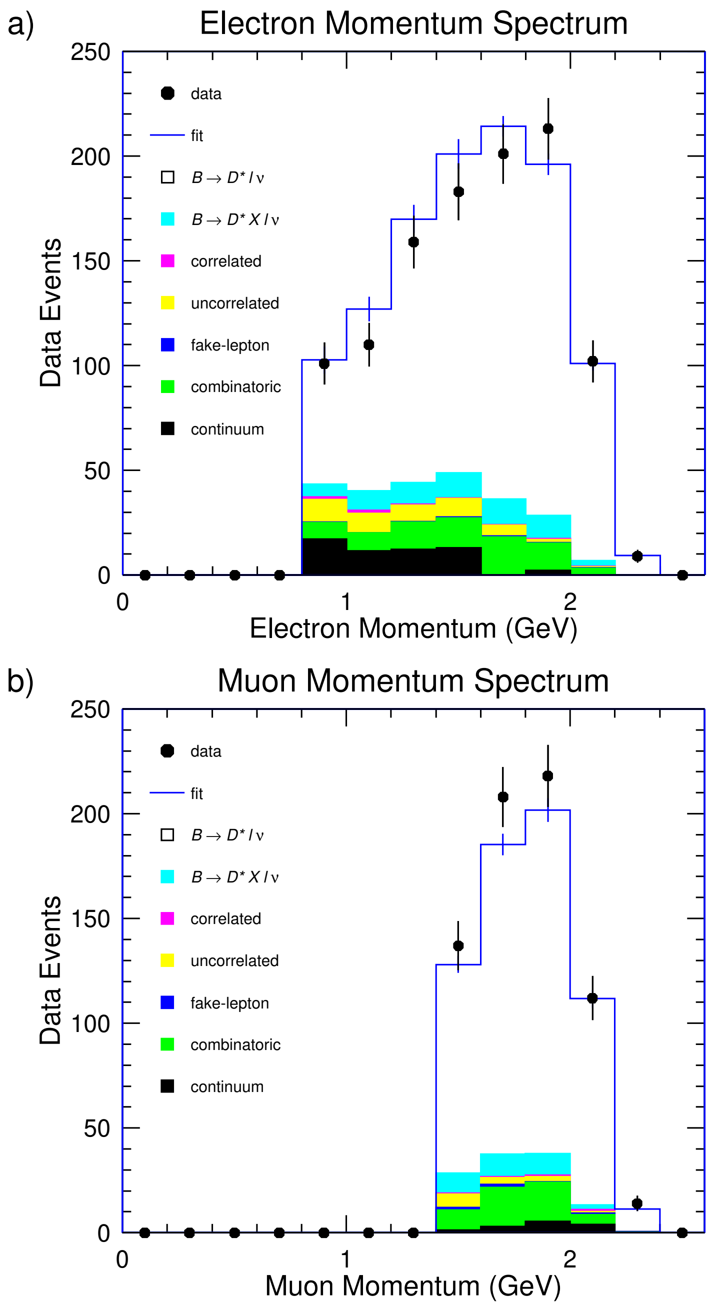

Figure 3.18: The reconstructed (a) electron and (b) muon momentum spectra compared with the fit in the physical region $-1 < \cos\theta_{BY} < 1$. The points are the reconstructed spectra, while the seven histograms are the $\bar{B}^0 \to D^{*+}\ell^-\bar{\nu}$ signal and the six listed backgrounds.

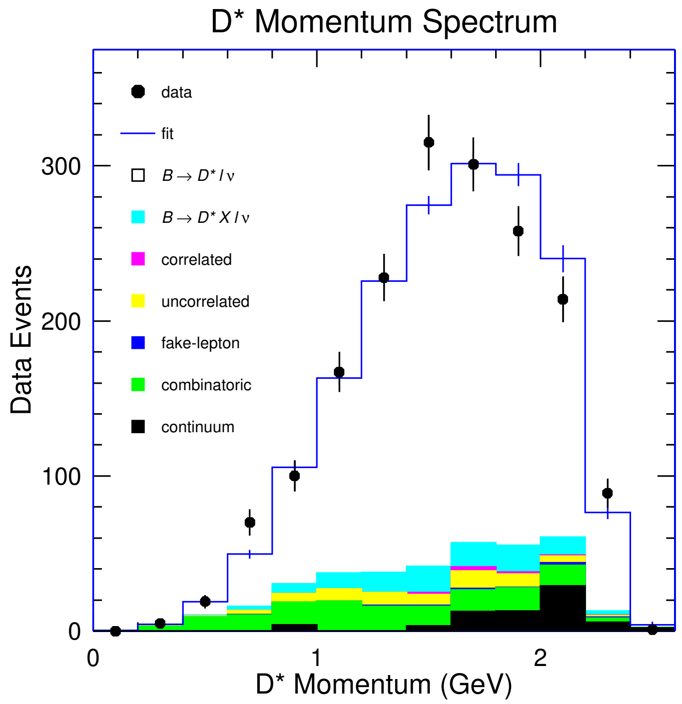

Figure 3.19: The reconstructed D^{*+} momentum spectrum compared with the fit in the physical region $-1 < \cos\theta_{BY} < 1$. The points are the reconstructed spectrum, while the seven histograms are the $\bar{B}^0 \to D^{*+}\ell^-\bar{\nu}$ signal and the six listed backgrounds.

measurements are correlated, but some are not. I calculate these uncorrelated systematic uncertainties with the same methods I describe in Chapter 4 and the Appendices. The systematic uncertainties associated with lepton identification and lepton fake rates are obviously not correlated between electrons and muons. In addition, the difference between the electron and muon momentum spectra affects both the combinatoric scale factor and the slow pion momentum spectrum. I calculate separate combinatoric scale factors for electrons and muons; these scale factors have uncorrelated statistical uncertainties. I also calculate the systematic

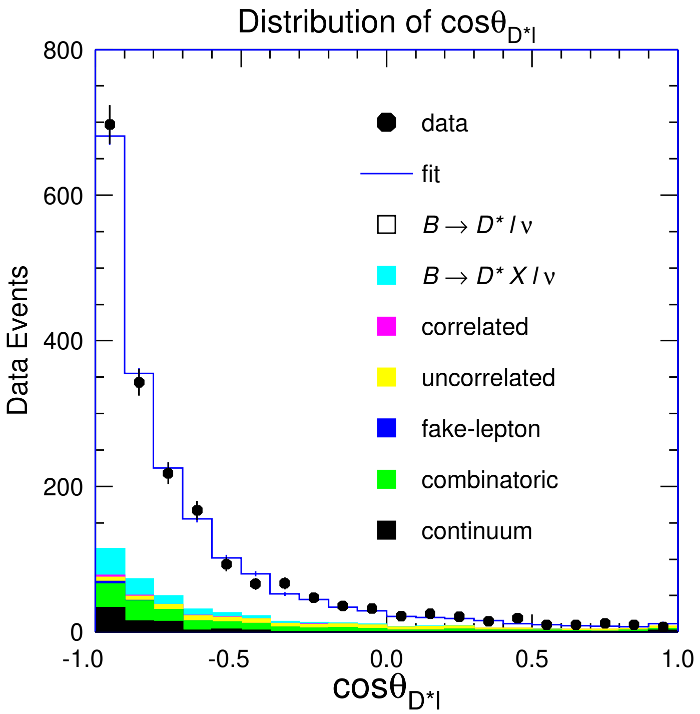

Figure 3.20: The reconstructed $\cos\theta_{D^*\ell}$ distribution compared with the fit in the physical region $-1 < \cos\theta_{BY} < 1$. The points are the reconstructed distribution, while the seven histograms are the $\bar{B}^0 \to D^{*+}\ell^-\bar{\nu}$ signal and the six listed backgrounds. The data are fit with the cut $\cos\theta_{D^*\ell} < 0$.

uncertainty due to slow pion reconstruction with the different lepton momentum cuts. I conclude that the difference in branching fractions between electrons and muons, $\Delta\mathcal{B}_{e-\mu}$, is

$$\Delta\mathcal{B}_{e-\mu} = (-0.68 \pm 0.42 \pm 0.30) \times 10^{-2}, \tag{3.25}$$

where I list both statistical and systematic uncertainties. This difference is 1.3 standard deviations in size. I suggest in Section 4.10 that the Monte Carlo overestimates the electron reconstruction efficiency due to the method I use to identify electrons. If so, I would expect this branching fraction difference to be smaller with the final recompress `CEID` package.

I also divide the data into first and second-half samples. I separately fit the 4s2–6 datasets, containing $1.59\,\mathrm{fb}^{-1}$ of on-resonance data, and the 4s7–G datasets, containing $1.55\,\mathrm{fb}^{-1}$. I obtain a first-half branching fraction of $(5.05 \pm 0.26) \times 10^{-2}$, and a second-half branching fraction of $(5.80 \pm 0.28) \times 10^{-2}$. The uncertainties on the combinatoric scale factor and the number of $B\bar{B}$ events are uncorrelated between the first and second half of the CLEO II data. The slow pion efficiency systematic uncertainties are largely uncorrelated between these subsets, as they test the tuning of the Monte Carlo, which is done on a dataset-by-dataset level. The exception is the uncertainty due to the amount of material in the inner detector. I obtain branching fraction difference between the first and second halves, $\Delta\mathcal{B}_{1-2}$, of

$$\Delta\mathcal{B}_{1-2} = (-0.75 \pm 0.38 \pm 0.25) \times 10^{-2}, \tag{3.26}$$

This is again a 1.6 standard deviation effect. This difference. is not large enough to cause concern. I conclude that the analysis method gives reasonably consistent results between the first and second-half subsamples.

CHAPTER 4

MEASUREMENT UNCERTAINTIES

The measurement of $\mathcal{B}(\bar{B}^0 \to D^{*+}\ell^-\bar{\nu})$ is subject to a number of sources of uncertainty. In this chapter I list and quantify the various sources of systematic error in my measurement. I also give the portion of the statistical uncertainty in the branching fraction measurement due to the estimation of the various backgrounds.

4.1 Continuum Background

I describe in Section 3.2.1 how I estimate the continuum background with events taken off the $\Upsilon(4S)$ resonance. The scale factor I use to normalize this background is very well known, and it contributes no significant systematic error to the branching fraction measurement. I therefore assign no systematic error associated with the continuum background.

My estimate of the continuum background contributes a statistical uncertainty of 0.94% to the branching fraction measurement. I establish this uncertainty through a branching-fraction fit with zero error assigned to the combinatoric background. The statistical statistical uncertainty due to the continuum background is the quadratic difference between the fractional statistical uncertainties of the two fits. In the following sections, I employ this procedure to establish the statistical uncertainties associated with each of the other backgrounds and with the Monte Carlo $D^{*+}\ell^-\bar{\nu}$ signal distribution.

4.2 Combinatoric Background

My estimate of the combinatoric background, which I describe in Section 3.2.2, is subject to two sources of systematic error. The first is the difference between the shapes of the $\cos\theta_{BY}$ distributions for the true combinatoric background and for the events in the Δm sideband region I use to model this background. The second source of error is the normalization of the background, that is, the combinatoric scale factor.

In Monte Carlo, the $\cos\theta_{BY}$ distribution of the estimated combinatoric background does not agree perfectly with the true background distribution. I illustrate this effect in Figure 4.1. To focus solely on the difference between the shapes of these distributions, I normalize the estimated combinatoric background to the same number of events as the tagged background. (This normalization is equivalent to using the correct combinatoric scale factor, the ratio of combinatoric background events in the Δm signal and sideband regions.) The estimated background distribution is clearly broader than the true shape, and it is also shifted slightly to higher $\cos\theta_{BY}$.

I establish the systematic effect of this shape difference on the branching fraction with several fits to the generic Monte Carlo. These fits are similar to that

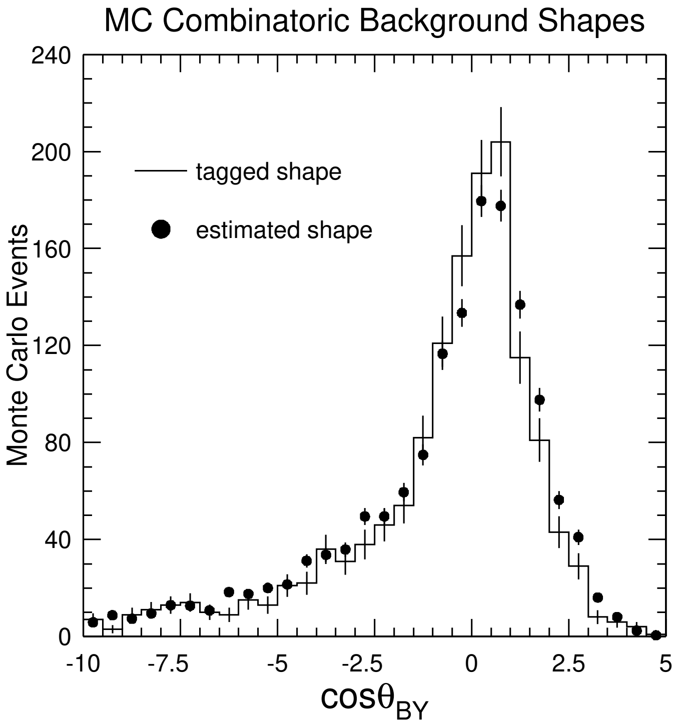

Figure 4.1: The histogram gives the $\cos\theta_{BY}$ distribution of the tagged combinatoric background in the generic Monte Carlo. The points show the combinatoric background estimate derived from the Δm sideband region. I normalize the estimated background distribution to the same number of events as the tagged background.

described in Section 3.3.2. I first fit the generic Monte Carlo with the tagged combinatoric background distribution as my "estimate" of the combinatoric background. I next fit with the combinatoric distribution from the Δm sideband. For this study, I use the correct combinatoric scale factor. Replacing the tagged with the estimated distribution increases the branching fraction by $1.21 \pm 0.47\%$. The error on this quantity is due to the statistical uncertainty in the background distributions. In this study, I use the correct combinatoric scale factor when I subtract combinatoric backgrounds in the construction of the signal and $D^{*+}X\ell^-\bar{\nu}$ fitting distributions.

The normalization of the combinatoric background involves several sources of measurement error. The first is an overall bias in the method I use to establish the combinatoric scale factor. In generic Monte Carlo, I measure the true scale factor to be 0.244 ± 0.007 by counting tagged combinatoric background events in the Δm signal and sideband regions. However, my estimate of this scale factor, which I obtain from the $m(K\pi)$ sideband region as I describe in Section 3.2.2, is 0.206 ± 0.005. This method underestimates the combinatoric scale factor by $15.8 \pm 3.1\%$.

The combinatoric scale factor extracted from the $m(K\pi)$ sideband in data, as I describe in Section 3.2.2, is 0.250 ± 0.015. This scale factor includes a -9.9% correction due to the Monte Carlo subtraction of $D^0 \to \pi^+\pi^-$. That correction has an uncertainty of 6% due to the uncertainty in the branching fraction for this mode. The correction also depends on the production rate of D^{*+}'s in the Monte Carlo, which is consistent with data at the 5% level. (I present a comparison of the Monte Carlo D^{*+} yields with data in Section 4.4 and Figure 4.5.) The uncertainty in the Monte Carlo $D^0 \to \pi^+\pi^-$ correction is therefore 8% of itself, the quadratic sum of the two uncertainties. When scaled by the size of this correction, this uncertainty is negligible compared to the statistical uncertainty on the scale factor.

I assess the sensitivity of the measured branching fraction to the combinatoric scale factor by redoing the fit to data with different values of the scale factor. In each fit, I use the same scale factor for all combinatoric subtractions — in the computation of the combinatoric and fake-lepton backgrounds and the signal and $D^{*+}X\ell^-\bar{\nu}$ fit distributions. I vary the combinatoric scale factor by $\pm17\%$ in this study, and thus obtain variations of 0.74% in the branching fraction. With this information, I translate the $-15.8\pm3.1\%$ bias in the combinatoric scale factor to a $+0.68\pm0.14\%$ bias in the branching fraction. Furthermore, the 6.0% measurement uncertainty in the combinatoric scale factor in data corresponds to a small 0.26% uncertainty.

The systematic uncertainty in the branching fraction associated with the combinatoric background therefore consists of three parts: a $+1.21\pm0.47\%$ bias due to shape considerations, a $+0.69\pm0.14\%$ bias due to the method used to estimate the combinatoric scale factor, and a 0.26% uncertainty due to the statistics of the scale factor calculation. I do not correct for this bias; I take it as a systematic uncertainty to my measurement. The two sources of bias are correlated and must be added linearly, but all the other values can be added in quadrature. I thus obtain an overall value of 1.97% for the systematic error due to the combinatoric background subtraction.

The combinatoric background also contributes a statistical uncertainty of 0.60% to my measurement of the branching fraction. I establish this number with the method outlined in Section 4.1.

Table 4.1: The results of the fake-lepton background systematic error study. The table gives the change in the $\bar{B}^0 \to D^{*+}\ell^-\bar{\nu}$ branching ratio corresponding to each variation in the lepton fake rates. The average magnitudes of the positive and negative variations in each fake rate are added in quadrature to compute the total systematic uncertainty.

fake rate variation		uncert. (%)
$e^{\pm}$, $0.8 \leq p_e < 1.4\,\mathrm{GeV}$	$\uparrow$	$+0.019$
	$\downarrow$	-0.019
$e^{\pm}$, $1.4 \leq p_e \leq 2.4\,\mathrm{GeV}$	$\uparrow$	-0.057
	$\downarrow$	$+0.057$
$\mu^{\pm}$, $1.4 \leq p_\mu \leq 2.4\,\mathrm{GeV}$	$\uparrow$	-0.300
	$\downarrow$	$+0.300$
total		0.306

4.3 Fake-Lepton Background

The systematic error associated with the fake-lepton background arises from the uncertainties in the lepton fake rates given in Table 3.2. I vary each fake rate by its uncertainty to establish the corresponding uncertainty in the $\bar{B}^0 \to D^{*+}\ell^-\bar{\nu}$ branching fraction. I present the results of this study in Table 4.1. I vary each fake rate both up and down. To compute the total systematic error, I add in quadrature the average magnitudes of the fake rate variations. Based on this study, I assign a systematic uncertainty of 0.31% to the fake-lepton background.

The fake-lepton background contributes a statistical uncertainty of 0.07% to the branching fraction measurement, computed as in Section 4.1.

4.4 Uncorrelated-Lepton Background

The uncorrelated-lepton background is due to events in which the D^{*+} is produced in the decay of one B meson, while the lepton comes from the decay of the other B. The two B mesons are produced nearly at rest, and they decay independently. As a result, the underlying angular distributions of the D^* and lepton in this type of event are not significantly correlated, and this background is therefore referred to as the uncorrelated-lepton background.

While the underlying D^{*+} and lepton angular distributions comprising the uncorrelated-lepton background are not significantly correlated, it is important to note that the CLEO detector acceptance does introduce some correlation to the observed distributions. As Figure 4.2 shows, the underlying $\cos\theta_{D^*\ell}$ distribution of the uncorrelated-lepton is nearly uniform, as the D^{*+} and lepton directions are nearly completely uncorrelated. However, the observed distribution will exhibit some angular structure. In this analysis, I do not consider leptons with $|\cos\theta_\ell| > 0.7071$. My reconstruction acceptance for D^{*+} also falls rapidly above $|\cos\theta_{D^*}| > 0.8$. This dropoff is a consequence of the fiducial acceptance of the CLEO detector for charged slow pions, as the slow pion direction is strongly correlated with that of the D^{*+}. If the D^{*+} is transverse, the acceptance for uncorrelated leptons will be unity for high or low values of $\cos\theta_{D^*\ell}$, but around 0.5 for $\cos\theta_{D^*\ell}$ near zero. The fiducial acceptances for both D^{*+}'s and leptons therefore imply that the detected uncorrelated-background $\cos\theta_{D^*\ell}$ distribution is not uniform, but that it is instead lower for small $|\cos\theta_{D^*\ell}|$ values than for high. This effect is illustrated

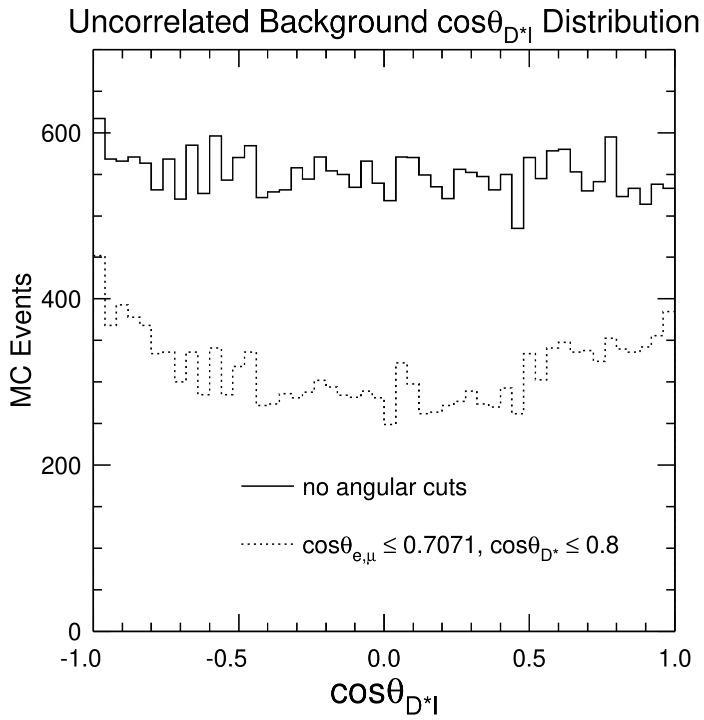

Figure 4.2: The distribution in $\cos\theta_{D^*\ell}$ of the uncorrelated-lepton background in one million generator-level Monte Carlo events. The solid histogram shows the distribution of all possible uncorrelated background events, imposing only the momentum cuts $0.8 \leq\ p_e \leq 2.4$, $1.4 \leq p_\mu \leq 2.4$. The slight slope is due to the relative motion of the two B mesons. The dotted histogram gives the distribution after angular cuts are applied on the directions of the D^{*+} and the lepton, introducing some curvature.

by the dotted histogram in Figure 4.2.

To correctly account for this fiducial effect on the uncorrelated background distribution, I estimate this lepton background with a sum of with Monte Carlo distributions that is constrained to match the inclusive D^* and lepton spectra observed in data.

Due to the physics of B meson decay, there are correlations between the flavor

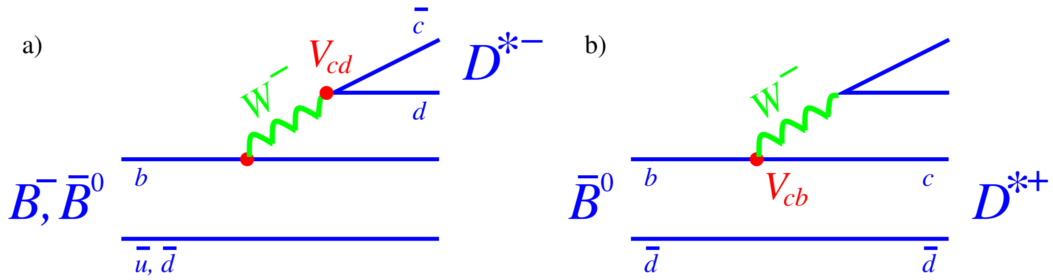

Figure 4.3: Feynman diagrams for (a) upper and (b) lower-vertex D^{*+} production in B decay. Note that in upper-vertex production, the D^* is produced through the virtual W, and that it contains a charm quark of opposite flavor to those involved in lower-vertex D^* production.

of a parent B and the flavors of its most common D^{*+} or lepton daughters. As there are also flavor correlations between the two B mesons produced in an $\Upsilon(4S)$ decay, there are in turn flavor correlations between the D^{*+} and the lepton in the uncorrelated-lepton background.

In most B decays, the b quark converts to a charm quark through the emission of a virtual W boson. If this c quark then combines with a light quark to form a charged D^* meson, the D^* charge will reflect the identity of the parent B. $\bar{B}^0$'s and B^-'s decay to D^{*+}'s in this manner, while B^0's and B^+'s decay to D^{*-}'s. This processes is referred to as "lower-vertex" production of D^*'s in B meson decay. The label "lower" refers to the position of the charm-quark production vertex in a typical Feynman diagram of a B-meson decay, as in Figure 4.3b. The process is also called "right-sign" D^* production, as roughly 90% of $B \to D^*X$ decays are lower-vertex decays, with this flavor correlation.

In contrast, a charm quark produced at the "upper" W vertex will be of the opposite flavor from one produced at the lower vertex. Thus, "upper-vertex" production of charged D^* mesons yields D^{*-}'s in $\bar{B}^0$ and B^- decay, and D^{*+}'s in B^0 and B^+ decay. Such production is also referred to as "wrong-sign" D^* production, as only about 10% of D^*'s produced in B decay have this flavor correlation with the parent B meson.

A similar situation exists in the decay of B mesons to leptons. Leptons are produced in the decay of B mesons at the upper vertex of a virtual W boson. Therefore, a "primary" lepton — one produced in the initial B decay — will have a definite flavor correlation with the parent B: a semileptonic $\bar{B}^0$ or B^- decay will produce a negatively charged lepton, while semileptonic B^0 and B^+ decays produce positive leptons. Primary leptons are also referred to as "right-sign" leptons, as they comprise the majority of leptons produced in B decay. Only about 15% of leptons above 0.8 GeV are secondary.

A "secondary" lepton is one produced in the subsequent decay of the products of the initial B-meson decay. These leptons usually have charges opposite those of primary leptons. The semileptonic decay of a c quark produced in b quark decay produces a negative lepton, while that of a $\bar{c}$ quark produced in $\bar{b}$ decay gives rise to a positive lepton. However, there are other production mechanisms for secondary leptons that produce leptons of the same sign as primary leptons. Examples include the semileptonic decay of an upper-vertex D^* meson, τ decay, ψ decay, and photon conversion. Thus, while all "wrong-sign" leptons are secondary, not all secondary leptons are wrong-sign. Furthermore, not all "right-sign" leptons are primary. Nonetheless, I will refer to all right-sign leptons as primary; in practice about

95% of right-sign leptons are actually primary. Likewise, I will refer to wrong-sign secondary leptons simply as secondary leptons.

Most $\Upsilon(4S)$ decays produce two B mesons of opposite flavor — a B^- and a B^+ meson, or a B^0 and a $\bar{B}^0$. If one B decay produces a D^* and the other a lepton, the most likely scenario — that involving both a lower-vertex D^* and a primary lepton — gives rise to a D^* and a lepton of the same sign. Such events do not contribute a background to my analysis, as I require that the D^* and lepton have opposite charges to be consistent with a $\bar{B}^0 \to D^{*+}\ell^-\bar{\nu}$ decay. In order to contribute a background to the analysis, a uncorrelated-lepton event must either 1) contain an upper-vertex D^* decay, 2) contain a secondary lepton, or 3) contain either two B^0 or two $\bar{B}^0$ decays as a result of B^0–$\bar{B}^0$ mixing.

To estimate the uncorrelated-lepton background, I first identify tagged uncorrelated background events in the generic Monte Carlo sample. I require that both the D^* and the lepton be correctly reconstructed, and that they be the daughters of different B mesons. I divide the uncorrelated-lepton events into six categories:

1) B^+B^- event, upper-vertex D^*, primary lepton

2) B^+B^- event, lower-vertex D^*, secondary lepton

3) $B^0\bar{B}^0$ event, upper-vertex D^*, primary lepton

4) $B^0\bar{B}^0$ event, lower-vertex D^*, secondary lepton

5) B^0B^0 or $\bar{B}^0\bar{B}^0$ event, lower-vertex D^*, primary lepton

6) B^0B^0 or $\bar{B}^0\bar{B}^0$ event, upper-vertex D^*, secondary lepton

In each category, I normalize the Monte Carlo to the number of $B\bar{B}$ events in data on a dataset-by-dataset basis, and then sum over datasets. For categories 3–6, I further renormalize the Monte Carlo dataset-by-dataset to a consistent level of mixing. This mixing level is characterized by χ_d, the fraction of $\Upsilon(4S)$ decays to two neutral B mesons in which both B's decay as either B^0's or $\bar{B}^0$'s. The quantity χ_d is also the total probability that a B^0 decays as a $\bar{B}^0$, or vice-versa. I normalize to the result of a recent measurement of χ_d at CLEO [53],

$$\chi_d = 0.198 \pm 0.013 \pm 0.014. \tag{4.1}$$

The uncertainties here are statistical and systematic. The CLEO result is a direct measurement of χ_d.

In Figure 4.4, I plot the $\cos\theta_{BY}$ distributions of the six uncorrelated-background categories, divided into high ($p_{D^*} > 1.3\,\mathrm{GeV}$) and low ($p_{D^*} \leq 1.3\,\mathrm{GeV}$) D^{*+} momentum regions. In each plot, the low-p_{D^*} events tend to have lower values of $\cos\theta_{BY}$. When the D^* momentum is low, the total mass of the D^*-lepton system is less than it would be with a higher D^* momentum. The the mass of "missing" particles that would have to be added to form a B-meson is correspondingly higher. As higher "missing mass" values correspond to lower values of $\cos\theta_{BY}$, the low-p_{D^*} event have lower $\cos\theta_{BY}$ values than the high-p_{D^*} events.

Several other features of the uncorrelated background are notable in Figure 4.4. The largest contribution comes from Category 5, mixed events with primary leptons and lower-vertex D^{*+}'s. These events tend to have both hard leptons and hard D^{*+}'s, and most of this category populates the region $\cos\theta_{BY} > 0$. In contrast, there are nearly no Category 6 events, as these events suffer both the secondary-

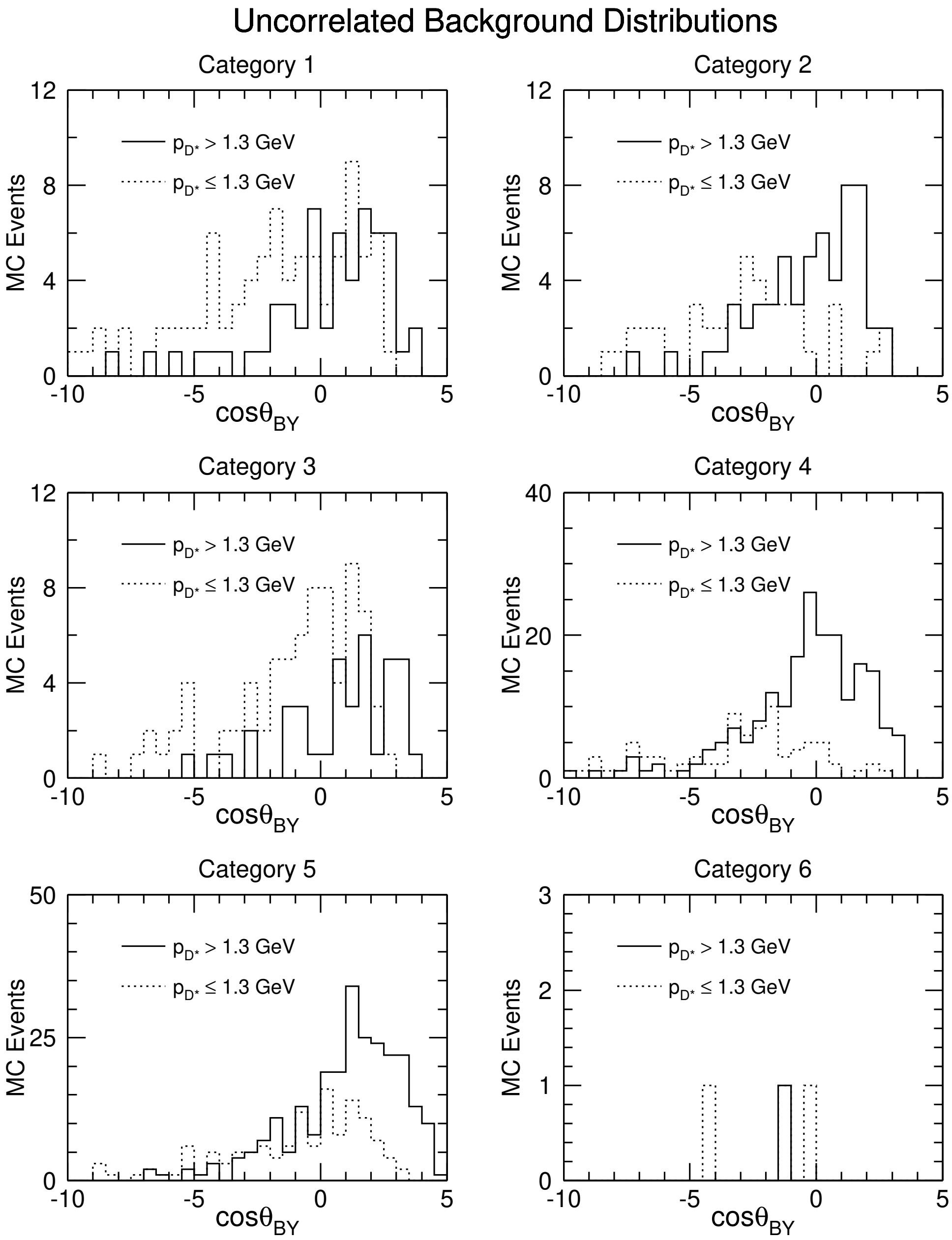

Figure 4.4: The $\cos\theta_{BY}$ distributions for each category of uncorrelated-lepton background. I define the six categories in the text. In each plot, the solid histogram shows the distribution of events in which the D^{*+} momentum is above 1.3 GeV, while the dotted histogram show events below that value. The events are tagged from reconstructed generic Monte Carlo.

lepton and upper-vertex-D^{*+} suppressions.

Both Categories 2 and 4 contain lower-vertex D^{*+}'s and secondary leptons. As the lower-vertex D^{*+} production rate is significantly higher in $\bar{B}^0$ than in B^- decay, Category 4 contains more more events than Category 2. (In fact, $\bar{B}^0 \to D^{*+}\ell^-\bar{\nu}$ itself contributes significantly to this difference.) In contrast, the upper-vertex D^{*+} production rates are similar between $\bar{B}^0$ and B^- decays. As a result, Categories 1 and 3, which contain upper-vertex D^{*+}'s and primary leptons, contain numbers of events which are more similar.

My estimate of the uncorrelated-lepton background is a weighted sum of twelve different background components. These twelve components consist of the six uncorrelated background categories, each divided into high and low D^{*+} momentum components as in Figure 4.4. If the Monte Carlo perfectly matched the data, each weight would have a value of unity. I use the weights to adjust the uncorrelated-lepton background to account for differences between the data and Monte Carlo inclusive D^{*+} and lepton spectra. I then vary the weights to establish a systematic uncertainty.

The first factor in each weight accounts for the difference between the inclusive D^{*+} production rates in data and Monte Carlo. CLEO Monte Carlo includes about 5% more charged D^*'s per event than are observed in data. I show the reconstructed D^{*+} spectra in data and Monte Carlo in Figure 4.5. The ratio R of data to Monte Carlo D^{*+}'s is 0.965 ± 0.027 for $p_{D^*} \leq 1.3\,\mathrm{GeV}$; $R = 0.957 \pm 0.023$ for $p_{D^*} > 1.3\,\mathrm{GeV}$. The errors reflect the statistical uncertainties in the D^{*+} yields from both the Monte Carlo sample and from the data.

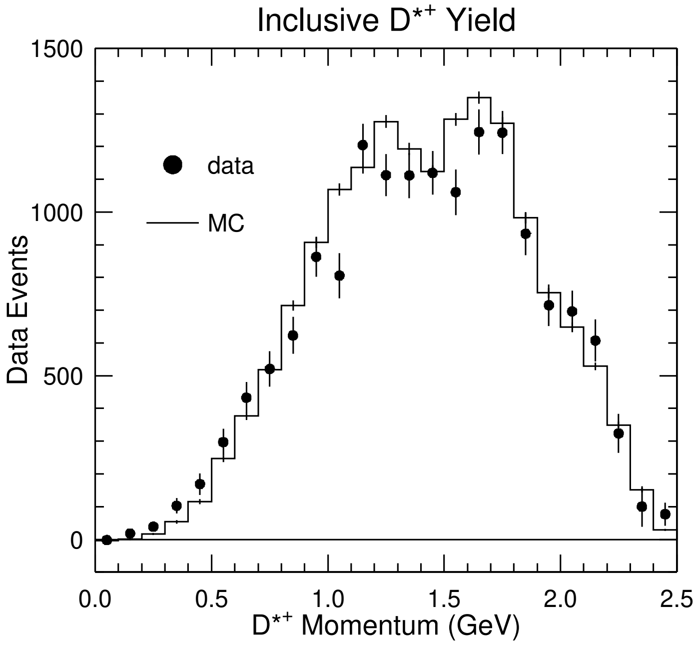

Figure 4.5: The inclusive D^{*+} yields in data and Monte Carlo as a function of momentum. The points give the yield of reconstructed D^{*+} mesons in CLEO II data, while the histogram shows the yield in generic Monte Carlo, scaled to the same luminosity as the data. I extract these yields with the same reconstruction techniques I use to find D^{*+}'s in $D^{*+}\ell^-\bar{\nu}$ events, but without the requirement that a lepton be present in the event. To extract the yields, I do continuum and combinatoric background subtractions similar to those I describe in Sections 3.2.1 and 3.2.2, but in bins of D^{*+} momentum.

I show the contributions of lower and upper-vertex D^{*+} production to the inclusive D^{*+} spectrum in generic Monte Carlo in Figure 4.6. Upper-vertex production accounts for 8% of all Monte Carlo D^*'s, including 15% of D^*'s below 1.3 GeV and 4% above 1.3 GeV. I refer to this quantity below as the upper-vertex fraction fraction F.

My baseline assumption is that the amount of upper-vertex D^{*+} production in

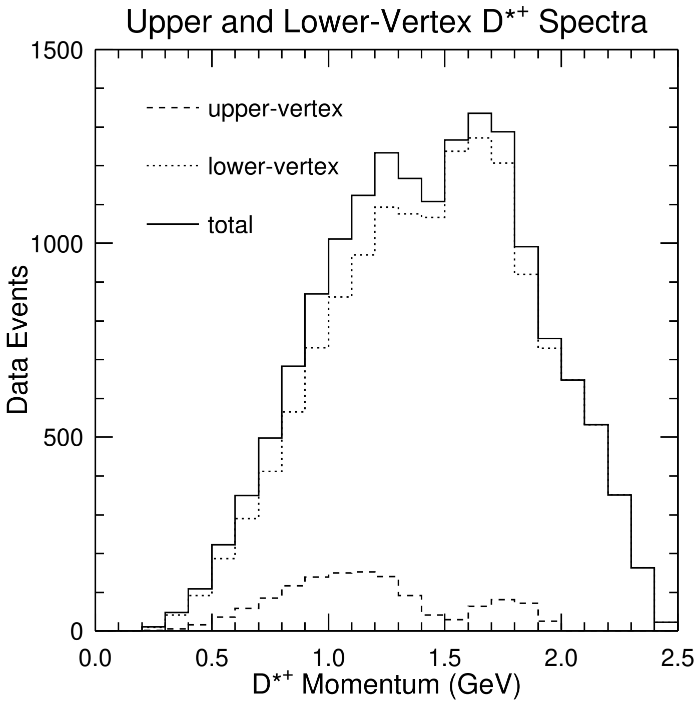

Figure 4.6: The momentum spectra of upper and lower-vertex D^{*+} mesons. The distributions are from generator-level Monte Carlo, each scaled by the momentum-dependent inclusive D^{*+} reconstruction efficiency measured in generic Monte Carlo. The yields are normalized to the luminosity of the CLEO II data.

the Monte Carlo is correct. The rate in the Monte Carlo is a best guess at the absolute upper-vertex D^{*+} rate, not at the fraction of D^{*+} production that occurs via this channel. I therefore fix the level of upper-vertex production, and adjust the level of lower-vertex production to match the inclusive D^{*+} rate. There are large uncertainties in the expected upper-vertex production rates, on the order of 50%. I therefore vary the weights of the upper-vertex uncorrelated-lepton background components by 50% to establish a systematic error. For each upper-vertex scale factor S_{UV}, I calculate a lower-vertex scale factor S_{LV}:

$$S_{LV} = \frac{R - F * S_{UV}}{1 - F * S_{UV}}. \tag{4.2}$$

Here R is the ratio of inclusive data to Monte Carlo D^{*+} rates, and F is the upper-vertex fraction. Values for each quantity in both low and high D^{*+} momentum regions are given above.

The second factor in each weight normalizes the lepton spectra. The primary and secondary lepton spectra have been measured directly at CLEO [54]. Bonnie Valant-Spaight compares these measured rates to the recompress generic Monte Carlo in the course of her analysis of $B^- \to D^{*0}\ell^-\bar{\nu}$ [43]. She finds that the primary and secondary-lepton momentum spectra in the generic Monte Carlo are similar in distribution to those observed in the data. The measured inclusive $B \to X\ell^-\bar{\nu}$ branching fraction for leptons above 0.8 GeV is $(8.99 \pm 0.39) \times 10^{-2}$; the Monte Carlo branching fraction, from a sample of 50,000 generic Monte Carlo events, is $(9.18 \pm 0.07) \times 10^{-2}$. These figures are consistent to within 5%. I therefore use a baseline weight of unity for each uncorrelated-lepton background component including primary leptons, and vary this weight by 5% to establish a systematic uncertainty.

Valant-Spaight also finds the secondary lepton branching fraction for leptons above 0.8 GeV to be $(1.83 \pm 0.03) \times 10^{-2}$ in Monte Carlo, substantially higher than the measured rate of $(1.53 \pm 0.12) \times 10^{-2}$. The secondary rate in data is thus 0.836 that in Monte Carlo, with a 29% uncertainty. I use that scale factor and variation for background components that include secondary leptons.

Table 4.2: The results of the uncorrelated background systematic error study. The background variations are described in the text. The change in the $\bar{B}^0 \to D^{*+}\ell^-\bar{\nu}$ branching ratio produced by each variation is given. The average magnitudes of the positive and negative background variations are added in quadrature to compute the total systematic uncertainty.

variation		uncert. (%)
upper-vertex fraction, $p_{D^*} \leq 1.3$	$\uparrow$	-0.038
	$\downarrow$	$+0.036$
upper-vertex fraction, $p_{D^*} > 1.3$	$\uparrow$	-0.095
	$\downarrow$	$+0.095$
D^{*+} rate ratio, $p_{D^*} \leq 1.3$	$\uparrow$	$+0.006$
	$\downarrow$	-0.006
D^{*+} rate ratio, $p_{D^*} > 1.3$	$\uparrow$	-0.036
	$\downarrow$	$+0.036$
primary lepton rate	$\uparrow$	-0.067
	$\downarrow$	$+0.067$
secondary lepton rate	$\uparrow$	-0.018
	$\downarrow$	$+0.018$
mixing	$\uparrow$	-0.085
	$\downarrow$	$+0.085$
total		0.154

The third and final factor in each weight controls the level of mixing. To assign a systematic error based on the uncertainty in the level of mixing, I vary χ_d according to its measurement uncertainty and calculate the weights:

$$w_{\mathrm{mixed}} = \frac{\chi_d}{(\chi_d)_{\mathrm{base}}} \tag{4.3}$$

$$w_{\mathrm{unmixed}} = \frac{1-\chi_d}{(1-\chi_d)_{\mathrm{base}}} \tag{4.4}$$

In these equations, $(\chi_d)_{\mathrm{base}}$ is the baseline level of mixing given in Equation 4.1. These weights are applied to the mixed and unmixed components of the uncorrelated background. No mixing-related weight is applied to the B^+B^- components.

I perform a total of seven variations in the uncorrelated-lepton background. For each, I vary the relevant parameter both up and down and quantify the fractional change in the the $\bar{B}^0 \to D^{*+}\ell^-\bar{\nu}$ branching fraction. The seven studies are variation of upper-vertex fraction for both low and high D^{*+} momentum, variation of the data-to-Monte Carlo D^{*+} rates for both low and high momentum, variation of the primary and secondary lepton rates, and variation of the level of mixing. I summarize the results of these studies in Table 4.2.

To obtain the final systematic uncertainty due to the uncorrelated-lepton background, I add in quadrature the average magnitude of the two variations in each study. The total result is a 0.15% systematic uncertainty in the $\bar{B}^0 \to D^{*+}\ell^-\bar{\nu}$ branching fraction.

The statistical uncertainty in the uncorrelated-lepton background is 0.31%. This uncertainty is entirely due to Monte Carlo statistics and is unrelated to the amount of data I use in the analysis.

4.5 Correlated Background

The correlated background includes contributions from several different physics processes. The background distribution I use is a sum of 13 different background categories, each tagged from the generic Monte Carlo. In several cases the CLEO

Monte Carlo does not use the best available measurement of the rate of a particular process. In these cases I reweight the Monte Carlo background distribution to a more recent measurement.

I summarize the categories of correlated background in Table 4.3. With each process, I list the number of estimated background events in the $\cos\theta_{BY}$ fit region ($-6.0 \leq \cos\theta_{BY} \leq 1.5$), the branching fraction and its uncertainty, and the source of that branching fraction. Finally, I give the fractional change in the $\bar{B}^0 \to D^{*+}\ell^-\bar{\nu}$ branching fraction that I measure when I vary each component by its uncertainty.

No measurements exist of several of the background processes listed in Table 4.3. In these cases, I simply use the branching fractions assumed in the CLEO Monte Carlo. I list those branching fractions in the Table, and give in parentheses the fractional amounts by which I vary these backgrounds. For the "D^*nX" mode, "nX" refers to three or more additional mesons that can be either pions, ρ mesons, or η mesons. These decays are not assigned specific branching fractions in the CLEO Monte Carlo but are instead generated with a hadronic fragmentation model. The "$D^{**}X$" mode refers to two body decays of the B to P-wave D-meson states and either a π or ρ. Finally, I vary the D^*D and $D^*D\pi$ modes in concert, as these modes have not been measured and the physics processes behind them are similar. I do the same for the $D^*\tau\nu$ and $D^*\pi\tau\nu$ modes.

For each contributing process, I take the average of the fractional variations in the $D^{*+}\ell^-\bar{\nu}$ branching fraction that I obtain by varying the component background levels up and down. I add these variations in quadrature to yield a systematic

Table 4.3: The results of the correlated background systematic error study. I list background B-decay modes, their sizes in the $\cos\theta_{BY}$ fit region, and their branching fractions. I vary these branching fractions by one standard deviation to establish the effect on $\mathcal{B}(\bar{B}^0 \to D^{*+}\ell^-\bar{\nu})$. The average magnitudes of the positive and negative background mode variations are added in quadrature to compute the total systematic uncertainty.

Background	events	branching fraction	source		uncert. (%)
$D^{(*)}D^{(*)}K^{(*)}$	4.7 ± 1.0	8.0×10^{-2} ($\pm 50\%$)	CLEO MC	$\uparrow$	$+0.139$
				$\downarrow$	-0.139
$D_s^* D^*$	8.4 ± 1.3	$(2.0 \pm 0.7) \times 10^{-2}$	PDG'98 [3]	$\uparrow$	$+0.102$
				$\downarrow$	-0.103
$D^* D$	6.1 ± 1.1	1.7×10^{-3} ($\pm 50\%$)	CLEO MC	$\uparrow$	$+0.084$
$D^* D \pi$	0.4 ± 0.3	1.0×10^{-3} ($\pm 50\%$)	CLEO MC	$\downarrow$	-0.085
$D_s D^*$	6.9 ± 1.2	$(0.96 \pm 0.34) \times 10^{-2}$	PDG'98 [3]	$\uparrow$	$+0.066$
				$\downarrow$	-0.067
$D^* D^*$	0.7 ± 0.2	$(6.2^{+4.1}_{-3.1}) \times 10^{-4}$	CLEO'99	$\uparrow$	$+0.019$
			[55]	$\downarrow$	-0.014
$D^* \tau \nu$	10.1 ± 1.4	2.4×10^{-2} ($\pm 25\%$)	CLEO MC	$\uparrow$	$+0.111$
$D^* \pi \tau \nu$	0.2 ± 0.2	0.3×10^{-2} ($\pm 25\%$)	CLEO MC	$\downarrow$	-0.112
$D^* \rho^{\pm}$	1.0 ± 1.1	$(6.7 \pm 3.3) \times 10^{-3}$	PDG'98 [3]	$\uparrow$	-0.033
				$\downarrow$	$+0.032$
$D^{**} X$	0.6 ± 0.3	6.9×10^{-3} ($\pm 50\%$)	CLEO MC	$\uparrow$	$+0.013$
				$\downarrow$	-0.013
$D^* \pi^{\pm}(\pi^0, \eta)$	1.2 ± 0.7	$(1.5 \pm 0.5) \times 10^{-2}$	PDG'98 [3]	$\uparrow$	$+0.010$
				$\downarrow$	-0.011
$D^* a_1^{\pm}$	0.3 ± 0.3	$(1.30 \pm 0.27) \times 10^{-2}$	PDG'98 [3]	$\uparrow$	-0.004
				$\downarrow$	$+0.004$
D^*nX	0.4 ± 0.3	($\pm 50\%$)	CLEO MC	$\uparrow$	$+0.006$
				$\downarrow$	-0.006
total					0.236

uncertainty of 0.24% due to the correlated background.

The correlated background also contributes 0.17% to the statistical uncertainty in the branching-fraction fit. As in the case of the uncorrelated background, this statistical uncertainty is entirely due to the amount of generic Monte Carlo available, and not to the amount of data I use in this measurement.

4.6 $D^{*+}X\ell^-\bar{\nu}$ Background

I obtain the $D^{*+}X\ell^-\bar{\nu}$ distribution for the branching-fraction fit from 40,000 events of dedicated $D^{*+}X\ell^-\bar{\nu}$ Monte Carlo, as described in Section 3.2.6. This background sample is composed of six different B-decay modes. I use generator-level information to classify the tagged reconstructed $D^{*+}X\ell^-\bar{\nu}$ events from this sample by parent B-decay mode. I plot the reconstructed $\cos\theta_{BY}$ distributions of these six modes in Figure 4.7. There are notable differences between the distributions. The narrow resonant D_1 and D_2^* modes peak near the physical region of $\cos\theta_{BY}$, with tails to negative $\cos\theta_{BY}$. When these decay modes are misreconstructed as $\bar{B}^0 \to D^{*+}\ell^-\bar{\nu}$, the missing system X consists only of a soft pion from the $D^{**} \to D^{*+}\pi$ decay. The amount of missing mass is typically not large, so the reconstructed $\cos\theta_{BY}$ distribution peaks near the physical region. In contrast, the distribution of $B \to D^{*+}\pi\ell^-\bar{\nu}$ events peaks less than the narrow D^{**} modes, and has a larger tail to negative $\cos\theta_{BY}$. The pion in this nonresonant decay mode can be more energetic, and the missing mass therefore greater than in the resonant modes.

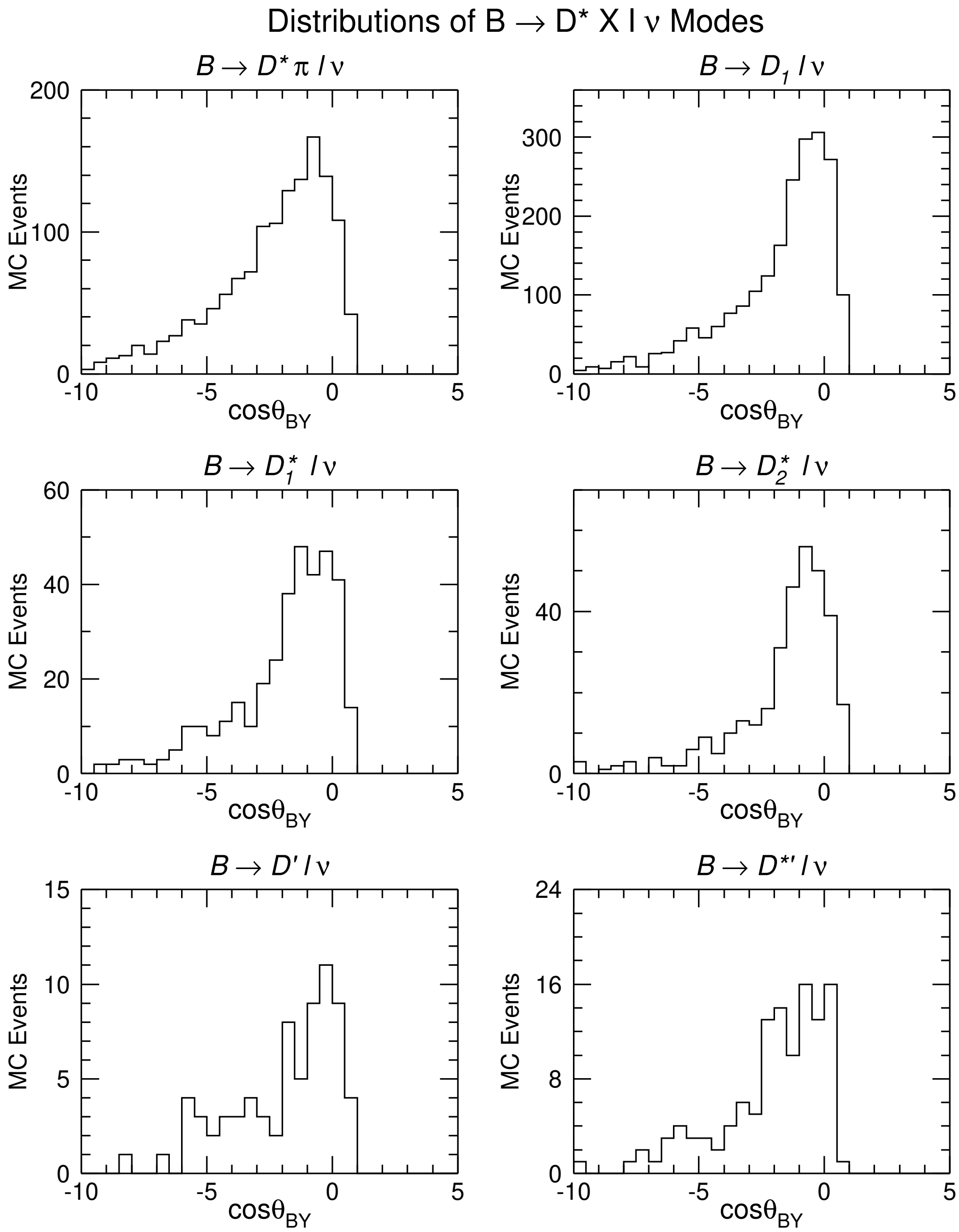

Figure 4.7: Monte Carlo $\cos\theta_{BY}$ distributions of the $\bar{B}^0 \to D^{*+}X\ell^-\bar{\nu}$ background. The histograms show the distributions of the six components of this background. The entries are tagged reconstructed events from 40,000 $D^{*+}X\ell^-\bar{\nu}$ Monte Carlo events.

I allow the overall $B \to D^{*+}X\ell^-\bar{\nu}$ branching fraction to float in the $\cos\theta_{BY}$ fit, so the ignorance of the inclusive $D^{*+}X\ell^-\bar{\nu}$ rate does not pose a problem. The unknown relative branching fractions of the different modes are an issue, since variation of these relative contributions changes the overall $\cos\theta_{BY}$ distribution of this background. Furthermore, the distribution of events within each mode depends on the form factors used in the Monte Carlo simulation, and these form factors are themselves poorly-known. However, it is reasonable to assume that the form-factor uncertainty in the $\cos\theta_{BY}$ distribution of each mode is smaller than the differences between the distributions of different modes. While the relative rates of the six modes are not known, the fraction of the $D^{*+}X\ell^-\bar{\nu}$ background contributed by each is obviously between 0–100%. I therefore assess the systematic uncertainty associated with the $B \to D^{*+}X\ell^-\bar{\nu}$ background by combining the $\cos\theta_{BY}$ distributions of the six component modes in the most extreme manner: I replace the baseline $D^{*+}X\ell^-\bar{\nu}$ distribution with that of each mode in turn, and I redo the $\bar{B}^0 \to D^{*+}\ell^-\bar{\nu}$ branching-fraction fit. Each fit corresponds to turning the branching fraction of one mode up to 100% of the inclusive $B \to D^{*+}X\ell^-\bar{\nu}$ rate, and turning the others down to zero.

I give the results of this study in Table 4.4. The modes that give the greatest change in the $D^{*+}\ell^-\bar{\nu}$ branching fraction are $B \to D^{*+}\pi\ell^-\bar{\nu}$ and $B \to D_2^*\ell^-\bar{\nu}$. As I mention above, these modes differ the most in $\cos\theta_{BY}$ distribution. I take the variation with the greatest effect on the branching fraction as a conservative estimate of the $B \to D^{*+}X\ell^-\bar{\nu}$ systematic uncertainty. I therefore assign a 2.24% uncertainty to this source.

Table 4.4: The results of the $\bar{B}^0 \to D^{*+}X\ell^-\bar{\nu}$ background systematic error study. The table gives the change in the $\bar{B}^0 \to D^{*+}\ell^-\bar{\nu}$ branching fraction produced by replacing the total $D^{*+}X\ell^-\bar{\nu}$ distribution with each submode in the branching-fraction fit.

$D^{*+}X\ell^-\bar{\nu}$ mode	$\mathrm{d}\mathcal{B}/\mathcal{B}\,(\%)$
$B \to D^{*+}\pi\ell^-\bar{\nu}$	2.24
$B \to D_1\ell^-\bar{\nu}$	−1.44
$B \to D_1^*\ell^-\bar{\nu}$	0.08
$B \to D_2^*\ell^-\bar{\nu}$	−1.93
$B \to D'\ell^-\bar{\nu}$	−1.07
$B \to D^{*\prime}\ell^-\bar{\nu}$	0.66

The $D^{*+}X\ell^-\bar{\nu}$ background distribution contributes 0.25% to the statistical uncertainty in the $D^{*+}\ell^-\bar{\nu}$ branching-fraction fit.

4.7 Monte Carlo Signal Shape

The CLEO recompress Monte Carlo generates $\bar{B}^0 \to D^{*+}\ell^-\bar{\nu}$ decays with the linear form-factor parameterization defined by Equation 1.36. The form-factor parameters used are the central values of a CLEO combined fit to $\bar{B}^0 \to D^{*+}\ell^-\bar{\nu}$ and $B^+ \to D^{*0}\ell^-\bar{\nu}$ [50]:

$$\begin{aligned} R_1 &= 1.24 \pm 0.26 \pm 0.12, \\ R_2 &= 0.72 \pm 0.18 \pm 0.07, \\ \rho^2 &= 0.92 \pm 0.12 \pm 0.06. \end{aligned} \tag{4.5}$$

(For notational simplicity, the ρ^2 here is the $\rho^2_{h_{A_1}}$ of Section 1.3.) The correlations between these three measurements are given by the correlation coefficients:

$$\begin{aligned} C_{R_1 R_2} &= -0.814, \\ C_{R_1 \rho^2} &= +0.618, \\ C_{R_2 \rho^2} &= -0.815. \end{aligned} \tag{4.6}$$

My measurement relies on a $\bar{B}^0 \to D^{*+}\ell^-\bar{\nu}$ distribution and normalization based on the central values above. It is sensitive to the form-factor parameters to the extent that they affect either the shape or the normalization of the signal $\cos\theta_{BY}$ distribution I use in my branching-fraction fit. In principle, I could study this issue by generating sets of signal Monte Carlo with different values for the form-factor parameters. This approach would be costly in computer resources. It would furthermore be limited by the statistical size of the signal Monte Carlo samples — my 100,000 event $D^{*+}\ell^-\bar{\nu}$ signal distribution contributes 0.86% to the statistical uncertainty in the branching-fraction fit.

I instead study the dependence of my branching fraction measurement on the form-factor parameters with a reweighting technique. This technique allows me to model the normalized $\cos\theta_{BY}$ distributions corresponding to different choices of the form factor parameters (R_1, R_2, ρ^2) with the same set of Monte Carlo events. I first use generator-level information to compute the decay distribution variables (q^2, $\cos\theta_\ell$, $\cos\theta_V$, χ) for each tagged $D^{*+}\ell^-\bar{\nu}$ event in the reconstructed signal Monte Carlo sample. For each tagged event, I calculate two differential decay rates, one for the baseline form-factor parameters, and the other for a variant

Table 4.5: The results of the $\bar{B}^0 \to D^{*+}\ell^-\bar{\nu}$ form-factor variation study. I give the $\bar{B}^0 \to D^{*+}\ell^-\bar{\nu}$ branching fraction returned by the fit for each set of form-factor parameters. I list the fractional change in $\mathcal{B}(\bar{B}^0 \to D^{*+}\ell^-\bar{\nu})$ for each of the six variations. I compute $\partial\mathcal{B}/\partial x$ (where x is R_1, R_2, or ρ^2) by averaging the magnitudes of the positive and negative variations.

	R_1	R_2	ρ^2	$\mathcal{B}\,(\times 10^{-2})$	$\Delta\mathcal{B}/\mathcal{B}\,(\%)$	$\partial\mathcal{B}/\partial x\,(\times 10^{-2})$
baseline	1.24	0.72	0.92	5.378	—	—
R_1 up	1.526	0.72	0.92	5.210	-3.12	-0.625
R_1 down	0.954	0.72	0.92	5.568	$+3.54$	
R_2 up	1.24	0.913	0.92	5.371	-0.13	-0.030
R_2 down	1.24	0.529	0.92	5.383	$+0.08$	
ρ^2 up	1.24	0.72	1.054	5.465	$+1.61$	$+0.606$
ρ^2 down	1.24	0.72	0.786	5.302	-1.41	

parameter set. I weight the event by the ratio of differential decay rates, corrected by the ratio of integrated decay rates for the two models. Finally, I fit the data using the baseline and variant $\cos\theta_{BY}$ distributions, and I compare the $D^{*+}\ell^-\bar{\nu}$ yields.

I present the results of these variations in Table 4.5. I vary each of the form factor parameters independently by one standard deviation in each direction. (The baseline is the tagged $D^{*+}\ell^-\bar{\nu}$ signal distribution, rather than the continuum-subtracted distribution, so the baseline branching fraction value differs slightly from the value I give in Section 3.3.3.) I give the fractional change in the $\bar{B}^0 \to D^{*+}\ell^-\bar{\nu}$ branching fraction for each variation. I average the positive and negative variations to estimate the differential change in branching fraction $\partial\mathcal{B}/\partial x$, where $x_i = (R_1, R_2, \rho^2)$ are the form-factor parameters.

I compute the systematic uncertainty due to the form-factor parameters with the error propagation equation:

$$(\delta\mathcal{B})^2 = \sum_{i,j} C_{ij} \left(\frac{\partial\mathcal{B}}{\partial x_i}\right) \left(\frac{\partial\mathcal{B}}{\partial x_j}\right). \tag{4.7}$$

The matrix C_{ij} is the covariance matrix of the measured form-factor parameters. Explicitly, it has the form:

$$C = \begin{pmatrix} (\delta R_1)^2 & C_{R_1R_2}(\delta R_1)(\delta R_2) & C_{R_1\rho^2}(\delta R_1)(\delta\rho^2) \\ C_{R_1R_2}(\delta R_1)(\delta R_2) & (\delta R_2)^2 & C_{R_2\rho^2}(\delta R_2)(\delta\rho^2) \\ C_{R_1\rho^2}(\delta R_1)(\delta\rho^2) & C_{R_2\rho^2}(\delta R_2)(\delta\rho^2) & (\delta\rho^2)^2 \end{pmatrix}, \tag{4.8}$$

where the δx_i are the one-standard-deviation measurement uncertainties. I use this approach to explicitly take into account the large correlations between the form-factor parameters. With the parameter uncertainties of Equation 4.5, the correlation coefficients of Equation 4.6, and the differential branching fraction changes of Table 4.5, I compute $\delta\mathcal{B} = 0.141 \times 10^{-2}$. This implies a 2.62% systematic uncertainty in the measured branching fraction due to uncertainty in the form-factor parameters.

The form-factor variations I describe above have minimal effects on the shape of the reconstructed $\cos\theta_{BY}$ distribution of $\bar{B}^0 \to D^{*+}\ell^-\bar{\nu}$ events, as illustrated by Figure 4.8. These variations primarily affect the normalization of the distribution, which changes because the form-factor variations affect the efficiencies of my analysis cuts. In particular, the form-factor variations shift the lepton momentum spectrum and the distribution of $\cos\theta_{D^*\ell}$. I give an example of these shifts in Figure 4.9, based on my variation of R_1 downwards from 1.24 to 0.954. This change softens the lepton momentum spectrum, which reduces the fraction of lep-

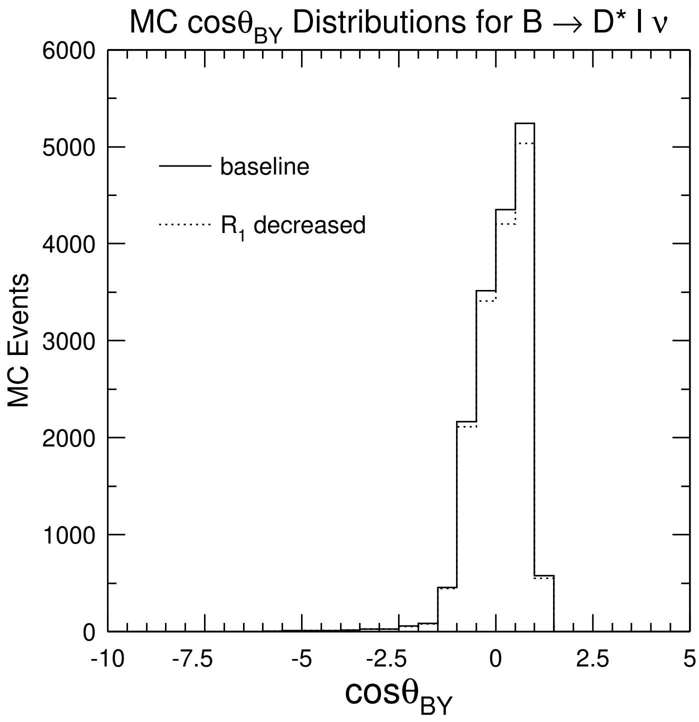

Figure 4.8: Effect of varying the $\bar{B}^0 \to D^{*+}\ell^-\bar{\nu}$ form factor on the $\cos\theta_{BY}$ distribution. The solid histogram corresponds to the baseline form-factor parameters (Equation 4.5). The dotted histogram is reweighted to new form factors with R_1 decreased by one standard deviation. The shapes of the distributions are similar, but their areas differ. Both histograms are based on tagged reconstructed candidates from a sample of 100,000 signal Monte Carlo events.

tons above my lower lepton-momentum cuts at 0.8 GeV for electrons and 1.4 GeV for muons. In a generator-level study, the reduction in R_1 decreases the efficiency of the lepton cut by 1.7%. This change also reduces the fraction of $D^{*+}\ell^-\bar{\nu}$ events which satisfy my cut of $\cos\theta_{D^*\ell} < 0$. The reduction in R_1 decreases the efficiency of the $\cos\theta_{D^*\ell}$ cut by 1.6%. Both cuts together are 2.7% less efficient when I reduce R_1. These efficiency variations are the primary reason the reduction in R_1 changes

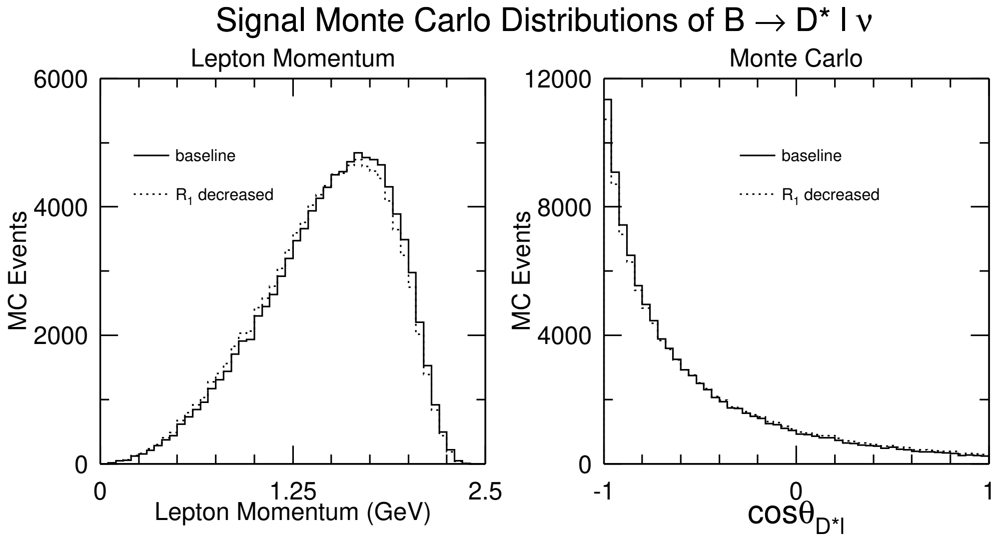

Figure 4.9: The generator-level distributions of lepton momentum and $\cos\theta_{D^*\ell}$ in 100,000 $\bar{B}^0 \to D^{*+}\ell^-\bar{\nu}$ Monte Carlo events. The solid histograms give the distributions with the baseline form-factor parameters, while the dotted histograms show the reweighted distributions with R_1 decreased by one standard deviation.

the $\bar{B}^0 \to D^{*+}\ell^-\bar{\nu}$ fit yield by 3.5%.

The $\bar{B}^0 \to D^{*+}\ell^-\bar{\nu}$ event distribution contributes 0.85% to the statistical uncertainty in the branching-fraction fit, established with the method of Section 4.1

4.8 B Momentum and Mass

My measurement of the $\bar{B}^0 \to D^{*+}\ell^-\bar{\nu}$ branching ratio relies on the reconstruction of $\cos\theta_{BY}$ for candidate events in the data. I calculate this quantity for each event with Equation 3.11. I make this calculation assuming specific values of the $\bar{B}^0$ momentum and mass. I use a dataset-dependent average $\bar{B}^0$ momentum and a specific value for the $\bar{B}^0$ mass. The values I used are based on precise measurements of the CLEO data, as I detail in Section 3.1.5.

The $\cos\theta_{BY}$ distribution is sensitive to the values I use for the $\bar{B}^0$ mass and momentum. For example, if I increase the $\bar{B}^0$-momentum value I use in reconstruction, the $\cos\theta_{BY}$ peak becomes narrower. Such a change in the shape of the $\cos\theta_{BY}$ distribution will affect the $\bar{B}^0 \to D^{*+}\ell^-\bar{\nu}$ branching fraction I extract by fitting the distribution. My measurement is therefore sensitive to the uncertainties in the measurements of average $\bar{B}^0$ momentum and of the $\bar{B}^0$ mass.

The average $\bar{B}^0$ momenta in data, given in the first column of Table 3.1, have a measurement uncertainty of 1.6 MeV. To measure the effect of this uncertainty on the $D^{*+}\ell^-\bar{\nu}$ branching fraction, I recompute $\cos\theta_{BY}$ for all data events after increasing the assumed $\bar{B}^0$ momentum by 1.6 MeV for all datasets. I then redo the branching-fraction fit. I do the same after shifting the average $\bar{B}^0$ momentum values downwards from their central values. The 1.6 MeV shifts produce an average 0.26% change in the branching fraction, so I assign that value as the systematic error.

I perform a similar study for the $\bar{B}^0$ mass. I vary the measured $\bar{B}^0$ mass, given by Equation 3.15, by its uncertainty and recompute $\cos\theta_{BY}$ in all data events. The fits to the variant $\cos\theta_{BY}$ distributions return a 0.11% shift in the $\bar{B}^0 \to D^{*+}\ell^-\bar{\nu}$ branching fraction. I take that value for the systematic error due to the uncertainty in the B^0 mass.

In performing the variations above, I only change the calculation of $\cos\theta_{BY}$ for data events. I make no changes in the $\cos\theta_{BY}$ distributions of the backgrounds I model with generic Monte Carlo, or in the $\bar{B}^0 \to D^{*+}\ell^-\bar{\nu}$ or $B \to D^{*+}X\ell^-\bar{\nu}$ fitting distributions from signal Monte Carlo. In Monte Carlo, I determine the average $\bar{B}^0$ momentum directly with generator-level information. I also know the $\bar{B}^0$ mass used in Monte Carlo generation, namely 5280.0 MeV. The average $\bar{B}^0$ momentum in Monte Carlo events is slightly different than it is in the data; likewise, the Monte Carlo $\bar{B}^0$ mass is higher than the measured value. However, studies indicate that these differences do not bias the $\cos\theta_{BY}$ distribution in Monte Carlo, so long as I reconstruct $\cos\theta_{BY}$ with the appropriate $\bar{B}^0$-momentum and mass values. The $\bar{B}^0$ mass and average momentum values therefore introduce no uncertainty to the Monte Carlo distributions, as their values in this case are known exactly.

4.9 Tracking Efficiencies

Understanding the systematic uncertainty due to tracking efficiency, particularly the slow pion tracking efficiency, is a critical component of the $\bar{B}^0 \to D^{*+}\ell^-\bar{\nu}$ branching fraction measurement. Appendices A and B detail the studies I have done to understand these effects. I conclude that the slow pion reconstruction efficiency contributes a 2.6% systematic uncertainty to this analysis.

Based on studies detailed in Appendix B, I conclude that the relevant uncertainty for the hard kaon and pion that I use to reconstruct the D^0 meson is 0.7% per track. The lepton, as it is not used in a mass peak, does not need to be as well-reconstructed, and contributes only a 0.5% uncertainty. The tracking uncertainties are correlated between the three hard tracks. I assign a total systematic error of 1.9% due to hard track reconstruction.

4.10 Lepton Identification

I do my analysis on the recompress data and Monte Carlo, but with the `PRELIB` `CEID` weights in data and the `PRELIB` efficiency histograms in Monte Carlo. As of this writing, the recompress `CEID` is still a work in progress, and the final efficiencies are not yet available. The difference between the `PRELIB` and recompress weights is small. However, the `PRELIB` efficiency histograms were subject to a methodological bias. As a result, the Monte Carlo likely overestimates the electron efficiency by as much as 3% [56]. This type of bias would lead me to measure a branching fraction lower than the true value.

Muon identification is in better shape. The muon efficiencies in data and Monte Carlo agree to 1.6% [31] over the momentum range I use in this analysis, $1.4 \leq p_\mu \leq 2.4\,\mathrm{GeV}$.

I assign a conservative 3% systematic error to lepton identification.

4.11 Absolute Normalization

The uncertainties on the values I assume for the D^{*+}-decay component branching fractions, for f_{00}, and for the absolute absolute number of $B\bar{B}$ pairs in the CLEO II data contribute to the overall systematic uncertainty in the $\bar{B}^0 \to D^{*+}\ell^-\bar{\nu}$ branching fraction. The $D^{*+} \to D^0\pi^+$ and $D^0 \to K^-\pi^+$ branching fractions in Equations 3.19–3.20 contribute a total systematic error of 2.56%. The uncertainty in the measurement of f_{00} contributes an additional 3.8% systematic error. The established uncertainty in the total number of $B\bar{B}$ pairs in CLEO II data is 1.8% [57].

4.12 Summary

In Table 4.6, I summarize the various sources of statistical and systematic error detailed in this chapter. The net systematic error in my measurement of $\mathcal{B}(\bar{B}^0 \to D^{*+}\ell^-\bar{\nu})$ is 7.7%. The largest systematic uncertainty is the 3.8% due to the measurement of f_{00}. However, my measurement and its systematic error can easily be updated with any better future measurement of f_{00}. The same is true of the component branching fractions of the D^{*+} decay chain. The lepton identification efficiency contributes the next largest systematic error, at 3%. This error should fall to 2% with the final recompress `CEID`. Next in size, at 2.6%, is the uncertainty due to the $\bar{B}^0 \to D^{*+}\ell^-\bar{\nu}$ form factors. These form factors affect the normalization and distribution of the the $D^{*+}\ell^-\bar{\nu}$ signal in the branching-fraction fit.

The dominant systematic error in the previous CLEO measurement of the $\bar{B}^0 \to D^{*+}\ell^-\bar{\nu}$ branching fraction [9] was the 5% uncertainty assigned to the slow pion reconstruction efficiency. This source of error no longer dominates the branching fraction measurement. I have reduced this uncertainty to 2.6% through the extensive studies I detail in the Appendices.

Table 4.6: Uncertainties for the $\bar{B}^0 \to D^{*+}\ell^-\bar{\nu}$ branching-fraction measurement. I list the sources of uncertainty detailed in this chapter. The second column gives the statistical uncertainty associated with the signal and background $\cos\theta_{BY}$ distributions used in the branching-fraction fit. The third column lists the systematic uncertainties. The total systematic error in the final row is the sum of the various systematic errors in quadrature.

source	statistical (%)	systematic (%)
Continuum Background	0.94	—
Combinatoric Background	0.60	1.97
Fake-Lepton Background	0.07	0.31
Uncorrelated Background	0.31	0.15
Correlated Background	0.17	0.24
$D^{*+}X\ell^-\bar{\nu}$ Background	0.25	2.24
Monte Carlo $D^{*+}\ell^-\bar{\nu}$ Distribution	0.85	2.62
B momentum		0.26
B mass		0.11
Slow Pion Efficiency		2.6
Tracking Efficiency		1.9
Lepton Identification		3.0
D^{*+} Decay Branching Fractions		2.56
f_{00}		3.8
$N_{B\bar{B}}$		1.8
Total		7.7

CHAPTER 5

DISCUSSION AND IMPLICATIONS

I make my measurement of the branching fraction of $\bar{B}^0 \to D^{*+}\ell^-\bar{\nu}$ with a fit to the distribution of $\cos\theta_{BY}$ in the CLEO II data, as I describe in Section 3.3. This fit gives the result $\mathcal{B}(\bar{B}^0 \to D^{*+}\ell^-\bar{\nu}) = (5.40 \pm 0.19) \times 10^{-2}$, where the error returned by the fit is purely statistical. This error includes statistical contributions from my estimates of all the sources of background. It also includes statistical contributions from the signal Monte Carlo used to model the $\bar{B}^0 \to D^{*+}\ell^-\bar{\nu}$ and $B \to D^{*+}X\ell^-\bar{\nu}$ distributions.

In general, one expects the statistical error to decline as the inverse square-root of the amount of data used in an analysis. Many of the distributions I use in the branching-fraction fit are based on Monte Carlo — those of the uncorrelated, correlated, and $D^{*+}X\ell^-\bar{\nu}$ backgrounds and of the $D^{*+}\ell^-\bar{\nu}$ signal. According to Table 4.6, the uncertainty in these distributions accounts for 0.95 of the 3.54% statistical error in my branching-fraction fit. This component of the statistical error depends on the amount of Monte Carlo I use in the analysis, not on the amount of data. Since the Monte Carlo statistical uncertainties are unrelated to the amount of experimental data, I include them in the final systematic error. The fractional statistical error in my measurement of the $\bar{B}^0 \to D^{*+}\ell^-\bar{\nu}$ branching fraction is therefore 3.40%. My total fractional systematic error from the sources I examine in Chapter 4 is 7.7%. I add the 0.95% Monte Carlo statistical error in quadrature to obtain a final systematic error of 7.8%. My branching-fraction measurement is thus:

$$\mathcal{B}(\bar{B}^0 \to D^{*+}\ell^-\bar{\nu}) = (5.40 \pm 0.18 \pm 0.42) \times 10^{-2}. \tag{5.1}$$

The CLEO collaboration published an earlier measurement of this branching fraction in 1995 [9], based a smaller data sample:

$$\mathcal{B}(\bar{B}^0 \to D^{*+}\ell^-\bar{\nu}) = (4.69 \pm 0.33 \pm 0.47) \times 10^{-2}. \tag{5.2}$$

This result and its error are updated to use the same values of the $D^{*+} \to D^0\pi^+$ and $D^0 \to K^-\pi^+$ branching fractions I use in my measurement (Equations 3.19 and 3.20). The 1995 CLEO analysis took advantage of a CLEO measurement of $\bar{B}^0(D^0 \to K^-\pi^+)$ [58] to cancel a 4% `PRELIB` tracking systematic error. To correctly update the previous CLEO measurement to use the same $D^0 \to K^-\pi^+$ branching fraction, I therefore add this 4% error to the systematic error. Finally, I correct the $\bar{B}^0 \to D^{*+}\ell^-\bar{\nu}$ branching fraction measurement to use the same value for f_{00} (Equation 3.22). The 1995 CLEO result was presented with the assumption that $f_{00} \equiv 0.5$, so this correction increases the systematic error of the measurement.

My analysis improves on both the statistical and systematic errors of the previous CLEO measurement. The statistical error is decreased from 7.1% to 3.4%, more than a factor of two. This improvement can be attributed to several sources. I use slightly more than twice as much CLEO II data in my analysis, $3.14\,\mathrm{fb}^{-1}$ compared to $1.55\,\mathrm{fb}^{-1}$. The increase in statistics reduces the expected statistical error from 7.1% to 5.0%. The remaining 32% decrease in the statistical error, from 5.0% to 3.4%, is due to improvements in the analysis technique. I reconstruct a significantly higher fraction of $\bar{B}^0 \to D^{*+}\ell^-\bar{\nu}$ decays than the previous CLEO analysis. This increase in efficiency is from 9.54% to roughly 16%, though differences in method make a direct efficiency comparison difficult. The improvement is primarily due to vertexing, which improves the measurement of the slow pion and thus brings more $D^{*+}\ell^-\bar{\nu}$ events into the Δm peak. Vertexing and the Kalman fitter also allow me to make a tighter cut on Δm, which reduces backgrounds and thus the statistical contributions of those backgrounds to the measurement error. Finally, the use of $D^{*+}X\ell^-\bar{\nu}$ Monte Carlo to model this background in the fit eliminates a 2.4% statistical error in the previous CLEO measurement.

The 7.8% systematic error in my measurement is likewise an improvement over the (corrected) 10.0% error in the previous CLEO analysis. This decrease is primarily due to the work I did to improve the understanding of CLEO slow pion reconstruction efficiency. The previous measurement assigned a 5% uncertainty based on the level of agreement in the slow pion efficiency between data and Monte Carlo. In the Appendices, I describe my measurement of this agreement between the recompress data and Monte Carlo. I conclude that the systematic uncertainty due to the slow pion reconstruction efficiency is 2.6%, a factor of two improvement over the old 5% value.

My central value of the $\bar{B}^0 \to D^{*+}\ell^-\bar{\nu}$ branching fraction, 5.40×10^{-2}, is higher than the (corrected) central value of the previous result, 4.69×10^{-2}. To compare the two analyses, I redo my analysis with the same data used in the

1995 CLEO measurement, namely the 4s2–6 datasets. The branching-fraction fit returns the value $\mathcal{B}(\bar{B}^0 \to D^{*+}\ell^-\bar{\nu}) = (5.05 \pm 0.26) \times 10^{-2}$. The method of the previous CLEO analysis therefore gives a value 7.1% lower than my method with the same data.

To establish the level of consistency between these two measurements, I must examine the correlation between their uncertainties. My approach enjoys a greater reconstruction efficiency than the previous measurement, so I assume the $D^{*+}\ell^-\bar{\nu}$ events I reconstruct are a superset of those in the old analysis. I therefore subtract the fractional statistical errors in quadrature to obtain a 5.0% statistical error on the difference in measured branching fractions. Many parts of the systematic errors of the two measurements are uncorrelated due to the substantial differences between the two methods. The previous CLEO measurement was made with pre-recompress tracking, which differs substantially from the recompress, particularly for the earliest CLEO II datasets. For this reason the uncertainties due to tracking efficiency are largely uncorrelated between the two measurements. I assume only that the number of $B\bar{B}$ events and the lepton identification efficiencies are correlated between the two measurements. As I have corrected the old CLEO measurement with more recent values of $\mathcal{B}(D^{*+} \to D^0\pi^+)$, $\mathcal{B}(D^0 \to K^-\pi^+)$ and f_{00}, I also exclude the uncertainty due to these quantities. The uncorrelated component of the systematic error in my measurement is thus 5.1%. If one excludes these same components, but includes the 4.0% `PRELIB` tracking uncertainty, the uncorrelated component of the systematic error in the old measurement is 8.7%. I therefore conclude that the old CLEO measurement of $\mathcal{B}(\bar{B}^0 \to D^{*+}\ell^-\bar{\nu})$ differs

Table 5.1: Measurements of the $\bar{B}^0 \to D^{*+}\ell^-\bar{\nu}$ branching fraction. The measurements are listed by collaboration with the year of publication. I give both the values originally published and values corrected to common baselines as described in the text.

Collaboration	Date	Ref.	$\mathcal{B}(\bar{B}^0 \to D^{*+}\ell^-\bar{\nu})$ $(\times 10^{-2})$ quoted	corrected
ARGUS	1994	[59]	$4.5 \pm 0.3 \pm 0.4$	$4.6 \pm 0.3 \pm 0.4$
CLEO	1995	[9]	$4.49 \pm 0.32 \pm 0.39$	$4.69 \pm 0.33 \pm 0.47$
DELPHI	1996	[60]	$5.52 \pm 0.17 \pm 0.68$	$5.52 \pm 0.17 \pm 0.66$
ALEPH	1997	[62]	$5.53 \pm 0.26 \pm 0.52$	$5.42 \pm 0.26 \pm 0.47$
OPAL (superseded)	1997	[61]	$5.08 \pm 0.21 \pm 0.66$	$4.96 \pm 0.20 \pm 0.62$
DELPHI (preliminary)	1999	[63]	$5.22 \pm 0.12 \pm 0.55$	$5.24 \pm 0.12 \pm 0.58$
OPAL	2000	[64]	$5.26 \pm 0.20 \pm 0.46$	$5.32 \pm 0.20 \pm 0.46$
BELLE (preliminary)	2000	[65]	$4.74 \pm 0.25 \pm 0.51$	$4.89 \pm 0.26 \pm 0.56$
this result			$5.40 \pm 0.18 \pm 0.42$	

from the result of my method when applied to the same data by

$$\frac{\delta\mathcal{B}}{\mathcal{B}} = -7.1 \pm 11.8\%. \tag{5.3}$$

The two results differ by less than one standard deviation, and are therefore consistent with each other.

The branching fraction $\mathcal{B}(\bar{B}^0 \to D^{*+}\ell^-\bar{\nu})$ has been measured by other experiments. I give some of these results in Table 5.1. I present both the values originally published and values I have corrected in several ways to allow fair comparisons. I also plot the corrected values in Figure 5.1. I correct all of the measurements to use a common value for the $D^{*+} \to D^0\pi^+$ branching fraction, that of Equation 3.19. The other corrections are specific to the nature of the experiment, as

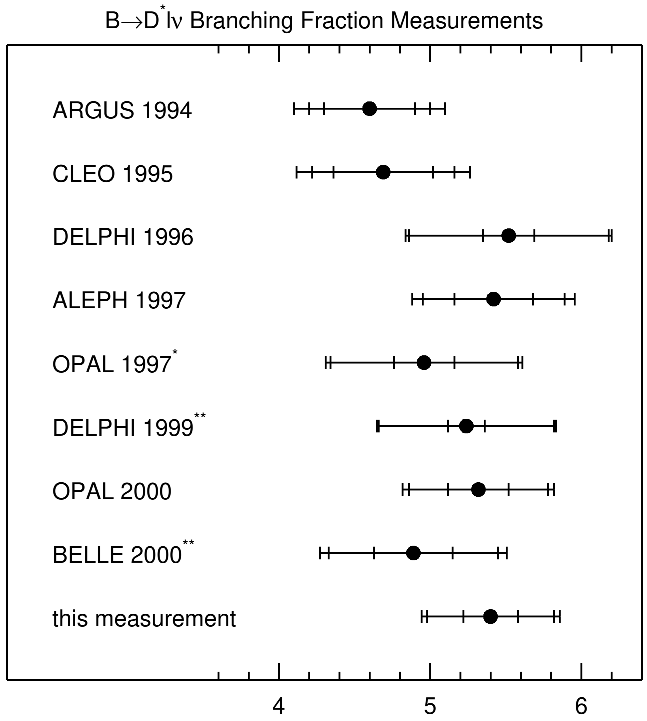

Figure 5.1: A plot of the corrected $\mathcal{B}(\bar{B}^0 \to D^{*+}\ell^-\bar{\nu})$ measurements listed in Table 5.1. The statistical, systematic, and combined error intervals are indicated for each analysis. The 1997 OPAL analysis flagged by an asterisk (*) is superseded by the 2000 OPAL measurement; the analyses flagged by two asterisks are preliminary results.

$\mathcal{B}(\bar{B}^0 \to D^{*+}\ell^-\bar{\nu})$ measurements have been made in e^+e^- collider experiments running at both the $\Upsilon(4S)$ and Z resonances.

ARGUS was an e^+e^- collider experiment running on the $\Upsilon(4S)$ resonance, similar to CLEO. BELLE is a new $\Upsilon(4S)$ e^+e^- experiment, in which the electron and positron beams in the KEKB collider have different energies. I have corrected the measurements by both of these collaborations to use a common value of f_{00} (Equation 3.22). This adjustment increases the systematic errors of the other

$\Upsilon(4S)$ measurements, as all were presented with the assumption that $f_{00} \equiv 0.5$. As I describe above, the 1995 CLEO result is also corrected to use the same value of $\mathcal{B}(D^0 \to K^-\pi^+)$ as my analysis. The BELLE result already assumes this value, while the ARGUS analysis does not depend on the D^0 decay fractions as it uses a D^{*+} partial reconstruction technique.

ALEPH, DELPHI, and OPAL are all LEP experiments. Their measurements are based on data from e^+e^- collisions at the Z-boson pole, at a center-of-mass energy of 91.2 GeV. In such events, $\bar{B}^0$ mesons are produced in the decay of virtual Z bosons to pairs of b quarks. The measurements are therefore dependent on the $\bar{B}^0$ production rate in Z decays. This production rate is the product of two factors. The first, R_b, is the branching fraction of $Z \to b\bar{b}$ decays. I normalize all the LEP experiments to the 1998 PDG value [3]

$$R_b = (21.69 \pm 0.12) \times 10^{-2}. \tag{5.4}$$

The second factor in the $\bar{B}^0$ production rate is the probability that a b quark produced in Z decay will hadronize into a $\bar{B}^0$ meson. This probability is variously written f_{B^0}, f_{B_d}, or f_d. I normalize to the 1998 PDG value

$$f_d = (39.7^{+1.8}_{-2.2}) \times 10^{-2}. \tag{5.5}$$

I average the asymmetric errors to a 5.0% systematic uncertainty. Knowledge of f_d is improving rapidly; the current preliminary value according to the LEP B-oscillations working group [66] is $f_d = (40.0 \pm 1.0) \times 10^{-2}$. This result reduces the corresponding component of the $\mathcal{B}(\bar{B}^0 \to D^{*+}\ell^-\bar{\nu})$ systematic error from 5.0% to 2.6%. However, it should be noted that the determinations of f_d assume equal production rates for $\bar{B}^0$ and B^- mesons — equivalent to the assumption that $f_{00} = f_{+-}$ in $\Upsilon(4S)$ decay.

I do not correct the values for $\mathcal{B}(D \to K^-\pi^+)$ assumed in the LEP measurements. The LEP measurements all either reconstruct multiple D^0 decay modes, combine full and partial reconstruction results, or use partial reconstruction exclusively. As such, I cannot reweight only one component of a given measurement and accurately compute a corrected result. The corrections would all be less than 1%.

Historically, the $\Upsilon(4S)$ measurements of $\mathcal{B}(\bar{B}^0 \to D^{*+}\ell^-\bar{\nu})$ have been lower than those made at the Z pole. The ARGUS result and the 1995 CLEO measurement are both around 4.5%, whereas the LEP results are all over 5.0%. The Particle Data Group world average value [3] of $(4.60 \pm 0.27) \times 10^{-2}$ was dominated by ARGUS and CLEO results. That average does not include the last two LEP results in the table. However, my present result is higher than previous $\Upsilon(4S)$ values and is in line with the LEP measurements.

The LEP experiments have several advantages and disadvantages relative to CLEO. Like CLEO, they enjoy very large data samples, on the order of millions of $Z \to b\bar{b}$ events. The B mesons produced at LEP are boosted to high energies, so LEP analyses do not contend with curling slow pions. Furthermore, all leptons from $\bar{B}^0 \to D^{*+}\ell^-\bar{\nu}$ decays are hard and can therefore all be detected. The absence of lepton momentum cutoffs makes the form-factor dependences of the type I discuss in Section 4.7 relatively unimportant.

LEP measurements are subject to several systematic errors that do not arise in experiments at the $\Upsilon(4S)$. One reason is that that reconstruction techniques differ markedly from those used at CLEO. The LEP analyses typically rely heavily on vertexing to identify $D^{*+}\ell^-\bar{\nu}$ decays. In the reconstruction of parent particles they use requirements that tracks fit well to a common vertex instead of cuts on reconstructed mass variables such as $m(K\pi)$ or Δm. B mesons produced at LEP are highly boosted, so their decays can be clearly identified in vertex chambers. However, the LEP detectors do not measure the momenta of these boosted tracks nearly so well as does CLEO.

Other than reconstruction issues, the dominant source of systematic uncertainty in the LEP analyses is the $D^{*+}X\ell^-\bar{\nu}$ background. I use the angle $\cos\theta_{BY}$ to separate reconstructed $D^{*+}X\ell^-\bar{\nu}$ from $D^{*+}\ell^-\bar{\nu}$ events. This technique is fundamentally based on distinguishing the two modes based on the missing mass of the X system. This approach is not open to the LEP experiments, as they lack sufficient resolution to distinguish signal and background in this variable. Instead, they rely heavily on models of the $D^{*+}X\ell^-\bar{\nu}$ background, and suffer large associated systematic errors.

My present result is competitive statistically with the individual LEP measurements shown in Table 5.1. It also has a systematic error substantially smaller than any of these results. My measurement is therefore the most precise single determination of $\mathcal{B}(\bar{B}^0 \to D^{*+}\ell^-\bar{\nu})$ to date.

A higher value for the $\bar{B}^0 \to D^{*+}\ell^-\bar{\nu}$ branching fraction helps to resolve a historical discrepancy in the overall picture of B decays. Several measurements of the inclusive $\bar{B}^0 \to X\ell^-\bar{\nu}$ branching fraction have been made, most notably a

Table 5.2: Inclusive and exclusive measurements of semileptonic B-decay branching fractions. All values are 1998 Particle Data Group results, with the exception of a more recent CLEO result for $\mathcal{B}(\bar{B}^0 \to D^+\ell^-\bar{\nu})$. Note that the sum of exclusive modes is less than the inclusive rate.

Mode	$\mathcal{B}\,(\times 10^{-2})$
$\bar{B}^0 \to X\ell^-\bar{\nu}$ inclusive	10.50 ± 0.80
$\bar{B}^0 \to D^+\ell^-\bar{\nu}$	2.09 ± 0.22
$\bar{B}^0 \to D^{*+}\ell^-\bar{\nu}$	4.60 ± 0.27
$\bar{B}^0 \to D^{(*)}X\ell^-\bar{\nu}$	2.26 ± 0.44
$\bar{B}^0 \to X_u\,\ell^-\bar{\nu}$	0.15 ± 0.10
Sum of exclusive modes	9.10 ± 0.57

CLEO result [67] that dominates the PDG world average branching fraction [3] of $(10.5 \pm 0.8) \times 10^{-2}$. This inclusive rate must be the sum of the exclusive modes I list in Table 5.2. I give the 1998 PDG world average branching fraction value for each mode, with the exception of $\bar{B}^0 \to D^+\ell^-\bar{\nu}$, for which I give the the recent CLEO result [39]. The $\bar{B}^0 \to D^{(*)}X\ell^-\bar{\nu}$ branching fraction includes both nonresonant semileptonic $DX\ell^-\bar{\nu}$ and $D^*X\ell^-\bar{\nu}$ decays as well as $D^{**}\ell^-\bar{\nu}$; it is the ALEPH result [38] I refer to in Section 3.1.4. The last mode, $\bar{B}^0 \to X_u\,\ell^-\bar{\nu}$, is the sum of all semileptonic $\bar{B}^0$ decays that involve a $b \to c\,\ell^-\bar{\nu}$ transition. In Table 5.2, I also give the sum of the exclusive modes. The sum of these exclusive branching fractions adds up to less than the measured inclusive branching fraction. The deficit is $(1.40 \pm 0.98) \times 10^{-2}$, a discrepancy of 1.4 standard deviatons. However, if I replace the old world average value of $\mathcal{B}(\bar{B}^0 \to D^{*+}\ell^-\bar{\nu})$ with my present result, I obtain a revised exclusive sum of $(9.90 \pm 0.68) \times 10^{-2}$. This new total decreases the discrepancy between the inclusive branching fraction and the exclusive sum to

$(0.60 \pm 1.05) \times 10^{-2}$, well under a standard deviaton.

My analysis of the $\bar{B}^0 \to D^{*+}\ell^-\bar{\nu}$ branching fraction also provides the basis for a remeasurement of $|V_{cb}|$ currently in progress at CLEO. The preliminary result [68], based on the w distribution of the $\bar{B}^0 \to D^{*+}\ell^-\bar{\nu}$ decay mode, is $\mathcal{F}(1)|V_{cb}| = 0.0424 \pm 0.0018 \pm 0.0019$, where the two errors are statistical and systematic. The final measurement will incorporate data from both $\bar{B}^0 \to D^{*+}\ell^-\bar{\nu}$ and $B^- \to D^{*0}\ell^-\bar{\nu}$ decays, and should be the most precise single measurement of $|V_{cb}|$.

APPENDIX A

TRACKING EFFICIENCY STUDIES:

`PRELIB` SLOW PION RESULTS

This Appendix and the next describe a set of studies of the slow pion reconstruction efficiency at CLEO. Appendix B also details the application of the same techniques to hard tracks. This Appendix originally appeared in 1998 as a CLEO internal note, CBX 99-101. Appendix B recently appeared as CBX 2000-32. Both the slow pion and hard track reconstruction efficiency contribute significant systematic uncertainties to the measurement of $\bar{B}^0 \to D^{*+}\ell^-\bar{\nu}$. As understanding of these efficiencies is both critical and integral to my analysis, I reproduce the contents of these two CBX notes here.

In this Appendix, I describe the results of several studies of the CLEO slow charged pion reconstruction efficiency in the 4sC dataset done with the `PRELIB` code library. I examine the influence of event environment on this efficiency by embedding Monte Carlo tracks into both data and Monte Carlo events. In addition, I quantify the sensitivity of the Monte Carlo single-track efficiency to details of the simulation.

A.1 Introduction

The efficiency with which slow charged pions are reconstructed at CLEO plays an important role in many physics analyses. This efficiency depends strongly not only on the signals a slow pion leaves as evidence that it has passed through our detector, but also on the effects of the other particles in the event. A nearby or overlapping track can distort or eliminate hit information and confuse pattern recognition algorithms, greatly reducing the chance that the CLEO software will correctly reconstruct the soft track from already limited information. The principal goal of this work is to examine the effects this "event environment" has on the reconstruction of slow charged pions, and to quantify the uncertainty in efficiency produced by our imperfect understanding of these effects.

My basic technique is to embed single Monte Carlo slow pion tracks into sets of data and Monte Carlo "bed" events. I then measure the frequency with which I can successfully reconstruct the embedded track. By comparing the efficiencies with which I find the tracks embedded in data and Monte Carlo, I measure the difference in event environment effects between the two.

The focus of these studies is on the discrepancy in efficiency between data and Monte Carlo, rather than on the absolute magnitude of the efficiency. Any absolute track finding efficiency will be highly sensitive to the cuts made on the track. This study is limited to comparisons of the measured momentum and direction of the embedded track to those with which it was generated. In a real analysis, the cuts that shape slow pion efficiency are made on variables such as the D^{*+}–D^0 mass difference. These variables are not available in this single-track embedding study.

(It is possible to get around the limitations on the types of cuts available in a embedding study. One can generate full $\bar{B}^0 \to D^{*+}\ell^-\bar{\nu}$ decays at QQ level, thus producing slow pions according to the spectrum of this decay mode. The generator level properties of all particles in the event can then be recorded. A variant `decay.dec` can be used to force every particle except the slow pion to decay to a neutrino, thus leaving no track in the detector. One can then study the efficiency effects of a variety of cuts by combining the reconstructed slow pion parameters with the generated properties of the other particles in the event. Karl Ecklund has used this technique in his studies of the neutral slow pion efficiency.)

This Appendix reports on the results I obtained in 1998 based on `PRELIB` data and Monte Carlo. I used only 4sC data and Monte Carlo in my studies. I plan to shift the focus of these studies to the recompress data and Monte Carlo. My recompress studies will encompass all CLEO II datasets. In an effort to make the results of these studies useful for CLEO collaborators engaged in `PRELIB` analyses, I also give estimates of the systematic uncertainties that exist in the single-track slow pion efficiency.

My slow pion embedding studies are based on the techniques Ken Bloom used to study the track finding efficiency at higher momenta [69].

A.2 Embedding Technique

A.2.1 Selection of Bed Events

The first requirement of an embedding study is a set of bed events. My study uses two sets of bed events, a set of 5000 data events and a set of 5000 Monte Carlo events. These bed events are also used in Karl Ecklund's study of the neutral slow pion efficiency.

We selected 5000 bed events from on-resonance data in the 4sC dataset using the following five cuts:

- $N_{\text{tracks}} > 4$
- $R_2 \leq 0.3$
- Well-identified lepton:
  - `dpthmu` > 5 *or* `r2elec` > 3
  - `muqual` $= 0$
- $0.8 \leq p_\ell \leq 2.4\,\text{GeV}$
- $|\cos\theta_\ell| < 0.71$

We calculated both R_2 and the number of tracks using only tracks having `kincd` values greater than or equal to 0 or equal to or -2 that were approved by the `TRKMNG` processor (Trackman Next Generation). We required the same properties of the lepton track.

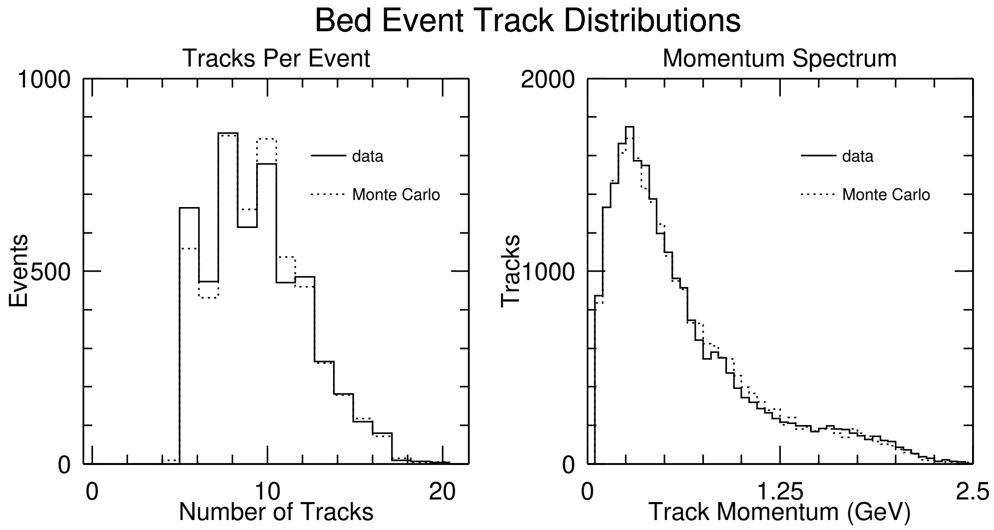

Figure A.1: Track distributions in the data and Monte Carlo bed events. The solid lines represent the data distributions, and the dashed the Monte Carlo. The first plot shows the distribution of the number of tracks per event passing the cuts given in the text. The second is the momentum distribution of these tracks.

We constructed a similar set of bed events for Monte Carlo using a combination of generic $B\bar{B}$ and continuum ($q\bar{q}$) Monte Carlo events. We applied the same cuts to these events as we did when choosing our data bed events. Our final sample of 5000 Monte Carlo events contains 4247 $B\bar{B}$ events and 753 $q\bar{q}$ events. This ratio reflects both the relative cross-sections for $B\bar{B}$ and continuum events at the $\Upsilon(4S)$ resonance and the differing rates at which such events pass the above cuts.

Figure A.1 compares the number of tracks per event and the momentum distribution of tracks in the data and Monte Carlo bed events.

A.2.2 Embedding Details

I generated 50,000 single-track Monte Carlo slow pion events at each of the following six momenta: 60, 80, 100, 150, 200, and 250 MeV. I generated these slow pions isotropically in sets of 5000, and I created equal numbers of positively and negatively charged pions. I simulated the detector response to these pions using the standard `PRELIB CLEOG` detector simulation.

Embedding a single track into an event requires a method for combining the detector information from two CLEO events. This task is problematic for CLEO software, as `CLEVER` jobs are able to deal with only one `.fzx` file at a time. The solution to this problem is to make use of the `STRP` and `MERG` processors. These processors were developed for the purposes of merging detector noise, taken from random trigger runs, into Monte Carlo events.

Accordingly, the hit information from each file of 5000 single tracks was extracted from the `CLEOG` output `.fzx` file by the `STRP` processor. This hit information was next merged into my sets of data and Monte Carlo bed events. Reconstruction of the embedded tracks was done with the archived 4sC `PASS2` executable of the sets of merged events.

A.2.3 Calculation of Efficiencies

The basic premise of my efficiency calculation is to count the number of events in which an embedded track is found, and then to divide by the number of events into which I embedded a track. In order to do so, I need a cut that defines a "found"

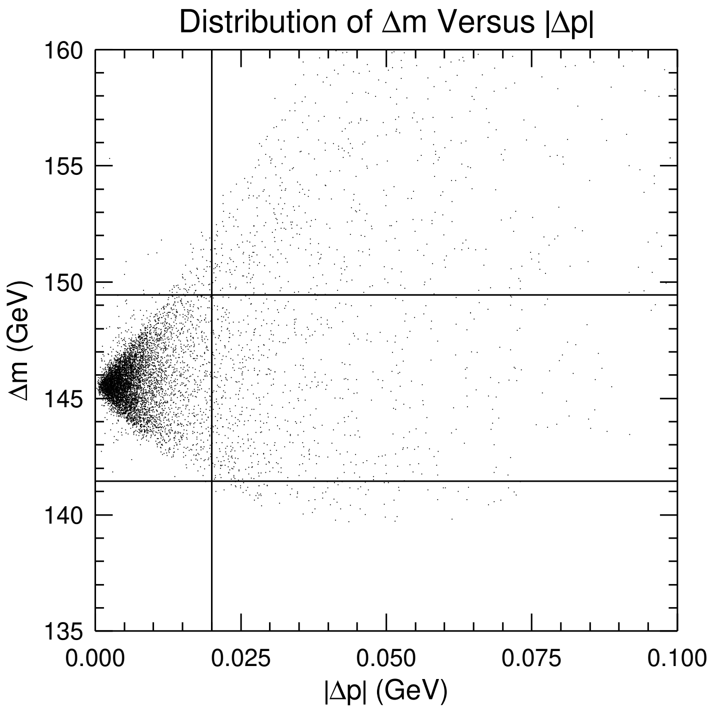

Figure A.2: The distribution of Δm versus $|\vec{\Delta p}|$ for D^{*+} decay. This plot shows the correlation between Δm, the D^{*+}–D^0 mass difference, and $|\vec{\Delta p}|$, the vector difference in three-momentum between the generated and reconstructed slow pion. The horizontal lines show typical Δm cuts for D^{*+} reconstruction, while the vertical line illustrates the fiducial given in Equation A.1. The points are from tagged D^{*+} decays in $\bar{B}^0 \to D^{*+}\ell^-\bar{\nu}$ signal Monte Carlo.

soft track. The standard fiducial cut used in this analysis is:

$$|\vec{\Delta p}| < 0.02\,\mathrm{GeV}. \tag{A.1}$$

Here $\vec{\Delta p}$ is the vector difference in three-momentum between the generator-level parameters of the embedded pion and the reconstructed soft track. (Figure A.2 gives a sense of how this cut compares to a Δm cut used in D^{*+} reconstruction.) In addition, I always require that the reconstructed track have the same sign as the generated pion. These two cuts are the only ones of any kind made on the soft tracks. In particular, no cuts were made on the `kincd` value of a track, nor was `TRKMNG` approval required for the reconstructed tracks. The `TRKMNG` processor will occasionally approve the back half of a curler, thus discarding the outgoing track even if it would otherwise pass my cut.

For every slow pion I embed, I search for tracks passing the fiducial cut in three classes of events. I first look in the single-track Monte Carlo event to see if the slow pion can be successfully reconstructed before the addition of event environment effects. I next look in the "embedded' event, the result of embedding my track into the bed event. Finally, I look at the bed event without the embedded track, in order to determine if background tracks are present. This procedure checks whether the slow pion can be reconstructed in the presence of event environment effects.

For each event in each of these three classes, I count the number of tracks that pass my fiducial cut. I record three numbers: n_{st}, the number of tracks passing the cut in the single-track event; n_{embed}, the "found" track count of the embedded event; and n_{bed}, the number of background tracks that pass the cut in the bed event. The range of each of these three numbers extends above one. As I do not use `TRKMNG` to veto either multiple passes of curlers or "ghost pairs," it is possible for a single slow pion to produce two tracks that will pass my cuts.

To calculate efficiencies, I count the number of events in which a slow pion is found, and divide by the number of slow pions I generated. I represent the total number of slow pions generated at a given momentum by N_{tot}. I next define two conditions:

$$n_{\mathrm{st}} \geq 1 \tag{A.2}$$

$$n_{\mathrm{embed}} - n_{\mathrm{bed}} \geq 1 \tag{A.3}$$

The number of single-track events that satisfy Equation A.2 is N_{st}, the number of events in which I find at least one track that passes my fiducial cuts. Finally, N_{embed} is the number of events that satisfy Equation A.3. This quantity is the number of events in which I find tracks that pass my cuts but were not present in the background bed event.

With these numbers I define three efficiencies. The single-track efficiency ϵ_{st} is:

$$\epsilon_{\mathrm{st}} = \frac{N_{\mathrm{st}}}{N_{\mathrm{tot}}}. \tag{A.4}$$

When I embed single tracks into Monte Carlo, I define a Monte Carlo embedding efficiency ϵ_{MC}:

$$\epsilon_{\mathrm{MC}} = \frac{N_{\mathrm{embed}}}{N_{\mathrm{tot}}}. \tag{A.5}$$

The efficiency after embedding into data events, ϵ_{data}, is defined likewise.

A.3 Features of the Single-Track Efficiency

An examination of the angular structure of the single-track efficiency at several slow pion momenta illustrates several factors that influence the overall shape of the slow pion efficiency versus momentum. I show the total slow track efficiency at each of the six momenta I have examined in Figure A.3. The efficiencies in this

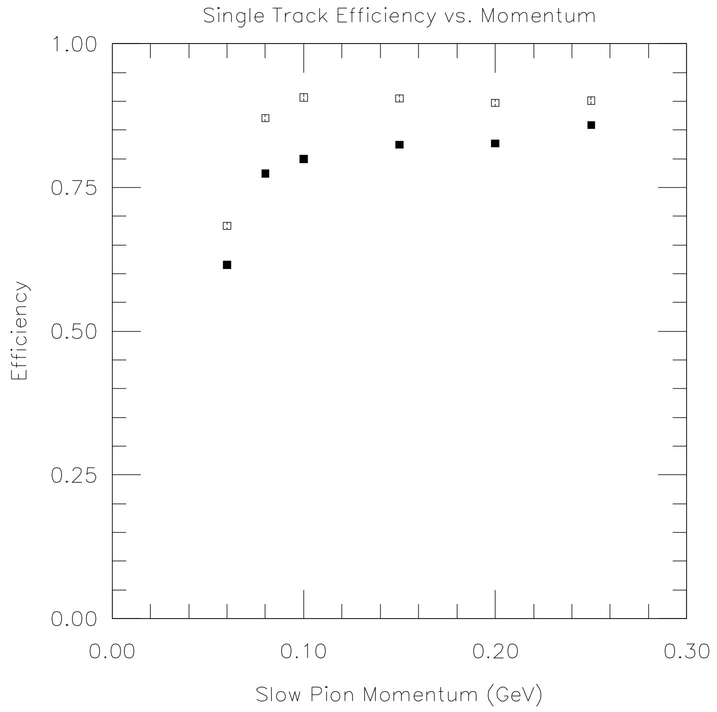

Figure A.3: The slow pion single-track efficiency as a function of momentum. The open (upper) points plot the efficiency with the cut of Equation A.6, which is sensitive only to the transverse parameters of the track. The filled (lower) points give the efficiency with the additional constraint of Equation A.7 on the quality of the z reconstruction. These efficiencies are integrated over all generated slow pion directions. The statistical error bars are smaller than the plot symbols.

plot are integrated over all slow pion directions. In Figure A.4, I plot the angular structure of the slow pion efficiency at each momentum.

To illustrate the effects that poor z information has on track finding, I generated these plots with fiducial cuts that differ from my standard track finding cut (Equation A.1). In both Figures A.3 and A.4, the upper open boxes show the

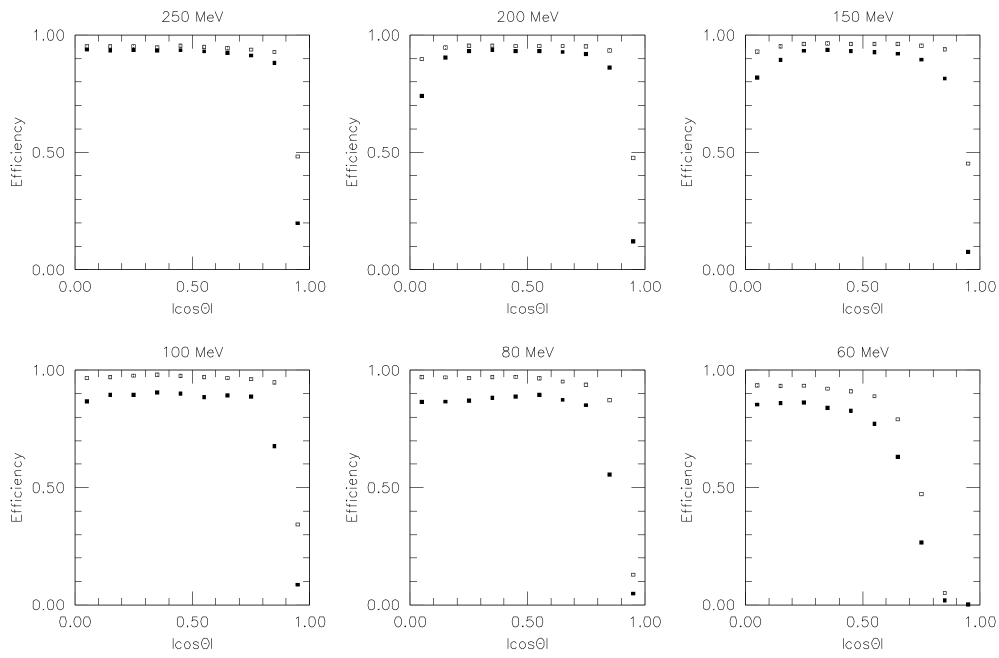

Figure A.4: The slow pion single-track efficiency as a function of the direction of the generated pion, for six pion momentum values. The open (upper) points show the efficiency with the cut of Equation A.6 on the transverse track reconstruction. The filled (lower) points depict the efficiency with the cuts of both Equations A.6 and A.7. The requirement of good z reconstruction produces the differences between the two sets of points.

efficiency calculated with the fiducial cut:

$$|\Delta\vec{p}_{\mathrm{T}}| < 0.02\,\mathrm{GeV}. \tag{A.6}$$

$\Delta\vec{p}_{\mathrm{T}}$ is the vector difference between the transverse momentum of the generated slow pion and the reconstructed soft track. This cut places no constraints on the quality of the z information associated with the track. The lower filled boxes plot the efficiency after an additional cut is applied:

$$|\Delta p_z| < 0.02\,\mathrm{GeV}. \tag{A.7}$$

This cut on the z component of momentum requires that tracks additionally have good z measurements to be deemed "found." Note that the combination of these two cuts (Equations A.5 and A.6) is slightly looser than the cut of Equation A.1.

For both sets of points, the slow pion efficiency falls off precipitously for large values of $|\cos\theta|$. This feature is due simply to the fact that CLEO cannot reconstruct tracks that head down the beam pipe. The angular reach of the CLEO detector for soft tracks falls off as we decrease the track momentum. This is the dominant cause of the drop in slow pion efficiency as we decrease the pion momentum.

These plots illustrate an interesting effect that curlers have on the slow pion efficiency. Slow pions produced at the interaction point will curl in the CLEO detector only in a fairly limited momentum range. Slow pions with a transverse momenta above 200 MeV will exit the outer wall of the drift chamber and stop in material farther from the interaction point. Below 100 MeV soft pions lose energy very quickly before they can execute a full circle through the detector. Curlers are therefore most important in the transverse momentum range of 100–200 MeV. Of course, understanding the slow pion efficiency is most important in exactly this range. Below 100 MeV, CLEO rapidly loses the ability to detect slow pions; the slow pion spectrum from $\bar{B}^0 \to D^{*+}\ell^-\bar{\nu}$, for example, does not extend far above 200 MeV.

From Figure A.4, we see that curlers affect the slow pion efficiency most dramatically for small values of $|\cos\theta|$. The comparison of the efficiencies with and without constraints on the z measurement reveals that the primary culprit in this efficiency loss is poor z information. I conclude that while the partial overlap of r–ϕ information in the tracking chambers does reduce the efficiency for slow pion reconstruction, a far more substantial loss in efficiency is due to the overlap or confusion of z information from multiple passes of the curling pion. For curling tracks with significant z momentum, this overlap in cathode hits disappears, and the efficiency jumps. Thus, the efficiency for r–ϕ reconstruction of slow pions is roughly flat down to 100 MeV in Figure A.3, but falls off for three-dimensional reconstruction. In particular, the efficiency steps down between 250 and 200 MeV, due to the introduction of curling tracks with little z momentum.

Finally, these plots show the substantial role that the limited availability of z information plays on the slow pion efficiency at 100 MeV and below. In this momentum range, the constraint on z reconstruction reduces the efficiency by 10% or more over the full angular range. Low momentum tracks are generally plagued by a lack of z information. At best, they can accumulate hits in three cathode layers: the VD inner and outer cathodes, and the DR inner cathodes. 60 MeV pions frequently pass through only one of these layers, the VD inner cathode. For such tracks, we are forced to fall back on VD charge division, a less effective tool, and our slow track efficiency suffers.

A.4 Results of the Embedding Study

I plot the efficiency to reconstruct tracks in data and Monte Carlo versus momentum in Figure A.5. For reference, I also show the single-track efficiency. All three

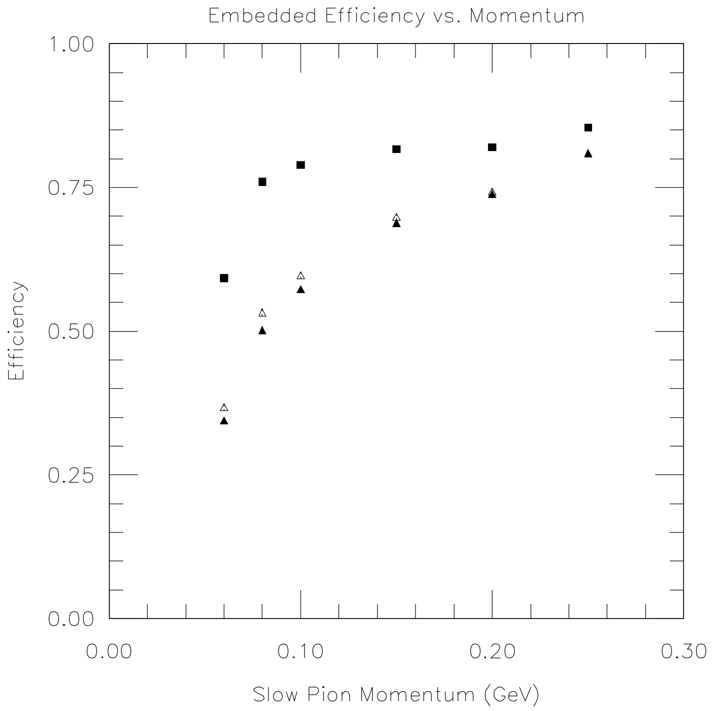

Figure A.5: The embedded slow pion efficiency as a function of momentum. The open triangles show the efficiency for reconstructing pions embedded in data, while the filled triangles represent the efficiency for pions embedded in Monte Carlo. For reference, the filled squares show the single-track efficiency. All three sets of points were calculated with the cut of Equation A.1, and represent the efficiency integrated over all embedded pion directions.

sets of points were calculated with fiducial cut of Equation A.1. The numerical efficiencies are listed in Table A.1. The efficiency to reconstruct tracks embedded in Monte Carlo is systematically lower than in data. This effect is strongest for slow pion momenta of 100 MeV and below. This difference in efficiency must be due to a difference in event environment between data and Monte Carlo. The exact nature of this difference is unknown. Table A.1 gives the magnitude of this

Table A.1: The embedded slow pion efficiencies in data and Monte Carlo. The fourth column give the absolute efficiency difference between the two, while the last column gives the difference as a fraction of the Monte Carlo efficiency.

p_π (MeV)	$\epsilon_{\rm MC}$	$\epsilon_{\rm data}$	$\Delta\epsilon$ absolute	$\Delta\epsilon$ rel. (%)
60	0.3701 ± 0.0022	0.3930 ± 0.0022	0.0229 ± 0.0031	6.19 ± 0.86
80	0.5363 ± 0.0022	0.5668 ± 0.0022	0.0305 ± 0.0032	5.69 ± 0.61
100	0.6063 ± 0.0022	0.6321 ± 0.0022	0.0258 ± 0.0031	4.26 ± 0.52
150	0.7105 ± 0.0020	0.7207 ± 0.0020	0.0102 ± 0.0029	1.44 ± 0.41
200	0.7568 ± 0.0019	0.7614 ± 0.0019	0.0045 ± 0.0027	0.60 ± 0.36
250	0.8183 ± 0.0017	0.8191 ± 0.0017	0.0009 ± 0.0025	0.11 ± 0.30

shift, both in absolute efficiency terms and relative to the reconstruction efficiency of single tracks embedded in data.

A.5 Problems with `CLEOG` in `PRELIB`

Detailed examination of the hits produced by `CLEOG` with the CleoXD event display tool revealed two unexpected irregularities. Further investigation has indicated that these problems are common to all `PRELIB` Monte Carlo.

With the exception of TDC values in the VD, ADC and TDC values produced by the CLEO detector are 12-bit integers, falling in the range of 0–4095 counts. In the case of the VD TDC values, a “stale data bit” can be set, indicating that a hit dates from a previous beam crossing. The exact bit set has varied during the history of CLEO; the 15th bit is now used for this purpose.

In `PRELIB` Monte Carlo `.fzx` files, however, it is possible to observe both negative ADC values, and TDC values far in excess of 4095 counts. The high TDC values can be seen in all three tracking devices, the PT, VD, and DR.

These anomalous ADC and TDC values do not appear to have dramatic effects on the quality of our Monte Carlo as it affects most CLEO analyses. Hits with these anomalous values are handled in a reasonable manner by `PASS2`. However, the high TDC values are symptomatic of a general mishandling by `PRELIB CLEOG` of daughter particles produced significantly later than the beam crossing time.

With substantial assistance from Craig Prescott, I have created a modified version of `PRELIB CLEOG` in which late daughters are handled correctly, and all anomalous ADC and TDC values have been eliminated. The effects of these changes on slow pion efficiency are addressed as a systematic error in Section A.6. The net effect is a 3.5% drop in slow pion efficiency at 60 MeV, with no appreciable change at higher momenta.

I embedded 60 MeV tracks created with this modified `CLEOG` into both data and Monte Carlo. I found a 6.2% difference in the embedded efficiencies, consistent with the value given in Table A.1. Hits with anomalous ADC and TDC values are altered or deleted by the embedding process, but the end results is that the same hits are embedded into data and Monte Carlo. My embedding studies are therefore valid despite these small problems with the `PRELIB CLEOG` output.

The following two sections discuss the problems with `PRELIB CLEOG` in some detail. Readers not interested in these details may omit these sections, but are nonetheless encouraged to appreciate Figure A.6.

A.5.1 Negative ADC Values

Aesthetic objections aside, negative ADC values do not appear to cause any problems in `PRELIB` Monte Carlo. No lower limits are ever placed on ADC values in track reconstruction, as doing so would exclude those wires that collected the most charge.

In the CLEO tracking chambers, the ADC value of a channel measures the amount of charge deposited on that channel. When no charge is deposited, the ADC value will be equal to a pedestal value, typically around 3800 ADC counts. The deposition of charge on a wire causes the ADC value to drop below pedestal. In the `CLEOG` detector simulation, the relationship between the amount of charge deposited and the drop in the ADC value from pedestal is assumed to be linear. In data, the ADC value cannot drop below zero counts, regardless of how much charge is deposited in a cell. In `PRELIB` Monte Carlo, however, large amounts of charge in cell give rise to negative ADC values.

Negative ADC values are a problem when single-track events are stripped and then merged into data or Monte Carlo. Those hits having negative ADC values are deleted during this process. This deletion is unsurprising when one considers that the `STRP` and `MERG` processors were developed to merge random trigger data into Monte Carlo. Real data hits never have negative ADC values, making the deletion of a presumably suspect hit having such a value quite reasonable.

In my modified version of `CLEOG`, negative ADC are reset to 0. This change has also been implemented for all recompress Monte Carlo.

A.5.2 Large TDC Values

The large TDC values observed in PRELIB Monte Carlo are associated with daughter particles produced well after the beam crossing time. For most CLEO analyses, these late hits only pose a problem when they overlap with hits from other tracks. In that case, they contribute additional charge to the original hit, and can thereby distort the charge information used in both the cathodes and in VD charge division.

The TDC value of a CLEO hit establishes the time at which a signal was recorded on a sense wire. This time is used to determine how closely a track passed to the wire. The relationship between TDC values and time is determined through channel-by-channel calibration of all tracking devices. The time-to-TDC relationship is roughly linear in the physical region, but is modeled by a polynomial for higher accuracy.

The presence of a signal on a wire in one of the tracking chambers triggers the rampdown of a capacitor in the electronics for that channel. If the CLEO trigger requirements are met, the rampdown is halted at the time of the "L0 gate." This gate occurs at a set delay after the beam crossing. The TDC value is simply a digitization of this frozen voltage. Those TDC values passing "crate cuts" are then read out by the electronics. The crate cuts eliminate TDC values near pedestal, which indicate that no signal was recoded on the wire, and TDC values near zero, which are characteristic of noise.

Under this scheme, the detector is never sensitive to signals that arrive after the L0 gate. Any signal occurring at or after the L0 gate will leave the capacitor fully charged, and consequently the TDC value will remain at pedestal. However, `PRELIB` Monte Carlo is entirely ignorant of the L0 gate, and will create wire hits with times greater than the L0-gate time. Consequently, the `CLEOG` detector simulation will produce hits with TDC values greater than pedestal. These TDC values are generated by feeding times after the L0 gate into the time-to-TDC relationship calibrated for TDC values below pedestal.

Slow pion tracks provide the most spectacular illustration of this effect. An example of the interaction of a 60 MeV pion with the CLEO detector is shown in Figure A.6. A typical 60 MeV pion will lose energy very quickly in the CLEO detector, and will generally come to rest in either the structure of the PT or VD or the surrounding material. The pion will then typically decay at rest to a muon. This muon, having only 30 MeV of momentum, travels very little distance before it again stops in the detector material. The muon subsequently decays to an electron.

The granddaughter electron, which can have a momentum as high as 50 MeV, often spirals around many times in the 1.5 Tesla magnetic field, gradually losing energy. As this electron is not produced until the decay of its parent muon, characterized by the 2.2 μs muon lifetime, the CLEO detector will not record any evidence of this daughter electron in the event producing the grandparent pion. (The daughter electrons can, however, contribute a background for subsequent CLEO events.) The `PRELIB CLEOG` detector simulation, on the other hand, records hits produced by these daughter electrons, assigning them spectacularly large TDC values, ranging as high as 24,000 TDC counts.

In the normal analysis of CLEO data, these late hits are vetoed through the application of crate cuts to the `CLEOG` output. These cuts are applied by the `MERG`

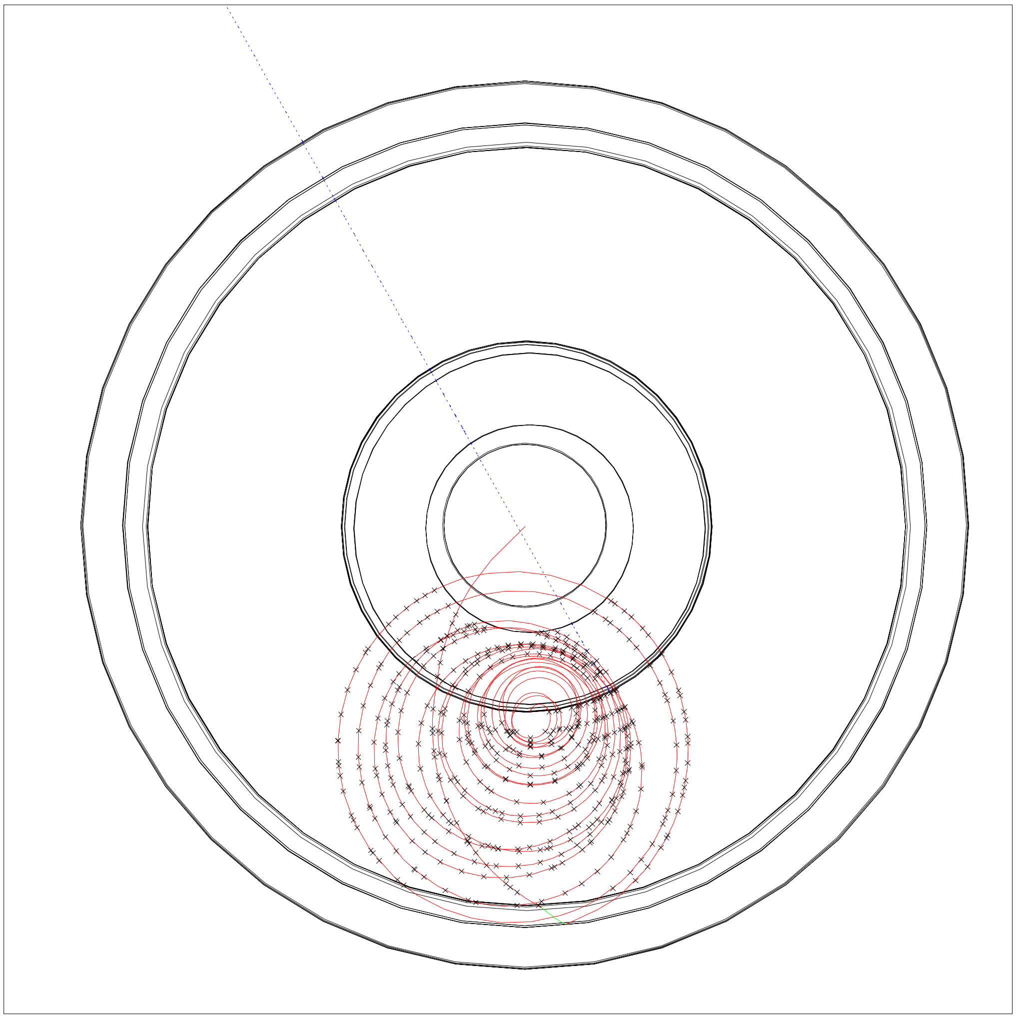

Figure A.6: CLEOG display of a 60 MeV pion. The pion stops in the VD outer wall, then decays at rest to a muon. The muon travels only a short distance to the VD support pipe before stopping. The muon at rest eventually decays to an electron, which spirals around many times, slowing loosing energy. Crosses along the track mark the points of closest approach to tracking chamber wires. These positions are used in the generation of Monte Carlo hits. The straight dotted line is a photon radiated by the spiraling electron.

processor in the course of merging random noise into Monte Carlo events. For this reason, it is important that `PRELIB` random noise always be merged into Monte Carlo events before they are analyzed.

Hits with high TDC values get treated in a curious way by the combination of the `STRP` processor and the `MERG` random noise input line. In the VD anodes, high TDC hits are simply assumed to have the stale data bit set, and are therefore ignored. Outside of the VD anodes, the high TDC value is converted to a 12-bit integer by truncating the higher bits. The resulting integer is then subjected to the crate cuts. As a result, the hits are sometimes deleted, and otherwise assigned TDC values in the physical range; they are therefore fully capable of distorting pattern recognition. Nonetheless, these problems do not invalidate my embedding studies, as the same set of hits are embedded into data and Monte Carlo events.

The real problem associated with high TDC values is not the values themselves, but the underlying problem with `CLEOG` that they illustrate. In the detector simulation, when a daughter electron produces a hit on a wire that has already recorded a signal from an earlier particle, the charge deposited by that electron is added to that deposited by the earlier particle. In the actual CLEO detector, no such effect occurs. Like the TDC value, the ADC value is associated with a frozen voltage. This voltage is unaffected by the late passage of the daughter electron, hence the electron contributes nothing to the ADC value.

Low momentum tracks in CLEO suffer from a paucity of reliable z information. They do not reach the stereo wires in the DR, and often reach only one or two of the four cathode layers. An essential tool for measuring the z momentum of these low momentum tracks is charge division in the VD. The VD records ADC values on both ends of every sense wire. By comparing the charge that reaches each end of the VD, it is possible to estimate where the track passed along the VD axis. However, when the hits from a low momentum pion track are incorrectly overlaid by the hits from a delayed daughter electron, the charge information from the pion track is lost.

A similar effect can occur in both the VD and DR cathodes. If a daughter electron deposits charge on a cathode pad which has already recorded a hit from the parent track, the shapes of the cathode charge distribution across multiple pads can be distorted. This distortion reduces the quality of z information available from the cathode hits.

The treatment of daughter electrons produced nanoseconds after the beam crossing will also contribute an event environment difference between data and Monte Carlo for low momentum tracks.

A.6 Effects of Monte Carlo Uncertainties and Errors on the Single-Track Efficiency

In my embedding studies, I insert Monte Carlo tracks into both data and Monte Carlo events. These studies address the effects that the two event environments have on the reconstruction efficiency. Embedding studies do not address how well the Monte Carlo models the detector response to single tracks. In order for my embedding results to be of use to CLEO `PRELIB` analyses, I supplement them in this section with a study of how uncertainties in the CLEOG detector simulation lead to uncertainties in the single-track reconstruction efficiency.

I examine the systematic uncertainty in single-track slow pion efficiency due to six different sources: uncertainty in hit efficiency, drift distance smearing, the amount of material in the detector, charge division smearing, the generation of Monte Carlo at a magnetic field different from the actual CLEO field, and the mishandling of late hits in PRELIB CLEOG. The last two are small, correctable errors which will be eliminated in recompress Monte Carlo. The six effects are common to all PRELIB Monte Carlo.

I study the influences of these six effects with a series of "knob-turning" studies. I run sets of 50,000 slow pions through modified versions of CLEOG, and comparing the results to the standard PRELIB CLEOG. Each effect is examined in a separate study. In all cases, the cut of Equation A.1 was used to calculate efficiencies.

A.6.1 Monte Carlo Uncertainties

Four important Monte Carlo uncertainties have potentially significant impacts on the reconstruction efficiency for soft tracks. The first is the individual hit efficiency, the probability that a track will produce a hit when passing through a cell in our tracking chamber. This hit efficiency is tuned in the Monte Carlo to make the simulation resemble the data. Second is the smearing of drift distances, that is, the distance that ions drift between a track and the nearest sense wire in the tracking chamber. Finally, the third effect is the amount of material in the detector. The CLEOG detector simulation uses a model of the detector and descriptions of the

Table A.2: The effect of hit efficiency on slow pion efficiency. For each momentum, the second column gives the reconstruction efficiency with the standard PRELIB CLEOG Monte Carlo, and the third column the reconstruction efficiency obtained with a variant Monte Carlo in which the hit efficiency has been reduced by 5%. The last column expresses the variation as a fraction of the efficiency with the standard Monte Carlo.

p_π (MeV)	$\epsilon_{\rm ref}$	$\epsilon_{\rm hiteff}$	variation (%)
60	0.5923 ± 0.0022	0.5849 ± 0.0022	1.26 ± 0.53
80	0.7601 ± 0.0019	0.7500 ± 0.0020	1.33 ± 0.36
100	0.7893 ± 0.0018	0.7771 ± 0.0019	1.55 ± 0.33
150	0.8165 ± 0.0017	0.8048 ± 0.0018	1.43 ± 0.30
200	0.8200 ± 0.0017	0.8108 ± 0.0018	1.13 ± 0.30
250	0.8544 ± 0.0016	0.8522 ± 0.0016	0.25 ± 0.26

relevant properties of the detector materials, but this description is unavoidably imperfect.

In the first study, I decrease the hit efficiency by 5%. In the second, I increase the width of the Gaussian used to smear the drift distances by 15%. These variations are the same as those used in Ken Bloom's study of single-track systematics for higher momentum tracks [69]. They are twice as large as the systematic uncertainty in the Monte Carlo parameters [69, 70]. The results of these studies are given in Tables A.2 and A.3. The variations in reconstruction efficiency are expressed as a fraction of the efficiency found for the standard PRELIB CLEOG. The statistical uncertainty in the measurement is also listed.

The 5% decrease in hit efficiency produces only small changes in track reconstruction efficiency over the entire slow pion momentum region. The maximum change of 1.6% occurs at 100 MeV. The variation in drift distance smearing pro-

Table A.3: The effect of drift distance smearing on slow pion efficiency. As in Table A.2, the second column gives the efficiency with the standard Monte Carlo. The third column gives the efficiency obtained after increasing the drift distance smearing by 15%. The fractional variation between the two is given in the third column.

p_π (MeV)	$\epsilon_{\rm ref}$	$\epsilon_{\rm smear}$	variation (%)
60	0.5923 ± 0.0022	0.5864 ± 0.0022	1.00 ± 0.53
80	0.7601 ± 0.0019	0.7582 ± 0.0019	0.24 ± 0.36
100	0.7893 ± 0.0018	0.7698 ± 0.0019	2.47 ± 0.33
150	0.8165 ± 0.0017	0.7867 ± 0.0018	3.65 ± 0.31
200	0.8200 ± 0.0017	0.7942 ± 0.0018	3.15 ± 0.30
250	0.8544 ± 0.0016	0.8426 ± 0.0016	1.38 ± 0.27

duces a larger effect at 100 MeV and above, which reaches 3.7% at 150 MeV, but the effect falls below 1% for slow pion momentum values below 100 MeV. Drift distance smearing is an important systematic uncertainty above 100 MeV, but it has much less effect on the efficiency below 100 MeV, where multiple scattering and other effects dominate the efficiency.

In the third study, I first increase and then decrease the density of all materials in the central detector by 10%, the level to which the amount of material in the inner detector is known [71]. The results are listed in Table A.4. For all six momenta an increase in the amount of material produces a larger shift than a decrease. The systematic errors listed were derived from the effect of adding detector material in `CLEOG`. For pions with 80 MeV or more of momentum, this 10% variation produces only small changes in the efficiency, less than 1%. However, at 60 MeV, the same variation in material is extremely important, as it produces changes as large as 9%

Table A.4: The effect of detector material on slow pion efficiency. The second column is the same reference efficiency as in Tables A.2 and A.3. The third and fourth columns list the efficiencies which result from increasing and decreasing the material in the central detector by 10%. The fractional variation in the last column corresponds to that produced by increasing the amount of material.

p_π (MeV)	$\epsilon_{\rm ref}$	$\epsilon_{+10\%}$	$\epsilon_{-10\%}$	variation (%)
60	0.5923 ± 0.0022	0.5391 ± 0.0022	0.6301 ± 0.0022	8.98 ± 0.51
80	0.7601 ± 0.0019	0.7550 ± 0.0019	0.7617 ± 0.0019	0.67 ± 0.36
100	0.7893 ± 0.0018	0.7843 ± 0.0019	0.7905 ± 0.0018	0.63 ± 0.33
150	0.8165 ± 0.0017	0.8100 ± 0.0018	0.8138 ± 0.0018	0.79 ± 0.30
200	0.8200 ± 0.0017	0.8173 ± 0.0017	0.8207 ± 0.0017	0.33 ± 0.30
250	0.8544 ± 0.0016	0.8487 ± 0.0016	0.8588 ± 0.0016	0.66 ± 0.27

in the reconstruction efficiency. As discussed in Section A.5, at such low momenta nearly all pions stop in the inner detector material.

In the CLEO II detector, signals was read out from both ends of the VD. A larger signal is typically recorded on the end of the wire closer to the physical hit. The z position of a hit can frequently be measured with a resolution of approximately three centimeters through a comparison of the signals from the two ends of a wire. This "charge division" information is used in CLEO as a last resort, when a track lacks sufficient z information from either stereo wires or cathodes. Overall, charge division is rarely used in the reconstruction of CLEO tracks, but it is used frequently at the lowest track momenta. Charge division information is used in the reconstruction of over 80% of 60 MeV tracks.

The smearing of charge division information was hardwired in `PRELIB CLEOG`.

Table A.5: The effect of charge division smearing on slow pion efficiency. As in Table A.2, the second column gives the efficiency with the standard Monte Carlo. The third column gives the efficiency obtained after tuning the charge division smearing to better match the data. The fractional variation between the two is given in the third column.

p_π (MeV)	ϵ_{ref}	ϵ_{qdiv}	variation (%)
60	0.5923 ± 0.0022	0.5872 ± 0.0022	0.86 ± 0.53
80	0.7601 ± 0.0019	0.7412 ± 0.0020	2.48 ± 0.36
100	0.7893 ± 0.0018	0.7797 ± 0.0019	1.22 ± 0.33
150	0.8165 ± 0.0017	0.8128 ± 0.0018	0.45 ± 0.30
200	0.8200 ± 0.0017	0.8210 ± 0.0017	0.11 ± 0.30
250	0.8544 ± 0.0016	0.8547 ± 0.0016	0.04 ± 0.26

I compared the distributions of charge division residuals between data and Monte Carlo in the 4sC dataset. I found that these distributions were narrower in Monte Carlo than in data by roughly a factor of two. The `PRELIB` Monte Carlo therefore underestimates the smearing of charge division residuals.

To establish a systematic uncertainty associated with this effect, I tuned the charge division smearing in Monte Carlo so that it better simulated the data. (I undertook this project as part of the recompress Monte Carlo turning effort, so it was actually performed with the recompress `CLEOG`, rather than the `PRELIB` version.) I then created a variant `PRELIB CLEOG` using the my tuned charge division constants. This knob-turning study uses the difference between the hardwired and tuned charge division constants to estimate the systematic uncertainty produced in the slow pion reconstruction efficiency.

I show the results of this comparison in Table A.5. The greatest uncertainty is present at pion momenta of 80 and 100 MeV. At 80 MeV the variation is 2.5%. Above 100 MeV the variation falls below 0.5%.

A.6.2 Magnetic Field Effects

The magnitude of the CLEO magnetic field is slightly less than 1.5 Tesla. A magnetic field value of exactly 1.5 T has typically been used in the generation of `PRELIB` Monte Carlo. Thus, `CLEOG` generates a pattern of hits in the detector under the assumption that the magnetic field is exactly 1.5 T. The CLEO magnetic field is measured and its magnitude recorded in each data run; this value is typically 1.4861 T. A further consideration is that the central magnetic field is not necessarily equal to the field at the measurement point. An empirical "`BFUDGE`" correction factor equal to 1.0032 is therefore also included in the analysis of CLEO data.

In my embedding study, I have used slow pion tracks generated with a 1.5 T magnetic field. For consistency, I have reconstructed all tracks in both data and Monte Carlo under the assumption that the magnetic field is actually 1.5 T.

So long as I reconstruct tracks with the same momentum at which they were generated, this magnetic field shift between data and Monte Carlo produces no problems — to first order. However, if the slow pion efficiency is directly sensitive to the track curvature, a higher order effect may be important. A 100 MeV track seeing a magnetic field of 1.5 T will curve more strongly than one in a 1.4861 T field. While the difference is only a 1% effect, that 1% difference corresponds to a 1 MeV shift in momentum, and in the region below 100 MeV, the sharp dropoff in absolute efficiency is of the order of 1% per MeV. Under the hypothesis that this

Table A.6: The effect of magnetic field on slow pion efficiency. For each momentum in the first column, I give the slow pion efficiency obtained with Monte Carlo magnetic fields of 1.5 and 1.4861 Tesla. The final column gives the variation as a fraction of the 1.5 T result, as that value was used to generate `PRELIB` Monte Carlo.

p_π (MeV)	$\epsilon_{1.5}$	$\epsilon_{1.4861}$	variation (%)
60	0.5923 ± 0.0022	0.5901 ± 0.0022	0.38 ± 0.53
80	0.7601 ± 0.0019	0.7625 ± 0.0019	0.32 ± 0.36
100	0.7893 ± 0.0018	0.7871 ± 0.0018	0.29 ± 0.33
150	0.8165 ± 0.0017	0.8126 ± 0.0018	0.47 ± 0.30
200	0.8200 ± 0.0017	0.8191 ± 0.0017	0.12 ± 0.30
250	0.8544 ± 0.0016	0.8544 ± 0.0016	0.01 ± 0.26

dropoff in efficiency is due directly to the drop in track curvature, Monte Carlo tracks with momenta less than 100 MeV should be reconstructed with around 1% less efficiency when subjected to a 1.5 T magnetic field instead of the true CLEO magnetic field.

To examine this effect, I compare the efficiencies of Monte Carlo slow pions generated with magnetic field strengths of 1.5 and 1.4861 Tesla. The relative efficiencies at each slow pion momentum are given in Table A.6. No shift can be resolved with this statistical precision. I therefore conclude that the drop in slow pion efficiency with decreasing momentum is not due primarily to the increase in track curvature.

Figure A.4 provides supporting evidence for this conclusion. This figure plots the efficiency as a function of angle for each slow pion momentum. As the track angle increases across each plot, the transverse momentum decreases, and the track

Table A.7: The variation in slow pion efficiency due to late hits in `PRELIB CLEOG`. The second column gives the efficiency found with `PRELIB CLEOG`. A new version of `CLEOG` in which these late hit effects have been repaired was used to calculate the efficiencies given in the third column. The variation as a fraction of the reference `PRELIB CLEOG` is given last.

p_π (MeV)	$\epsilon_{\rm ref}$	$\epsilon_{\rm new}$	variation (%)
60	0.5923 ± 0.0022	0.5718 ± 0.0022	3.45 ± 0.52
80	0.7601 ± 0.0019	0.7601 ± 0.0019	0.00 ± 0.36
100	0.7893 ± 0.0018	0.7880 ± 0.0018	0.16 ± 0.33
150	0.8165 ± 0.0017	0.8135 ± 0.0018	0.36 ± 0.30
200	0.8200 ± 0.0017	0.8198 ± 0.0017	0.02 ± 0.30
250	0.8544 ± 0.0016	0.8539 ± 0.0016	0.05 ± 0.26

curvature increases. Under the hypothesis that the drop in slow pion efficiency below 100 MeV is due to the increase in track curvature, we would expect the efficiencies in Figure A.4 to fall as the track angle increases. Instead, each plot shows a plateau in efficiency across a range of curvature, which indicates that the efficiency is not directly sensitive to the track curvature.

A.6.3 Late Hit Effects

As described above in the section covering the topic of high TDC values, `PRELIB CLEOG` does not deal with late hits correctly. This error can affect the slow pion efficiency by corrupting both the VD charge information and cathode hits. This problem is important for pions below 100 MeV, which typically stop in the CLEO detector, and then eventually decay to electrons via muons. To show the magnitude of this effect, I measured the single-track efficiency with both the standard `PRELIB`

CLEOG, and with my modified version, in which these effects have been eliminated. Table A.7 gives my results.

The existence of these late hits does not affect the slow pion efficiency at 80 MeV and above. However, the late hits inflate the Monte Carlo slow pion efficiency at 60 MeV. This effect is due to the artificial presence of late cathode hits in PRELIB Monte Carlo. These cathode hits are produced by daughter particles of the slow pion, and they tend to be near the original track. Since the late cathode hits of the daughter lie near the track of the parent pion, the addition of these hits to the reconstructed track information can actually improve the quality of the fit.

A.6.4 Net Systematic Uncertainty

The net systematic uncertainty in single-track efficiency can be calculated based on the variations in reconstruction efficiency presented above. I give this combined systematic uncertainty in Table A.8. To get the values in this table, I used half of the variations listed in Tables A.2 and A.3.

The limited statistical precision of the knob-turning studies contributes a statistical component to the combined systematic uncertainty. The six variations in Monte Carlo slow pion efficiency given in Tables A.2–A.7 were all calculated with a common baseline. Hence, a direct combination of the statistical uncertainties in quadrature would exaggerate the size of the net statistical uncertainty. Instead, I expressed the net systematic error as a function of the common baseline and six variant efficiencies, and derived the net statistical component from this formula. The statistical portions of the uncertainties are listed second in Table A.8. (I keep

Table A.8: Net single-track systematic error. The net systematic uncertainty in slow pion efficiency calculated from the variations given in Tables A.2–A.7. The portion of the uncertainty due to the statistical precision of the knob-turning studies is listed second.

p_π (MeV)	uncertainty (%)
60	9.70 ± 0.68
80	2.67 ± 0.46
100	2.03 ± 0.51
150	2.24 ± 0.43
200	1.71 ± 0.36
250	0.97 ± 0.33

the purely statistical components of the systematic uncertainty distinct for use in calculating the integrated integrated slow pion uncertainty in the next section.)

At 100 MeV and above, the total systematic error for single tracks is dominated by the uncertainty in drift distance smearing. At the lowest momenta, the error is dominated by the uncertainty in the amount of material in the central detector, followed by the late hit systematic error.

A.7 Conclusions

I summarize the results of my studies in Table A.9. At each of six slow charged pion momenta, I give the shift in slow pion reconstruction efficiency due to the difference in event environment between data and Monte Carlo. I also list the total uncertainty in the efficiency, including both the single-track systematic uncertainties and all purely statistical effects.

Table A.9: Event environment shifts in slow pion reconstruction efficiency. For each slow pion momentum, I list the event environment shift followed by the total uncertainty in the efficiency. The uncertainty includes both single-track systematic uncertainties and all statistical uncertainties. The shifts are completely correlated between different momenta, while the uncertainties are more than 90% correlated.

p_π (MeV)	shift $\pm$ uncertainty (%)
60	6.19 ± 9.76
80	5.69 ± 2.78
100	4.26 ± 2.16
150	1.44 ± 2.31
200	0.60 ± 1.79
250	0.11 ± 1.07

The number of most interest to CLEO analyses is the uncertainty in the slow pion efficiency integrated over a particular slow pion momentum spectrum. Such a calculation requires a momentum spectrum; I use the `QQ` level momentum spectrum of slow pions produced by D^{*+} decays in $B\bar{B}$ events in the `PRELIB` Monte Carlo. Because I have examined the efficiency at six discrete slow pion momenta, I bin the slow pion distribution as shown in Table A.10. I assume the slow pion efficiency to be zero below 50 MeV. (This is approximately correct; a 50 MeV cut on the reconstructed pion momentum would eliminate any discrepancy.) For the other momentum bins, I use the Monte Carlo embedded efficiency (Table A.1) to arrive at a distribution of reconstructed slow pions.

I have calculated the net uncertainty in the slow pion efficiency in four different ways. The first method is the most conservative. In this method, I treat the difference in embedded efficiency between data and Monte Carlo as a systematic

Table A.10: The distribution of slow pions produced by D^{*+} decays in $B\bar{B}$ events. The binning is given in the first column.

p_π range (MeV)	events
0– 50	178655
50– 70	196860
70– 90	241005
90–125	400495
125–175	313275
175–225	79600
225 on up	1165

uncertainty. For each slow pion momentum, I add the entries in the last columns of Tables A.1 and A.8 together linearly to produce an net systematic error. I separately add the purely statistical components of this net systematic in quadrature. Next, I sum the systematic error over the six momentum bins, weighting each bin by the distribution of reconstructed slow pions. This is again a linear sum, as both the systematic shifts due to event environment and the single-track systematic errors are completely correlated between slow pion momentum bins. I add the purely statistical components of the net systematic error in quadrature over slow pion momenta. Finally, I add the purely statistical component to the rest of the systematic error. This method yields a total systematic uncertainty, integrated over the slow pion momentum spectrum, of 6.5%.

The difference in embedded efficiency between data and Monte Carlo is a well measured effect; its size and direction are known. As such, it can be treated not as an uncertainty, but as a correction to be applied to the Monte Carlo efficiency.

My second method adopts this approach. I apply the shifts in the last column of Table A.1 to the reconstructed slow pion distribution, and I combine the statistical uncertainties in these shifts with those in Table A.8. I then calculate the total systematic uncertainty as in the first method, with the shifted slow pion distribution instead of the observed one. Taking this approach, I compute a net systematic uncertainty of 3.0%.

My last two methods are modified versions of the first two. The uncertainty in the slow pion efficiency at 60 MeV is substantially larger than at the higher momentum values. I can therefore reduce the net systematic uncertainty by imposing a slow pion momentum cut at 70 MeV. The improvement comes at a cost; the cut eliminates about 10% of the slow pions found relative to a 50 MeV cut. My third method is identical to the first save for the addition of this 70 MeV slow pion momentum cut. This third method yields a net systematic uncertainty of 5.5%. Finally, my fourth method is simply the second plus the 70 MeV cut; I obtain an integrated systematic error of only 2.2% with this procedure.

The statistical component of these integrated systematic errors is small. To determine the size of this contribution, I recalculate the net systematic errors after artificially setting all the statistical components of the various uncertainties to zero. The changes in the integrated systematic errors are all 0.1% or less. My results therefore would not be substantially improved by running these studies with larger numbers of slow pions.

I have performed all of my studies using the 4sC dataset exclusively. In particular, I have used the archived 4sC `PASS2` executable for all track reconstruction, and generated Monte Carlo events using 4sC constants. The slow pion efficiency is known to differ across the various CLEO datasets. Substantial changes in the tracking code were made between the 4s4 and 4s5 datasets; these changes improved the efficiency for finding the lowest momentum pions. In addition, the overall performance of the CLEO detector has degraded as the apparatus has aged. These changes in detector performance are modeled through dataset by dataset tuning of the Monte Carlo, and the same tracking code is run on data and Monte Carlo events. In principle, the uncertainty in the slow pion efficiency should not be affected significantly by variations in the efficiency itself between datasets. However, I have not tested this assumption in any way.

I intend to do further embedding studies with the recompress data and Monte Carlo. The recompress Monte Carlo promises several improvements. It will be free from all artificial late hit effects. The uncertainties in hit efficiency and drift distance smearing are expected to be reduced significantly thanks to careful tuning of the Monte Carlo by the Monte Carlo tracking group [72]. Once recompress Monte Carlo is available for all CLEO II datasets, I will extend my efficiency studies across them all.

APPENDIX B

TRACKING EFFICIENCY STUDIES: RECOMPRESS RESULTS

In this Appendix, I describe the results of several studies of the CLEO II charged track reconstruction efficiency. I do these studies in a dataset-balanced way across the CLEO II recompress data. I examine the influence of event environment on this efficiency by embedding Monte Carlo tracks into both data and Monte Carlo events. In addition, I quantify the sensitivity of the Monte Carlo single track efficiency to details of the simulation. I apply these methods to samples of soft tracks, below 250 MeV, and hard tracks, between 0.5 and 2.0 GeV.

B.1 Introduction

In Appendix A, I present several studies of the charged slow pion reconstruction efficiency done with the `PRELIB` code library and the 4sC dataset. These studies were originally done before the recompress project was complete. In this Appendix, I have apply similar techniques to the full recompress CLEO II data sample, including the 4s2–G datasets. As Appendix A already describes the principles behind these studies in detail, I limit myself here to summaries of the techniques, with longer explanations where my techniques have changed. This Appendix is a slightly-modified version of a CLEO internal note, CBX 2000-32.

The basic goal of these slow pion studies is not to measure the absolute magnitude of the slow pion efficiency. It is instead to quantify any relative difference in slow pion efficiency between data and Monte Carlo, and the uncertainty in this quantity. The overall reconstruction efficiency for a particular analysis is typically extracted from a signal Monte Carlo sample. The data-MC relative efficiency difference and its uncertainty can then be used to establish a systematic error due to slow pion reconstruction.

I present two types of studies in this CBX. The first is the "embedding" study. The principal difference in the reconstruction efficiency between data and Monte Carlo is due to the "event environment." This term refers to the effects of the hits due to other tracks in an event on the reconstruction of the slow pion track. I measure this effect by "embedding" slow pion tracks into both data and Monte Carlo "bed" events — that is, inserting the hits of a slow pion track into another event. I compare the efficiencies for reconstructing similar sets of tracks between data and Monte Carlo events to measure any efficiency difference due to event environment. Were I to measure a significant event environment effect, I could then correct for it in my analysis. I present the results of my embedding study of slow pion tracks in Section B.2.

The second type of study is the "knob-turning" study. The embedding study does not address the question of how a Monte Carlo slow pion track might differ intrinsically from a data slow pion track. The uncertainties in the tuning of the CLEO detector simulation in Monte Carlo can thus lead to uncertainties in the slow pion efficiency. The baseline in a knob-turning study is the reconstruction efficiency for single slow pion tracks generated with the standard `CLEOG` library. I also create a variant `CLEOG` job in which I have varied some tuned Monte Carlo parameter by its uncertainty, turning the "knob" of that parameter. The difference between the slow pion reconstruction efficiencies measured with the variant `CLEOG` and the baseline establishes the uncertainty in the slow pion efficiency due to the uncertainty in that particular knob. I present the results of several knob-turning studies of slow pion tracks in Section B.3.

My interest in the slow pion efficiency stems from the fact that it contributes the largest systematic uncertainty to my analysis of $\bar{B}^0 \to D^{*+}\ell^-\bar{\nu}$. The standard 5% uncertainty in the slow pion efficiency leads directly to a 5% systematic error in the branching fraction for this decay. Accordingly, I have used the momentum spectrum of slow pions produced in $\bar{B}^0 \to D^{*+}\ell^-\bar{\nu}$ decays at the $\Upsilon(4S)$ as the basis for the studies presented here. In order to make these results more generally useful, I also present the uncertainties in the slow pion efficiency as a function of pion momentum in Section B.4.

The techniques I use for slow pions can also be used to examine the reconstruction efficiency of hard tracks. I present the results of a set of efficiency studies on tracks between 0.5 and 2.0 GeV in Section B.5.

I summarize and discuss my results in Section B.6.

B.2 Slow Pion Embedding Study

The slow pion embedding study has undergone several changes in detail and one change in philosophy since I did the `PRELIB` study presented in Appendix A. I now select bed events covering all the recompress CLEO II data sample, not just one dataset. I use single-track events generated across the slow pion momentum spectrum, rather than single tracks generated at discrete momenta. My standard definition of a "found" slow pion is now based on a D^*–D mass difference calculated with the reconstructed slow pion, not the similarity between the reconstructed and generated slow pion momentum.

The philosophical change is in the treatment of the continuum background. In both studies I compare the reconstruction efficiency for tracks embedded in data events to that for tracks embedded in Monte Carlo. In the `PRELIB` study, I used only data bed events from on-resonance running, and my Monte Carlo sample included both $B\bar{B}$ and continuum bed events. In the present study, I embed tracks in both on and off-resonance data, and I do a continuum subtraction to compute the reconstruction efficiency for tracks embedded in data $B\bar{B}$ events. I compare this result to the efficiency I measure for tracks embedded in Monte Carlo $B\bar{B}$ events. This method eliminates any need to model the continuum background, and any systematic errors due to such modeling. The cost is a doubling in the number of bed events from data, and a need to run more embedding jobs.

B.2.1 Selection of Bed Events

I select 20,000 bed events each from on-resonance data, off-resonance data, and generic $B\bar{B}$ Monte Carlo. These events are required to pass the following cuts:

- $N_{\text{tracks}} > 4$
- $R_2 \leq 0.4$
- Well-identified lepton:
  - `dpthmu` > 5 *or* – `r2elec` > 3
  - `muqual` $= 0$
- $0.8 \leq p_\ell \leq 2.4\,\text{GeV}$
- $|\cos\theta_\ell| < 0.71$

The only difference between these cuts and those used in the `PRELIB` embedding study is that the R_2 cut is increased from 0.3 to 0.4, in order to match the cut used in the $D^{*+}\ell^-\bar{\nu}$ analysis. I calculate both R_2 and the number of tracks using only tracks with good z information (`kincd` $\neq -1, -3$) that are approved by the Trackman processor. I require the same properties of the lepton track.

I choose the bed events to be uniformly balanced across the 4s2–G datasets. I use the on-resonance luminosities reported in `cleog_runs.dat` to determine the number of bed events to select in each dataset. For each dataset, I then randomly select this number of events from among those that pass my cuts. The random selection ensures that the bed events are distributed uniformly in each dataset. For on-resonance data, this method yields a set of events distributed uniformly across all 4s2–G on-resonance running. In the case of off-resonance data, the events are selected uniformly within each dataset, and weighted dataset-to-dataset in a way that accounts for the differences in the ratio of on to off-resonance luminosity between datasets.

Given the list of bed events from the hadron skims, I construct a skim of these events in the `.fzx` format required by the embedding machinery. As the bed events are chosen to be distributed uniformly across the full 4s2–G dataset, this process requires running `CLEVER` skim jobs on nearly 200 tapes.

The cuts above have an efficiency $\epsilon_{\mathrm{onres}} = 4.494 \pm 0.006\%$ for on-resonance events and $\epsilon_{\mathrm{cont}} = 1.370 \pm 0.005\%$ for off-resonance events in the hadron skim. The fraction of $B\bar{B}$ events in the on-resonance data is $f_{B\bar{B}} = 17.7 \pm 0.3\%$. Based on this information I can determine the cut efficiency $\epsilon_{B\bar{B}}$ for $B\bar{B}$ events. The total number of on-resonance events N_{onres} is the sum of the numbers of $B\bar{B}$ events, $N_{B\bar{B}}$ and continuum events, N_{cont}:

$$N_{\mathrm{onres}} = N_{B\bar{B}} + N_{\mathrm{cont}}. \tag{B.1}$$

The numbers of events that pass the cuts above are:

$$\epsilon_{\mathrm{onres}} N_{\mathrm{onres}} = \epsilon_{B\bar{B}} N_{B\bar{B}} + \epsilon_{\mathrm{cont}} N_{\mathrm{cont}}. \tag{B.2}$$

Solving for $\epsilon_{B\bar{B}}$ gives

$$\begin{aligned} \epsilon_{B\bar{B}} &= \frac{1}{N_{B\bar{B}}}(\epsilon_{\mathrm{onres}} N_{\mathrm{onres}} - \epsilon_{\mathrm{cont}} N_{\mathrm{cont}}) && \text{(B.3)} \\ &= \left(\frac{1}{f_{B\bar{B}}}\right)\epsilon_{\mathrm{onres}} - \left(\frac{1 - f_{B\bar{B}}}{f_{B\bar{B}}}\right)\epsilon_{\mathrm{cont}}. && \text{(B.4)} \end{aligned}$$

With the on- and off-resonance efficiencies above I obtain $\epsilon_{B\bar{B}} = 19.0 \pm 0.3\%$. The fraction $x_{B\bar{B}}$ of on-resonance events that pass the cuts is given by

$$x_{B\bar{B}} = 1 - (1 - f_{B\bar{B}})\frac{\epsilon_{\mathrm{cont}}}{\epsilon_{\mathrm{on}}}. \tag{B.5}$$

This equation gives $x_{B\bar{B}} = 74.9 \pm 0.1\%$.

I generate $B\bar{B}$ Monte Carlo bed events with the same dataset distribution as the data bed events. I use the `CLEOG` multi-run feature to ensure that the events are correctly distributed across each dataset. I find the efficiency of my bed event selection cuts to be $18.9 \pm 0.1\%$ in $B\bar{B}$ Monte Carlo, a value consistent with that obtained from data.

B.2.2 Generation of Single-Track Events

I generate single-track slow pions distributed according to the momentum spectrum of slow pions from $\bar{B}^0 \to D^{*+}\ell^-\bar{\nu}$ decay. I do so with the method I outlined parenthetically in Appendix A. I generate full $\bar{B}^0 \to D^{*+}\ell^-\bar{\nu}$ decays at generator level. I use a variant `decay.dec` that forces every particle other than the slow pion to decay to a neutrino. As a result, only the slow pion track produces hits in the `CLEOG` detector simulation. I generate two sets of 20,000 slow charged pions, one of π^+ and the other of π^- tracks. I ensure the correct distribution across and within datasets with the same methods I use for the $B\bar{B}$ Monte Carlo bed events. For later use, I record not only the generator-level properties of the slow pion, but those of the other particles in the $\bar{B}^0 \to D^{*+}\ell^-\bar{\nu}$ decay.

B.2.3 Calculation of Efficiencies

My criterion for a "found" slow pion is based on the cuts I use in my $\bar{B}^0 \to D^{*+}\ell^-\bar{\nu}$ analysis. I combine the reconstructed slow pion π_s with the generator-level D meson produced in the same Monte Carlo D^* meson decay. I compute the mass $m(D\pi_s)$ corresponding to the sum of the four-vectors of the generator-level D and reconstructed π_s. With this information I can calculate the value of:

$$\Delta m = m(D\pi_s) - m_D. \tag{B.6}$$

Here m_D is the known Monte Carlo input D^0 mass, 1.8646 GeV. I then use the same cut on Δm as I employ in my analysis:

$$143.44 \leq \Delta m \leq 147.44\,\text{MeV}. \tag{B.7}$$

This cut is a 4 MeV window centered on the central Δm value of 145.44 MeV.

I impose a few additional cuts on the reconstructed slow pion track:

- correct charge
- not a z-escape track
- not a dredge-seed track
- `kincd` $\neq -1, -3$ (track has z-information)
- $|\cos\theta| \leq 0.7071$ **if** charge division used

I require that the track have the right sign, have good z information, and that it not be a z-escape or dredge-seed track. I do not accept tracks that are fit with charge-division information outside the "good barrel" region. Raw charge division information is converted to a z position with a set of conversion constants. These constants were tuned on tracks from CLEO II data, but only with tracks in the good barrel region. The constants are therefore only valid inside this angular region, and track fits that use charge-division information outside this angular region are not reliable. I do *not* place any cuts on Trackman variables for the slow pion, nor do I cut on variables such as `dbcd` or `z0cd`. I do not explicitly require that the slow pion track be Kalman-fit. However, in each of the slow pion studies described below, I find that all slow pion tracks passing my cuts are Kalman-fit tracks. Every slow pion result would therefore be identical with a Kalman-fit requirement.

In my efficiency calculations, I only consider slow pions that satisfy the cut:

- $|\cos\theta_\pi| \leq 0.90$.

This cut is placed on the generator-level slow pion. I do not consider tracks with dip angles greater than 0.9 in my analysis. Such tracks pass through the endcap of the VD, and the level to which the material in the VD endcap — including not only the endcap itself but pins, connectors, cables, etc. — is correctly modeled in Monte Carlo not well known. By neglecting these tracks I eliminate any sensitivity to this lack of information. In this embedding study, I find that fewer than 0.5% of the slow pions reconstructed after embedding in data have dip angles greater than 0.9, so this requirement costs little in efficiency.

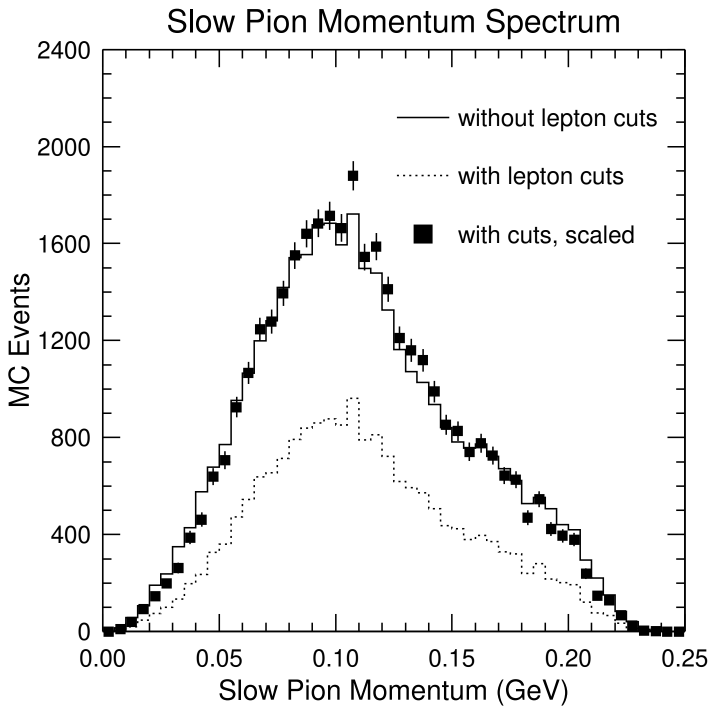

Figure B.1: The momentum spectrum of embedded slow pions. The solid histogram plots the spectrum of all slow pions generated, while the dotted shows the spectrum of those that pass the generator-level lepton cuts given in the text. With the points, I show the second spectrum normalized to the same area as the first.

I also place some cuts on the generator-level lepton:

- $0.8 \leq p_e \leq 2.4\mathrm{GeV}$
- $1.4 \leq p_\mu \leq 2.4\mathrm{GeV}$
- $|\cos\theta_\ell| \leq 0.7071$
- $\cos\theta_{D^*\ell} \leq 0$

Obviously only one of the first two cuts is imposed, depending on the species of

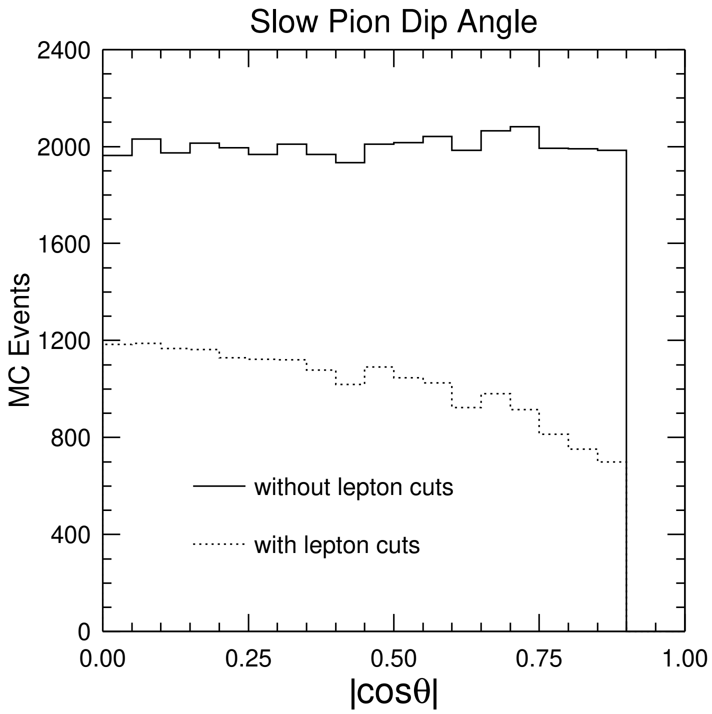

Figure B.2: The angular distribution of embedded slow pions. The solid histogram plots the spectrum of all slow pions generated, while the dotted shows the spectrum of those that pass the generator-level lepton cuts given in the text.

lepton generated in the event. The last cut is on the opening angle between the D^* and the lepton in the lab frame. These cuts are imposed simply for consistency with the $D^{*+}\ell^-\bar{\nu}$ analysis. The effect of these cuts, beyond a reduction in statistics, is a slight softening of the slow pion momentum spectrum, illustrated in Figure B.1. They also change the shape of the slow pion angular distribution, as I show in Figure B.2.

The definitions of the reconstruction efficiencies are similar to those in my `PRELIB` study. On an event by event basis, I require that more tracks pass my

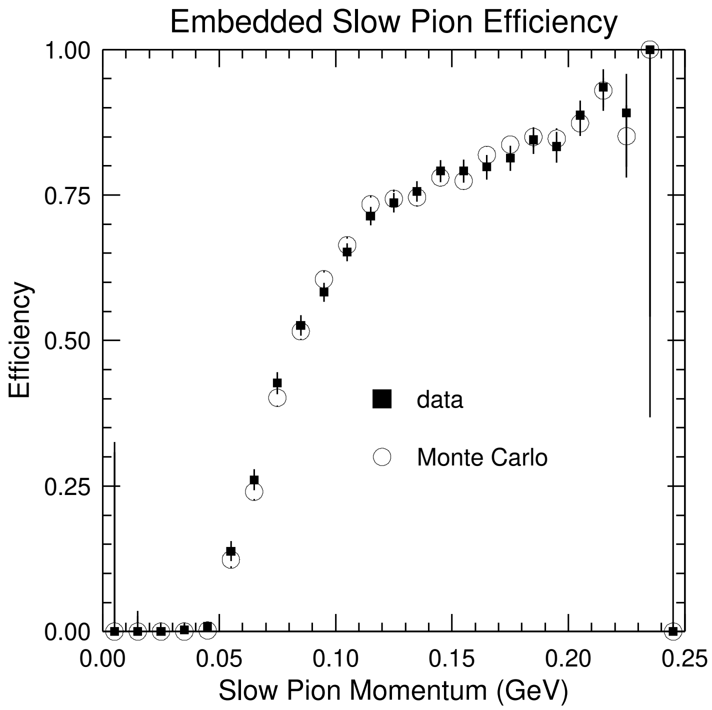

Figure B.3: The embedded slow pion efficiency as a function of momentum. The solid squares show the efficiency for reconstructing pions embedded in data, while the open circles represent the efficiency for pions embedded in Monte Carlo.

standard cut in the embedded event than in the bed event. The on-resonance reconstruction efficiency, for example, is the ratio of the number of events that satisfy this criterion to the total number of events embedded in on-resonance events:

$$\epsilon_{\text{on}} = \frac{N_{\text{embed}}}{N_{\text{tot}}}, \tag{B.8}$$

where events failing the generator-level cuts on the lepton and slow pion have been excluded from consideration. The off-resonance efficiency ϵ_{off} and Monte Carlo efficiency ϵ_{MC} are similarly defined.

I do a continuum background subtraction to the data in order to compare the

Table B.1: The embedded slow pion efficiencies in data and Monte Carlo. The efficiency for data is derived with Equation B.9. Both $\epsilon_{\rm data}$ and $\epsilon_{\rm MC}$ refer to reconstruction efficiencies for tracks embedded in $B\bar{B}$events.

bed	efficiency (%)
$\epsilon_{\rm on}$	59.21 ± 0.37
$\epsilon_{\rm off}$	60.27 ± 0.36
$\epsilon_{\rm data}$	58.86 ± 0.50
$\epsilon_{\rm MC}$	58.90 ± 0.37

data and Monte Carlo embedding efficiencies. The formula for the efficiency after embedding in $B\bar{B}$ events in data is:

$$\epsilon_{\rm data} = \left(\frac{1}{x_{B\bar{B}}}\right)\epsilon_{\rm on} - \left(\frac{1 - x_{B\bar{B}}}{x_{B\bar{B}}}\right)\epsilon_{\rm off}. \tag{B.9}$$

I plot the reconstruction efficiencies for slow pion tracks embedded in data and Monte Carlo versus slow pion momentum in Figure B.3. I present the embedded slow pion efficiencies for data and Monte Carlo in Table B.1. The uncertainty in $x_{B\bar{B}}$ introduces negligible uncertainty to the calculation of $\epsilon_{\rm data}$.

The relative efficiency difference between data and Monte Carlo embedded efficiencies is:

$$\frac{\Delta\epsilon_{\rm emb.}}{\epsilon} = \frac{\epsilon_{\rm data} - \epsilon_{\rm MC}}{\epsilon_{\rm MC}} \tag{B.10}$$

I find this relative efficiency difference to be $-0.07 \pm 1.06\%$.

B.2.4 The "Plus-One-Track" Systematic Uncertainty

I choose the cuts with which I select bed events to obtain samples that closely resemble $\bar{B}^0 \to D^{*+}\ell^-\bar{\nu}$ events in track environment, so that the embedding study

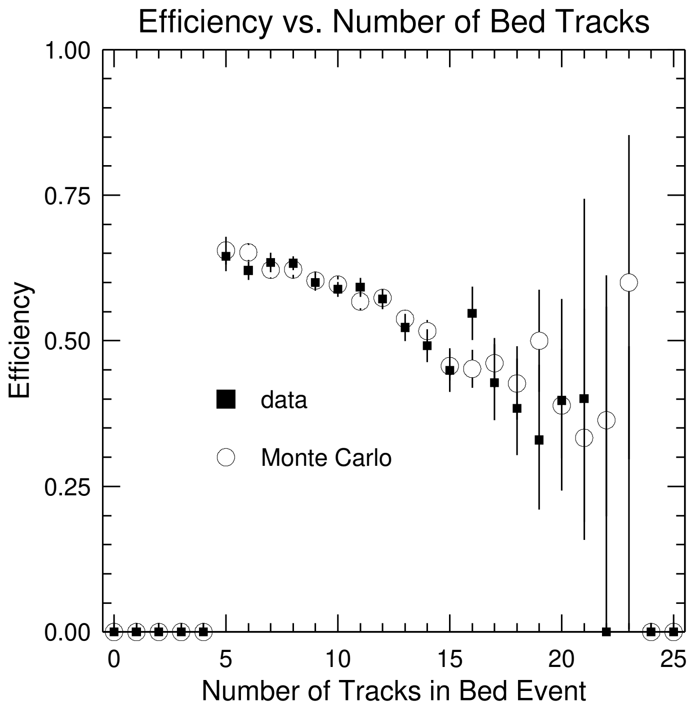

Figure B.4: The embedded slow pion efficiency as a function of the number of tracks in the bed event. The solid squares show the efficiency for reconstructing pions embedded in data, while the open circles represent the efficiency for pions embedded in Monte Carlo.

will reflect the relevant difference between data and Monte Carlo. However, there is one notable difference between a $\bar{B}^0 \to D^{*+}\ell^-\bar{\nu}$ event and an embedded track event. The characteristic number of tracks in $\bar{B}^0 \to D^{*+}\ell^-\bar{\nu}$ candidate events and in my bed events are similar. The embedded events, on the other hand, generally have a track multiplicity greater by one track — the track I embedded. In principle, this "plus-one-track" effect could bias the embedding study.

The slow track efficiency decreases as the number of other tracks in the event increases. Events containing more tracks simply have more cluttered event envi-

Table B.2: The mean reconstructed track multiplicity for several types of events, and the slope of the dependence of the embedded slow pion efficiency on the number of tracks in the bed event.

	data	MC
$\overline{N}$ (candidate signal)	9.75 ± 0.06	9.79 ± 0.02
$\overline{N}$ (bed events)	9.81 ± 0.03	9.87 ± 0.02
$\overline{N}$ (embedded events)	10.74 ± 0.05	10.84 ± 0.04
$\delta\epsilon/\delta N$ (%/track)	-1.55 ± 0.19	-1.67 ± 0.14

ronments. This effect is illustrated in Figure B.4. Nonetheless, the embedding study still makes a fair comparison: the plus-one-track effect is similar for both data and Monte Carlo bed events, so any bias must be a second-order effect.

I quantify the plus-one-track effect in the following way. I measure the mean number of reconstructed tracks in candidate $\bar{B}^0 \to D^{*+}\ell^-\bar{\nu}$ signal events for both data and Monte Carlo. I also measure the mean track multiplicity in embedded events in which I have found the embedded slow pion, according to my standard definition (Equation B.7). These multiplicities are listed in Table B.2. For reference, I also list the mean track multiplicities of my bed events, which are similar to those of the candidate signal events. It can clearly be seen that the mean reconstructed track multiplicity is approximately one track more when an embedded track is found than in the bed events.

In Table B.2, I also give the slope of the decline in slow track efficiency with the track multiplicity, which I obtain by a linear fit to the points in Figure B.4. The shift in the measured efficiency due to the presence of an additional track in the event is then given by:

$$\delta\epsilon = \left(\frac{\delta\epsilon}{\delta N}\right)(\overline{N}_{embedded} - \overline{N}_{signal}). \tag{B.11}$$

This equation gives $\delta\epsilon_{\rm data} = -1.45 \pm 0.20\%$, and $\delta\epsilon_{\rm MC} = -1.62 \pm 0.15\%$. The plus-one-track bias is the difference between these shifts, or a $0.17 \pm 0.25\%$ absolute tracking efficiency shift, tending to make the slow pion efficiency in data appear that amount higher relative to Monte Carlo. The statistical limitations of the study are due primarily to the measurement of the decline in tracking efficiency with the number of tracks in the bed event.

To establish a systematic uncertainty for the embedding study, I must scale the absolute tracking bias by the embedded efficiency. I add the magnitude and statistical uncertainty of the bias in quadrature, and divide by the efficiency of embedding in data (58.86%) to arrive at a systematic uncertainty of 0.52%.

B.3 Slow Pion Knob-Turning Studies

I perform four knob-turning studies to assess the effect of uncertainties in the recompress Monte Carlo tunings on the slow pion systematic error. The four knobs are a subset of those I studied in the `PRELIB` analysis (Appendix A): material in the inner detector, drift distance smearing, charge division smearing, and tracking chamber hit efficiency.

I have eliminated two knobs that were specific to `PRELIB` and not relevant to the recompress data. The standard `PRELIB` Monte Carlo was generated with a higher magnetic field magnitude, 1.5000 Tesla, than the actual CLEO data value, typically 1.4861 Tesla. I was unable to measure a statistically significant shift due to this effect in the PRELIB study, so long as tracks were always reconstructed with the same magnetic field value assumed in their generation. Recompress Monte Carlo is generated with the correct magnetic field value, which eliminates this possible source of discrepancy.

A bug in the PRELIB CLEOG processor caused late hits to be handled incorrectly in certain situations, an effect I described in the first CBX. This bug inflated the reconstruction efficiency of 60 MeV tracks by a relative amount of 3.6%. This bug was fixed for the recompress CLEOG.

My baseline for the knob turning studies is simply the efficiency with which I can reconstruct single slow pion tracks embedded into empty Monte Carlo events. I generate the slow pions in exactly the same manner as described in Section B.2.2. The baseline slow track efficiency is $69.74 \pm 0.34\%$. I calculate this efficiency with the same technique described in Section B.2.3, albeit there are no tracks in the empty bed events. The momentum dependence of this efficiency can be seen in any of Figures B.5–B.9.

B.3.1 Material Knob

In my first knob-turning study I increase the amount of material in the central detector by 10%. I accomplish this change by increasing the density of all materials in the central detector by that fraction. The 10% value is the level to which the amount of material in the inner detector is known [71]. I varied the material in the PRELIB study by this same amount. I illustrate the resulting change ver-

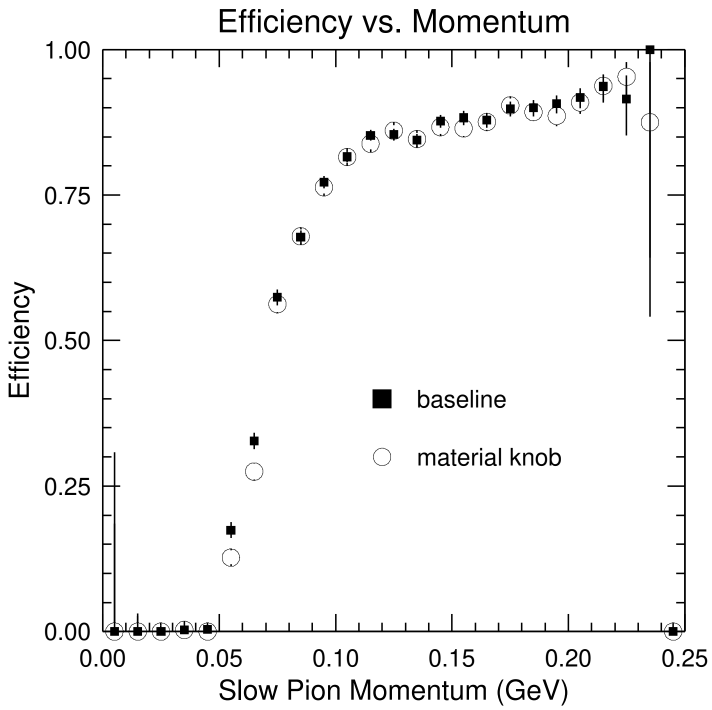

Figure B.5: The single-track slow pion efficiency as a function of momentum. The solid squares show the baseline single-track efficiency, while the open circles plot the efficiency with the material in the inner detector increased by 10%.

sus momentum in Figure B.5. The net efficiency over the slow pion momentum spectrum from $\bar{B}^0 \to D^{*+}\ell^-\bar{\nu}$ is $68.65 \pm 0.34\%$. The relative change in efficiency, corresponding to the systematic uncertainty due to material alone, is given by:

$$\frac{\Delta\epsilon_{\rm knob}}{\epsilon} = \frac{\epsilon_{\rm knob} - \epsilon_{\rm base}}{\epsilon_{\rm base}}. \tag{B.12}$$

This equation yields a relative efficiency change of $\Delta\epsilon_{\rm mat}/\epsilon = -1.58 \pm 0.69\%$ for the material knob.

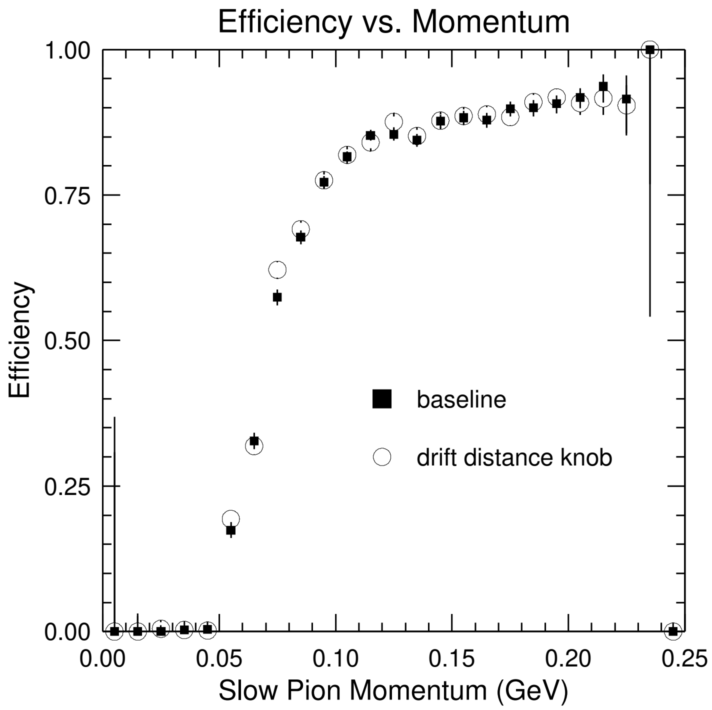

Figure B.6: The single-track slow pion efficiency as a function of momentum. The solid squares show the baseline single-track efficiency, while the open circles plot the efficiency with the drift distance smearing increased by 15%.

B.3.2 Drift Distance Smearing Knob

The second knob-turning study examines how the tuning of drift distance residuals relates to the slow pion efficiency. The widths of these distributions are tuned in the Monte Carlo to match the data through variation of a Gaussian used to smear the true Monte Carlo drift distances. A considerable amount of work was done to tune these distributions carefully for the recompress Monte Carlo [22]. The widths of these distributions are tuned directly, and the data and Monte Carlo distributions agree at the 2–3% level [73]. In the `PRELIB` Monte Carlo, the agreement was only to 7.5% [69, 70].

In my knob-turning study, I increase the width of the drift distance smearing by 15%, the same as the amount I used the the `PRELIB` study. The result is illustrated in Figure B.6. The net slow pion efficiency with the knob turned is $70.27 \pm 0.34\%$. As I turn the knob a factor of five farther than the expected data-MC variation, I scale the difference down by this factor to obtain a systematic uncertainty. The relative efficiency change is therefore $\Delta\epsilon_{\mathrm{smear}}/\epsilon = 0.15 \pm 0.14\%$.

B.3.3 Charge Division Smearing Knob

The third knob-turning study deals with the tuning of charge division residuals. CLEO measures track z position through a comparison of the relative amounts of charge collected on either end of the VD sense wires. The charge division residual is the difference between this measured z position and the reconstructed position of the track. In recompress Monte Carlo, the width of the residual distribution in each channel was tuned to better than the 5% level through adjustments to the width of a smearing Gaussian [74]. This change is a great improvement over the `PRELIB` situation, in which the smearings were hardwired based on studies early in the history of CLEO II, and were roughly a factor of two too small in the 4sC dataset. The `PRELIB` study compared an untuned, hardwired smearing width to a tuned amount, roughly a factor of two change. I increase the widths of the smearing Gaussians by 10% for this knob turning study. Figure B.7 plots the result. The net efficiency after turning the knob is $70.27 \pm 0.34\%$. Accounting

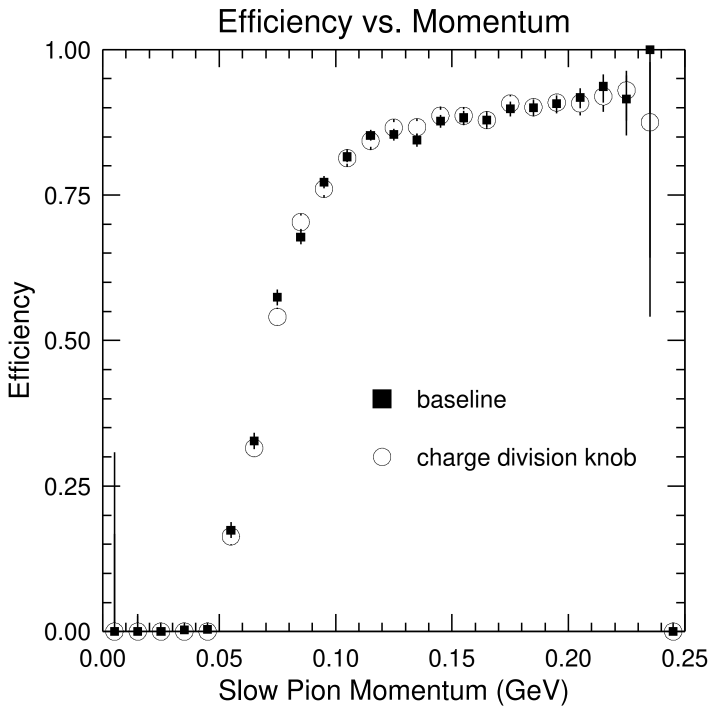

Figure B.7: The single-track slow pion efficiency as a function of momentum. The solid squares show the baseline single-track efficiency, while the open circles plot the efficiency with the charge division smearing increased by 10%.

for the twofold overturning of the knob, I find the relative efficiency change to be $\Delta\epsilon_{\rm qdiv}/\epsilon = -0.33 \pm 0.35\%$.

B.3.4 Hit Efficiency Knob

The final knob-turning study examines the effect of the single-hit efficiency in the three CLEO tracking chambers, the PT, VD, and DR. These efficiencies are affected by Monte Carlo tuning, but are not tuned directly, unlike the widths of the residual distributions. CLEO Monte Carlo tuning is done with tracks across the

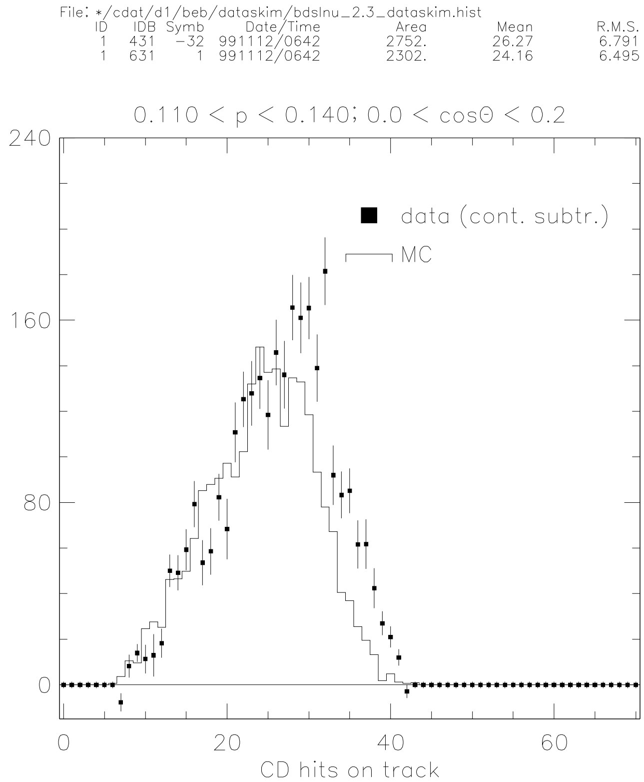

Figure B.8: The number of hits on data and Monte Carlo slow pion tracks in the region $110 < p_\pi < 140\,\mathrm{MeV}$, $0 < |\cos\theta_\pi| < 0.2$. The solid points show the data distribution, the histogram Monte Carlo.

full momentum spectrum. This sample naturally consists mostly of hard tracks, those above 250 MeV. For such tracks, the overall agreement in the number of hits on tracks between data and Monte Carlo is within a couple of percent [73], a nice cross-check that the tuning process is well-behaved.

For soft tracks, however, the picture is not so rosy. In certain regions of momentum and dip angle, I find soft pions in Monte Carlo to have up to 8% fewer hits than those in data. I show an example in Figure B.8. Furthermore, I find that the the size of the discrepancy differs among the three tracking devices. In order to

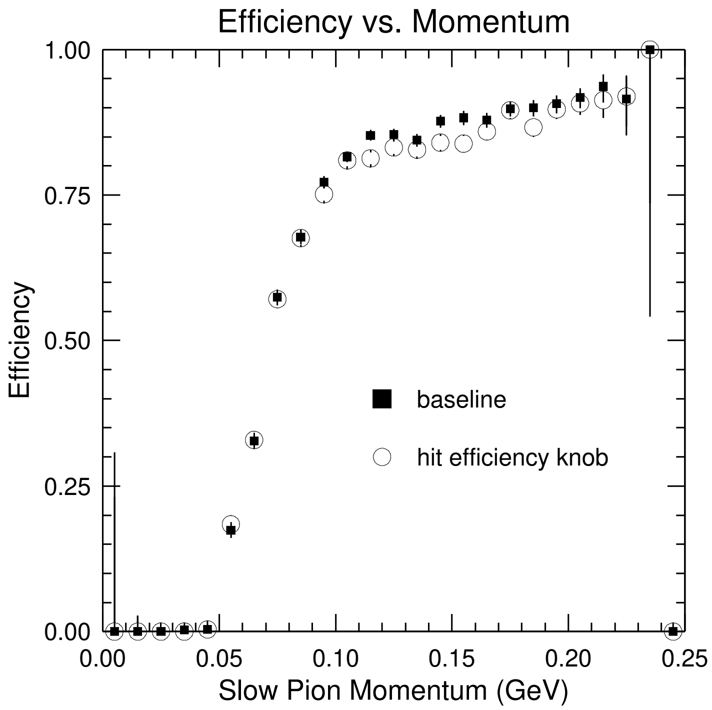

Figure B.9: The single-track slow pion efficiency as a function of momentum. The solid squares show the baseline single-track efficiency, while the open circles plot the efficiency with the tracking chamber hit efficiencies modified as described in the text.

obtain a variation sufficiently large to cover the difference between data and Monte Carlo, I simultaneously decrease the hit efficiency in the PT by 12%, in the VD by 8%, and in the DR by 22%. (I decreased the Monte Carlo hit efficiency instead of attempting to increase it to avoid saturation problems — the hit efficiency can always be decreased by a given fractional amount, but cannot always be increased, as it can not be greater than unity.) These changes decrease the number of hits on found tracks substantially, by amounts 30–40% greater than the difference between data and Monte Carlo. In the `PRELIB` study, a 5% variation was used, and I took

Table B.3: Summary of knob-turning results. The baseline efficiency, efficiency of each variant Monte Carlo, and associated systematic error are listed, followed by the combined systematic error.

knob	efficiency (%)	$\Delta\epsilon_{\text{knob}}/\epsilon$ (%)
(baseline)	69.75 ± 0.34	2.18 ± 0.76
material	68.65 ± 0.34	-1.58 ± 0.69
drift distance	70.27 ± 0.34	0.15 ± 0.14
charge division	69.29 ± 0.34	-0.33 ± 0.35
hit efficiency	68.29 ± 0.35	-1.46 ± 0.48
total		2.18 ± 0.76

this variation to be overkill by a factor of two. It is therefore likely that this effect was underestimated in the earlier study.

The effect of the change in hit efficiency is illustrated in Figure B.9. The net single-track slow pion efficiency after the change is $68.29 \pm 0.35\%$. After scaling the difference from the baseline down by 30%, I obtain $\Delta\epsilon_{\text{hiteff}}/\epsilon = -1.46 \pm 0.48\%$.

B.3.5 Combination of Knob-Turning Studies

I present the results of the four knob-turning studies in Table B.3. I also combine the four knobs in quadrature to obtain a net systematic uncertainty from knob-turning. As the four knob-turning studies share a common baseline, I propagate the statistical errors through a formula for the final systematic uncertainty in terms of the five efficiencies listed.

B.4 Summary of Slow Pion Efficiency Results

With the embedding study, I examine the effect of event environment on the slow pion efficiency. I find a data-Monte Carlo efficiency difference of $0.07\pm1.06\pm0.52\%$, where the first error is statistical and the second systematic. With the knob-turning studies, I examine how the level to which we believe the CLEO Monte Carlo to be correct affects the uncertainty in the slow pion efficiency. These studies indicate that the data-Monte Carlo agreement is good to the $2.18\pm0.76\%$ level. Combining all these numbers in quadrature, I conclude that the systematic uncertainty due to slow pion efficiency is 2.6% for the distribution of slow charged pions in the $D^{*+}\ell^-\bar{\nu}$ analysis.

B.4.1 Breakdown of Efficiency Results by Momentum and w

So that my results may be of general use, I perform the complete analysis in bins of slow pion momentum. I present the results in Table B.4, as an engineering table that other CLEO collaborators may use to compute the systemic uncertainty due to slow pion efficiency in their analyses. As such, values in the table are given to more digits than warranted by their individual statistical uncertainties. The extra digits are intended to allow accurate summation over any given slow pion momentum spectrum.

To generate Table B.4, I do not apply the cuts to the generator-level lepton that I use to calculate the slow pion efficiency for the $D^{*+}\ell^-\bar{\nu}$ analysis. The table therefore assumes that slow pions are uniformly distributed in $\cos\theta$. Without these

Table B.4: Slow pion efficiency results as a function of momentum. The first column is the measured shift due to event environment, as established by the embedding study. The next four columns break down the knob-turning results by momentum. The final column is the combined statistical uncertainty.

momentum	$\Delta\epsilon/\epsilon$ (%)					
(MeV)	env.	mat.	dist.	qdiv.	hit.	stat. err.
50 – 60	16.24	−24.11	0.71	−4.47	−0.28	14.87
60 – 70	8.92	−16.38	0.74	0.17	1.80	8.21
70 – 80	−1.45	−2.15	1.08	−1.17	1.13	4.65
80 – 90	−2.41	−0.88	0.10	−0.30	−1.92	3.53
90 – 100	−2.49	−1.84	−0.26	−0.28	−2.55	2.94
100 – 110	−0.16	1.82	0.26	−0.28	−0.10	2.61
110 – 120	−1.82	−1.58	−0.13	−1.04	−3.71	2.34
120 – 130	−1.43	−0.88	0.02	−0.08	−3.01	2.33
130 – 140	2.36	−1.02	−0.02	0.49	−2.08	2.59
140 – 150	−1.44	0.36	0.18	0.39	−1.03	2.49
150 – 160	1.11	0.18	0.39	0.97	−3.25	2.59
160 – 170	−3.46	0.71	0.13	−0.12	−0.84	2.58
170 – 180	−1.25	−0.65	−0.11	−0.93	−1.68	2.59
180 – 190	−1.93	−1.46	−0.08	−0.01	−1.86	2.86
190 – 200	−0.22	−2.55	−0.02	−0.56	−2.19	3.08
200 – 210	−0.82	0.06	−0.40	0.76	−0.23	3.21
210 – 220	−4.75	−1.83	−0.12	−2.29	−2.24	3.98
220 – 230	0.09	4.64	0.51	0.95	−0.31	9.54

cuts, the embedding study result is $\Delta\epsilon/\epsilon = -0.82 \pm 0.77 \pm 0.52\%$, while the knob-turning studies yield a combined $\Delta\epsilon/\epsilon = 2.19 \pm 0.56\%$. The net uncertainty in the slow pion efficiency for that spectrum is therefore still 2.6%.

In Table B.4, the second column, labeled "env.," lists the event environment difference between data and Monte Carlo, as determined in the embedding study. The next four columns give the results of the four knob turning studies as a function of momentum — the inner detector material study, labeled "mat."; the drift distance smearing study, labeled "dist."; the charge division study, labeled "qdiv."; and the hit efficiency study, labeled "hit." The final column is the combined statistical uncertainty of the embedding and knob-turning studies.

Table B.4 should be used with the following recipe to calculate the systematic uncertainty due to slow pion efficiency for a particular analysis. First, each row in the table should be weighted by the fraction of slow pions that fall in that momentum bin. The rows should then be summed over momentum bins. In performing these sums, the embedding shifts should be summed linearly over momentum, as the shifts are correlated between momentum bins. The results of the knob-turning studies should likewise be summed linearly. However, the statistical uncertainties are completely uncorrelated between momentum bins, and should be summed in quadrature.

These sums over momentum yield six numbers: 1) the total event environment difference between data and Monte Carlo; 2–5) the total effects of each of the four knob-turning studies, and 6) the total statistical error of the studies. These six numbers can simply be added in quadrature to give the final systematic uncertainty.

Table B.5: Slow pion efficiency results as a function of w. The first column is the measured shift due to event environment, as established by the embedding study. The next four columns break down the knob-turning results by momentum. The final column is the combined statistical uncertainty.

w	$\Delta\epsilon/\epsilon$ (%)					
	env.	mat.	dist.	qdiv.	hit.	stat. err.
1.000 – 1.051	9.68	−4.23	2.77	−1.59	5.16	14.80
1.051 – 1.102	6.58	−3.54	0.35	−1.02	1.21	7.50
1.102 – 1.153	−4.34	−5.75	0.60	−0.94	−1.27	4.79
1.153 – 1.204	0.41	−2.67	−0.25	−2.04	−3.40	3.75
1.204 – 1.255	−1.89	−1.20	0.03	0.06	−3.57	3.19
1.255 – 1.306	3.25	−2.54	0.16	−0.16	−0.44	3.01
1.306 – 1.357	−1.95	1.05	0.55	0.86	0.23	3.05
1.357 – 1.408	−0.44	−1.00	0.05	0.18	−1.40	2.82
1.408 – 1.459	−0.51	1.12	0.10	0.48	−2.18	2.61
1.459 – 1.510	3.93	−0.13	−0.23	−0.87	−0.87	3.47

An additional 0.52% should also be added to this final quadratic sum to account for the plus-one-track effect.

Finally, I give in Table B.5 my efficiency study results as a function of the generated value of the $\bar{B}^0 \to D^{*+}\ell^-\bar{\nu}$ form-factor parameter w. This table is organized identically to Table B.4. The results in this form are needed to evaluate the slow pion systematic error in the $|V_{cb}|$ analysis [68], in which $|V_{cb}|$ is extracted from a fit to the w distribution of $\bar{B}^0 \to D^{*+}\ell^-\bar{\nu}$ events. To create this table I apply the generator-level cuts on lepton momentum and direction. I apply the w-dependent cut on $\cos\theta_{D^*\ell}$ given in Table B.6 instead of the uniform cut $\cos\theta_{D^*\ell} < 0$. The w-dependent cut is over 99.9% efficient in each bin for signal events that pass

Table B.6: The w-dependent cut on $\cos\theta_{D^*\ell}$. This cut is used in the $|V_{cb}|$ analysis of $\bar{B}^0 \to D^{*+}\ell^-\bar{\nu}$ [68] and in the generation of Table B.5.

w	Max. $\cos\theta_{D^*\ell}$
1.000 – 1.051	none
1.051 – 1.102	none
1.102 – 1.153	none
1.153 – 1.204	none
1.204 – 1.255	none
1.255 – 1.306	0.25
1.306 – 1.357	0.0
1.357 – 1.408	-0.25
1.408 – 1.459	-0.5
1.459 – 1.510	-0.75

the lepton momentum cuts. The $|V_{cb}|$ analysis uses this approach to minimize the systematic uncertainty due to the $\bar{B}^0 \to D^{*+}\ell^-\bar{\nu}$ form factors, as the efficiency of the $\cos\theta_{D^*\ell} < 0$ cut changes slightly if the form factors are varied.

B.5 Hard Track Efficiency Studies

The methods I develop in the study of the slow pion efficiency are also applicable to the overall tracking efficiency. In this section, I present the results of embedding and knob-turning studies applied to the reconstruction of hard tracks.

B.5.1 Hard Track Embedding and Knob-Turning Studies

Though the general method for hard tracks is identical to that for soft tracks, there are several notable differences. The first is the distribution of tracks. I generate a sample of 80,000 charged pions, half of each sign. Unlike the slow pion case, these tracks are not generated according to the distribution of any physics process. I use a flat momentum distribution between 0.5 and 2.0 GeV and a flat $\cos\theta$ distribution. In the calculation of efficiencies, I consider only tracks with $|\cos\theta| < 0.9$ at the generator level, but I make no other generator level cuts.

I make several track-quality cuts on the reconstructed tracks. I make the same cuts as for the slow pion tracks, namely the requirements that the track have the correct sign, that it have z information, and that it be neither a dredge seed nor a z-escape fit. In addition, I make the following cuts:

- $\texttt{tng} \geq 0$
- $|\texttt{dbcd}| \geq 0.005\,\mathrm{m}$
- $|\texttt{z0cd}| \geq 0.05\,\mathrm{m}$

Note that I *do* use Trackman — to reject ghost pairs — whereas I did not use Trackman cuts on the slow pions.

My definition of a "found" high momentum track is that it pass the following cut:

$$\Delta|p| < 0.02\,\mathrm{GeV}. \tag{B.13}$$

where $\Delta|p|$ is the difference in the magnitudes of the generated and reconstructed

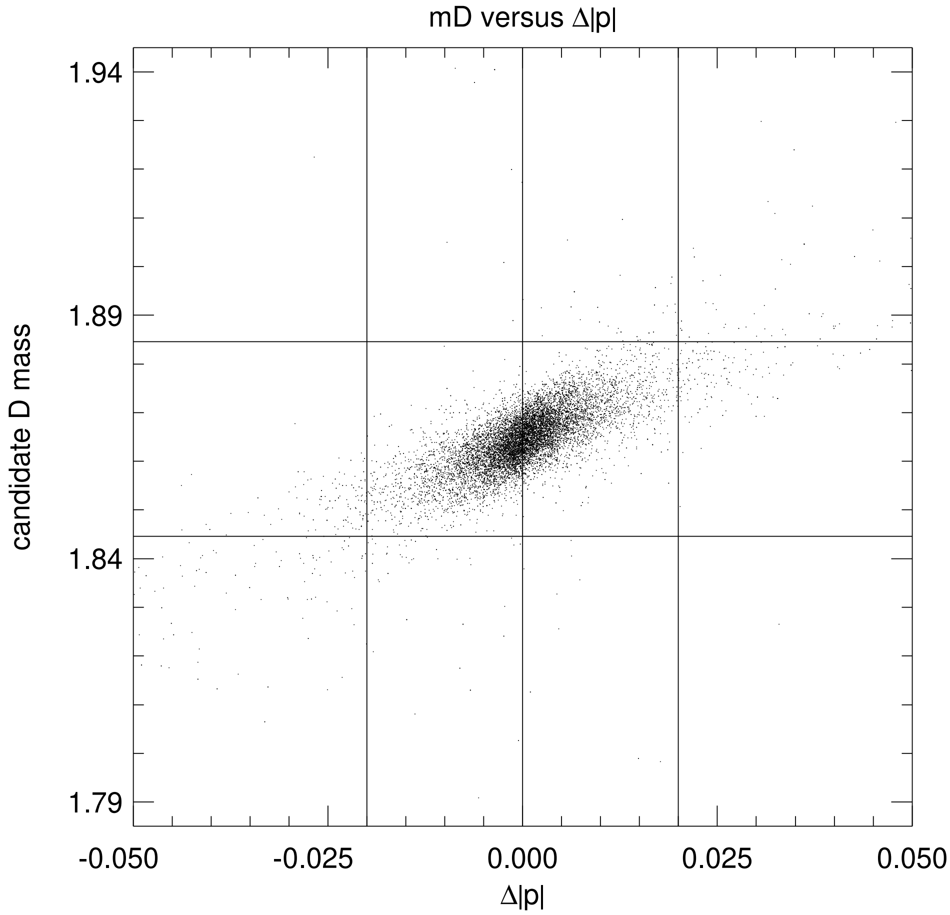

Figure B.10: The correlation between candidate D mass and $\Delta|p|$. Each point corresponds to a pion in a tagged $D^0 \to K^-\pi^+$ decay from a sample of Monte Carlo $\bar{B}^0 \to D^{*+}\ell^-\bar{\nu}$ decays. The horizontal axis gives the difference between the magnitudes of the generated and reconstructed pion momenta, while the vertical axis gives the mass of the reconstructed D meson. The Monte Carlo is generated with a D mass of 1.8646 GeV. The horizontal lines show the three-standard-deviation cut on $m(K\pi)$ used in the $\bar{B}^0 \to D^{*+}\ell^-\bar{\nu}$ analysis. The vertical lines show my $\Delta|p| < 0.02$ GeV cut. To make this plot, I place a tight cut on the quality of kaon reconstruction, $\Delta|p_K| \leq 0.01$ GeV, to illustrate only the effects of pion track mismeasurement.

Table B.7: The embedded hard track efficiencies in data and Monte Carlo. The efficiency for data is derived with Equation B.9. Both ϵ_{data} and ϵ_{MC} refer to reconstruction efficiencies for tracks embedded in $B\bar{B}$events.

bed	efficiency (%)
ϵ_{on}	87.84 ± 0.12
ϵ_{off}	88.06 ± 0.12
ϵ_{data}	87.77 ± 0.16
ϵ_{MC}	88.18 ± 0.12

pion momentum. I choose this variable because it is correlated with the difference between the reconstructed and true mass of D meson peaks formed from two charged tracks. This correlation is illustrated by Figure B.10.

I present the results of the hard track embedding study in Table B.7. I measure a relative data-Monte Carlo efficiency difference $\Delta\epsilon_{\mathrm{emb.}}/\epsilon = 0.47 \pm 0.30\%$.

I also examine the plus-one-track effect for high-momentum embedded tracks. I carry out a study identical to the slow pion case. I give the basic results in Table B.8. I plot the hard pion reconstruction efficiency as a function of the number of tracks in the bed event in Figure B.11. With Equation B.11, I find $\delta\epsilon_{\mathrm{data}} = -0.743 \pm 0.083\%$ and $\delta\epsilon_{\mathrm{MC}} = -0.736 \pm 0.053\%$, for an absolute tracking efficiency shift of $0.006 \pm 0.098\%$. I scale by the efficiency of embedding in data (87.77%) to obtain the systematic uncertainty of 0.11%.

I do only three knob-turning studies for hard tracks. I summarize the results in Table B.9. Charge division is never used for high-momentum tracks, so varying the Monte Carlo simulation of charge division smearing will not have an effect on high-momentum tracks. I study inner detector material and drift distance smearing in

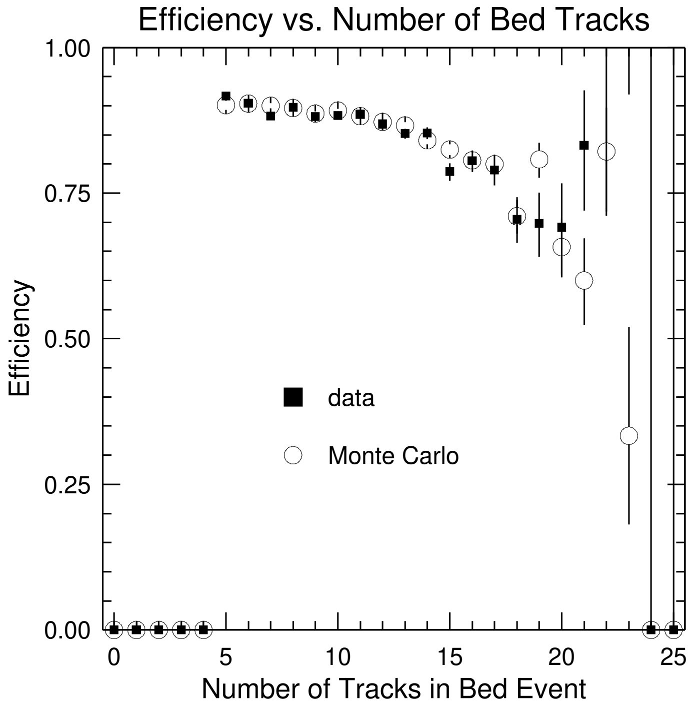

Figure B.11: The embedded hard pion efficiency as a function of the number of tracks in the bed event. The solid squares show the efficiency for reconstructing pions embedded in data, while the open circles represent the efficiency for pions embedded in Monte Carlo.

Table B.8: The mean reconstructed track multiplicity for several types of events, and the slope of the dependence of the embedded slow pion efficiency on the number of tracks in the bed event.

	data	MC
$\overline{N}$ (candidate signal)	9.75 ± 0.06	9.79 ± 0.02
$\overline{N}$ (bed events)	9.81 ± 0.03	9.87 ± 0.02
$\overline{N}$ (embedded events)	10.70 ± 0.04	10.78 ± 0.02
$\delta\epsilon/\delta N$ (%/track)	-0.78 ± 0.07	-0.74 ± 0.05

Table B.9: Summary of high-momentum knob-turning results. The baseline efficiency, efficiency of each variant Monte Carlo, and associated systematic error are listed, followed by the combined systematic error.

knob	efficiency (%)	$\Delta\epsilon_{\rm knob}/\epsilon$ (%)
(baseline)	92.84 ± 0.10	
material	92.54 ± 0.10	-0.32 ± 0.12
drift distance	92.98 ± 0.10	0.03 ± 0.03
hit efficiency	93.07 ± 0.10	0.26 ± 0.12
total		0.41 ± 0.12

exactly the same manner I describe above for the slow pions.

As I suggest in Section B.3.4, the agreement in the number of hits on tracks between data and Monte Carlo is much better for hard tracks than for soft. For this knob-turning study, I vary the hit efficiency by 4% in the PT, by 1% in the VD, and by 1.5% in the DR. I find these variations sufficient to cover the differences I observe in the number of hits on tracks.

In summary, the high-momentum embedding result is $0.47 \pm 0.30 \pm 0.11\%$, citing both statistical and systematic errors. The knob-turning result is $0.41 \pm 0.12\%$. The combination of all these numbers in quadrature yields an 0.7% per track tracking efficiency systematic.

In some CLEO analyses, only tracks in the "good barrel" region $|\cos\theta| \leq 0.7071$ are considered. I have carried out all the hard track efficiency studies considering only tracks in that angular region. In this case, I find an event environment effect with the embedding study of $\Delta\epsilon/\epsilon = 0.32 \pm 0.30 \pm 0.11\%$. The knob-turning studies add an additional systematic uncertainty $\Delta\epsilon/\epsilon = 0.41 \pm 0.14\%$.

The total systematic uncertainty for tracks in the good barrel region, with the cut of Equation B.13, is therefore 0.6% per track.

B.5.2 Effects of Cut Tightness

Both the embedding and knob-turning studies are structured around a particular meaning of a reconstruction efficiency. To be counted as a "found" track, the chamber hits produced by a charged particle must not only be reconstructed into a track, but that track must be measured to a certain level of accuracy. Thus, for both the slow and hard track efficiency studies, I have been careful to chose the level of accuracy appropriate for my own analysis, the study of the decay $\bar{B}^0 \to D^{*+}\ell^-\bar{\nu}$. These cuts have reflected the measurement accuracy needed to fall within D and D^* mass peaks.

In many cases, CLEO analyses do not need such levels of accuracy. For example, the lepton in a semileptonic analysis is not used to form a mass peak, and the overall candidate reconstruction efficiency is therefore not as sensitive to the measurement of the lepton track parameters as it is to those of the other tracks in the event. In "neutrino reconstruction" analyses, it is important to know the agreement between data and Monte Carlo in simply reconstructing tracks, with the accuracy of the reconstruction of secondary importance.

To address this issue, I examine the effects of loosening a cut that defines a "found" track on the reconstruction efficiencies and on the tracking systematic error. I present the results of these studies in Tables B.10 and B.11. Table B.10 gives results for tracks in the region $|\cos\theta| \leq 0.9$, while Table B.11 gives figures

Table B.10: Hard tracking efficiency versus cut tightness, $|\cos\theta| \leq 0.9$. As a function of the tightness of the cut, I list the reconstruction efficiencies and systematic errors from the embedding and knob-turning studies performed with high momentum tracks. The final column gives the combined systematic uncertainty for each cut.

$\lvert\vec{\Delta p}\rvert$ cut (GeV)	embedding		knob-turning		systematic (%)
	$\epsilon_{\rm MC}$ (%)	$\Delta\epsilon/\epsilon$ (%)	$\epsilon_{\rm base}$ (%)	$\Delta\epsilon/\epsilon$ (%)	
0.01	65.94 ± 0.25	1.39 ± 0.69	73.05 ± 0.17	1.35 ± 0.32	2.09
0.02	85.04 ± 0.19	0.53 ± 0.43	91.07 ± 0.11	0.46 ± 0.13	0.84
0.03	89.61 ± 0.16	0.35 ± 0.36	94.56 ± 0.09	0.34 ± 0.10	0.62
0.04	91.15 ± 0.15	0.32 ± 0.34	95.50 ± 0.08	0.26 ± 0.09	0.55
0.05	91.89 ± 0.15	0.23 ± 0.33	95.95 ± 0.07	0.26 ± 0.09	0.50
0.07	92.81 ± 0.14	0.22 ± 0.31	96.42 ± 0.07	0.22 ± 0.08	0.46
0.11	93.43 ± 0.13	0.28 ± 0.30	96.76 ± 0.07	0.18 ± 0.09	0.47
0.20	94.17 ± 0.13	0.35 ± 0.29	97.30 ± 0.06	0.18 ± 0.10	0.51
∞			97.87 ± 0.06	0.10 ± 0.07	

for the subset good barrel region $|\cos\theta| \leq 0.7071$.

I perform these studies with various cuts on the variable $|\vec{\Delta p}|$. This quantity is the magnitude of the vector difference between the generated and reconstructed track three-momenta. This variable is sensitive to the measurements of both the magnitude of the track momentum and the track direction. A 0.02 GeV cut on $|\vec{\Delta p}|$ is therefore tighter than the 0.02 GeV cut on $\Delta|p|$ I use in Section B.5.1. As a result, the systematic uncertainties listed in Tables B.10 and B.11 are greater than the 0.7% systematic uncertainty I calculate above.

The first column in each table gives the cut used. The second column is the efficiency to reconstruct hard tracks embedded in Monte Carlo with the given cut,

Table B.11: Hard tracking efficiency versus cut tightness, $|\cos\theta| \leq 0.7071$. As a function of the tightness of the cut, I list the reconstruction efficiencies and systematic errors from the embedding and knob-turning studies performed with high momentum tracks. The final column gives the combined systematic uncertainty for each cut.

$\lvert\vec{\Delta p}\rvert$ cut	embedding		knob-turning		systematic
(GeV)	ϵ_{MC} (%)	$\Delta\epsilon/\epsilon$ (%)	ϵ_{base} (%)	$\Delta\epsilon/\epsilon$ (%)	(%)
0.01	67.86 ± 0.28	1.22 ± 0.75	74.92 ± 0.18	1.13 ± 0.30	1.85
0.02	86.70 ± 0.21	0.34 ± 0.45	92.25 ± 0.11	0.49 ± 0.16	0.77
0.03	90.85 ± 0.17	0.26 ± 0.38	95.24 ± 0.09	0.27 ± 0.14	0.56
0.04	92.19 ± 0.16	0.33 ± 0.35	95.94 ± 0.08	0.23 ± 0.14	0.57
0.05	92.80 ± 0.16	0.21 ± 0.34	96.31 ± 0.08	0.21 ± 0.12	0.48
0.07	93.62 ± 0.15	0.21 ± 0.33	96.70 ± 0.08	0.20 ± 0.11	0.47
0.11	94.18 ± 0.14	0.28 ± 0.32	97.00 ± 0.07	0.14 ± 0.11	0.47
0.20	94.86 ± 0.14	0.34 ± 0.31	97.51 ± 0.07	0.08 ± 0.10	0.49
∞			98.06 ± 0.06	0.06 ± 0.10	

while the third column lists the systematic error from the embedding study. I use only 40,000 hard tracks to obtain the embedding numbers in these two columns.

The fourth and fifth columns give results from knob-turning studies with the given track reconstruction cut. I perform these studies with the full set of 80,000 tracks. The fourth column shows the efficiency with which single Monte Carlo tracks can be reconstructed for each cut, and the fifth column presents the systematic error from the knob-turning studies. The last column in each row gives the total systematic uncertainty for each cut, obtained by summing the embedding and knob-turning results in quadrature, along with an 0.11% plus-one-track systematic.

It is important to note that all these studies are done on the same set of tracks. The efficiencies and systematic errors are highly correlated between rows, and the rows in Tables B.10 and B.11 are likewise correlated.

Tables B.10 and B.11 show that the more precisely data and Monte Carlo track reconstruction must agree, the higher the assigned tracking systematic should be. However, for situations in which the required measurement accuracy of reconstructed tracks is less important, the systematic uncertainty levels off at around 0.5% per track.

The last row in Tables B.10 and B.11 is labeled as a cut on $|\vec{\Delta p}|$ at infinity. By this labeling I mean that I make no requirement on the track reconstruction parameters. Instead, I simply require that a track of the right sign be found in the event. I can only calculate such an efficiency with the single-track events I use in the knob-turning studies, as discarding the track reconstruction cut leaves no way to subtract the background of tracks in the bed event of an embedding study.

This final row addresses a different meaning of tracking efficiency, namely the efficiency to simply reconstruct the hits into a track in a clean environment, without considering how well the track parameters are measured. This sort of issue is also addressed in Jon Urheim's study [75] of track finding efficiency in tau decays. Urheim finds the difference in tracking efficiency between data and Monte Carlo to be $0.05 \pm 0.11\%$. This level of agreement is comparable to the figure $0.06 \pm 0.10\%$ I obtain with very different methods. Urheim's study and my own examine very different track momentum spectra and angular distributions.

B.6 Conclusions

I use both embedding and knob-turning studies to establish the systematic uncertainty due to slow pion efficiency for the study of $\bar{B}^0 \to D^{*+}\ell^-\bar{\nu}$ to be 2.6%. I provide an engineering table that will allow the reader to compute the systematic uncertainty for other slow pion momentum spectra. I also provide a similar breakdown versus the form factor variable w so that my studies can be used to determine systematic errors in the extraction of the CKM matrix element $|V_{cb}|$ from the analysis of $\bar{B}^0 \to D^{*+}\ell^-\bar{\nu}$.

I have also applied these methods to the study of hard track reconstruction efficiency. For tracks used in a D mass peak, which must be measured sufficiently well for the candidate to fall within the mass peak, I find a reconstruction systematic of 0.7% per track. In situations in which measurement of track parameters is less important, I conclude that a 0.5% per track systematic is sufficient.

REFERENCES

[1] N. Cabibbo, Phys. Rev. Lett. **10**, 531 (1963); M. Kobayashi and T. Maskawa, Prog. Theor. Phys. **49**, 652 (1973).

[2] L.-L. Chau and W.-Y. Keung, Phys. Rev. Lett. **53**, 1802 (1984); H. Harari and M. Leurer, Phys. Lett. B **181**, 123 (1986); H. Fritzsch and J. Plankl, Phys. Rev. D **35**, 1732 (1987); F. Botella and L.-L. Chau, Phys. Lett. B **168**, 97 (1986).

[3] Particle Data Group, "Review of Particle Properties," Eur. Phys. J. C **3**, 1 (1998).

[4] L. Wolfenstein, Phys. Rev. Lett. **51**, 1945 (1983).

[5] J. B. Richman and P. R. Burchat, Rev. Mod. Phys. **67**, 893 (1995).

[6] N. Isgur and M. B. Wise, Phys. Lett. B **232**, 113 (1989); N. Isgur and M. B. Wise, Phys. Lett. B **237**, 527 (1990).

[7] M. E. Luke, Phys. Lett. B **252**, 447 (1990).

[8] The BaBar Physics Book, P. F. Harrison and H. R. Quinn, Editors, SLAC_R_504 (1998).

[9] B. Barish *et al.* (CLEO Collaboration), Phys. Rev. D **51**, 1014 (1995) (hep-ex/9406005).

[10] J. Duboscq *et al.* (CLEO Collaboration), Phys. Rev. Lett. **76**, 3898 (1996).

[11] I. Caprini, L. Lellouch, and M. Neubert, Nucl. Phys. B **530**, 153 (1998) (hep-ph/9712417).

[12] M. Neubert, Phys. Rep. **245**, 259 (1994).

[13] P. Franzini and J. Lee-Franzini, Ann. Rev. Nucl. Part. Sci. 33, 1 (1983); G. Finocchiaro *et al.* (CUSB Collaboration), Phys. Rev. Lett. **45**, 222 (1980); T. Bohringer *et al.* (CUSB Collaboration), Phys. Rev. Lett. **44**, 1111 (1980).

[14] Y. Kubota *et al.* (CLEO Collaboration), Nucl. Instrum. Methods **A320**, 66 (1992).

[15] S. Sanghera, CLEO internal note CBX 95-38.

[16] D. Kreinick, CLEO internal note CSN 91/317.

[17] K. Berkelman, CLEO internal note CSN 95/342.

[18] P. Avery, CLEO internal notes CBX 91-12 and 92-40.

[19] R. Kutschke and A. Ryd, CLEO internal note CBX 96-20.

[20] S. Roberts *et al.*, CLEO internal note CBX 96-103.

[21] R. Brun *et al.*, GEANT 3.15, CERN DD/EE/84-1.

[22] V. Boisvert, CLEO internal note CBX 98-70.

[23] B. Gittelman *et al.*, CLEO internal note CBX 91-82.

[24] C. H. Wang *et al.*, CLEO internal note CBX 91-52.

[25] B. K. Heltsley, CLEO internal note CBX 92-108.

[26] B. K. Heltsley *et al.*, CLEO internal note CBX 95-35.

[27] T. Riehle, CLEO internal note to be released.

[28] Mark Palmer, private communication.

[29] B. K. Heltsley, CLEO internal note CBX 92-117.

[30] G. Wei, T. Skwarnicki, and R. Stroynowski, CLEO internal note CBX 94-72.

[31] K. Ecklund, B. Valant-Spaight, B. Berger, and R. Patterson, CLEO internal note CBX 00-54, Section 6.5.

[32] A. Weinstein, CLEO internal note CSN 96/347.

[33] G. Fox and S. Wolfram, Phys. Rev. Lett. **41**, 1581 (1978).

[34] `<http://www.lns.cornell.edu/restricted/CLEO/buzzwords/cdcc.doc>`. `MOTRSH` organizes the output of the `CDCC` routine [25] into a convenient form.

[35] G. Brandenburg *et al.* (CLEO Collaboration), Phys. Rev. D **61**, 07002 (2000) (hep-ex/9907057); T. U. Lee *et al.*, CLEO internal notes CBX 96-59, 97-17a, 98-53, 98-54, and 99-14.

[36] W. T. Ford, CLEO internal note CSN 94/329; updates to this note can be found in the file `/cleo/clib/cvssrc/vcfit/doc/README`.

[37] A. Anastassov *et al.* (CLEO Collaboration), Phys. Rev. Lett. **80**, 4127 (1998); A. Bellerive *et al.*, CLEO internal notes CBX 96-47, 97-50, and 98-11.

[38] D. Buskulic *et al.* (ALEPH Collaboration), Z. Phys. C **73**, 601 (1997); D. Buskulic *et al.* (ALEPH Collaboration), Phys. Lett. B **345**, 103 (1995).

[39] J. Bartelt *et al.* (CLEO Collaboration), Phys. Rev. Lett. **82**, 3746 (1999) (hep-ex/9811042); Y. Liu and R. Patterson, CLEO internal notes CBX 98-20 and 98-72.

[40] V. Fadeyev and R. Stroynowski, CLEO internal note CBX 00-43.

[41] K. Ecklund, B. Valant-Spaight, B. Berger, and R. Patterson, CLEO internal note CBX 00-54, Sections 6.6,6.7.

[42] S. E. Csorna *et al.* (CLEO Collaboration), Phys. Rev. D **61**, 111101 (2000) (hep-ex/0001013); A. Ershov, CLEO internal note CBX 99-64.

[43] B. Valant-Spaight *et al.*, CLEO internal note CBX 99-34

[44] Karl Ecklund, private communication, based on Reference [27]

[45] J. L. Goity and W. Roberts, Phys. Rev. D **51**, 3459 (1995).

[46] N. Isgur and D. Scora, Phys. Rev. D **52**, 2783 (1995). See also N. Isgur *et al.*, Phys. Rev. D **39**, 799 (1989).

[47] S. Anderson *et al.* (CLEO Collaboration), CLEO CONF 99-6 (CLEO 1999 conference paper); H. Nelson and T. Nelson, CLEO internal note CBX 86-62.

[48] P. Abreu *et al.* (DELPHI Collaboration), Phys. Lett. B **426**, 231 (1998), and references therein.

[49] P. Avery *et al.* (CLEO Collaboration), Phys. Lett. B **331**, 236 (1994).

[50] A. Anastassov *et al.* (CLEO Collaboration), CLEO CONF 96-8 (CLEO 1996 conference paper). This conference result combined the $\bar{B}^0 \to D^{*+}\ell^-\bar{\nu}$ form-factor data published in Reference [10] with $B^- \to D^{*0}\ell^-\bar{\nu}$ data. CLEO did not publish the combined result, but the central values from the combined analysis are used in the CLEO Monte Carlo.

[51] J. Bartelt *et al.* (CLEO Collaboration), Phys. Rev. Lett. **80**, 3919 (1998) (hep-ex/9711011); M. Dickson, CLEO internal notes CBX 96-61 and 97-77.

[52] J. P. Alexander *et al.* (CLEO Collaboration), CLEO preprint CLNS 00/1670, submitted to Phys. Rev. Lett. (hep-ex/0006002); S. Schuh and S. Stone, CLEO internal note CBX 00-7.

[53] B. H. Behrens *et al.* (CLEO Collaboration), CLEO preprint CLNS 00-1668, submitted to Phys. Rev. Lett. (hep-ex/0005013); A. Foland and P. Drell, CLEO internal note CBX 99-50; A. Foland *et al.*, CLEO internal note CBX 98-14.

[54] B. Barish *et al.* (CLEO Collaboration), Phys. Rev. Lett. **76**, 1570 (1996).

[55] M. Artuso *et al.* (CLEO Collaboration), Phys. Rev. Lett. **82**, 3020 (1999) (hep-ex/9811027); D. Jaffe *et al.*, CLEO internal note CBX 98-57 . The CBX result is in error by 30% due to an incorrectly-applied 15% efficiency correction.

[56] Mark Palmer, private communication.

[57] Dave Besson, electronic mail to the CLEO mailing list.

[58] D. S. Akerib *et al.* (CLEO Collaboration), Phys. Rev. Lett. **71**, 3070 (1993).

[59] H. Albrecht *et al.* (ARGUS Collaboration), Phys. Lett. B **324**, 249 (1994).

[60] P. Abreu *et al.* (DELPHI Collaboration), Z. Phys. C **71**, 539 (1996).

[61] K. Ackerstaff *et al.* (OPAL Collaboration), Phys. Lett. B **395**, 128 (1997).

[62] D. Buskulic *et al.* (ALEPH Collaboration), Phys. Lett. B **395**, 373 (1997).

[63] M. Margoni and F. Simonetto for the DELPHI Collaboration, DELPHI 99-107 CONF 294 (DELPHI 1999 conference paper).

[64] G. Abbiendi *et al.* (OPAL Collaboration), CERN preprint CERN-EP-2000-32, submitted to Phys. Lett. B. This result supersedes that of Reference [61].

[65] A. Abashian *et al.* (BELLE Collaboration), BELLE-CONF-0013 (BELLE 2000 conference paper).

[66] Recent results of the LEP B-oscillations working group are presented at `http://www.cern.ch/LEPBOSC`.

[67] M. Artuso *et al.* (CLEO Collaboration), Phys. Lett. B **399**, 321 (1997) (hep-ex/9701013).

[68] J. P. Alexander *et al.* (CLEO Collaboration), CLEO CONF 00-03 (CLEO 2000 conference paper); K. Ecklund, B. Valant-Spaight, B. Berger, and R. Patterson, CLEO internal note CBX 00-54.

[69] K. Bloom *et al.*, CLEO internal note CBX 96-101.

[70] I. Kravchenko *et al.*, CLEO internal note CBX 97-10.

[71] B. Heltsley *et al.*, CLEO internal note CBX 95-35, Reference 18.

[72] Craig Prescott, private communication.

[73] R. Briere, private communication.

[74] B. Berger, private communication. (!)

[75] J. Urheim, CLEO internal note CBX 99-53.

[76] This is a dummy page.

[77] This is not part of the thesis.